# A study on auto-ignition of poly(oxymethylene) dimethyl ethers and their mixtures with the primary reference fuel 90

A thesis accepted by the Faculty of Aerospace Engineering and Geodesy
of the University of Stuttgart in fulfillment of the requirements
for the degree of Doctor of Engineering Sciences (Dr.-Ing.)

by

**John Mburu Ngugi**
born in Mũrang'a County, Kenya

Main referee: Prof. Dr. rer. nat. Uwe Riedel

Co-referee: Prof. Dr.-Ing. Stefanos Fasoulas

Date of defense: 07.03.2023

Institute of Combustion Technology for Aerospace Engineering
University of Stuttgart

2023

*Printed and/or published with the support of the*
*German Academic Exchange Service*

# Acknowledgements

The current work was carried out at the Institute of Combustion Technology of the German Aerospace Center (DLR) in Stuttgart from October 2018 to December 2022, while I was on the DAAD scholarship.

First, I would like to thank my supervisor, Prof. Dr. Uwe Riedel, for his support and guidance. Thank you, Prof., for trusting me and allowing me to join your research team. I would also like to express my gratitude to my advisors, Dr. Marina Braun-Unkhoff and Dr. Clemens Naumann, for their generous support and guidance throughout my PhD research. I thank you for your helpful suggestions and comments on improving my work, and for having time to discuss my progress.

I would like to thank Mr. Norbert Ackermann and Jürgen Zahel for their technical assistance during the measurements. Additionally, I want to thank Dr. Sandra Richter for measuring the laminar burning velocities of the fuels under consideration. These measurements supplemented the experimental data I obtained for ignition delay times and allowed a comprehensive study of the oxidation chemistry of oxymethylene ethers. Thanks also to Dr. Trupti Kathrotia for working on the DLR concise reaction model, thus enabling a comparison between experimental and calculated data.

I also thank the entire Department of Chemical Kinetics and Analytics team at DLR for their support in various ways and for the wonderful working environment. In this regard, I want to acknowledge the shock tube team headed by Dr. Clemens Naumann for the many hikes and unforgettable moments.

I want to express my gratitude to my family, especially my parents, for their love, encouragement, and moral support throughout my PhD studies. In a special way, I want to thank my dear wife and our lovely kids for their love, understanding, and unending support until the completion of this research work.

I would like to thank Dedan Kimathi University of Technology, Kenya, for granting me academic leave to pursue my PhD in Germany. I also gratefully acknowledge the financial support of both the National Research Fund of Kenya (NRF) and Deutscher Akademischer Austauschdienst (DAAD) under the framework of the Kenyan-German Postgraduate Training Programme, 2018/2019 (57399475).

# Contents

# List of Figures

# List of Tables

# Nomenclature

| | |
|---|---|
| $a$ | Coefficients in the NASA polynomials |
| $c$ | Velocity of sound (m $s^{-1}$) |
| $A$ | Pre-exponential factor in Arrhenius equation |
| $A_s$ | Species s in the elementary reaction |
| $c_p$ | Specific heat capacity at constant pressure (J $K^{-1}$ $kg^{-1}$) |
| $c_{pi}$ | Specific heat capacity at constant pressure of species $i$ (J $K^{-1}$ $kg^{-1}$) |
| $c_v$ | Specific heat capacity at constant volume (J $K^{-1}$ $kg^{-1}$) |
| $c_{vi}$ | Specific heat capacity at constant volume of species $i$ (J $K^{-1}$ $kg^{-1}$) |
| $C_s$ | Molar concentration of species s (mol) |
| $E_a$ | Activation energy (J $mol^{-1}$) |
| $F$ | Broadening factor in the Troe formulation of rate expression |
| $\Delta {G_r}^o$ | Molar standard Gibbs free energy (J $mol^{-1}$) |
| $h_k$ | Specific enthalpy of species $k$ (J $kg^{-1}$) |
| $\Delta {H_i}^o$ | Molar standard enthalpy of reaction (J $mol^{-1}$) |
| $k_o$ | Rate coefficient at low pressure |
| $k_{c,i}$ | Equilibrium constant of a chemical reaction $i$ |
| $k_\infty$ | Rate coefficient at high pressure |
| $k_r$ | Rate constant of elementary reaction r |
| M | Third body molecule within chemical reaction |
| $\bar{M}$ | Averaged molar mass (kg $mol^{-1}$) |
| $M_1$ | Mach number of the incident shock wave |
| $n$ | Temperature exponent |
| $p$ | Pressure |
| $r_i$ | Rate coefficient of a stoichiometric reaction $i$ (mol $s^{-1}$) |
| $R$ | Universal gas constant (= 8.314 J $K^{-1}$ $mol^{-1}$) |
| $S$ | Number of species in the reaction mechanism |
| $S_i$ | Sensitivity coefficient for individual reaction |
| $\Delta {S_i}^o$ | Molar standard entropy of reaction (J $mol^{-1}$ $K^{-1}$) |
| $T$ | Temperature (K) |
| $T^o$ | Standard temperature (= 298.15 K) |
| $\dot{w}_k$ | Production rate of species $k$ (mol $m^{-3}$) |
| $X_i$ | Mole fraction of species $i$ |
| $Y_i$ | Mass fraction of species $i$ |

## Greek Letters

| | |
|---|---|
| $\gamma$ | Ratio of specific heat capacities ($c_p$ / $c_v$) |
| $v^{(p)}$ | Stoichiometric coefficient of species s in the products of reaction r |
| $v^{(e)}$ | Stoichiometric coefficient of species s in the educts of reaction r |
| $\lambda$ | Wavelength (m) |
| $\rho$ | Density (kg m$^3$) |
| $\tau_{ign}$ | Ignition delay time |
| $\Phi$ | Fuel-air equivalence ratio |

## Subscripts

| | |
|---|---|
| i | Number of substance |
| p | At constant reactor pressure |
| v | At constant reactor volume |
| $r$ | Elementary reaction step |
| $s$ | Species $s$ |

## Superscripts

| | |
|---|---|
| e | Educts (reactants) |
| o | Conditions at standard state of pressure and temperature |
| n | Temperature exponent in Arrhenius equation |
| p | Products |

## Abbreviations

| | |
|---|---|
| Bw | Blastwave ignition |
| CI | Compression ignition engine |
| CN | Cetane number |
| EF | End-flange or end wall |
| FWHM | Full width at half maximum |
| GC/MS | Gas chromatography–mass spectrometry |
| GHG | Greenhouse gas |
| HC | Hydrocarbon |

| | |
|---|---|
| HPCV | High-pressure combustion vessel |
| HRR | Heat release rate |
| IDT | Ignition delay time |
| Ign | Ignition |
| JSR | Jet stirred reactor |
| MON | Motor octane number |
| MFC | Mass Flow Controller |
| $NO_x$ | Nitrogen oxides (NO + $NO_2$) |
| $OME_n$ | Poly(oxymethylene) ether of n degree of polymerization |
| OMEs | Poly(oxymethylene) ethers (collectively) |
| PAH | Polycyclic aromatic hydrocarbons |
| PCB | Pressure transducer of PCB Synotech GmBH |
| PRF | Primary reference fuel |
| PtL | Power-to-liquid |
| RON | Research octane number |
| RCM | Rapid compression machine |
| ST | Shock tube |
| TSI | Threshold sooting index |

# Kurzfassung

Aktuell gibt es im Verkehrssektor starke Bestrebungen, den Anteil fossiler Kraftstoffe durch die Anwendung von erneuerbaren und $CO_2$-neutralen Kraftstoffen, sogenannten nachhaltigen Kraftstoffen, zu verringern. Ein weiterer Aspekt ist das Bestreben, auch die Emissionen von Ruß und Feinstaubpartikeln im Abgas zu reduzieren und so die Gesundheitsbelastung gerade in Ballungszentren zu verringern. Zu diesen nachhaltigen Kraftstoffen gehören die Polyoxymethylendimethylether ($OME_n$, n = 1-5; zusammenfassend auch OMEs), welche ein hohes Rußminderungspotential besitzen und als Drop-in-Kraftstoff konventionellen Kraftstoffen zugemischt werden können, da sie hohe Cetanzahlen und schnelle Verdampfungsraten aufweisen. Die Bewertung der Möglichkeiten der motorischen Anwendung der OMEs und die Entwicklung sicherer und kraftstoffeffizienter Motoren erfordern ein umfassendes Verständnis der Verbrennungseigenschaften der OMEs; hierzu zählen die Zündverzugszeiten (ignition delay times – IDTs) und die laminaren Flammengeschwindigkeiten (laminar burning velocities – LBVs).
In der vorliegenden Arbeit wurden die Zündverzugszeiten stöchiometrischer Mischungen von jeweils Dimethylether (DME, auch bezeichnet als $OME_0$), $OME_1$, $OME_2$, *iso*-$OME_2$ (Trimethylorthoformiat) und $OME_4$ mit synthetischer Luft in einer 1:5-Verdünnung mit Stickstoff hinter reflektierten Stoßwellen experimentell bestimmt. Die Messungen erfolgten im Stoßrohr bei $T$ = 800-2000 K für Atmosphärendruck (1 bar) und erhöhten Drücken von 4 bar und 16 bar. Da OMEs als geeignete alternative Mischkomponenten für fossile Kraftstoffe diskutiert werden, wurde zudem der Einfluss auf die Zündverzugszeiten bei der Zumischung von $OME_1$, $OME_2$ und *iso*-$OME_2$ zu einem Benzinsurrogat, dem sogen. Primary Reference Fuel (PRF90: 90% *iso*-Oktan + 10% *n*-Heptan, Angabe bezogen auf flüssige Volumenanteile), untersucht. Im Einzelnen wurden die Zündverzugszeiten von Mischungen aus PRF90 mit synthetischer Luft sowie der Kraftstoffmischungen 70% $OME_1$ + 30% PRF90, 70% $OME_2$ + 30% PRF90 und 70% *iso*-$OME_2$ + 30% PRF90, jeweils ebenfalls in Mischung mit synthetischer Luft, gemessen. Gemessen wurden stets stöchiometrische Mischungen im Stoßrohr in einer 1:5 Verdünnung mit Stickstoff in einem Temperaturbereich mit $T$ = 950-2000 K und Drücken von 1-16 bar. Die experimentell bestimmten Daten der Zündverzugszeiten wurden mit den Ergebnissen aus Modellierungen, die mit dem DLR-eigenen Reaktionsmechanismus DLR-Concise von Kathrotia *et al.* [1] wie auch in der Literatur verfügbaren Modellen erhalten wurden, verglichen. Ergänzt werden die jeweiligen Daten der Zündverzugszeiten der reinen Kraftstoffe wie auch der Kraftstoffmischungen mit entsprechenden experimentellen Daten für die laminare Flammgeschwindigkeit, die durch Ngugi *et al.* [2–6] veröffentlicht sind. Diese Messungen wurden nach der Winkelmethode bei $p$ = 1 bar, 3 bar und 6 bar, über einen Bereich des Kraftstoff-Luft-Verhältnisses ($\varphi$) von 0,6 bis 1,8 und einer konstanten Vorheiztemperatur von 473 K durchgeführt . Die erhaltenen Ergebnisse erweitern den Datensatz für die Bewertung der

Leistungsfähigkeit der verwendeten Reaktionsmodelle.
Der Vergleich der experimentellen Daten für die reinen OMEs ($OME_0$, $OME_1$, $OME_2$ und $OME_4$), welche sowohl für Zündverzugszeiten als auch für Flammengeschwindigkeiten unter gleichen Bedingungen erhoben wurden, zeigt den Einfluss der Kettenlänge auf die Reaktivität der OMEs. Die gemessenen Werte der Zündverzugszeiten für die vier OMEs konvergieren unabhängig vom Druck bei Temperaturen über 1450 K. Unterhalb von 1450 K zeigt $OME_4$ die kürzesten gemessenen Zündverzugszeiten, $OME_0$ (DME) die längsten. Aus dieser Beobachtung lässt sich ableiten, dass die Reaktivität der OMEs mit größer werdender Kettenlänge zunimmt. Diese Schlussfolgerung wird gestützt durch die Messergebnisse der laminaren Flammengeschwindigkeiten, welche zeigen, dass $OME_4$ die höchsten Werte bei allen Drücken und übFer den gesamten betrachteten Bereich des Äquivalenzverhältnisses aufweist. Die Daten der Zündverzugszeiten für $OME_2$ und $OME_4$ liegen bei allen betrachteten Bedingungen nah beieinander, was anzeigt, dass für die OMEs die Zunahme der Reaktivität mit wachsender Kettenlänge abnimmt. Mit diesem Ergebnis konsistent sind die ähnlichen Werte der laminaren Flammengeschwindigkeiten für $OME_2$ und $OME_4$ bei $\varphi < 1{,}0$. Der Vergleich zwischen den Messergebnissen und den Modellierungen, für welche der DLR-Concise Mechanismus [1] sowie die Mechanismen von Cai *et al.* [7] und Niu *et al.* [8] verwendet wurden, zeigt, dass alle drei Modelle zufriedenstellend die gemessenen Zündverzugszeiten der reinen OMEs für die meisten Bedingungen wiedergeben können. Zwischen den gemessenen und berechneten Flammengeschwindigkeiten wurden hingegen für die Mehrheit der OME-Luft-Mischungen für die betrachteten Bedingungen größere Abweichungen erhalten.
Die gemessenen Daten der Zündverzugszeiten zeigen ferner, dass $OME_2$ und $OME_4$ bei $T \leq 1100\,\mathrm{K}$ ein Vorzündverhalten aufweisen, insbesondere bei 4 bar und 16 bar, was sich an dem vor der Hauptzündung auftretenden Anstieg an $OH^*$ und $CH^*$ zeigt. Durch die Vorzündung wurde zudem eine starke Störung des Druckprofils beobachtet. Der Vergleich zwischen den Messungen und den Rechnungen mit dem DLR-Concise [1] sowie den Modellen von Cai *et al.* [7] und Niu *et al.*[8] lassen erkennen, dass die drei Modelle im Rahmen der Messunsicherheiten zufriedenstellend die Hauptzündung wiedergeben können. Mit den Modellen von Cai *et al.* [7] und Niu *et al.* [8] kann zudem das im Experiment für $OME_2$ und $OME_4$ beobachtete Vorzündverhalten adäquat nachvollzogen werden. Die Ergebnisse zeigen, dass diese Eigenschaft eine Folge des Reaktionsverhaltens bei niedrigen Temperaturen ist. Da die Niedertemperaturchemie im DLR-Concise Mechanismus fehlt, zeigen die Modellierungsergebnisse keine Vorzündung. Der Vergleich der gemessenen Daten für *iso*-$OME_2$ und $OME_2$ zeigt, dass beide Kraftstoffe ähnliche Zündverzugszeiten aufweisen. Ähnlich zu den Ergebnissen der Zündverzugszeiten sind die gemessenen laminaren Flammengeschwindigkeiten von *iso*-$OME_2$ und $OME_2$ im brennstoffmageren bis hin zum stöchiometrischen Bereich relativ ähnlich. Dagegen sind die Flammengeschwindigkeiten von $OME_2$ im brennstoffreichen Gebiet deutlich höher, um bis zu 30% bei $\varphi > 1{,}50$ und 1 bar. Die mit dem DLR-Concise Mechanismus vorhergesagten Daten

stimmen mit den gemessenen Daten der Zündverzugszeiten für *iso*-$OME_2$ bei allen Drücken und $T \geq 1250\,K$ überein, aber überbestimmen die gemessenen Flammengeschwindigkeiten über den ganzen Stöchiometriebereich.
Die Ergebnisse, die für die Kraftstoffmischungen erhalten wurden, werden für die gleichen Bedingungen mit denen der reinen Kraftstoffe ($OME_1$, $OME_2$ und *iso*-$OME_2$) und PRF90 verglichen. Damit zeigen die Ergebnisse insgesamt, dass die reinen OMEs eine höhere Reaktivität aufweisen. Die Zündverzugszeiten der Kraftstoffmischungen ($OME_1$ / PRF90, $OME_2$ / PRF90 und *iso*-$OME_2$ / PRF90) sind kürzer als die von PRF90 und länger als die der reinen OMEs, was zeigt, dass die Zugabe von OMEs die Reaktivität des PRF90 erhöht, da die Reaktivität der reinen OMEs selbst deutlich höher als die von PRF90 ist Dieses Ergebnis wurde auch mit der Erhöhung der Flammengeschwindigkeit der Kraftstoffmischungen nachgewiesen [2–6]. Der Einfluss auf die Zündverzugszeiten bei Erhöhung des Anteils an $OME_1$ von 0-100% in Mischungen aus $OME_1$ und PRF90 folgt aus den Messungen wie auch aus den Modellierungen mit dem DLR-Concise Mechanismus. Die Ergebnisse zeigen, dass die Zündverzugszeiten der Mischungen nach schwachem nichtlinearen Verhalten abnehmen, wenn der $OME_1$-Anteil im Bereich von 0-50% erhöht wird. Die Verringerung der Zündverzugszeiten ist ausgeprägter bei Mischungen mit einem Anteil von über 50% $OME_1$. Der Vergleich der gemessenen und berechneten Daten zeigt, dass das DLR-Concise Modell im Rahmen der experimentellen Unsicherheiten zufriedenstellend die experimentell bestimmten Werte der Zündverzugszeiten wie auch die der laminaren Flammengeschwindigkeiten für die Kraftstoffmischungen und die reinen Kraftstoffe wiedergeben kann.
In der vorliegenden Arbeit wurden zum ersten Mal Daten für die Zündverzugszeiten von reinen OMEs ($OME_0$, $OME_1$, $OME_2$, *iso*-$OME_2$ und $OME_4$) und von Mischungen aus jeweils $OME_1$, $OME_2$ und *iso*-$OME_2$ mit einem Benzinsurrogat (PRF90) im mittleren und hohen Temperaturbereich ($T$ = 800-2000 K) bei Atmosphärendruck (1 bar) und erhöhten Drücken von 4 bar und 16 bar erhoben. Insbesondere gibt diese Arbeit ein Verständnis über das Phänomen der Vorzündung, welches bei den Stoßrohrexperimenten im Niedertemperaturbereich beobachtet wurde. Die Ergebnisse ermöglichen auch eine Überprüfung der Relevanz der in den Reaktionsmechanismen für $OME_2$ und $OME_4$ eingebundenen Niedertemperaturchemie. Die Ergebnisse, die im Rahmen der systematischen Untersuchung erhalten wurden, erweitern mit fünf untersuchten Reinkraftstoffen sowie verschiedenen Kraftstoffmischungen die experimentellen Datensätze, auch hinsichtlich der gewählten Messbedingungen (Druck, Temperatur, Brennstoff-Luft-Verhältnis), welche für eine gründliche Evaluierung und Optimierung der chemisch kinetischen Reaktionsmodelle zur Vorhersage der fundamentalen Verbrennungseigenschaften von OMEs benötigt werden.

# Abstract

Presently, the transportation sector is struggling to reduce its share of fossil fuels, by employing renewable fuels which are carbon-neutral and, in addition, may reduce engine-out emissions of soot and particulate matter. Among the renewables, poly(oxymethylene) dimethyl ethers ($OME_n$, n = 1-5; collectively named as OMEs) have an excellent soot reduction potential and can act as a drop-in fuel component in conventional engines due to their high cetane numbers and fast evaporation rates. A comprehensive understanding of the fundamental combustion properties of OMEs, such as ignition delay times (IDTs) and laminar burning velocities (LBVs), is essential for the evaluation of their engine application potential and the development of safer and more fuel-efficient engines (LBVs).

In this work, IDTs of stoichiometric mixtures of dimethyl ether ($OME_0$), $OME_1$, $OME_2$, *iso*-$OME_2$ (trimethyl orthoformate, *i.e.*, $HC(OCH_3)_3$), and $OME_4$ with synthetic air diluted 1:5 with nitrogen were measured behind reflected shock waves in a shock tube at $T$ = 800-2000 K for atmospheric (1 bar) and elevated pressures at 4 and 16 bar. In addition, since OMEs are discussed as suitable alternative blending compounds for fossil-based fuels, the effect of the addition of $OME_1$, $OME_2$, and *iso*-$OME_2$ to a gasoline surrogate, the primary reference fuel 90 (PRF90: 90% *iso*-octane + 10% *n*-heptane by liquid vol.), on IDTs was investigated. In detail, IDTs of mixtures of PRF90 / synthetic air and of blends (by liquid vol.) of 70% $OME_1$ + 30% PRF90, 70% $OME_2$ + 30% PRF90, and 70% *iso*-$OME_2$ + 30% PRF90 with synthetic air, all diluted 1:5 with nitrogen at stoichiometric condition, were measured in a shock tube in the temperature range $T$ = 950-2000 K for pressures between 1-16 bar.

The experimentally determined IDT data sets have been compared with the results of predictions made using the in-house reaction DLR-Concise model by Kathrotia *et al.* [1] and public domain reaction models taken from the literature. Furthermore, the data obtained for IDTs of the neat and blended fuels are supplemented with corresponding experimental data for the laminar burning velocities (LBVs) published by Ngugi *et al.* [2–6]. These measurements were performed using the cone angle method at $p$ / bar = 1, 3, and 6, fuel-air ratios ($\varphi$) ranging between 0.6 and 1.8, and at a constant preheat temperature of 473 K. The results obtained are augmenting the data sets for evaluating the performance of the used reaction models.

The comparison of the experimental data obtained under similar conditions for the IDTs – as well as for the LBVs of pure OMEs ($OME_0$, $OME_1$, $OME_2$, and $OME_4$) — are made to bring out the effect

of chain length on the reactivity of OMEs. The measured values for IDTs of the four OMEs converge at temperatures above 1450 K independent of pressure, whereas at temperatures below 1450 K, the measured IDTs are shortest for $OME_4$ and longest for $OME_0$ (DME). From this observation, it is concluded that the reactivity of OMEs increases with an increase in the chain length. This finding is supported by the results of laminar burning velocity measurements, which are highest for $OME_4$ at all pressures and over the entire equivalence ratio range considered. Further, the IDT data for $OME_2$ and $OME_4$ are close for all the conditions investigated indicating that for OMEs, the increase in reactivity is reducing as chain length increases. Similar to this, LBV values of $OME_2$ and $OME_4$ are close for $\varphi \leq 1.0$. The comparison between measurements and predictions using DLR-Concise [1], Cai *et al.* [7] and Niu *et al.* [8] models reveal that the three models satisfactorily predict the measured IDTs of pure OMEs for most of the conditions. On the other hand, larger deviations were observed between measured and calculated laminar flame speeds (LFSs) for most of the OME-air mixtures and conditions covered.

The measured IDT data revealed that $OME_2$ and $OME_4$ exhibit a pre-ignition behavior at $T \leq 1100\,\mathrm{K}$, particularly at 4 and 16 bar, as demonstrated by an earlier increase in OH* and CH* before the main ignition. A strong perturbation on the pressure profile due to pre-ignition heat release was also observed. The comparison between measurements and predictions using the DLR-Concise [1] as well as the models of Cai *et al.* [7] and Niu *et al.* [8] indicates that the models satisfactorily predict the main ignitions within experimental uncertainty. Further, the models of Cai *et al.* [7] and Niu *et al.* [8] adequately account for the pre-ignition behavior observed in the measurements. The results show that pre-ignition is a consequence of the reaction behavior at low temperatures. Since the low-temperature chemistry is absent in the DLR-Concise mechanism, the modeling results do not show pre-ignition. The comparison of the measured data for *iso*-$OME_2$ and $OME_2$ shows that the two fuels have similar IDTs. Similar to the IDTs, the measured LBVs of *iso*-$OME_2$ and $OME_2$ are relatively similar in the fuel-lean up to the stoichiometric domain. However, under fuel-rich conditions, the LBVs of $OME_2$ are significantly higher, *i.e.*, by up to 30% at fuel-air ratio $\varphi > 1.50$ and 1 bar. For all pressures, the DLR-Concise model matches the measured ignition delay times data of *iso*-$OME_2$ for $T \geq 1250\,\mathrm{K}$, but overpredicts the measured LBVs in the whole stoichiometry regime.

The results obtained for the blended fuels are compared to those of the pure fuels ($OME_1$, $OME_2$, and *iso*-$OME_2$) and PRF90 for the same conditions. The results show that IDTs of the fuel blends ($OME_1$ / PRF90, $OME_2$ / PRF90, and *iso*-$OME_2$ / PRF90) are shorter than those of PRF90 and longer than those of the pure OMEs, showing that the addition of OMEs increases the reactivity of PRF90

since the reactivity of pure OMEs is significantly higher than that of PRF90. This finding is also demonstrated by an increase in the LBVs of the fuel blends [2–6]. The impact of increasing the $OME_1$ fraction from 0-100% on the IDTs of $OME_1$ / PRF90 blends is inferred from measurements as well as from predictions with the DLR-Concise model. The results show that IDTs of the blends decrease in a weakly non-linear fashion by increasing $OME_1$ fractions from 0-50%. The reduction of IDTs of the blend is stronger for blends with over 50% $OME_1$ fractions. The comparison of measured and predicted data showed that the DLR-Concise model satisfactorily reproduced the experimental data for IDTs and LBVs of the blended and the neat fuels within the experimental uncertainty.
In the current study, significant new data for ignition delay time data of pure OMEs ($OME_0$, $OME_1$, $OME_2$, *iso*-$OME_2$, and $OME_4$) and of blends of $OME_1$, $OME_2$, and *iso*-$OME_2$ with a gasoline surrogate (PRF90) in the mid- to the high-temperature regime ($T$ = 800-2000 K) at atmospheric (1 bar) and elevated pressures at 4 and 16 bar were obtained. In particular, this work characterizes pre-ignition behavior, which was observed in the shock tube experiments in the low-temperature regime. The results make it possible to test the implementation of low-temperature chemistry of $OME_2$ and $OME_4$ in the chemical kinetic reaction models. The results of this systematic analysis of the five neat fuels and the blended fuels under consideration have broadened the experimental data sets in terms of the chosen experimental conditions (pressure, temperature, and fuel-to-air ratio) required for rigorous testing, thus improving chemical kinetic models focusing on fundamental combustion properties for OMEs.

# 1 Introduction

## 1.1 Motivation

Global petroleum and liquid fuel consumption have recovered from the massive drop caused by the COVID-19 pandemic and is predicted to rise by 2.1 million barrels per day to an average of about 101.5 million barrels per day in 2023 [9]. Combustion of fossil-derived liquid fuels will continue to account for a large share of the global energy demand which is projected to increase by 50% by 2050 as economies and populations continue to grow [9, 10]. This is also despite the worldwide projected increase in consumption of renewable energy of 3% per year [10]. However, the use of fossil fuels is connected to two major concerns: (i) Crude oil is a finite resource that will be depleted in the future, thus reducing the supply of fossil fuels; and (ii) the combustion of fossil fuels releases carbon dioxide ($CO_2$), a greenhouse gas (GHG) which is prominently connected to climate change [11]. Furthermore, due to stringent emission standards, soot and particulate matter (PM) emissions are a concern [12, 13].

Presently, the transport sector, *i.e.* has the highest reliance on fossil fuels and accounts for 37% of direct $CO_2$ emissions, with road transport accounting for nearly three quarters of total transport-related $CO_2$ emissions worldwide [14]. If the current trends continue, combustion-related $CO_2$ emissions will continue to increase through 2050 [10]. To reach carbon neutrality by 2050 as set out under the Paris Agreement [15], the European Union [16] has set a roadmap to achieve a 55% reduction target of greenhouse gas emissions by 2030 compared to 1990 levels. The transport sector's emissions in Europe should be reduced by between 36–42% from current levels by 2030 and approach zero by 2044–2048 to achieve this ambitious goal while assuming a linear decline path [17]. Thus, it is widely accepted that a wide range of approaches is needed for low-emission transport systems [18–20], such as electric batteries, hydrogen, and alternative fuels obtained through non-conventional sources. However, in addition to technological challenges such as energy storage and the performance of batteries, a new infrastructure for hydrogen distribution is required. While in the long term, these concepts are highly promising, the use of alternative fuels as blending components or substitutes offers a promising solution within the already existing infrastructure and engines, thus allowing their use in today's engines with almost no modification [21–23]. The use of alternative fuels, particularly oxygenated fuels, provides the opportunity to improve both the overall $CO_2$ balance and the local emissions, such as soot particles. The

requirements of diesel engines to meet stringent emission regulation norms such as Euro VI are already high but may become even more stringent with the currently discussed Euro VII [13, 24]. As a result, there has been a major focus on the reduction of, in particular, $CO_2$ emissions in the transport sector through the deployment of low-emission advanced alternative fuels, such as ethers, alcohols, and renewable synthetic fuels.

## 1.2 Poly(oxymethylene) dimethyl ethers

Alternative fuels, particularly oxygenated ones, can efficiently tackle the challenges associated with conventional fuels. Alcohols, biodiesel, and ethers are the most appealing oxygenated alternative fuel categories that might serve as neat engine fuels or blending components [23]. In recent years, poly(oxymethylene) dimethyl ethers abbreviated as $OME_n$ or $PODE_n$ (and collectively as OMEs) are a class of ethers that have recently sparked much interest as neat fuels or as additives to conventional fuels [21, 25]. The general molecular formula of $OME_n$ is $CH_3O(CH_2O)_nCH_3$, where n denotes the degree of polymerization ranging from 1 to 7. These oxygenated oligomers are promising synthetic fuel candidates that have been shown in recent studies to be highly effective at lowering emissions of soot and soot precursors [25–30]. The soot and particulate matter reduction tendencies for $OME_n$ are attributed to: (i) Their high oxygen content (typically > 35% by mass) which is due to the presence of the -(O-$CH_2$)- group in their molecule, and (ii) to the absence of direct C-C bonds in their molecular chain so that direct pathways leading to the formation of alkenes do not exist. Since alkenes are important precursors in soot formation, OMEs thus offer the potential to reduce the formation of soot and particulate matter (PM) [31]. Also, due to their low soot emission tendencies, combustion of $OME_n$ / diesel blends has the potential to overcome the classical soot versus $NO_x$ trade-off, and thus could reach the much discussed Euro VII $NO_x$ level limit (0.2 g / kWh) [24]. OMEs have further attractive thermophysical properties such as high cetane numbers (see Table 1.1) and faster mixing with air due to their, in general, lower boiling points compared to diesel fuel compounds, such as aromatics and long-chained hydrocarbons [32]. Moreover, OMEs have the potential to be employed immediately as drop-in fuels since they can be used in diesel engines with little modification; their deployment would be possible through the existing distribution infrastructure. To this end, OMEs have been presented as a promising alternative fuel or blending components for fossil diesel, particularly for application in automobiles. In addition, OMEs have the potential for application in the maritime sector as neat or blending

component for marine diesel since they require limited modifications to the engine and fuel supply system. Also, OMEs do not contain surphur (S). However, pilot studies and studies on viability and sustainability of OMEs in maritime sector are needed to establish the potential.

### 1.2.1 Production of oxymethylene ethers (OMEs)

Sustainable production and efficient distribution of potential fuels are key aspects affecting their utilization. OMEs can be produced on large-scale from methanol, which itself can be made renewably in two most prominent ways, see Fig. 1.1: (i) From sustainable sources through gasification or fermentation of biomass, *e.g.*, cellulose, sugars, starch; and (ii) by exploiting the Power-to-Liquid (PtL) technology which is based on electrochemically generated hydrogen by combining the use of (excess) renewable electricity, *e.g.*, from wind power or photovoltaics, and renewable chemical precursors, such as carbon dioxide, enabling the production of liquid fuels [7, 21]. For instance, $CO_2$ can be captured from industrial point sources such as manufacture of steel or cement [33, 34].

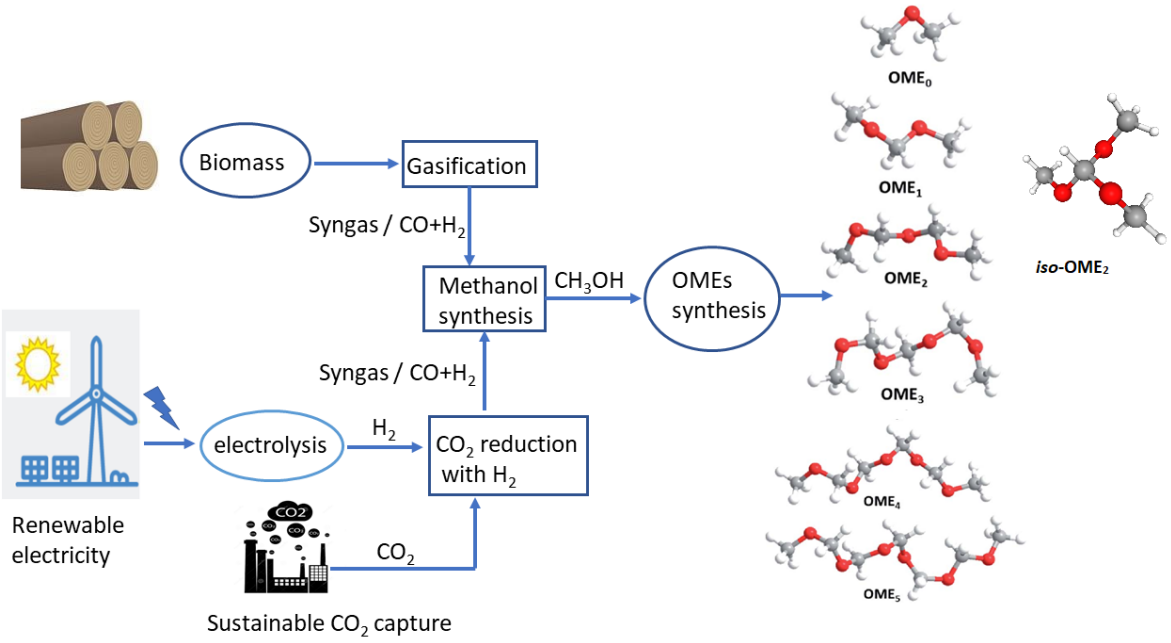


**Figure 1.1:** Production routes of OMEs based on methanol generated from biomass and renewable electricity; where $OME_0$ represents DME.

Briefly, OMEs are synthesized from compounds that provide a methoxy end group ($CH_3O$-) such as methanol ($CH_3OH$), dimethyl ether (DME), and dimethoxymethane ($OME_1$), and $CH_2O$ chain group, such as formaldehyde ($CH_2O$) and trioxane ($(CH_2O)_3$) [35]. All these products are produced

from methanol at the very beginning. The synthesis technique for OMEs from methanol is not given here because it has already been addressed in the literature, for example, by Liu *et al.* [25] and Baranoski *et al.* [36].

### 1.2.2 Physicochemical properties of OMEs

A fuel must comply with specifications and regulations for a specific region; for example, the EN 590 standardization for the European region describes the physical properties that all automotive diesel fuel must meet. Table 1.1 summarizes the key properties of $OME_{0-5}$ along with those of conventional gasoline and diesel. $OME_3$ to $OME_5$ have cetane values of 67, 76, and 90, which are

**Table 1.1:** Key properties of DME, $OME_{1-5}$, gasoline, and diesel [36–38]

| Property | DME | Diesel | Gasoline | $OME_1$ | $OME_2$ | $OME_3$ | $OME_4$ | $OME_5$ |
|---|---|---|---|---|---|---|---|---|
| Chemical formula | $CH_3OCH_3$ | $C_8$-$C_{25}$ | $C_4$-$C_{12}$ | $C_3H_8O_2$ | $C_4H_{10}O_3$ | $C_5H_{12}O_4$ | $C_6H_{14}O_5$ | $C_7H_{16}O_6$ |
| Molar mass (g/mol) | 46.07 | 150 - 250 | 60 - 150 | 76.09 | 106.12 | 136.14 | 166.17 | 196.2 |
| Carbon content (mass%) | 52.2 | 86 | 86.5 | 47.35 | 45.3 | 44.11 | 47.19 | 42.85 |
| Hydrogen content (mass%) | 13 | 14 | 13.5 | 10.6 | 9.5 | 8.88 | 7.95 | 8.22 |
| Oxygen content (mass%) | 34.8 | | | 42 | 45.2 | 47 | 48.1 | 48.93 |
| Vapor pressure at 20°C (bar) | 5.1 | 0.01 | 0.005 | 0.44 | | | | |
| Liquid density at 20°C ($kg/m^3$) | 660 | 800-840 | 715-780 | 860 | 968.7 | 1030 | 1070 | 1104.5 |
| LHV (MJ/kg) | 27.6 | 42.5 | 41.9 - 44.2 | 22.4 | 20.6 | 19.4 | 18.7 | 18.1 |
| Octane number (RON) | | | 90 - 100 | | | | | |
| Cetane number (CN) | 55 - 60 | 40 - 55 | 8 - 14 | 29 | 63 | 67 | 76 | 90 |

greater than the minimum value of 51 required by EN 590 for commercial diesel. In addition, the flash points of $OME_3$ to $OME_5$ vary from 53.5 to 115.0 °C matching the EN 590 lower limit. The viscosity of OMEs decreases with an increase in (-$CH_2O$-) units, thus the risk of clogging the fuel system for $n > 5$, *i.e.*, $OME_6$ and $OME_7$ [37]. Also, $OME_6$ and $OME_7$ are solids at room temperature and thus they are not suitable fuels in the classical sense. Thus, $OME_{3-5}$, because of their high cetane numbers and diesel-compatible boiling range, are suitable fuel additives for use in diesel engines with only slight modifications required for the fuel supply system. On the other hand, $OME_n$ with $n < 3$ are not suitable for use in diesel engines due to their low vapor pressure and flash point compared to diesel, and thus, they do not meet the safety criterion [37]. In addition, they have lower boiling temperatures [39]. For $OME_1$, its low cetane number (CN = 29) further limits its use in diesel engines [25]. Dimethyl ether (DME, $OME_0$) on the other hand, is gaseous at room temperature; thus, the high vapor pressures cause a phase separation when mixed with

diesel [27]. Despite the challenges limiting the use of $OME_1$ and $OME_2$ in diesel engines, they are attractive cetane boosters for blending with gasoline. The introduction of high cetane boosters such as ethers (diethyl ether), has enabled gasoline to be used in novel compression ignition engines, *i.e.*, the homogeneous-charge compression ignition (HCCI) engine operation mode, with enhanced combustion and emission characteristics [40–42].

### 1.2.3 Alternative applications for OMEs

Besides the application of OMEs as alternative fuels or additive components for conventional fuels, they are being investigated for use in a variety of sectors other than transportation. Schappals *et al.* [43], studied the application of OMEs as $CO_2$ physical absorbents. They evaluated the $CO_2$ solubility in $OME_2$, $OME_3$, and $OME_4$ and reported that OMEs are promising candidates. Currently, investigations on the use of $OME_{3-5}$ as an alternative ether-like solvent have recently increased due to the efficiency of $OME_1$ as a solvent for a wide range of applications, *e.g.*, aerosols, paints, extraction, synthesis, and many more [44]. Zhenova *et al.* [44] investigated the solvation characteristics of $OME_{3-5}$ and its individual components ($OME_3$, $OME_4$, and $OME_5$) and discovered they are similar to standard commercial ether solvents like 1,4-dioxane. They showed that the use of an $OME_{3-5}$ mixture as a solvent performed well in the dissolution of polystyrene and the removal of paints and coatings, implying that $OME_{3-5}$ can replace dichloromethane in polymer recycling, polymer welding, and cleaning applications [44]. They also discovered that when OMEs were utilized as solvents, peroxide formation, which is one of the main problems associated with standard ether solvents, proceeded slower in OMEs than in conventional solvents, implying a higher safety record. The use of OMEs as a solvent opens the door to complement diesel engine applications that are currently being studied. This might increase their demand, hence providing a way to scale up production and reduce the costs of OMEs.

## 1.3 Ignition delay time (IDT) and laminar burning velocity (LBV)

Many researchers have been working on the development of accurate and reliable chemical kinetic models for conventional and alternative fuels to promote their use as alternative (engine) fuels. Kinetic targets, such as ignition delay times, laminar burning velocities, and species histories obtained over a wide range of temperature, pressure, and equivalence ratios, are required for validating and optimizing reaction mechanisms towards defined targets. The ignition delay time $\tau_{ign}$ is an important physicochemical property of a combustible fuel-oxidizer mixture needed for

the validation and optimization of detailed combustion models for describing the ignition of fuels over a wide range of conditions of temperature, pressure, and fuel-air ratio $\varphi$. It is also an important parameter in the design of the combustors of most engines, including internal combustion engines and gas turbines, amongst others. The dependency of ignition delay time on temperature, pressure and composition is crucial in describing liquid fuel combustion in diesel engines and other types of combustion chambers. For instance, the ignition delay time in diesel engines determines the phase of fuel-air mixing and heat release to enhance evaporation. In addition, since ignition phenomena are connected to the rate of heat release, which, if too fast, might induce dynamic instabilities, auto-ignition is thus significant from a safety view point. Ignition delay time measurements are carried out in shock tubes (ST) and rapid compression machines (RCM). Shock tubes provide well-controlled and nearly ideal conditions of temperature and pressure for studying auto-ignition phenomena at a wide temperature range of up to 2000 K in this work. On the other hand, RCMs can be used for ignition delay time measurements in the temperature range between 600-1000 K. Laminar burning velocity (LBV) is an important fundamental combustion parameter that gives information regarding the reactivity, diffusivity, and exothermicity of a reacting premixed mixture. LBV describes the propagation of a planar flame into a quiescent unburned mixture ahead of the flame at a specific temperature and pressure. It is connected to the burning rate of the fuel in the combustion device, and therefore affects efficiency and exhaust emissions. Knowledge of LBVs is required for engine design and validation and optimization of detailed combustion models. In addition, it is also required in the estimation of the turbulent flame speed which is part of many flame propagation models used in CFD codes. The laminar burning velocity is dependent on the property of the mixture (fuel structure, stoichiometry) and thermodynamic parameters upon mixture ignition (pressure, temperature). In principle, a fuel with a higher laminar burning velocity also has a higher reactivity and vice versa. Measurements of laminar burning velocities are carried out in a laminar premixed flame where the oxidizer is mixed with the fuel prior to combustion. The most commonly used techniques for measurements of laminar burning velocities are the Bunsen flame method, the spherically expanding flame method, the heat flux method, and the counter flow method.

## 1.4 Scope and organization of this thesis

The primary objective of this work is to provide an extensive database of shock tube ignition delay times for several oxymethylene ethers (DME or $OME_0$, $OME_1$, $OME_2$, *iso*-$OME_2$, and $OME_4$) at a range of conditions ($T$, $p$, and $\varphi$) relevant for testing and improvement of chemical kinetic mechanisms. In addition, since future combustion engines will most likely exploit tailored mixtures of conventional and alternative fuels, ignition delay times of blends of $OME_1$, $OME_2$, and *iso*-$OME_2$ with the primary reference fuel 90 (PRF90) as a gasoline surrogate were measured. Furthermore, the ignition delay time data sets are augmented with corresponding data for laminar burning velocities as contained in Ngugi *et al.* [2–5] measured at DLR using the cone angle method, therefore expanding the data sets for evaluating the reaction models. The interpretation of the experimental findings is based on the available chemical kinetic models for OMEs. As a result, experimental data are compared to the results of calculations performed using an in-house model, the DLR-Concise model [1], and other public domain models obtained from the literature. The goal is to provide experimental data sets for validation while also identifying potential areas for improvement in the reaction models.

This work is organized into 5 chapters. In the current chapter, the background and scope of the study have been presented. In chapter 2, the overview of the literature on previous combustion studies on the investigated fuels is presented and the current gaps in the literature that are addressed in this work. Chapter 3 covers an overview on the theory of shock tubes, its operation principle, the method of measurements, including the preparation of mixtures for ignition delay time measurements, and the evaluation of experimental data. The last part of the chapter covers the chemical kinetic modeling approach, including the reaction mechanisms used in this study. Chapter 4 consists of the results and discussions. The experimental data obtained for each fuel are presented and discussed in detail, followed by a comparison of measured and predicted data. Finally, the results of the sensitivity analyses are presented. Chapter 5 covers the summary and conclusions of the main findings of this work.

# 2 Fuels investigated

## 2.1 Introduction

In this study, a series of neat oxymethylene ethers — DME (representing $OME_0$), $OME_1$, $OME_2$, *iso*-$OME_2$, and $OME_4$ and blends of selected oxymethylene ethers ($OME_1$, $OME_2$, *iso*-$OME_2$) — with a gasoline surrogate were investigated. The primary reference fuel 90 (PRF90: 90% *iso*-octane + 10% *n*-heptane, by liq. vol.) was used as a surrogate for gasoline. This chapter covers these investigated fuels in more detail. The underlying literature on previous fundamental combustion research performed, for instance, in shock tubes (ST), rapid compression machines (RCM), jet-stirred reactors, and flames, and many others, on the investigated fuels is presented, bringing out existing gaps that are addressed in this work.

## 2.2 Dimethyl ether (DME)

DME ($CH_3OCH_3$) is a prototype of a linear ether (see Fig. 2.1) that represents OME with n = 0, making it an important molecule to consider while studying OMEs. DME has been considered as substitute or additive component for conventional fuels and have been the most extensively investigated and evaluated in diesel engines [27, 45–47]. Furthermore, as the simplest linear ether combustion of DME have been studied widely in shock tubes, rapid compression machines, jet-stirred reactors, and plug flow reactors, among others, as well as chemical kinetic modeling, and have been widely reviewed in the literature [48, 49]. An overview of the numerous studies on IDTs measurements of DME / oxidizer mixtures performed in shock tubes (ST) and rapid compression machines (RCM) over a wide range of conditions are presented in Table 2.1. However, direct comparability between these measurements is not straightforward due to the variety in the specific grade of dilution and type of diluent selected in the different studies.

## 2.3 Oxymethylene ether-1 and -2 ($OME_1$ and $OME_2$)

Oxymethylene ether-1 and -2 represents the first and second member of the $OME_n$ family with the molecular formula of $CH_3O(CH_2O)_nCH_3$, with n = 1 and 2, respectively. The combustion of mixtures of $OME_1$ / diesel and $OME_1$ / diesel diesel in diesel engines has been shown to be very efficient in reducing emissions of hydrocarbon (HC), carbon monoxide (CO) and soot [50–55]. However, because of their high volatility, high-vapour pressure, low-flash point, and low boiling temperature in comparison to diesel fuel, $OME_1$ and $OME_2$ are less suitable diesel fuel additives; see section 1.2.2. Furthermore, the low cetane number (CN = 30) of $OME_1$ presented a challenge to its adoption as a diesel fuel additive. Despite the challenges limiting the adoption of $OME_1$ and

$OME_2$ in diesel engines, they are attractive cetane boosters for blending with gasoline as discussed in section 1.2.2. As the first member of the OMEs family, numerous fundamental experiments have characterized the combustion of $OME_1$ in shock tubes, rapid compression machines, jet-stirred reactors, and plug flow reactors, among others as reviewed, for example, by Shrestha *et al.* [56] and Gilliespie [57].

**Table 2.1:** Overview of measured ignition delay times of DME / oxidizer mixtures. ST — shock tube device, RCM — rapid compression machine.

| Mixture | $T$ / K | $p$ / bar | $\varphi$ | Method | Ref. |
|---|---|---|---|---|---|
| DME / air | 650 - 1300 | 13 and 40 | 1 | ST | [58] |
| DME / $O_2$ / Ar | 1200 - 1600 | 3.55 | 0.5 - 2.0 | ST | [59] |
| DME / $O_2$ / $N_2$ | 615 - 735 | 10-20 | 0.43 - 1.5 | RCM | [60] |
| DME / $O_2$ / Ar | 1175 - 1900 | 1.6-6.6 | 0.5 - 3.0 | ST | [61] |
| DME / air / $N_2$ | 700 - 1270 | 22 | 0.5 - 1.5 | ST | [62] |
| DME / $O_2$ / Ar | 1000 - 1600 | 1.2-20 | 0.5 - 2.0 | ST | [63] |

**Table 2.2:** Overview of measured ignition delay times of $OME_1$ / oxidizer mixtures and $OME_2$ / oxidizer mixtures. ST — shock tube device, RCM — rapid compression machine.

| Mixture | $T$ / K | $p$ / bar | $\varphi$ | Method | Ref. |
|---|---|---|---|---|---|
| $OME_1$ / $O_2$ / Ar | 1130-1855 | 1.013 - 3.55 | 0.5 - 2.0 | ST | [57] |
| $OME_1$ / air | 780-1330 | 9.11925 | 0.5 - 2.0 | ST | [57] |
| $OME_1$ / $O_2$ /Ar | 1103-1454 | 2.0265 - 10.1325 | 0.5 - 2.0 | ST | [64] |
| $OME_1$ / $O_2$ /Ar | 1100-1600 | 2.0265 - 10.1325 | 0.5 - 2.0 | ST | [65] |
| $OME_1$ / air | 790-1630 | 1 - 40 | 1 | ST | [66] |
| $OME_1$ / air | 590-790 | 1 - 40 | 1 | RCM | [66] |
| $OME_{1,2}$ / air | 550-680 | 10 and 15 | 0.5 - 2.0 | RCM | [56] |
| $OME_2$ / air | 663-1137 | 10 and 20 | 0.5 - 2.0 | RCM | [7] |
| $OME_2$ / air | 570-690 | 3 - 10 | 1.0 | RCM | [67] |

Table 2.2 summarizes the available literature on auto-ignition of $OME_1$ and $OME_2$. It is observed that there are few studies on auto-ignition of $OME_2$, with no data available for temperatures larger than 1137 K and for pressure of 1 bar. For $OME_1$, there are numerous studies on auto-ignition. However, direct comparability between these measurements is not straightforward due to the variety in the specific grade of dilution and type of diluent selected in the different studies.

## 2.4 Oxymethylene ether-3 and -4 ($OME_3$ and $OME_4$)

$OME_3$ and $OME_4$ have high cetane numbers and diesel-compatible boiling temperatures, making them desirable as diesel additives; see section 1.2. In addition, they have high oxygen contents, due to the presence of several -$CH_2O$- groups in their molecular structures, as demonstrated in Fig. 2.1. An overview of the literature concerning fundamental experiments and chemical kinetics of $OME_{2-4}$ is summarized in Table 2.3.

Cai *et al.* [7] studied the auto-ignition of $OME_2$, $OME_3$, and $OME_4$, *i.e.*, $OME_{2-4}$ in a shock tube at pressures of 10 and 20 bar, in the temperature range between 600 and 1150 K, and for the equivalence ratios of 0.5, 1.0, and 2.0. The results were used to develop a chemical kinetic mechanism for $OME_{2-4}$. The mechanism was derived using an automatic class-based mechanism generator in which reaction classes adopted from the $OME_1$ mechanism published by [60] were applied consistently to $OME_{2-4}$.

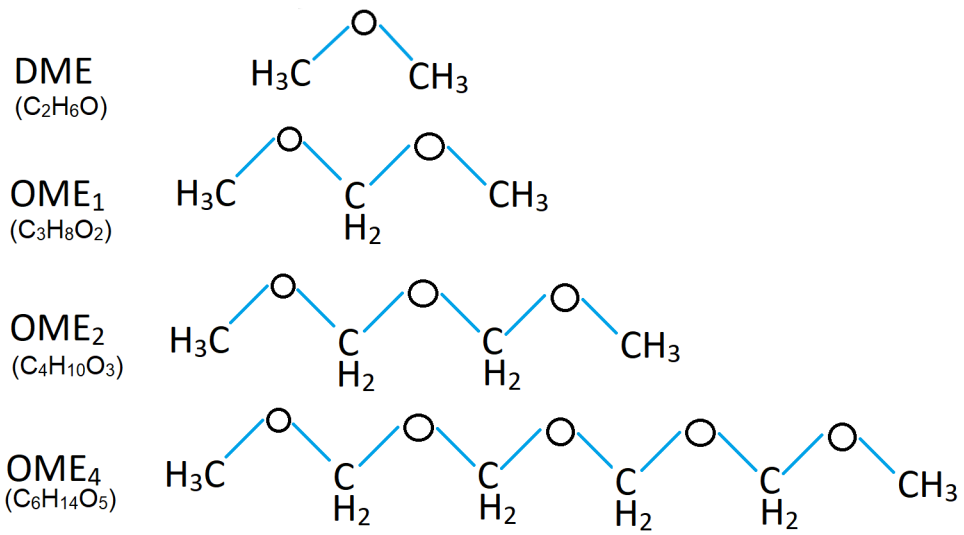


**Figure 2.1:** Molecular structures of the molecules studied in this work

Sun *et al.* [68] studied the laminar flame speeds of $OME_3$ / air mixtures through experiments and modeling. Laminar flame speeds of $OME_3$ / air were measured in a cylindrical bomb at a pressure of 1 atm and for $\varphi$-values between 0.7-1.6. The measurement of speciation data in a laminar premixed flame of $OME_3$ / air at low pressures of 33.33 mbar and $\varphi = 1.0$ was carried out in a McKenna burner equipped with a molecular beam sampling system, a reflectron mass spectrometer, and a synchrotron vacuum ultraviolet light source. The results were used to develop a high-temperature chemical kinetic model for $OME_3$.

He *et al.* [31] developed a chemical kinetic mechanism for the low and intermediate-temperature combustion of $OME_3$. The mechanism was validated using ignition delay time measurements in a rapid compression machine at temperatures ranging from 640 to 865 K, pressures ranging from 10 to 15 bar, and for three different $OME_3$ / $O_2$ / $N_2$ mixtures, see Table 2.3. They also carried out experiments in homogeneous charge compression ignition (HCCI) engines fueled using $OME_1$ to $OME_4$ mixtures. The comparison of the calculated results with the $OME_3$ model and the experimental measurements from the RCM and HCCI engines revealed that the mechanism matches the ignition delay time, pressure trace, and rate of heat release (HRR) profile at low and intermediate temperatures.

**Table 2.3:** Overview of previous experimental studies on $OME_3$ and $OME_4$. ST — shock tube, RCM — Rapid Compression Machine, LBV — Laminar burning velocities, * — pressure specified in atm, and ** — pressure specified in mbar.

| Fuel | Investigated Property | Method used | Investigated conditions | | | |
|---|---|---|---|---|---|---|
| | | | $T$ / K | $p$ / bar | $\varphi$ | Ref. |
| $OME_{3,4}$ | IDT | ST | 663 - 1137 | 10, 20 | 0.5 - 2.0 | [7] |
| $OME_3$ | IDT | RCM | 570 - 690 | 3-10 | 1 | [67] |
| $OME_3$ | LBV | Spherical bomb | 408 | 1* | 0.7 - 1.6 | [68] |
| | Flame structure | Laminar premixed flame | 408 | 33.33** | 1 | |
| $OME_3$ | IDT | RCM | 640–865 | 10 and 15 | 0.5 - 1.5 and $O_2 : N_2$ = 1:8 - 1:20 | [31] |
| $OME_3$ | IDT | RCM | 550 - 680 | 10 and 15 | 0.5 - 2.0 | [56] |

Drost *et al.* [67] investigated the auto-ignition of $OME_2$ / air and $OME_3$ / air mixtures in a rapid compression machine (RCM) at $\varphi$ = 1.0, pressures ranging from 3–10 bar, and temperatures ranging from 570 to 690 K. Eckart *et al.* [69] studied the laminar burning velocities and emission behavior of $OME_1$ and $OME_2$. Laminar burning velocities of $OME_1$ and $OME_2$ were measured using a heat flux burner at preheating temperatures between 383 and 401 K, and $\varphi$-values between 0.6-1.9 at atmospheric pressure. The results of the measurements were compared to the results of calculations made with the model of Cai *et al.* [7].

To this end, it is observed that experimental data sets on the auto-ignition of $OME_2$, $OME_3$, and $OME_4$ are limited, particularly for elevated temperatures greater than 690 K for $OME_2$, 865 K for $OME_3$, and 1140 K for $OME_4$; see Table 2.3. Auto-ignition of $OME_4$ has been reported only in the work of Cai *et al.* [7]. This thesis presents shock tube ignition delay times of stoichiometric mixtures $OME_2$ / synthetic air and $OME_4$ / synthetic air, all diluted 1:5 with nitrogen, at $p$ / bar = 1, 4, and 16 and for temperatures between 800 and 2000 K. Additionally, since DME ($OME_0$) and $OME_1$ serve as the starting point for research on OMEs, their ignition delay times were also examined under similar conditions to conduct a systematic study and to evaluate the impact of chain length on auto-ignition of OMEs.

## 2.5 Trimethyl orthoformate (*iso*-$OME_2$)

Trimethyl orthoformate (*iso*-$OME_2$) is a branched ether with the chemical formula $HC(OCH_3)_3$ that belongs to the family of ortho–esters. It is a branched isomer of oxymethylene ether-2 ($OME_2$) that due to its high oxygen content and lack of direct carbon-carbon bonds, has the potential to considerably limit the generation of soot particles [70]; see Fig. 2.2.

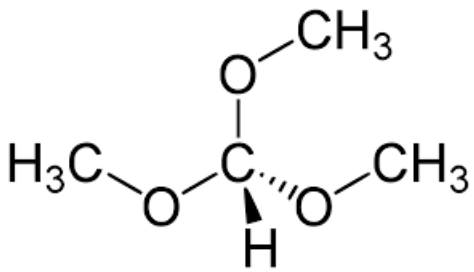


**Figure 2.2:** Molecular structure of Trimethyl orthoformate (*iso*-$OME_2$)

Research on the combustion of *iso*-$OME_2$ attracts researchers' interest because of its isometric structure to $OME_2$. *Iso*-$OME_2$ has been demonstrated to be an oxygenated fuel for direct oxidation in liquid-feed fuel cells [71–73]. Concerning their application in diesel engines, Yeh *et al.* [70] demonstrated that blending *iso*-$OME_2$ into diesel reduces emissions of particulate matter (PM)

and $NO_x$. Recently, Gaiser *et al.* [74] measured the speciation data of *iso*-$OME_2$ and $OME_2$ during oxidation in an atmospheric flow reactor at $\varphi$-values of 0.8 and 1.2, and for temperatures between 748 K and 1273 K.

Döntgen and Heufer [75] investigated the auto-ignition of *iso*-$OME_2$ through experiments and a modeling approach. They developed a detailed chemical kinetic model of *iso*-$OME_2$ based on the $OME_1$ model from Jacobs *et al.* [66]. For validation of their model, they measured ignition delay times of stoichiometric *iso*-$OME_2$ / air mixtures at pressures of 20 and 40 bar in the temperature range between 700 and 1000 K using the shock tube method. In another study, Döntgen *et al.* [76] reported on the rate coefficients for *iso*-$OME_2$ pyrolysis experimentally and theoretically. The pyrolysis of *iso*-$OME_2$ was investigated behind the reflected shockwave in a single pulse shock tube connected to a GC/MS in the temperature range between 1050 - 1300 K at an initial pressure of 2.3 bar. In addition, they developed a detailed chemical kinetics model for the pyrolysis of *iso*-$OME_2$.

In the present work, ignition delay times of stoichiometric mixtures of *iso*-$OME_2$ / synthetic air diluted 1:5 in $N_2$ were investigated behind the reflected shock wave in a shock tube at initial pressures of 1, 4, and 16 bar and for temperatures between 900 and 1700 K, thus expanding the experimental datasets for further development and improvement of reaction mechanisms of *iso*-$OME_2$.

## 2.6 Surrogate fuels

Conventional fuels derived from crude oil, such as gasoline and diesel, comprise many hydrocarbon classes, including *n*-alkanes, *iso*-alkanes, *cyclo*-alkanes, aromatic compounds, olefins, and others [77–80]. There is also extensive variability within these classes. For this reason, it is impossible to carry out a meaningful experimental investigation with conventional fuels if each of the components present must be considered. To overcome this limitation, a surrogate mixture of only a few representative components occurring in the complex ‘real” fuels is used to mimic the multi-component mixture. The specific surrogate composition defined should maintain both the chemical and physical properties of the real fuel considered, *i.e.*, laminar burning velocity, ignition delay time, density, viscosity, mixing, vaporization, and octane or cetane number as well as its spray behavior [81, 82]. Binary mixtures of *iso*-octane and *n*-heptane, referred to as ”primary reference fuels” (PRFs), are widely used to mimic gasoline with a focus on research octane number (RON) and motor octane number (MON), and thus reflect the target gasoline's ignition tendencies and heat release [80, 83, 84]. Ternary mixtures of *iso*-octane, *n*-heptane, and toluene have been suggested for enhanced reproducibility of the octane sensitivity S = RON - MON) [85, 86]. However, in terms of ignition and heat release, more accurate multi-component surrogate combinations are necessary

to replicate gasoline fuels' low-temperature (NTC regime) behaviour [79]. Researchers can employ multi-component surrogate formulations to capture additional target gasoline attributes such as carbon / hydrogen ratio, distillation curve, carbon types, emission pattern, and many more, which are required to better understand and model the complexity underlying the chemistry of gasoline combustion [79].

**Table 2.4:** Overview of previous experimental studies on ignition delay studies and laminar burning velocities of PRF - oxidizer mixtures. IDT — Ignition delay time, LBV — Laminar burning velocities.

| Fuel | Investigated Property | Investigated conditions | | | |
|---|---|---|---|---|---|
| | | $T$ / K | $p$ / bar | $\varphi$ | Ref. |
| PRF0, PRF60, PRF80, and RF90 | IDT | 700 - 1200 | 40 | 1.0 | [87] |
| PRF100 | IDT | 700 - 1250 | 13 - 40 | 0.5 - 2.0 | [87] |
| PRF84 | IDT | 715 -1500 | 10 - 40 | 0.5, 1.0 | [88] |
| PRF 70, PRF80, PRF91, and PRF95 | IDT | 700 - 1200 | 10 - 40 | 0.5, 1.0 | [89] |
| PRF90 | IDT | 1050 - 1750 | 1 - 16 | 1.0 Dilution (Ar) = 1:5 | [90] |
| PRF50 | LBV | 298 and 338 | 1 | 0.6 - 1.3 | [91] |
| PRF70, PRF85, and PRF95 | LBV | 358 | 6 | 0.8 - 1.6 | [92] |
| PRF87 | LBV | 373 | 10-25 | 0.7 - 1.2 | [93] |
| PRF90 | LBV | 298 | 1.01325 | 0.7 - 1.4 | [94] |
| PRF90 | LBV | 298 | 1.01325 | 0.8 - 1.3 | [95] |
| PRF90 | LBV | 358 - 450 | 1-10 | 0.8 - 1.2 | [96] |
| PRF90 | LBV | 473 | 1 - 6 | 0.5 - 2.0 | [90] |

For the gasoline surrogate – the primary reference fuel – there are several formulations [84, 87–89]. The primary reference fuel 90 (PRF90), a binary compound of 90% *iso*-octane ($i\mathrm{C_8H_{18}}$) and 10% *n*-heptane ($n\mathrm{C_7H_{16}}$) by liquid volume, was chosen to represent the gasoline surrogate in this work since it has been demonstrated to be a suitable gasoline reference fuel when studying the effects of knocking and ignition [87]. Detailed knowledge on fundamental combustion properties, *i.e.*, ignition delay times and laminar burning velocities, is a pre-requisite to enable a safe and reliable operation when using advanced fuels. For primary reference mixtures, an overview of data on auto-ignition and laminar burning velocity is given in Table 2.4.

In this work, ignition delay times of PRF90 / synthetic air mixtures diluted in nitrogen at

stoichiometric conditions were measured in a shock tube at $p$ / bar = 1, 4, and 16. The results obtained form the basis of comparison for the results obtained for blends of selected OMEs with PRF90 as a gasoline surrogate, as discussed in the following section.

## 2.7 OMEs / gasoline surrogate blends

Besides the research work on individual oxymethylene ethers (OMEs), detailed knowledge on fundamental combustion properties of blends of OMEs and surrogate mixtures for gasoline and diesel can provide useful references for their engine application. For $OME_1$ and $OME_2$, it has been shown that they are not suitable for use as diesel substitutes or blending compounds, because they have high vapor pressure, low-flash point, and low-boiling points, see section 1.2. However, it is well understood that blending of gasoline with high cetane boosters such as ethers among others has opened up the use of gasoline in compression ignition engines operating in homogeneous charge compression ignition (HCCI) mode leading to improved combustion and emission characteristics [40–42, 97]. Studies on the fundamental combustion kinetics of blends of OMEs and surrogate mixtures for gasoline and diesel are limited. The few studies available on this subject address the combustion of $OME_1$ with *n*-heptane as a gasoline surrogate [65, 98, 99], see Table 2.5.

Hu *et al.* studied the ignition delay times of $OME_1$ and its blends with *n*-heptane as a primary reference fuel for gasoline and diesel using the shock tube method at pressures of 2 and 10 atm, $\varphi$ = 0.5, 1.0, and 2.0, and $T$ = 1100-1600 K. The results obtained were used for the development of a chemical-kinetic model for the oxidation of $OME_1$ / *n*-heptane blends. Gao *et al.* [98] studied the oxidation of $OME_1$ /*n*-heptane mixtures using the atmospheric pressure jet-stirred reactor in the temperature range between 500-1100 K, $\varphi$ = 0.5-2.0, and at a residence time of 2.0 s, and developed a chemical kinetic model for describing low-temperature oxidation of $OME_1$ / *n*-heptane blends.

Goeb *et al.* [99] studied the ignition process and soot formation of $OME_1$ and its blend with *n*-dodecane as diesel surrogate fuel using a high-pressure spray chamber. The experimental data were used to validate their chemical kinetic mechanism for the oxidation of $OME_1$ / *n*-dodecane blends. Ren *et al.* [100] developed [100] developed a reduced $OME_3$ / primary reference fuels (PRF) blends chemical kinetic mechanism (145 species and 585 reactions) for predicting combustion and soot formation. The mechanism was extensively validated with ignition delay times, laminar burning velocities, and species concentration data for $OME_3$ and PRF drawn from the literature. The mechanism was further validated with $OME_3$ engine homogeneous charge compression ignition (HCCI) combustion data, *i.e.*, in-cylinder pressure, and heat release rate (HRR). Similarly, Lin *et al.* [101] developed a reduced $OME_3$ mechanism consisting of 61 species and 190 reactions. The mechanism was validated with literature data of ignition delay times and laminar burning velocities of $OME_3$ and various PRF blends. In addition, the mechanism was validated with $OME_3$

flame species concentration profiles data, and homogeneous charge compression ignition (HCCI) combustion data (in-cylinder pressure and heat release rate).

**Table 2.5:** Overview of previous experimental studies on $OME_1$ / conventional fuels. Method: ST — shock tube, JSR — jet stirred reactor, HPCV — high pressure combustion vessel.

| Fuel | Investigated Property | Method used | Investigated conditions | | | |
|---|---|---|---|---|---|---|
| | | | $T$ / K | $p$ / bar | $\varphi$ | Ref |
| $OME_1$ / *n*-heptane | Ignition delay time | ST | 1100 - 1600 | 2.0265, 10.1325 | 0.5 - 2.0 | [65] |
| $OME_1$ / *n*-heptane | Oxidation and speciation | JSR | 500 - 1100 K | 1.01325 | 0.5 - 2.0; $t_{res}$ = 2.0 s | [98] |
| $OME_1$ / *n*-dodecane | Spray combustion | | $T_{chamber}$ = 900 K; $T_{liq.fuel}$ = 363 K | $p_{chamber}$ = 60 $p_{injection}$ = 1500 | | [99] |

**Table 2.6:** Features of available reaction mechanisms for $OME_n$ + primary reference fuels (*n*-heptane + *iso*-octane).

| Reaction mechanism | Species | Reactions | Ref. |
|---|---|---|---|
| $OME_1$ + *n*-heptane | 662 | 3143 | [32] |
| $OME_3$ + PRF | 145 | 668 | [100] |
| $OME_3$ + PRF | 61 | 190 | [101] |

To this end, it has been demonstrated that combustion studies on the interaction of $OME_n$ and surrogate fuels are limited. Thus, this study seeks to enlarge the knowledge on combustion of blends of OMEs with surrogate mixtures for gasoline by presenting new experimental data for ignition delay times of blends $OME_1$ / PRF90, $OME_2$ / PRF90, and *iso*-$OME_2$ / PRF90 with synthetic air at $\varphi = 0.5$ and $p$ / bar = 1, 4, and 16. The ability of the DLR-Concise mechanism to predict the ignition delay times of the pure fuel components and binary mixtures is tested. The results obtained in this work will help to overcome challenges observed in the chemical kinetic modeling of fuel blends that are not seen when only testing pure fuels.

# 3 Experimental and modeling approach

## 3.1 Introduction

This chapter describes the experimental work done at the DLR Institute for Combustion Technology of DLR at Stuttgart on the ignition delay times of neat oxymethylene ethers (DME (or $OME_0$), $OME_1$, $OME_2$, *iso*-$OME_2$, and $OME_4$) and blends of $OME_1$, $OME_2$, and *iso*-$OME_2$ with the primary reference fuel 90 (PRF 90) as a gasoline surrogate. The shock tube facility and instrumentation, method of measurement, data acquisition, and processing techniques are all explained in this chapter. In the first section, the operation principle of the shock tube is described. The next sections present the experimental setup and procedure, mixture preparation, data processing, and experimental uncertainties. The last section of the chapter covers the chemical kinetic modeling technique, including the reaction models used, since the experimental data sets obtained are compared to predictions of detailed chemical kinetic reaction models.

## 3.2 Introduction to ignition delay times measurement

The ignition delay time ($\tau_{ign}$) is a characteristic quantity of any fuel-oxidizer mixture that is of major concern in various combustion devices such as gas turbines and automobile engines. It is the time interval between the initialization of the temperature and pressure of the mixture by shock heating and the onset of ignition. The events that occur during the ignition delay period are characterized by highly-complex radical-chain reactions governed by a chain branching mechanism [102]. The onset of ignition is characterized by an exponential rise in temperature and pressure, as well as an increase in the concentration of radicals, intermediate species, and molecular products such as $CO_2$, $H_2$, and $H_2O$ [102]. In addition, small hydrocarbon intermediate species, such as $C_2H_2$, $C_2H_4$, $C_3H_6$, and $CH_2O$ are also observed in the ignition delay time period [103]. Based on these ignition delay time processes, there are various ways of defining ignition delay times experimentally and numerically. For example, $\tau_{ign}$ can reasonably be defined as the time at which the peak or relative concentration of a species is reached. In addition, the $\tau_{ign}$ can also be based on the extrapolation of the maximum slope of a species or variable such as pressure and temperature to the zero-level signal. As a result, when comparing experimental data from various facilities and making comparisons between measurements and calculations, the criterion used to determine ignition delay time must be taken into account.

The ignition delay times are determined in the measurements of the present work are based on the chemiluminescence emission of electronically excited species CH* and OH* formed during the ignition process and determined by time of the maximum of CH* and OH* (alternatively); where '*' implies that these radicals are in an electronically excited state [104].

## 3.3 Introduction to shock tube

A shock tube is a very versatile device that, by exploiting gas dynamics and thermodynamic relations, a wide range of steady states of temperature and pressure can be established in the test section rapidly and in a highly reproducible manner. This makes it possible to mimic in the test section of the shock tube the various thermodynamic states observed in most combustion systems, such as those in combustion engines and gas turbines. For this reason, shock tubes are employed to study combustion properties such as ignition delay time, which is a fundamental combustion property required for the development and validation of reaction mechanisms [105]. Shock tubes are also employed to study species evolution data, *i.e.*, reactants, intermediate species, and product formation during pyrolysis or combustion events, thus providing direct evidence of the reactions taking place. In addition, shock tubes are vital tools for studying propagation of detonation waves, disintegration and evaporation of droplets, dissociation rates and molecular relaxation rates [106–109]. In this work, the shock tube method is employed in the investigation of the ignition delay times of all the fuel-oxidizer-diluent mixtures.

## 3.4 The operation principle of the shock tube

A shock tube in its basic form is a long tube divided into two sections, a high-pressure or driver section, and a low-pressure driven section. The two sections are initially separated by a diaphragm as shown in Fig. 3.1(a). Before the bursting of the diaphragm, the driven section is filled with a combustible mixture of fuel-oxidizer-diluent, and the driver section is filled with a driver gas such as helium or a tailored mixture of helium and argon. Tailoring the driver gas mixture is important for increasing the shock tube test time; see section 3.5. Conventionally, the conditions that prevail in the different sections of the tube during the various phases of an experiment are denoted by numbers from 1 to 6. For example, the conditions that prevail in the unperturbed, low-pressure driver section (denoted by 1) are represented with a subscript 1, *i.e.*, $T_1$, $p_1$, $\rho_1$, while the initial conditions prevailing on the high-pressure driver section (denoted by 4) are represented with a subscript 4, *i.e.*, $T_4$, $p_4$, and $\rho_4$, as shown in Fig. 3.1(a).

To burst the diaphragm, a pressure difference is applied across the membrane by increasing the pressure in the driver section. The bursting of the diaphragm creates an incident shock wave, a reflected shockwave, the contact surface, and a rarefaction (expansion) fan as shown in Fig. 3.1(b). The incident shock wave propagates toward the direction of the measurement plane while heating and compressing the driven gas, as shown in Fig. 3.1(b). Since the compression waves heat the gas they propagate in, the head compression wave is slower than the tail compression wave. The result is that the trailing waves will reach and superimpose with the head compression wave, leading

to the formation of a strong incident shock wave, *i.e.*, the shock wave achieves its full strength. It is assumed that the shock wave is established almost instantaneously after the rupture of the diaphragm.

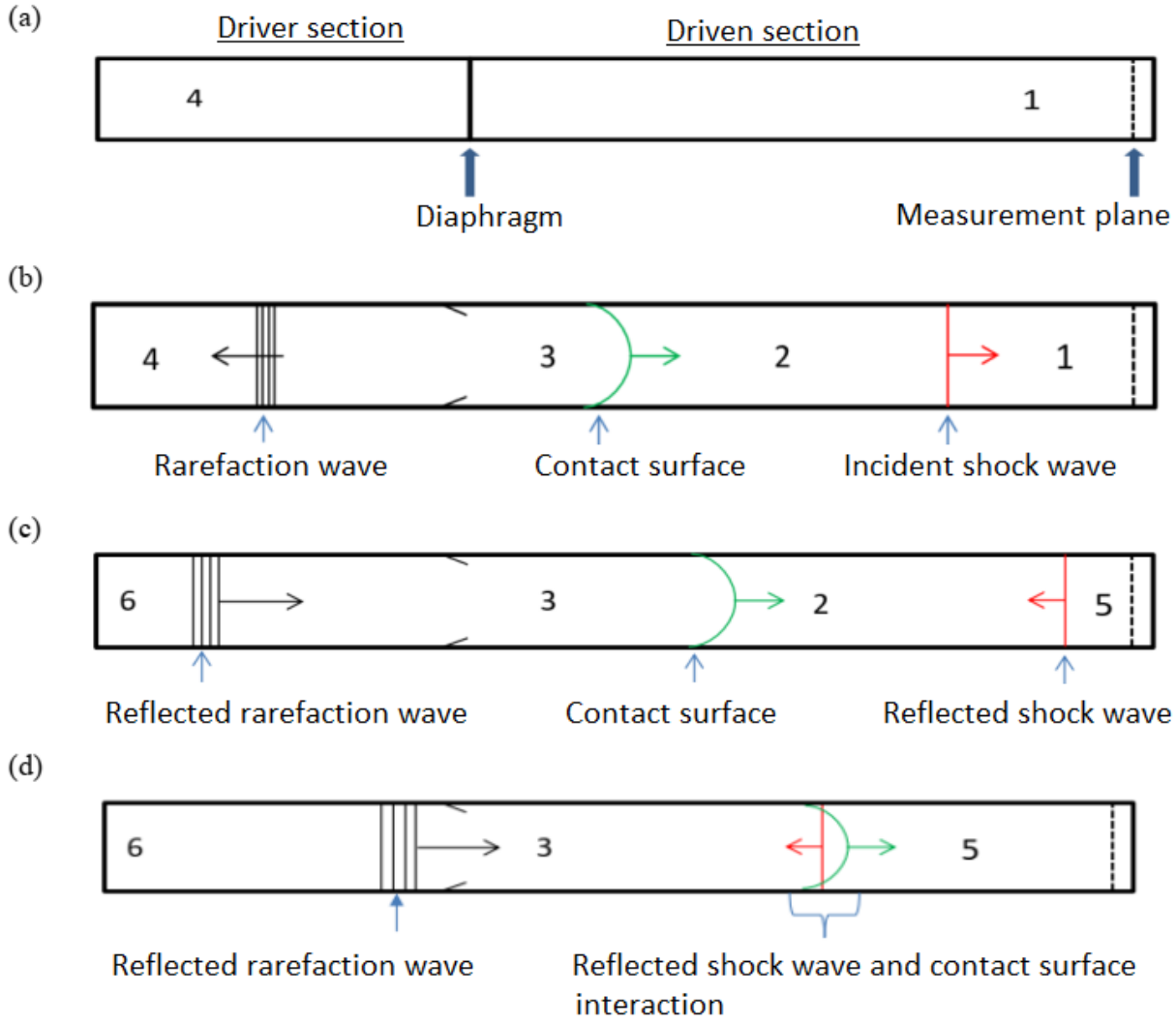


**Figure 3.1:** Functional principle of a shock tube – (a) State 1: Initial state in the shock tube; (b) State 2: The state of the shock tube after bursting of the diaphragm; (c) State 3: The state of the shock tube after reflection of waves at the end, and (d) State 4: Interaction of the reflected shock wave with the contact surface. The formation of the boundary layer behind the incident shock and the interaction of the reflected shock with the boundary layer are not shown.

The conditions prevailing between the shock front and the contact surface are denoted with a subscript 2, *i.e.*, $T_2$, $p_2$, $\rho_2$. The contact surface is the boundary between the driver gas and test gas and it moves in the same direction as the incidence shock wave as shown in Fig. 3.1(b-c). Ideally, it is assumed that this boundary is well defined but in reality, it is a zone characterized

by the displacement of the test gas into the boundary layer, inter-diffusion of gases, and some mixing [106]. Across the boundary (contact surface) it is evident that the pressure and velocity are identical $p_2 = p_3$ and $u_2 = u_3$), but the temperature and the density differ ($T_2 \neq T_3$ and $\rho_2 \neq \rho_3$), and thus the impedances.

On reaching the end wall, the incident shock is reflected and becomes the reflected shock wave as shown in Fig. 3.1 (c). The reflected shock wave propagates in the opposite direction to the incident shock wave as it heats and compresses the test gas for the second time and leaves it stagnant at state 5 ($T_5$, $p_5$, $\rho_5$), see Fig. 3.1(c). The subscript 5 is attached to the state behind the reflected shock wave. This stagnant region of high temperature and pressure is the test region or the region of observation and reaching this state represents the initialization of the reaction boundary conditions for the measurements, *i.e.*, for ignition delay times. Chemical reactions commence in the state of elevated temperatures and pressures established behind the reflected shock wave where various measurements such as shock velocity, light emissions, species evolution profiles, propagation of detonation waves, and disintegration and evaporation of droplets are carried out [106–108]. The state of elevated temperature and pressure behind the reflected shock wave is maintained for a while after which the test sample is quickly quenched by the decompression wave that results from the reflected shock's interaction with the contact surface [107]. It should be noted that, while both the incident and reflected shock waves raise the temperature of the gas, the temperature behind the incident shock wave is generally lower and insufficient to initiate meaningful chemical reactions when compared to the reflected shock wave. As a result, until the reflected shock wave has processed the gases, the system is assumed to be chemically frozen. Optical windows are provided in the diagnostic (test) section of the shock tube, usually at the end wall or end flange, where gas dynamic and ignition processes, as well as laser absorption measurements, are monitored. Visualization techniques include high-speed camera measurements, density gradient measurements (Schlieren imaging), and chemiluminescence measurements.

The rupture of the diaphragm also generates a series of expansion waves typically known as rarefaction fan in the driver section that propagates at the local speed of sound in the opposite direction to the incident shock wave, as shown in Fig. 3.1 (b). It should be noted that, since expansion waves cool the gas they propagate in, the head expansion wave is always faster than the tail expansion wave. The conditions prevailing between the contact surface and rarefaction wave are defined by subscript 3 ($T_3$, $p_3$, $\rho_3$). On hitting the end wall, the rarefaction wave is reflected leaving the gas behind at state 6 ($T_6$, $p_6$, $\rho_6$). The interaction of the reflected head rarefaction wave with the contact surface leads to decompression and quenching of the test gas, hence stopping all chemical reactions. Figure 3.2 shows the shock wave phenomena and the resulting changes in temperature and pressure due to the various wave phenomena in the shock tube. In Fig. 3.2, the regions 1-6 correspond to similar regions as explained in Fig. 3.1.

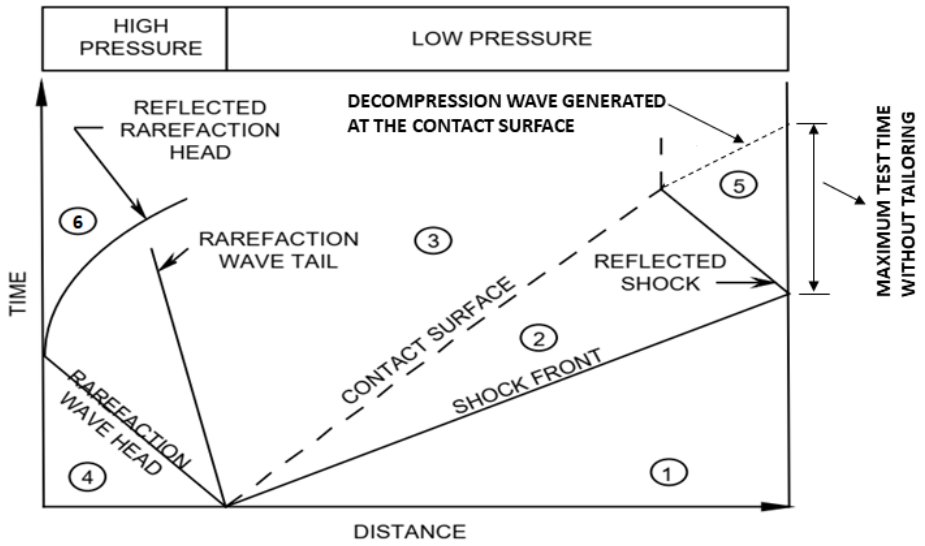


**Figure 3.2:** An *x-t* diagram illustrating the movements of the shock front, contact surface, rarefaction wave, and reflected shock wave [110, 111].

## 3.5 Shock tube test time and driver gas tailoring

To study combustion chemistry in shock tubes at low to intermediate temperatures, it is important to sustain the uniform conditions established behind the reflected shock wave for longer periods of time. This is because, at low and intermediate temperatures between 800-1400 K, reactions are slow and auto-ignition can occur in the order of several milliseconds, *i.e.*, up to 15 milliseconds. Shock tube test time refers to the time available for measurement in the state of elevated temperature and pressure behind the reflected shock wave. It is defined as the time between when the reflected shock wave is established at the end wall and the time when the first disturbance wave (compression or expansion) from the contact surface arrives at the end wall; see Fig. 3.2 [106]. The test time in many shock tubes using mostly helium as the driver gas component is in the order of 2-3 microseconds, depending also on the ratio of the lengths of the driven and driver sections. For investigations in high temperatures where short test times are realized, helium is used as the main component of the driver gas since it produces the required strong shocks owing to its low molecular weight.

To extend the experimental test times and thus to allow investigation in the low-temperature regime, the conditions behind the reflected shock wave can be extended by tailoring the interface between the driver and driven gas, *i.e.*, by mixing helium with a heavier gas such as argon and nitrogen. Tailoring adapts the impedance of the driver gas (mostly helium) to match that of the driven gas (mostly air). Impedance refers to the resistance of the reflected shock wave to propagating through another medium. When a shock wave, *e.g.*, the reflected shock wave propagating through a uniform medium encounters a second medium with different physical characteristics, *i.e.*, at the contact

surface, it is expected that the shock wave will be transmitted into the second medium and that a disturbance *i.e.*, a second shock wave or a rarefaction wave, will be formed and transmitted back into the original medium. In this case, the resulting disturbance will be larger when the impedance between the two media is unmatched. At the tailored condition, the reflected shock wave passes through the tailored contact surface with unchanged shock strength or unattenuated. In this case, the reflected rarefaction wave will decompress the reactive mixture, and this defines the maximum test time. The rule of thumb for tailoring the interface is that the specific internal energy ratio in gases at state 2 and state 3 be unity. Mathematically, this can be expressed as shown in Eqn. 3.1, where $c_{v,3} = c_{v,2}$, $E$ is the specific energy, $T$ is the temperature, $c_v$ is the heat capacity at constant volume, and $M$ is the molecular weight of the gases [112, 113]. This condition is caused by the requirement $\rho_2 = \rho_3$. The subscripts 2 and 3 represent the state upstream and downstream of the contact surface, respectively; see Fig. 3.1. This is the approximate rule for tailoring. The concept of tailoring the contact surface is explained in the literature, such as by [114–118].

$$\frac{E_3}{E_2} = \left[\frac{c_{v,3}.T_3}{M_3}\right] / \left[\frac{c_{v,2}.T_2}{M_2}\right] \tag{3.1}$$

## 3.6 Experimental setup and procedure

All ignition delay time measurements in this study were carried out in a shock tube with an internal diameter of 9.82 cm and driven and driver sections, respectively of 11.348 m and 5.18 m in length. Figure 3.3 shows the schematic diagram of the shock tube. This shock tube has been previously described [119, 120]. It has five major components: the driver, intermediate section, inlet system, driven section, and measurement section; see Fig. 3.3. The inlet section is a manifold attached at about the mid-section of the driven section, providing the ports for pumping down and for adding the test mixture into the driven section. Attached to the inlet manifold is the turbomolecular vacuum pump for evacuating the shock tube to low pressures of at least below $5^{*}10^{-6}$ mbar before each experiment. An intermediate section separates the driver from the driven section and allows the use of a double aluminum diaphragm to separate the driver section from the driven section. Thus, this shock tube can be operated in a double-diaphragm or a single-diaphragm mode. The single diaphragm configuration is applicable for experiments at low pressures of 1 bar where the applied pressure difference between the driven and the driver section is enough to rupture the diaphragm. On the other hand, the double-diaphragm configuration is utilized for shocks at elevated pressures of 4 and 16 bar. The double diaphragm configuration introduces a short buffer region between the driver and the driven section which is filled to half the pressure in the driver section. The shock is initiated by releasing the pressure in this section, thus rapturing the aluminum membranes. The advantage of this is that it serves to reduce the pressure load on each of the two

diaphragms and thus promotes the ability to control the experiment [108]. Because the volume of the intermediate section is so small in comparison to the volume of the driven section, the use of a double diaphragm does not affect the processes occurring in the shock tube. As a result, the pressure ratio $p_4 / p_1$ set at the start of the experiment is unaffected by the intermediate volume venting [121]. Hence, the application of the double-diaphragm configuration does not affect the application of the one-dimensional shock model equations applied to compute the conditions behind the reflected shock wave.

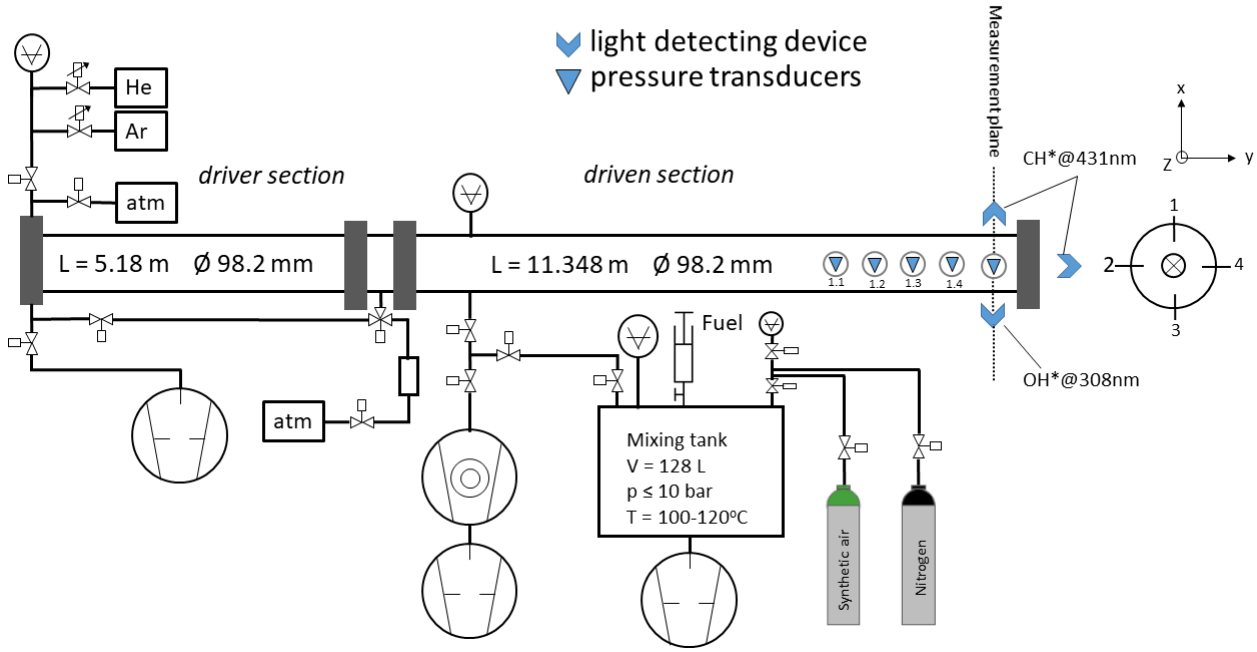


**Figure 3.3:** Schematic diagram of the shock tube with the measuring devices, preparation of fuel-oxidizer-$N_2$ mixture, and driver gas supply for determination of ignition delay times. L — length of the driver or driven section and ⌀ — diameter of the tube.

For this shock tube, the observation period is limited to about 3 ms when using helium as the only component of the driver gas because the decompression wave is generated following the Mach number change of the reflected shock wave after passing the contact surface. Thus, helium and argon mixtures, both with a purity of 99.996% or higher, were used as the components of the driver gas. The flow of the driver gas components was controlled by Bronkhorst (model E-7100-RAA) mass flow controllers.

## 3.7 The diagnostic section of shock tube

The diagnostic (or measurement) section of the shock tube is located close to the end wall, see Fig. 3.3. The first measurement plane $x$-$y$ has four 4 fast-acting piezoelectric pressure transducers (type

PCB113B24) mounted in the measurement planes 11, 12, 13, and 14 at ports 11.2 to 14.2 separated from each other by a constant distance of 20 cm. The last piezoelectric pressure transducer is located 17.8 cm from the end wall. The pressure transducers detect the pressure rise following the passage of the incident and reflected shock waves. The signals from the four pressure transducers are relayed into a low-noise voltage preamplifier (Scientific instruments SR560). The amplified signals are relayed to the Genesis high-speed data recorder and acquisition system (model IDH106) and the counters (model HAMEG HM 8123) which record the time for the incident and reflected shock wave or deflagration wave arrival at each pressure transducer. Three counters are used for the incident and three for the reflected shock wave. The recorded time intervals are used to calculate the velocity of the incident and reflected shock wave. The second measurement plane (*x*-*z*, also referred to as radial or side-on) located 10 mm from the end wall has two additional piezoelectric pressure transducers, Kistler (type 603B) and PCB (type 113A24) at position 1 (top) and 3 (bottom) respectively and two photomultipliers (type, HAMAMATSU® R3896) at position 2 and 4, respectively, see Fig. 3.3.

All the pressure transducers are shielded against heat transfer and hence signal drift by a layer of at least 1 mm coating of RTV106 high-temperature silicone rubber. The two photo multipliers (positions 2 and 4) detect the chemiluminescence of the excited OH* and CH* radicals observed at wavelengths of 308 nm and 431 nm, respectively. The narrow-band interference filters (Hugo Anders, FWHM = 5 nm) before the photomultipliers window ensure that only the photons of wavelengths 431 nm and 308 nm are detected for CH* and OH*, respectively. The signals from the photomultipliers are amplified by logarithmic amplifiers (model FEMTO HLVA-100). Located at the end wall is a sapphire glass window, where an additional photomultiplier (type, Hamamatsu® R3896) detects the chemiluminescence of CH* radicals at a wavelength of 431 nm in the axial direction through the window. All the pressure and emission signals were relayed to the Genesis high-speed data recorder and acquisition system (model IDH106). The recorded signals were then transferred to the in-house program for calculating the parameters behind the reflected shock wave and for signal filtering.

## 3.8 Mixture preparation procedure

Before starting each measurement, the ignitable mixtures of fuel / oxidizer / diluent are prepared. The detailed composition of the fuel / oxidizer mixtures studied is given in Table 3.1, where the dilution ratio of 1:5 means taking 1 part of the fuel / synthetic air mixture and 4 parts $N_2$ by molar fractions.

Due to the low-vapor pressure of the fuels investigated, the temperature of the mixing vessel was adapted to the minimum temperature required to keep the fuel / oxidizer / diluent mixtures in

gaseous form. The vessel was heated to 313 K for $OME_1$ (boiling point of 315 K), 353 K for PRF90 (boiling point of 373 K for *iso*-octane $iC_8H_{18}$ and *n*-heptane $nC_7H_{16}$), and 373 K for $OME_2$ (boiling point of 379 K), and 393 K for $OME_4$ (boiling point of 475 K).

Before preparing the combustible mixtures, the vessel is isolated from the shock tube, flushed with $N_2$, and evacuated to low pressures of below $10^{-5}$ mbar by a turbomolecular pump. The fuel-oxidizer-diluent mixtures were prepared according to Dalton's law of additive pressures as described in previous works [122]. The predetermined mass of fuel corresponding to its target partial pressure is weighed with a high precision balance (type Mettler Toledo XPR5003S, with an accuracy at 1000 g of ±0.0195 g) and then injected with a gas-tight syringe directly into the evacuated tank through the septum, see Fig. 3.3. The weight of the fuel was determined by weighing the syringe before and after injection. To ensure that all the fuel is fully evaporated, the actual partial pressure of the gas-phase fuel vapor is read from the pressure transducer and controlled with the calculated partial pressure (from the injected mass of fuel). Synthetic air (20% $O_2$ + 80% $N_2$) is then charged to meet the desired equivalence ratio.

The partial pressure of the fuel and synthetic air is controlled by a high-precision pressure transducer (type: ALTHEN-HI2010; sensitivity: 58.33257 mV/bar; tolerance: ± 0.09326 mV/bar). Finally, nitrogen is added to achieve the desired dilution ratio of 1:5, *i.e.*, 20% fuel-oxidizer mixture + 80% $N_2$. For DME which is a gaseous fuel at room temperature, the combustible mixture of DME / air / $N_2$ was prepared in a stainless-steel gas cylinder using the same procedure. The cylinder was then directly connected to the inlet manifold of the shock tube. Combustible mixtures with $OME_4$ were prepared by injecting the liquid fuel with a syringe onto passivated glass fibers and then evaporating and transporting it into the evacuated vessel by a stream of preheated nitrogen (@393 K). For combustible mixtures with DME, oxygen and nitrogen were charged separately and their ratios were set to mimic the composition of air, *i.e.*, $N_2$ / $O_2$ = 79 / 21 while also meeting the required $\varphi$ = 1.0 and dilution level of 1:5 with $N_2$. However, for simplicity, all the other combustible mixtures with synthetic air as an oxidizer, and nitrogen was charged to meet the required dilution level as described in this section. In this work, several multi-component fuel mixtures were investigated. For example, primary reference fuel 90 or PRF90 (a mixture of 90% *iso*-octane and 10% *n*-heptane, by liquid volume) and a mixture of 30% $OME_1$ / 70% PRF90 blend, and many others; see Table 3.1. These blended fuel mixtures were prepared in advance in a small glass container. The combustible mixtures with these fuels were then prepared via direct injection into the mixing vessel as previously described.

**Table 3.1:** Composition of the combustible mixtures for ignition delay time measurements. The quantities given include the decomposition products

| No. | Fuel | Composition (ppm) |
|---|---|---|
| 1 | DME / air / $N_2$ | 13104 DME<br>39298 $O_2$<br>947598 $N_2$ |
| 2 | $OME_1$ / synthetic air / $N_2$ | 9490 $OME_1$<br>38277 $O_2$<br>952233 $N_2$ |
| 3 | PRF90 / synthetic air / $N_2$ | 2872 $iC_8H_{18}$<br>319 $nC_7H_{16}$<br>39308 $O_2$<br>957901 $N_2$ |
| 4 | 30% PRF90 + 70% $OME_1$ / synthetic air / $N_2$ | 1612 $iC_8H_{18}$<br>179 $nC_7H_{16}$<br>4179 $OME_1$<br>38489 $O_2$<br>955541 $N_2$ |
| 5 | $OME_2$ / synthetic air / $N_2$ | 7428 $OME_2$<br>274 $OME_1$<br>133 $CH_3OH$<br>38493 $O_2$<br>953672 $N_2$ |
| 6 | *Iso*-$OME_2$ / synthetic air / $N_2$ | 564 $CH_3OH$<br>1031 $CH_3OCHO$<br>6210 iso-$OME_2$<br>38424 $O_2$<br>953772 $N_2$ |
| 7 | 30% PRF90 + 70% $OME_2$ / synthetic air / $N_2$ | 4029 $OME_2$<br>80 $OME_1$<br>44 $CH_3OH$<br>1602 $iC_8H_{18}$<br>178 $nC_7H_{16}$<br>38774 $O_2$<br>955291 $N_2$ |
| 8 | 30% PRF90 + 70% iso-$OME_2$ / synthetic air / $N_2$ | 3358 *iso*-$OME_2$<br>494 $CH_3OH$<br>299 $CH_3OCHO$<br>1601 *i*C8H18<br>178 $nC_7H_{16}$<br>38799 $O_2$<br>955270 $N_2$ |
| 9 | $OME_4$ / synthetic air / $N_2$ | 5407 $OME_4$<br>75 $OME_3$<br>44 $OME_1$<br>406 $CH_2O$<br>38898 $O_2$<br>955130 $N_2$ |

The gases used were obtained from Linde with the following purities: DME — 99.9%, $O_2$ — 99.9999%, $N_2$ — 99.9999%, and synthetic air — 99.999%. $OME_1$ was obtained from Sigma-Aldrich with a purity of 99.0%. *Iso*-octane and *n*-heptane were obtained from Merck both with a purity of 99.0%. $OME_2$ was obtained from Analytik-Service GmbH (ASG) with a purity of 98.81% — mass with the remaining part mainly $OME_1$, trimethyl orthoformate was obtained from Alfa Aesar with a purity of 99%.

### 3.8.1 Mixture quality control

In this work, all fuels investigated apart from dimethyl ether (DME) are low-vapor pressure fuels. Thus, to investigate these fuels, the mixing vessel and the shock tube were adapted to the predetermined temperature required to keep the fuel in gaseous form and avoid condensation; see section 3.8. This temperature can be lower than the boiling point of the fuel for low-fuel concentration experiments. The most unique aspect of this work was the monitoring of the quality of the mixture after preparation. Due to the high temperatures required to keep the fuels in gaseous form, it is obvious that some thermal degradation would occur. For this reason, the purity of every fuel as well as the composition of each fuel-oxidizer-diluent mixture was checked and monitored for thermo degradation products and residual compounds using gas chromatography[3]. $OME_1$ and methanol were identified in mixtures with $OME_2$. The average combined levels of $OME_1$ and methanol relative to $OME_2$ were within the range of 5%; see Table 3.1.

In combustible mixtures with $OME_4$, the thermal degradation products $OME_1$, $OME_3$, formaldehyde ($CH_2O$), and small amounts of methanol (≈10 ppm) were identified and monitored. The average decomposition product relative to $OME_4$ was less than 5%. The combustible mixtures with $OME_4$ had to be shocked within 2 hours for the levels of degradation products relative to $OME_4$ to be kept within a maximum range of 5%. To have a good comparison between the measurements and calculations in this work, the mixture composition from the experiments which is controlled by GC tests was used as an input during the calculations.

For demonstration, Fig. 3.4 shows an example of a gas chromatogram obtained from a sample drawn from the *iso*-$OME_2$ / synthetic air / $N_2$ mixture showing *iso*-$OME_2$ and decomposition products methyl formate ($CH_3OCHO$) and methanol. Details on the gas chromatography procedure can be found in the work of Schuler [123].

[3]The gas chromatography tests were carried out by Mr. Nobert Ackermann, DLR Stuttgart.

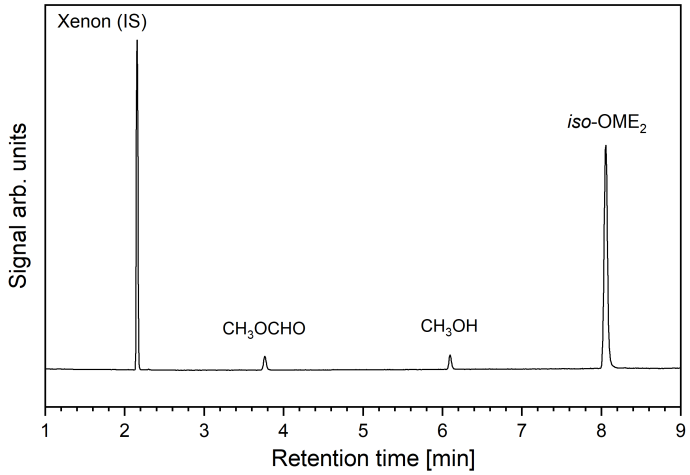


**Figure 3.4:** Gas chromatogram of the sample drawn from *iso*-$OME_2$ / synair /$N_2$ mixture. Xenon was used as an inert internal standard (IS). Column used: ZB-WAXplus.

## 3.9 Data processing

### 3.9.1 Incident shock velocities

The conditions directly behind the reflected shock $T_5(t/s = 0)$ and $p_5(t/s = 0)$ are determined by solving the Rankine-Hugoniot equations (see Appendix D) with initial gas composition, initial temperature $T_1$ and pressure $p_1$ of the driven gas, the Mach number ($M_1$) of the incident shock, and the thermodynamic data of each species as the input parameters. The inlet pressure $p_1$ is measured when the driven section is filled and $T_1$ is the initial temperature of the mixture which is also the temperature at which the driven section of the tube is heated. The Mach number ($M_1$) is determined from the incident shock velocity ($u_1$) and speed of sound at $T_1$ and $p_1$; see Eqn. D.6. The incident shock velocity ($u_1$) is derived from the recorded time intervals ($\Delta$t) between two pressure transducers and the distance ($\Delta x$) between two pressure transducers; see Eqn. 3.2.

$$u_1 = \frac{\Delta x}{\Delta t} \tag{3.2}$$

### 3.9.2 Determination of ignition delay time

All the ignition delay time values in this work were derived by measuring the time interval between the arrival of the incident shock wave at the end plate ($t/s = 0$) and the occurrence of the maximum emission of the excited CH* radical measured at the side port (radially) and through the end plate window as shown in Fig. 3.5. The radial signal is preferred for the ignition delay time measurements since the maximum emission is related to the ignition event directly behind the reflected shock wave. On the other hand, the signal through the end plate window integrates the emission of light from all locations in the tube, see Fig. 3.3;. In this work, the onset of ignition is monitored

by two methods: First, the CH* and OH* radicals emission at wavelengths of 431 nm and 308 nm respectively are observed radially (side-on) at the measurement and axially (head-on) through the end-plate window, by a narrow-band pass filter (Hugo Anders, FWHM = 10 nm) and detected by Hamamatsu R3896 photomultipliers, see Fig. 3.3. FEMTO HLVA-100 logarithmic amplifiers amplify the emission signal from the photomultipliers. Secondly, ignition is monitored at the measurement plane by measuring the pressure profile with a fast-response pressure transducer (Kistler 603B) (see Fig. 3.3) which is protected against flash temperature by a thin layer of RTV116 silicon rubber. A Savitzky – Golay filter is applied to smooth the pressure signal.

Figure 3.5 shows an example plot of pressure and normalized CH* emission signal (axial and radial) obtained from a single experiment for 70% $OME_1$ + 30% PRF90 / synthetic air at $\varphi = 1.0$ and dilution of 1:5 with $N_2$ with an initial temperature of 1156 K and initial pressure $p(t = 0) = 15$ bar behind the reflected shock wave. In the first stage, the pressure is observed to increase in two steps that respectively correspond to the passage of the incident and the reflected shock wave. For this case, after the reflected shock wave has passed, the pressure increases gradually in a linear way and reaches a maximum at about 2000 $\mu s$ due to viscous gas dynamics, *i.e.*, due to dampening of the reflected shock wave due to its interaction with the boundary layer left behind by the incident shock wave. After 2000 $\mu s$, a steeper increase in pressure is observed due to the combined effect of viscous gas dynamics and heat release. Thus, the steep rise in pressure and CH* emission after 1900 $\mu$s correspond to ignition and heat release.

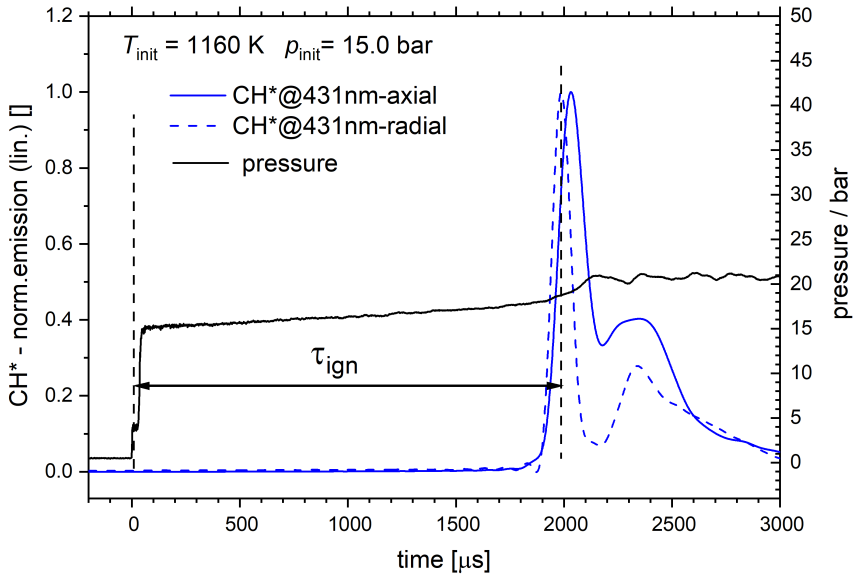


**Figure 3.5:** Example of pressure and emission signals (axial and radial) obtained for a single $OME_1$ + PRF90 (70:30) / synthetic air experiment: $\varphi = 1.0$, $p(t = 0) = 15$ bar, $T(t = 0) = 1160$ K, and a dilution of 1:5 with $N_2$.

### 3.9.3 Position and blast wave correction

The system is initialized during ignition delay time measurements by reaching the test temperature $T_5$ and pressure $p_5$ in the test region ($t/\mathrm{s} = 0$) via the formation of the reflected shock wave at the end wall. However, in our diagnostic system, time counting starts earlier when the incident shock wave passes the pressure transducer at the measurement plane (MP), 10 mm away from the end wall. As a result, ignition delay times derived from the radial port $t([\mathrm{CH}*])_{\mathrm{max}}$ must be corrected by subtracting the running time of the incident shock wave up to the end plate (EF), $t_{inc,\mathrm{EF}}$. In addition, the moving blast wave affects the interpretation of the results when they are conducted at a side-wall (radial port) location. Ignition is supposed to be observed first at the end wall location because the ignitable gas at the vicinity of the end wall is exposed longer to the high temperature and pressure conditions than further away and the ignition kernel propagates to the radial port for the emissions to be detected there [124, 125]. For this reason, the transit time of the blast wave $t_{BW}$ from the end wall to the measurement plane must be subtracted. Therefore, the ignition delay time at the radial port relative to the end wall is calculated using:

$$\tau_{\mathrm{ign}} = t([\mathrm{CH}^*])_{\mathrm{MP}} - t_{\mathrm{inc}} - t_{\mathrm{BW}} \tag{3.3}$$

The running time of the blast wave $t_{\mathrm{BW}}$ is approximated by the following equation:

$$t_{\mathrm{BW}} = \frac{\Delta x_{\mathrm{s}}}{u_{\mathrm{BW}}} = \frac{0.001\,\mathrm{m}}{u_5 * f} \tag{3.4}$$

where $x_{\mathrm{s}}$ is the distance of 0.01 m between the end wall and the measurement plane and $u_{\mathrm{bw}}$ is the velocity of the blast wave. The denominator on the right-hand side in Eqn. 3.4 represents an estimation of the blast wave velocity. Since the actual velocity of the blast wave can only be measured if the blast wave imprints a significant pressure signal on its way to the contact surface, the calculated velocity of the reflected shock wave $u_5$ is enhanced by an estimation factor $f$ which is based on suitable experiments, particularly in the high-temperature regime. The value of $f > 1$ since the blast wave catches up with the reflected shock wave as it propagates towards the contact surface.

### 3.9.4 Pressure profiles

It should be noted that, for this shock tube, the conditions immediately behind the reflected shock wave, *i.e.*, $T_5(t / \mathrm{s} = 0)$ and $p_5(t / \mathrm{s} = 0)$ can be regarded as constant for short observation times of up to 3 ms. For a longer observation period, non-ideal effects due to the dampening of the reflected shock wave following its interaction with the growing boundary layer left behind by the incident shock wave and its interaction with the contact surface make the initial state behind the reflected shock wave change in a time-dependent way; see Fig. 3.6. The result is an increase in pressure and thus also in temperature in time dependent manner behind the reflected shock wave. Without additional measures such as the use of driver inserts, staged filling, and dynamic mass flow reduction of the driver, post-shock compression pressure rise cannot be avoided even for non-ignitable mixtures [126, 127]. The extent of the pressure (and temperature) increase in the test section is dependent on various factors that influence the boundary layer interaction with the reflected shock wave such as test conditions, the diameter of the driven section, and the length of the driven section and thus varies from one facility to another [128].

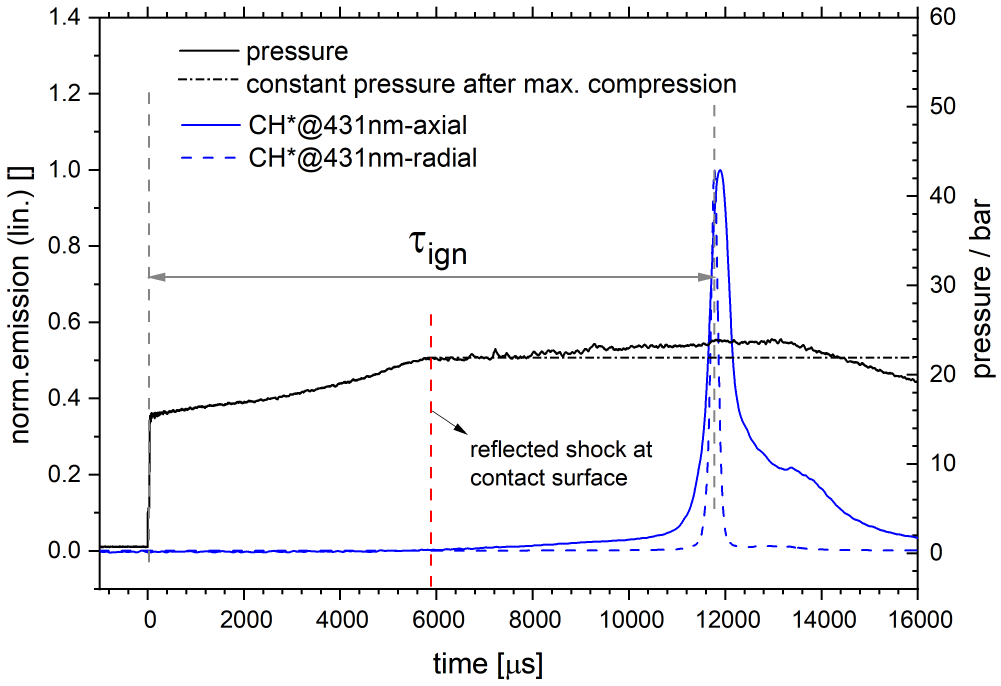


**Figure 3.6:** Example of pressure and emission signals (axial and radial) obtained for a single $OME_1$ + PRF90 (70:30) / synthetic air experiment: $\varphi = 1.0$, $p(t = 0) = 15$ bar, $T(t = 0) = 960$ K, and a dilution of 1:5 with $N_2$ using a driver gas composition of 85% helium and 15% argon.

Figure 3.6 is an example of an emission and pressure profile obtained for measurements with an extended observation period and thus with a very pronounced pressure profile. After the reflected shock wave has passed, the pressure increases gradually in a non-linear way and reaches

a maximum at about 5800 $\mu$s due to viscous gas dynamics, *i.e.*, due to dampening of the reflected shock wave due to its interaction with the boundary layer left behind by the incident shock wave that is causing a mismatch to the velocity of the gas behind the incident shock. Thus, the impulse of the gas cannot be compensated completely by being processed by the reflected shock but remains a residual impulse that further compresses the gas. From here, the pressure remains constant due to a change in the conditions determining attenuation of the reflected shock and then gradually rises from about 7100 $\mu$s after the reflected shock wave has passed the contact surface due to the influence of heat release and further attenuation as well as reflections from the burst diaphragms. Once the tailored condition is achieved, the pressure profile should remain constant (see dashed line in Fig. 3.6) after maximum compression is reached, even when the reflected shock wave passes the contact surface, until the reflected rarefaction decompresses the system or the mixture ignites because of the weak attenuation of the reflected shock wave front in the driver gas [120].

To account for the facility-dependent rise in pressure due to viscous gas dynamics when calculating ignition delay times, a normalized experimentally derived pressure profile $p(t) \,/\, p(t/\mathrm{s} = 0)$ is provided to the calculations: see *e.g.*, 3.6. The characteristic pressure profile $p(t)$ is derived from experiments without ignition (or from those with long ignition delay times) and with non-combustible mixtures with almost similar acoustic impedance as the test gas. For OMEs, due to their early heat release, the pressure profile is considered up to the point of distortion due to heat release. In this case, the pressure profiles from non-combustible mixtures with similar acoustic impedance provide the check for heat release in reactive experiments.

By considering the normalized pressure profiles from selected experiments, the pressure profile is derived by applying a non-linear fit as shown in Fig. 3.7. Because this pressure profiles do not show any distortions due to heat release, the fit is extrapolated at a constant level after maximum compression is reached, which is connected to the contact surface transition of the reflected shock front. Behind this point, the pressure should remain constant in a well-tailored case until the decompression due to the rarefaction wave arrives at the end wall; thus, the fit is extrapolated at constant level from there on providing a constant-pressure to the modeling conditions, too. Figure 3.7 is an example of the experimentally derived pressure profile determined for 70% $OME_1$ + 30% PRF90 / synthetic air at $\varphi$ = 1.0 and a dilution level of 1:5 with $N_2$ at (a) 4 bar and (b) 16',bar. It is observed that for 4 bar the pressure will rise to $p(t) \,/\, p(t = 0)\,(t/\mathrm{ms} = 4.7) = 1.38$ and for 16 bar to $p(t) \,/\, p(t = 0)\,(t/ms = 5.7) = 1.39$.

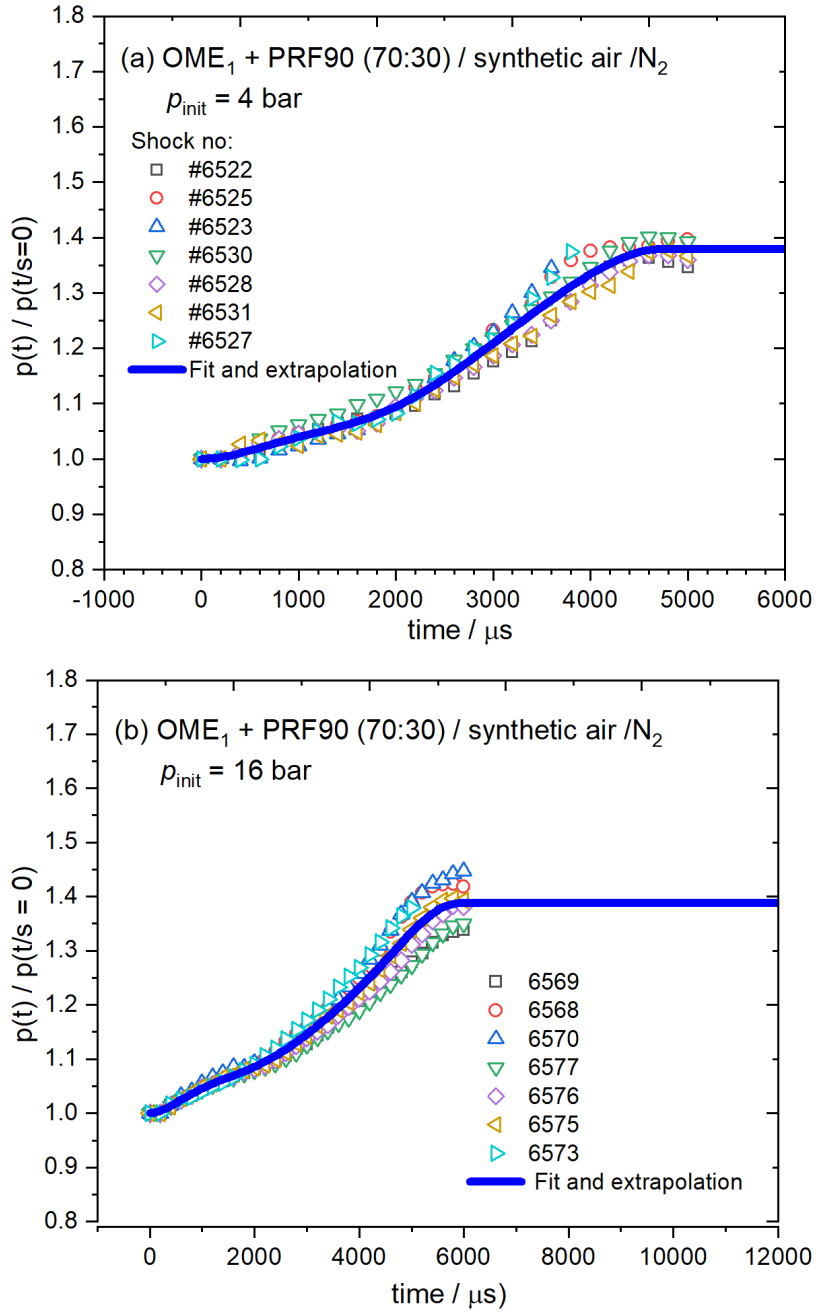


**Figure 3.7:** Regression curve for the mean pressure increase due to post-compression determined using suitable experiments for stoichiometric 70% $OME_1$ + 30% PRF90 / synthetic air mixtures (dilution of 1:5 with $N_2$) at initial pressure behind reflected shock wave of (a) 4 bar, and (b) 16 bar. The conditions for shocks are provided in Appendix K.

## 3.10 Discussion of experimental uncertainties

The ignition delay time uncertainty is attributed to several sources, some of which are more significant than others. The uncertainty in the measured ignition delay time value is attributed to uncertainties associated with:

(i) Determination of the ignition delay time itself,

(ii) determination of the velocity of the incident shock wave, and

(iii) mixture composition.

The error due to mixture composition is an error with minimal influence since the weight of the mass of the fuel injected is controlled by a high precision balance (type Mettler Toledo XPR5003S, with an accuracy at 1000 g of ±0.0195 g) and the partial pressure of the fuel is controlled by a high-precision pressure transducer (type: ALTHEN-HI2010; sensitivity: 58.33257 mV/bar; tolerance: ±0.09326 mV/bar), see section 3.8. For these reasons, the uncertainty due to mixture composition will not be considered further.

### 3.10.1 Uncertainties due to determination of the ignition delay time

Uncertainties in determining ignition delay times include those caused by the blast wave correction process, manual extraction of the CH* maximum, and the detection system's spatial resolution.

(i) As already mentioned in section 3.9.3, the measurements at the side-wall (side-on) location are related to the measurements at the end wall through a blast wave correction process. Since the true velocity of the blast wave is hard to obtain, the correction is based on the deflagration velocity of the highest temperature measurements in each series. At our experimental conditions, correction due to blast wave correction is up to 20 $\mu$s which can artificially shorten the radially (side-on) derived ignition delay times. This error is only significant for short ignition delay times, *i.e.*, less than 30 $\mu$s. For long ignition delay times, *i.e.*, above 3 ms, blast wave correction is insignificant because the correction is only a small percentage of the long ignition delay times. Due to this, the axially (head-on) derived ignition delay times are preferred for very short ignition delay times typically up to 30 $\mu s$ because for head-on emission detection there is no need to consider any transit time corrections of the deflagration wave after ignition. The detection setup comparison of both emission signals (radial with axial) decreases the inaccuracy of blast wave correction at the maximum temperatures to ±30%, despite the blast wave correction process being required for the radial port emission detection measurements [120].

(ii) The chemiluminescence maxima of CH* are read manually from the CH* emission profile. This process results in an error, especially for low-temperature shocks where the CH* emission profile is broad and with no clear maximum. This error is estimated to be in the range of a few microseconds and thus can be ignored.

(iii) Additionally, there is an experimental error on the side-wall data attributed to the spatial resolution of the side-wall CH* detection system. Although restricted by slits, light from a 6 mm diameter zone in the center of the tube reaches the detector of the photomultiplier via the optics of the side-wall detection system. The time it takes the combustion wave (blast wave) to pass through this region adds to the uncertainty of the side-wall IDTs. This error is determined to be about 12 $\mu$s at an average blast wave velocity of 500 m/s. This error is also insignificant since it makes up a small fraction of the long ignition delay times, *e.g.*, from 1 to 12 ms reported in our measurement.

### 3.10.2 Uncertainties due to incident shock wave velocity measurements

The uncertainty in the measured ignition delay time is more significantly influenced by the uncertainties in the initial temperature $T_5$ due to the strong coupling between chemicals kinetic rates and thus on ignition delay times on the temperature. The initial temperature $T_5$ and pressure $p_5$ behind the reflected shock wave are computed from the incident shock velocity, measured via the four piezo-electric pressure gauges at intervals of 200 mm using a one-dimensional shock model. Thus, uncertainty in $T_5$ and $p_5$ is predominantly due to the accuracy of shock velocity measurement. The relative error error in the measured incident shock wave velocity for this shock tube is about ±1%. This relative error $du_1/u_1$ leads ($\Rightarrow$) to an error in $dT_5$ / $T_5$ and $dp_5/p_5$; see Eqn. 3.5. By solving the 1-dimensional normal shock problem for the shock with $u_1 \pm du_1$ the error in incident shock velocity ($du_1$ / $u_1$) is translated into the error is $\pm\Delta T_5$ and $\pm\Delta p_5$. This process results in an uncertainty in $T_5$ of around ±15 K throughout the whole range of our data. In the ignition delay time plots, this will be shown as the uncertainty in the x-direction on the experimental data.

$$\frac{du_1}{u_1} \Rightarrow \left(\frac{dT_5}{T_5}, \frac{dp_5}{p_5}\right) \tag{3.5}$$

The uncertainty in ignition delay time due to the uncertainty $u_1 \pm du_1$ in incident shock velocity is approximated using a chemical-kinetic calculation using the DLR-Concise model [1], by taking the upper $(\Delta T_5, \Delta p_5)_{@u_1+du_1}$ and lower $(\Delta T_5, \Delta p_5)_{@u_1-du_1}$ limits in $T$ and $p$. Thus, y-direction error bars on the predicted ignition delay times using DLR-Concise model [1] depicts the sensitivity of the model to the experimental uncertainty error in temperature and pressure due to the error in the incident shockwave velocity.

## 3.11 Chemical kinetic modelling

### 3.11.1 Mechanism of OMEs combustion

The combustion of hydrocarbon fuels is governed by different sets of reactions at low and high-temperatures. The low-temperature chemistry dominates at temperatures of approximately 600-1100 K, while the high temperature chemistry is important at temperatures above 1100 K [129–131]. Figure. 3.8 illustrates a scheme for oxidation OMEs, which is based on the idea that the reaction classes are comparable to those of well-researched normal alkanes since the active reaction sites are still the carbon atoms in the structure of OMEs [25, 31]. OMEs are however different from regular saturated alkanes because of the absence of direct carbon-carbon bonds in their molecular structure and because of the arrangement of atoms, see Fig. 2.1. For this reason, the pathways that lead to formation of alkenes do not exist. Instead, when a double bond is formed, a carbonyl species (C=O) is produced ($\dot{R}$ <=> $\dot{R}'$ + Carbonyl) instead of alkenes ($\dot{R} \leftrightharpoons \dot{R}'$ + Alkene). In addition, the $HO_2$ elimination reaction $RO\dot{O}_2 \longrightarrow$alkene + $H\dot{O}_2$ and the reaction $\dot{Q}OOH \longrightarrow$alkene + $H\dot{O}_2$ which contribute to the formation of alkenes, at low temperatures in the mechanism for regular alkanes, does not appear in the oxidation processes for OMEs.

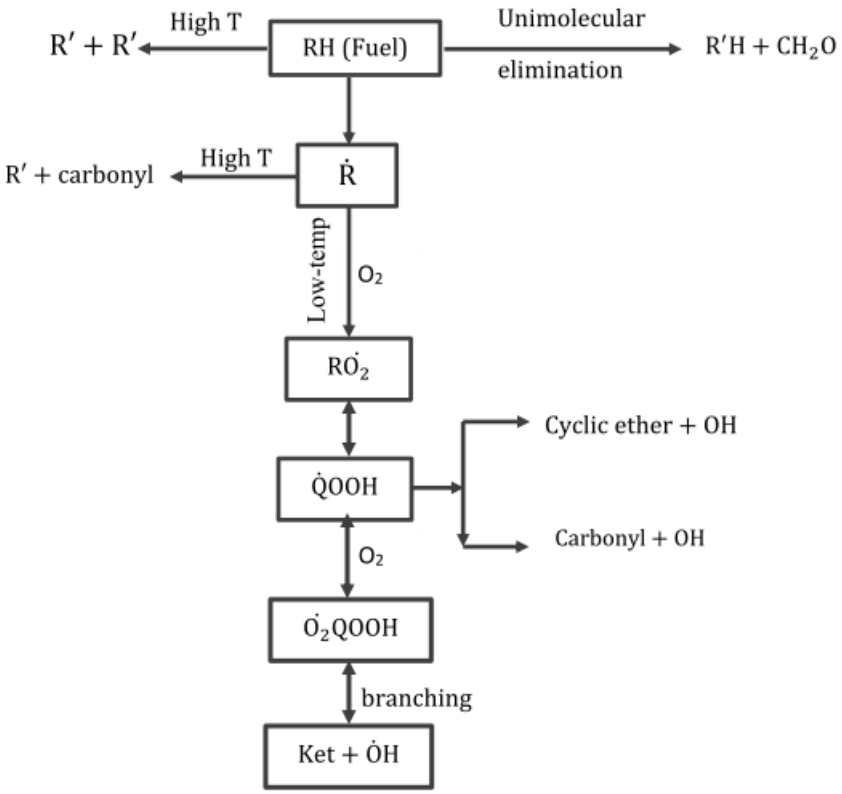


**Figure 3.8:** The primary reaction classes for OMEs [25, 31].

### 3.11.2 Reaction mechanisms for OMEs used in this work

The chemical-kinetic models adopted in this study for predicting the IDTs are summarized in Table 3.2.

- The DLR-Concise mechanism (313 species and 2148 reactions) by Kathrotia *et al.* [1] is a high to medium temperature semi-detailed reaction mechanism designed for surrogate modelling of a wide range of hydrocarbon fuels, *i.e.*, jet fuels, gasoline, and diesel. This model has been extended to include reactions of oxygenated species such as alcohols ($C_1$-$C_4$), oxymethylene ethers ($OME_n$, n = 0-5), and trimethyl orthoformate (*iso*-$OME_2$). The DLR-Concise model has been thoroughly validated for 70 pure hydrocarbon species against modeling with a wide range of experimental data from shock-tubes, laminar flames, jet-stirred reactors, and flow reactors. Due to its robustness, the DLR mechanism has been used in this work for modelling all neat and multi component fuels studied in this work, see Table 3.2.

**Table 3.2:** Summary of chemical kinetic models used in this work.

| Models | Species | Reactions | Fuel applied | Ref. |
|---|---|---|---|---|
| DLR-Concise | 313 | 2148 | DME, $OME_1$, $OME_2$, $OME_4$, *iso*-$OME_2$, PRF90, $OME_1$ / PRF90 blend, $OME_2$ / PRF90 blend, and *iso*-$OME_2$ / PRF90 blends | [1] |
| Cai *et al.* | 325 | 1639 | DME, $OME_1$, $OME_2$, $OME_4$ | [7] |
| Niu *et al.* | 101 | 429 | $OME_2$ and $OME_4$ | [8] |
| Aramco v3.0 | 581 | 3037 | DME | [132] |
| Polimi v1412 | 320 | 12381 | DME | [133] |
| Hu *et al.* | 662 | 3121 | $OME_1$ | [65] |
| Mehl *et al.* | 317 | 2634 | PRF90 | [134] |
| Cheng *et al.* | 1959 | 10386 | PRF90 | [79] |

- The Cai *et al.* [7] model is a low-to-high temperature oxidation mechanism (325 species and 1639 reactions) for $OME_{2-4}$. The widely validated $C_0$–$C_4$ base mechanism proposed by Blanquart *et al.* [135] was adopted. The reaction classes used for $OME_1$, $OME_3$ and $OME_4$ were similar to those applied Jacobs *et al.* [66] for $OME_1$ based on reaction for normal and 2-methyl alkanes as proposed by Sarathy *et al.* [131]. The mechanism is validated and optimized using ignition delay time data collected in a shock tube at pressures between 10 and 20 bar, temperatures between 600 and 1150 K, and equivalency ratios of 0.5, 1.0, and 2.0.

In this work, the mechanism is used for modelling IDTs of $OME_1$, $OME_2$ and $OME_4$. Based on this model, Niu *et al.* [8] developed a reduced mechanism for $OME_{1-6}$ consisting 101 species and 429 reactions. This model has been adopted in this work for $OME_2$ and $OME_4$.

- IDTs of dimethyl ether are additionally compared to predictions with the ARAMCO v3.0 mechanism (581 species, 3037 reactions) [132] and Polimi v1412 model [133]. The Aramco 3.0 mechanism has been developed to characterize the combustion of a wide range $C_1$–$C_4$ hydrocarbon species such as ethane, ethylene, acetylene, allene, propyne, propene, *n*-butane, *iso*-butane, *iso*-butene, 1-butene and 2-butene, and oxygenated species including formaldehyde, acetaldehyde, methanol, ethanol, and dimethyl ether. This mechanism has been validated against a large array of experimental measurements including data from shock tubes, rapid compression machines, flames, jet-stirred, and plug-flow reactors. The Polimi v1412 mechanism (317 species 12353 reactions) on the other hand, is a high and low temperature kinetic mechanism for primary reference fuels, alcohols (ethanol, propanol and butanol isomers), and ethers such as dimethyl ether, methyl- and ethyl-tertiary butyl ethers, and amongst others.

- IDTs of $OME_1$ are further compared to predictions using the model of Hu *et al.* [65] consisting of 662 species and 3121 reactions. The mechanism was developed for modelling IDTs of $OME_1$ / *n*-heptane blends. The mechanism was built by appending the sub-mechanism of $OME_1$ from Curran *et al.* [136] and the *n*-heptane model from the Lawrence Livermore National Laboratory (LLNL) [134] to the Aramco V1.3 [137] base model. The mechanism was validated with shock tube ignition delay times data for $OME_1$, $OME_1$ / *n*-heptane blends, and *n*-heptane obtained over a wide range of conditions; see section 2.7.

- For PRF90 mixture (gasoline surrogate), the measured data are further compared to the detailed gasoline surrogate model from Lawrence Livermore National Laboratory (LLNL) by Mehl *et al.* [134]. This low-to-high temperature model encompasses reactions for *n*-heptane, *iso*-octane, toluene, and $C_5$-$C_6$ olefins. It is widely validated using experimental data from shock tubes, stirred reactors, and rapid compression machines. In addition, the measured data for PRF90 is compared with predictions using the seven-component (*n*-butane, *n*-heptane, 2-methyl butane, 2-methyl hexane, *iso*-octane, 1-hexene, cyclopentane, toluene, and 1,2,4-trimethylbenzene) gasoline surrogate model from LLNL Laboratory by Cheng *et al.* [79].

### 3.11.3 Chemiluminescence mechanism

In the experimental investigations, IDTs were derived from the chemiluminescence of the electronically excited CH* radicals at both the radial (side-on) and axial (head-on) positions. In addition, the OH* was monitored at the side-on location. Ignition delay times were defined from the time of occurrence of the maximum of the excited CH* species. To be able to compare the experimental data with model predictions, the same criterion was adopted in calculations using the detailed models. The reaction models must therefore be able to describe the chemiluminescence of CH* and OH*. Kathrotia *et al.* [104] created a model describing the mechanisms leading to the chemiluminescence of OH* and CH* which is adopted in many reaction mechanisms; see Appendix C. In the present work, the models of Cai *et al.* [7], Hu *et al.* [65], LLNL mechanisms by Mehl *et al.* [134] and Cheng *et al.* [79], and Polimi V1412 [133] were all expanded with this chemiluminescence model [104] consisting of 15 species and 28 reactions (see Appendix C) as proposed by Kathrotia *et al.* [104] in order to use the same approach for determining ignition delay times.

### 3.11.4 Ignition delay times calculations

The measured IDTs are compared to the results of numerical predictions based on several reactions mechanisms, see Table 3.2. In this work, all ignition delay times are calculated based on the 0-dimensional homogeneous reactor model as implemented within the Chemkin II Package [138]. The initial composition of the mixture (see Table 3.1) and the initial temperature and pressure behind the reflected shock wave were specified as input parameters for the calculations. The peak of CH* emission was chosen as indicator of ignition, see section 3.9.2. In addition, a normalized experimentally derived pressure profile $p(t > 0) \,/\, p(t/s = 0)$ is provided to account for the facility-dependent rise in pressure and thus also in temperature due to gas dynamics, as explained before.

### 3.11.5 Sensitivity analysis

Sensitivity analysis calculations were performed with respect to the rate coefficient of each individual reaction to determine the important reactions driving ignition of oxymethylene ethers. The normalized sensitivity coefficient ($S_i$) with respect to the rate of each reaction is defined as,

$$S_i = \left( \frac{k_i^{\text{ref}}}{\tau_{\text{ign}}^{\text{ref}}} \right) * \left[ \frac{d\tau_{\text{ign}}}{dk_i} \right] \tag{3.6}$$

where the superscript 'ref' refers to the unperturbed system, $k_i$ is the rate co-coefficient of the $i^{th}$ reaction and $\tau_{\text{ign}}$ is the ignition delay time defined from the maximum of the CH* radical concentration. The reference system is computed using the unperturbed set of $k_i$ for all reactions.

When the rate of each reaction is multiplied by a perturbation factor, a new result for ignition delay time is obtained and compared to the value obtained for the unperturbed system. When using this approach, reactions with a negative sensitivity coefficient $S_i$ have a positive effect on the overall reactivity of the system, *i.e.*, shortens IDTs, and vice versa. The sensitivity analyses calculations were carried out using the Chemkin II package [138] with DLR extensions.

# 4 Results and Discussions

## 4.1 Introduction

In this chapter, first the results of the measured ignition delay times (IDTs) of 5 mixtures of the neat oxygenated fuels considered — dimethyl ether ($OME_0$), oxymethylene ethers-1, 2, and 4 ($OME_1$, $OME_2$, and $OME_4$), and *iso*-$OME_2$, with synthetic air as an oxidizer, will be presented and discussed. Then, the results of the measured ignition delay times for the specific gasoline surrogate called primary reference fuel 90 (PRF 90) consisting of 90% *iso*-octane and 10% *n*-heptane as well as three blends with three specific oxygenated fuels will be presented and discussed. In detail, blends (by liq. vol.) of (i) 70% $OME_1$ + 30% PRF90 / synthetic air, (ii) 70% $OME_2$ + 30% PRF90 / synthetic air, and of (iii) 70% *iso*-$OME_2$ + 30% PRF90 / synthetic air. Ignition delay times (IDTs) of all of these mixtures were measured for a wide range of conditions: fuel-air ratio $\varphi = 1.0$, dilution level of 1:5 with $N_2$, $T = 900–2000$ K, and initial pressures of 1, 4, and 16 bar. All experimental ignition delay time values reported within this thesis were determined from the peak of $CH^*$ emission detected radially (side-on), except for very short ignition delay times, where the axial (head-on) emission has been taken into account; for details, see section 3.9.2.

In addition to the results of the experimental investigation presented in this chapter, comparisons to numerical predictions made using the in-house model DLR-Concise [1] and several public domain models (see Table 3.2) will be given. Also, the results obtained for sensitivity analyses and reaction pathway analyses carried out to identify the dominant chemistry predicted by the detailed models are presented.

The IDTs data obtained in this work are supplemented by corresponding data for laminar burning velocities (LBV) – being also a fundamental combusting property – of the fuels considered allowing for a comprehensive study of the oxidation chemistry of OMEs and blends of OMEs with a gasoline surrogate as well as of their potential to serve as a possible transportation fuel. Note that the LBV data have been measured by my colleague, Sandra Richter and were presented in our (joint) publications (see Appendix A). Therefore, here only the LBV data are presented; details on the experimental setup and methodology for LBVs are given in the publications and even more, in the PhD thesis of Sandra Richter [121].

## 4.2 Neat oxygenated fuels

In this sub-section, the experimental and modeling efforts on ignition delay times of dimethyl ether ($OME_0$), oxymethylene ethers-1, 2, and 4 ($OME_1$, $OME_2$, and $OME_4$), and *iso*-$OME_2$, all with synthetic air as oxidizer will be presented and discussed. All the measurements were carried out at similar conditions under a wide range of conditions: fuel-air ratio $\varphi = 1.0$, dilution level of 1:5 with $N_2$, $T = 900–2000$ K, and initial pressures of 1, 4, and 16 bar.

### 4.2.1 Dimethyl ether (DME)

#### 4.2.1.1 Ignition delay times – Experimental results

The ignition delay times ($\tau_{ign}$) for the DME / air (21% $O_2$ + 79% $N_2$) mixture measured at $\varphi = 1.0$, dilution of 1:5 with $N_2$, and for $p$ / bar = 1 (squares), 4 (circles), and 16 (stars) are presented in Fig. 4.1. The specific experimental data for DME including the pressure profiles are provided in Appendix E. The measurements were carried out at $T$ =1000–1700 K. Ignition delay times were measured up to about 10 ms, see the dashed line. All ignition delay times are decreasing with increasing pressure for all the temperatures at all pressures indicating an increased reactivity of the system. The measured data exhibit a linear relationship with temperature up to about 1300 K depending on pressure thus following an Arrhenius behavior. At temperatures below 1300 K, the IDTs deviate slightly from this linear behavior, particularly for elevated pressures of 4 and 16 bar; they are becoming shorter mainly due to larger reactivity induced by the post-shock compression effect as discussed earlier in section 3.9.4.

#### 4.2.1.2 Ignition delay times – Results by model predictions

In Fig. 4.2, the measured ignition delay times (symbols) are compared to the results of predictions (curves) using four different chemical kinetic models: the DLR-Concise model [1], the Cai *et al.* model [7], the Polimi v1412 model [133], and the Aramco v3.0 model [132]; for more details, see Table 3.2. Since within DME oxidation, species with three carbon atoms and above (*i.e.*, C ≥ 3) are very difficult and thus unlikely to be formed, at least in noticeable amounts, the chemistry of C ≥ 3 species was removed when using the Aramco v3.0 and the Polimi v1412 models. Note that for elevated initial pressures ($p$ = 4 and 16 bar), a normalized experimentally derived pressure profile $p(t)$ / $p(t/s = 0)$ has been applied in the calculations to take care of the facility-dependent rise in pressure and thus, in temperature, too. The experimentally determined pressure profiles are also provided in Appendix E. The error bars on the predicted ignition delay times depict the sensitivity of the DLR-Concise model [1] to the experimental uncertainty error in

temperature and pressure due to the error in incident shockwave; see section 3.10.2.

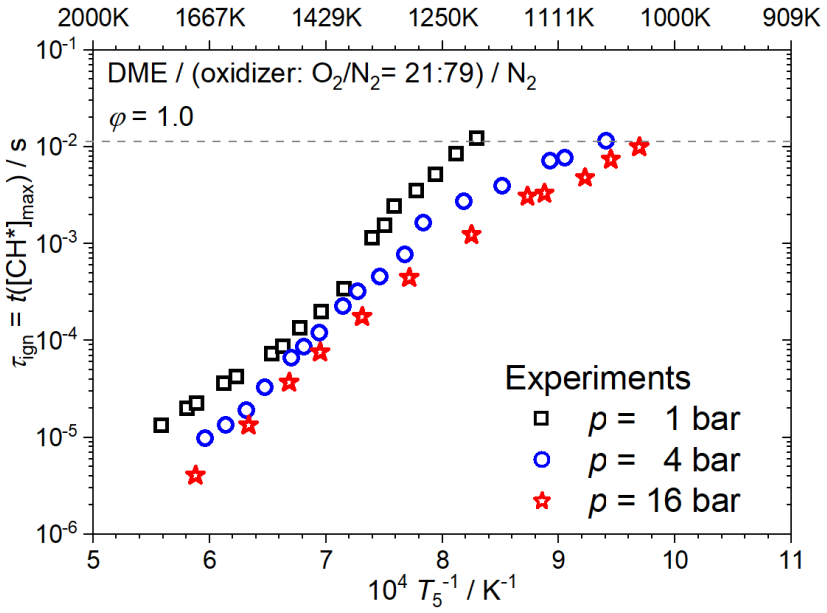


**Figure 4.1:** DME / air (21% $O_2$ + 79% $N_2$): Measured ignition delay time data for $\varphi = 1.0$, $p$ / bar = 1 (squares), 4 (circles), and 16 (stars), and dilution = 1:5 in $N_2$.

The results show that the Polimi v1412 model (black curve) matches the experimental data for most of the conditions. This model only underpredicts the measured data at $T \leq 1400$ K for 1 bar by about 50%. The models of DLR-Concise (red curve), Cai *et al.* (dashed green curve), and Aramco v3.0 (dotted blue curve), on the other hand, closely match the experimental data at $T \leq 1400$ K, at all pressures. However, at 4 and 16 bar, the DLR-Concise [1], Cai *et al.* [7], and Aramco v3.0 [132] models overpredict the measured data in the high-temperature regime – above 1400 K, with the DLR-Concise model being furthest away from the measurements at 4 and 16 bar. For example, at 4 bar, the DLR-Concise model [1] overpredicts the measured data by about 60% at 1600 K. The models of Cai *et al.* [7] and Aramco v3.0 [132] show predictions that are similar for all the temperature and pressure regimes covered. All reaction models using the pressure profile describe the non-linear dependence of the ignition delay time data with decreasing temperature and at elevated pressures.

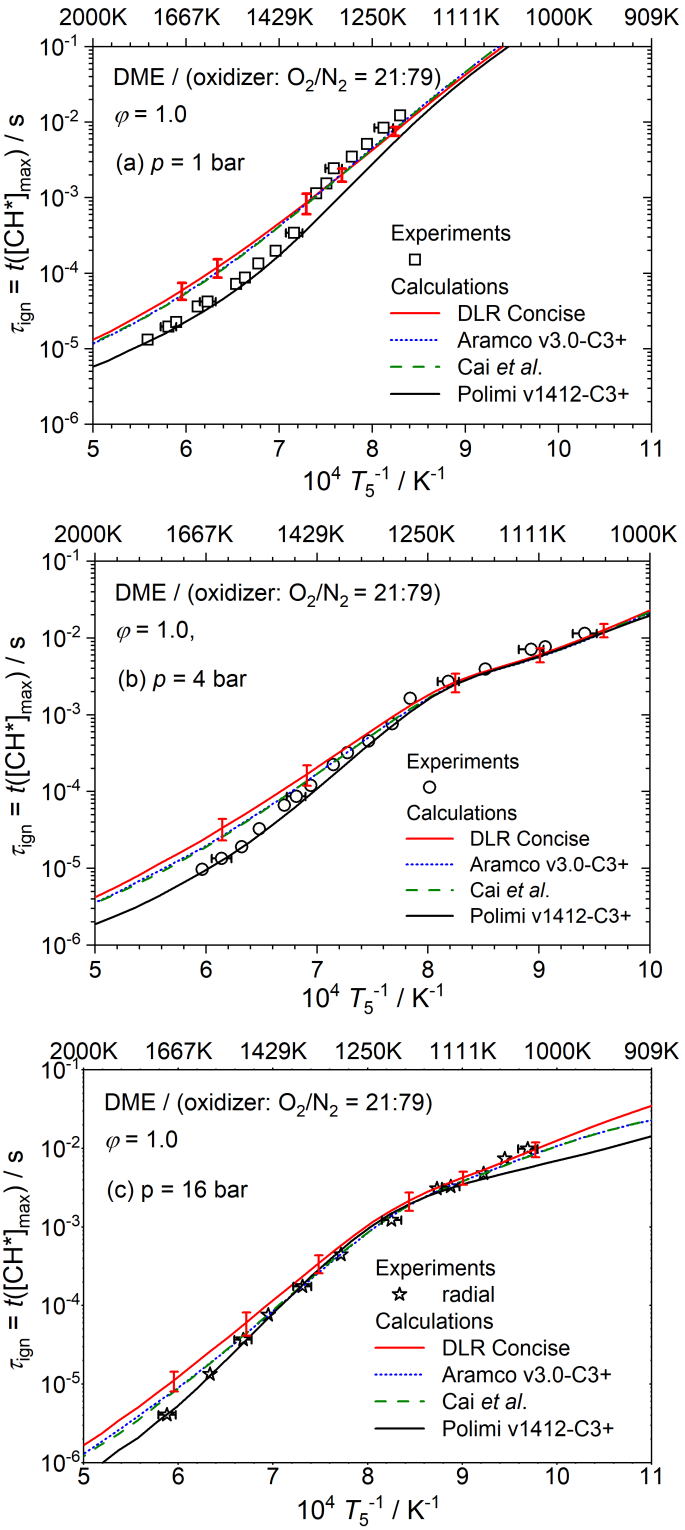


**Figure 4.2:** DME / air (21% $O_2$ + 79% $N_2$): Comparison of measured (symbols) and predicted (curves) ignition delay time data for $\varphi$ = 1.0, $p$ / bar = 1 (squares), 4 (circles), and 16 (stars), and dilution = 1:5 in $N_2$. Models used: (a) DLR-Concise (red curve) [1], (b) Aramco v3.0 (dotted blue curve) [132], (c) Cai *et al.* (dashed green curve) [7] and (d) Polimi v1412 ( black curve) [133].

#### 4.2.1.3 Sensitivity analysis and rate of production (ROP) analysis

Ignition delay time sensitivity calculations were performed for three temperatures, 1200 K, 1400 K, and 1600 K using the Polimi v1412 [133] and the DLR-Concise [1] models to determine the most important reactions driving the ignition of DME. The normalized sensitivity coefficient ($S_i$) with respect to the rate of each reaction is as defined in Eqn. 3.6. The Polimi v1412 model is chosen because it performed best with respect to the temperature and pressure dependencies. Thus, the results obtained are compared with those obtained using the in-house DLR-Concise model. The results of the sensitivity calculations are presented in Fig. 4.3(a) for the Polimi v1412 model and in Fig. 4.3(b) for the DLR-Concise model. For each model, the 15 most important reactions are displayed sorted according to $T = 1400$ K. Reactions with negative sensitivities are promoting reactions and vice versa.

Regardless of the specific model used: (i) The chain branching reaction $H + O_2 \rightleftharpoons O + OH$ is the most promoting reaction with a high negative sensitivity like it is typical for many hydrocarbon systems; and (ii) the decomposition reaction $DME\,(+M) \rightleftharpoons CH_3 + CH_3O\,(+M)$ due to the fission of the ether bond is the second most sensitive reaction promoting ignition of DME. This reaction produces the initial source of the radicals methyl ($CH_3$) and methoxy ($CH_3O$) with the latter easily reacting further to $CH_2O$ and H important for promoting further the ignition process. The reaction $CH_3 + HO_2 \rightleftharpoons CH_3O + OH$ is another important reaction that promotes ignition of DME. On the other hand, the reaction $CH_3 + HO_2 \rightleftharpoons CH_4 + O_2$ has the highest positive sensitivity coefficient in this system and therefore inhibits ignition of DME by producing stable species. In general, chain reactions involving OH, O, H, $CH_3$, and $HO_2$ are controlling the ignition process of DME. In addition, reactions involving formaldehyde $CH_2O$ are observed in the ignition regime. Formaldehyde is formed by H-abstraction from methoxy radical by H, O and $O_2$ radicals, and it is therefore an important species in oxidation of DME and ether-like fuels containing methoxy ends like OMEs. Sensitivity calculations of the DME ignition delay times were also done using DLR-Concise model for $T = 1200$ K at $p$ / bar = 1 (red), 4 green), and 16 (cyan). The results, which are reported in Fig. 4.4, show major similarities to those in Fig. 4.3(b): A comparison of the results shows that the temperature variation has a greater impact on reactions than the variation in pressure, *e.g.*, $CH_3 + HO_2 \rightleftharpoons CH_4 + O_2$ and $H + O_2 \rightleftharpoons O + OH$, except on those reactions involving collision partners, *e.g.*, $DME\,(+M) \rightleftharpoons CH_3 + CH_3O\,(+M)$ – these are more sensitive to pressure variation.

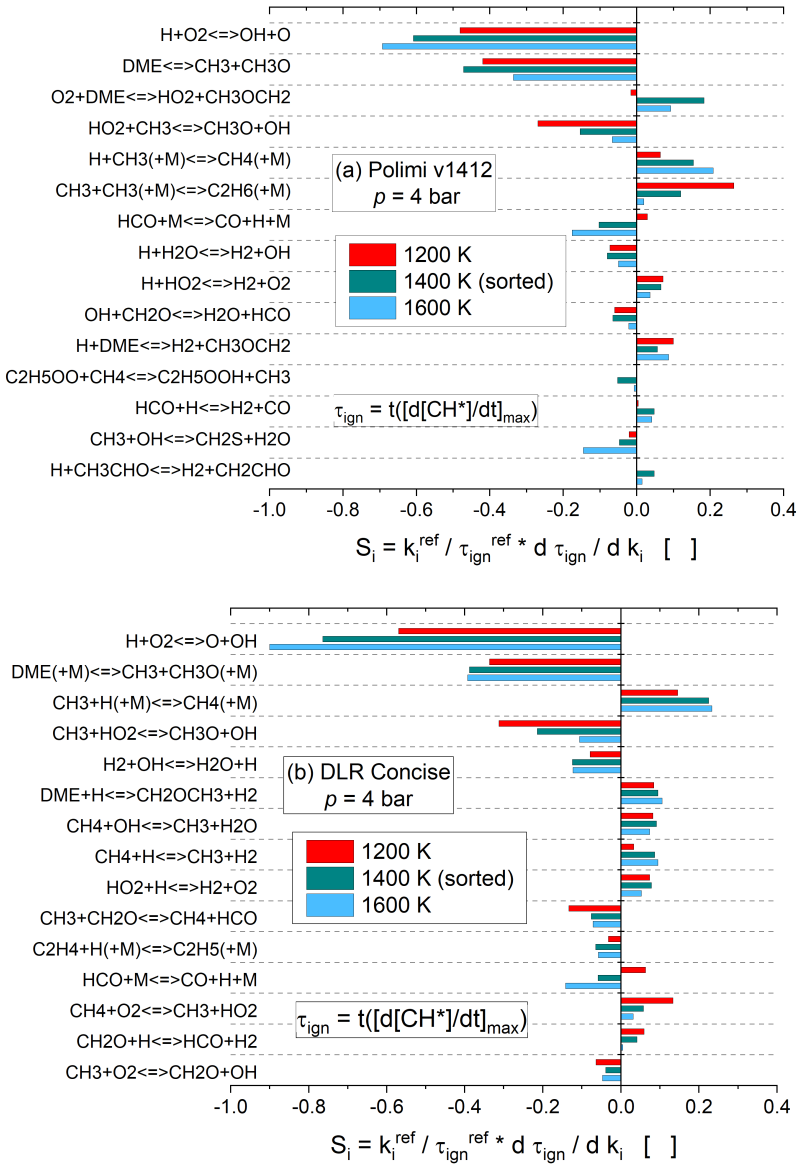


**Figure 4.3:** DME / air (21% $O_2$ + 79% $N_2$): IDT sensitivity coefficients calculated for three different temperatures at $\varphi = 1.0$, $p = 4$ bar, and dilution = 1:5 in $N_2$. Models used: (a) Polimi v1412 [133] and (b) DLR-Concise [1].

In summary, from sensitivity analysis, major similarities are observed between the two models with respect to specific reactions dominant in the ignition regime. However, as the DLR-Concise model [1] is overpredicting the measured data in the high temperature regime above 1400 K (see section 4.2.1.2), a normalized integral rate of production (ROP) analysis of the important radicals (O, H, OH, $CH_2O$, and $CH_3$) in the ignition regime was carried out at $p$ / bar = 4 and $T$ / K = 1600 K. The results obtained are compared to similar results obtained using the Polimi v1412 model [133] which was close to the measured IDT data for all $T > 1400$ K. The results obtained using the two models are presented in Fig. 4.5. It is observed that the calculation using the DLR-Concise model [1] shows

lower levels of most of these important species compared to the Polimi model. This finding could explain the longer ignition delay times predicted by the in-house model in the high temperatures regime.

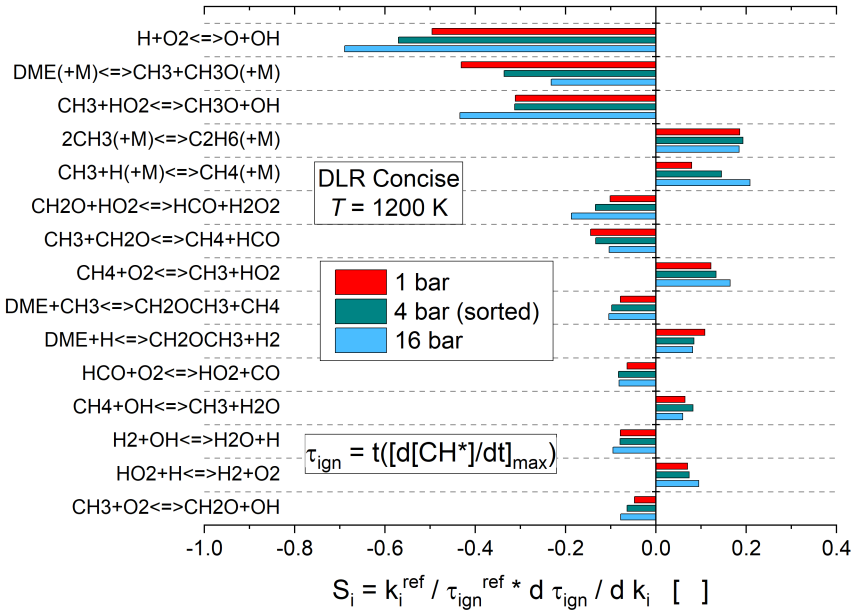


**Figure 4.4:** DME / air (21% $O_2$ + 79% $N_2$): IDT sensitivity coefficients calculated for three different pressures at $\varphi = 1.0$, $T = 1200$ K, and dilution = 1:5 in $N_2$. DLR-Concise model was used [1].

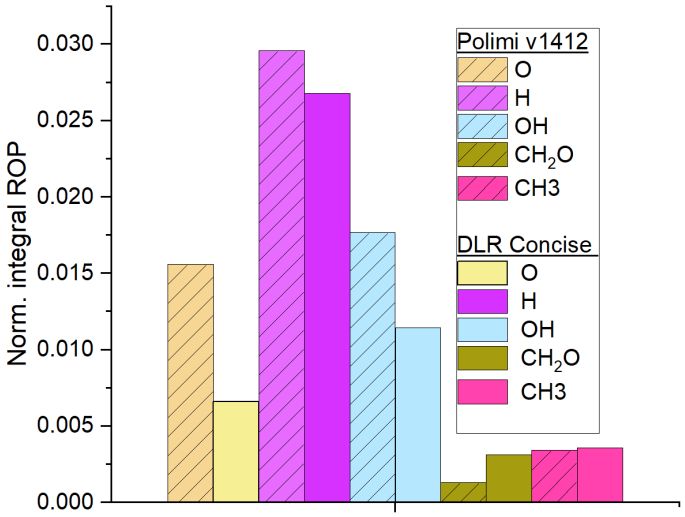


**Figure 4.5:** DME / air (21% $O_2$ + 79% $N_2$): Normalized integral rate of production of O, H, OH, $CH_2O$, and $CH_3$ radicals calculated at $p$ / bar = 4, $T$ / K = 1600, and dilution = 1:5 in $N_2$. Models used: Polimi v1412 [133] and DLR-Concise [1].

### 4.2.2 Oxymethylene ether-1 ($OME_1$: $CH_3OCH_2OCH_3$)

#### 4.2.2.1 Ignition delay times – Experimental results

Figure 4.6 shows the measured IDTs of stoichiometric $OME_1$ / synthetic air mixtures diluted 1:5 with $N_2$ for $p$ / bar = 1 (squares), 4 (circles), and 16 (stars). The experimental data including the experimentally derived pressure profiles are provided in Appendix F. Due to the high level of dilution applied (~95% with $N_2$), ignition delay times were measured up to 11 ms at 1 bar and 7 ms at 4 and 16 bar in the temperature $T$ = 1000-1800 K. For all pressures studied, the measured ignition delay times show a linear relationship with respect to the inverse temperature up to about 1300 K, *i.e.*, Arrhenius dependence. Below 1300 K, the experimentally obtained IDTs deviate from a linear behavior becoming shorter mainly due to viscous gas dynamics effects, see section 3.9.4.

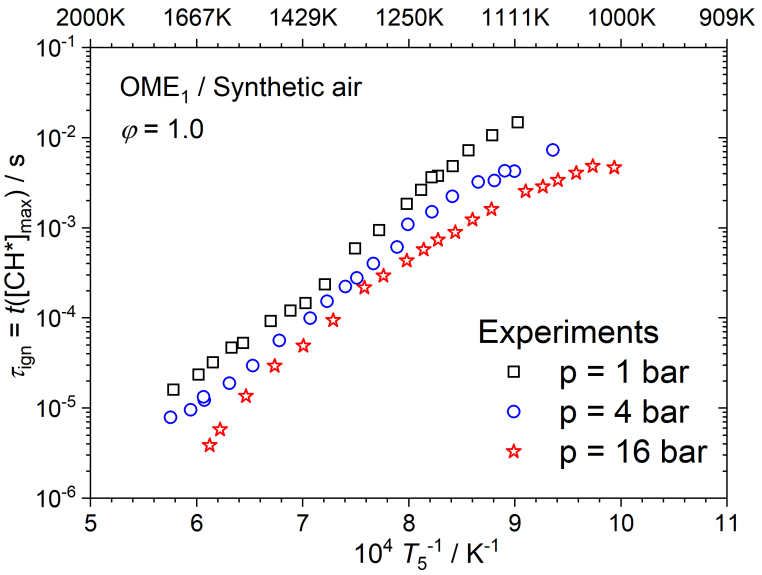


**Figure 4.6:** $OME_1$ / synthetic air (20% $O_2$ + 80% $N_2$): Measured ignition delay times for $\varphi$ = 1.0, $p$ / bar = 1 ( squares), 4 (circles), and 16 (stars), and dilution = 1:5 in $N_2$.

#### 4.2.2.2 Ignition delay times – Results by model predictions

In Fig. 4.7, the measured ignition delay time data of the studied $OME_1$ / synthetic air mixtures are compared to the results of predictions using three detailed chemical kinetic reaction models: DLR-Concise [1], Cai *et al.*[7], and Hu *et al.* [65]. The calculations at elevated pressures of 4 and 16 bar have been performed with the experimentally derived pressure profiles $p(t)$ / $p(t = 0)$ to account for pressure increases due to viscous gas dynamics and to disregard pressure increases due to heat release before ignition.

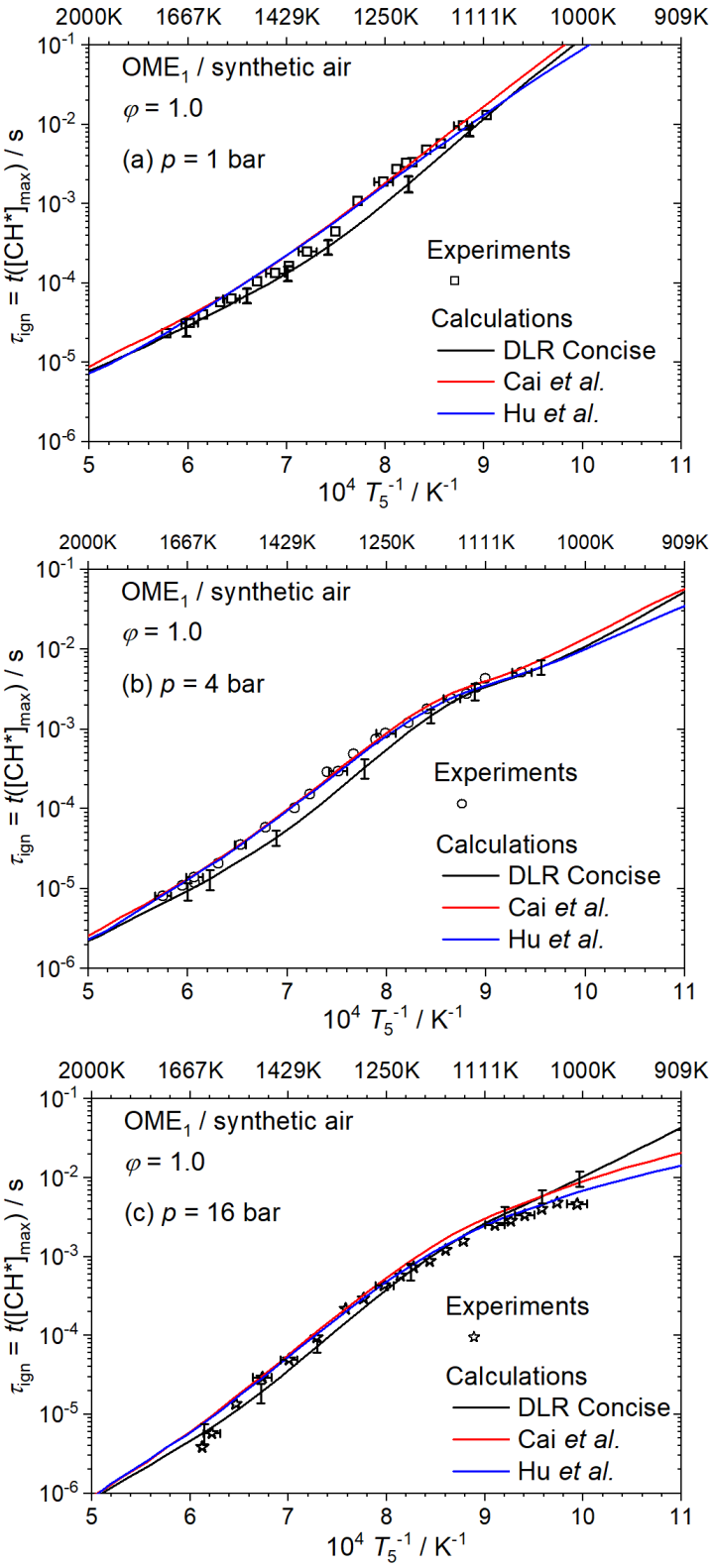


**Figure 4.7:** $OME_1$ / synthetic air (20% $O_2$ + 80% $N_2$): Comparison of measured data (symbols) and predicted (curves) ignition delay times for $\varphi = 1.0$, $p$ / bar = 1 (squares), 4 (circles), and 16 (stars), and dilution = 1:5 in $N_2$. Models used: (a) DLR-Concise (dark curve) [1], (b) Cai *et al.* (red curve) [7], and (c) Hu *et al.* (blue curve) [65].

The models of Cai *et al.* (red curves) [7] and Hu *et al.* (blue curves) [65] are closest to the experimental data at all the conditions investigated. These two models show very similar IDTs predictions in most conditions despite having a different $c_0$-$c_4$ base mechanism (see section 3.10). The DLR-Concise model [1], on the other hand, underpredicts the measured data, for 1 bar by about 50% for temperatures less than about 1350 K and by about 40% in the temperature range 1200 K and 1500 K for 4 bar. Under these conditions, it is seen that the predicted data is close to experimental values when the response of the DLR-Concise model [1] to the experimental error in $T_5$ and $P_5$ is considered; see error bars. The observed non-linear dependence of ignition delay time data with decreasing temperature, particularly notable at elevated pressures, is described well by all three reaction models using the experimental pressure profile.

#### 4.2.2.3 Ignition delay times – Sensitivity analysis

Sensitivity analysis of ignition delay times for $OME_1$ / synthetic air mixtures was done at $\varphi = 1.0$, $p = 4$ bar, and a dilution level of 1:5 with $N_2$. To account for model-specific differences, two different reaction models were used: the Cai *et al.* [7] and the DLR-Concise model [1]. The results obtained are shown in Fig. 4.8a for the Cai *et al.* model [7] and in Fig. 4.8b for the DLR-Concise model [1], respectively. Regardless of the model, ignition is promoted by chain branching reactions: $H + O_2 \rightleftharpoons O + OH$, $CH_3 + HO_2 \rightleftharpoons CH_3O + OH$, $HCO + M \rightleftharpoons CO + H + M$, and $H_2 + OH \rightleftharpoons H_2O + H$. According to the model of Cai *et al.* [7], the $OME_1$ system is promoted by two fuel pyrolysis reactions due to the fission of the ether bond: (i) $OME_1\,(+M) \rightleftharpoons CH_3OH + CH_3 + HCO\,(+M)$ and (ii) $OME_1\,(+M) \rightleftharpoons CH_3O + CH_3OCH_2\,(+M)$ and inhibited by the H-abstraction reaction $OME_1 + H \rightleftharpoons CH_3OCHOCH_3 + H_2$. On the other hand, when using the DLR-Concise model [1], the system is promoted by the pyrolysis reaction $OME_1 \rightleftharpoons CH_2OCH_3 + CH_3O$ and inhibited by the H-abstraction reaction $OME_1 + OH \rightleftharpoons$ OME1*-1 $+ H_2O$, where OME1*-1 represents the primary fuel radical $CH_3OCH_2OCH_2$ with a radical site at the terminal carbon atom.

In Fig. 4.9, the results of the sensitivity calculations showing the effect of pressure variation when using the (a) Cai *et al.* [7] and (b) Hu *et al.* [65] models are shown. It is seen that the pyrolysis reaction $OME_1\,(+M) \rightleftharpoons CH_3OH + CH_3 + HCO\,(+M)$ is important according to both models. This reaction is not included in the DLR-Concise model, and thus, does not appear in Fig. 4.8b. Interestingly, Figures 4.8 and 4.9 demonstrate significant similarities across the three models, with several identical reactions exhibiting almost identical behavior. The sensitivity analyses further reveal the importance of the various reactions varies with temperature. For example, by considering Figs. 4.8a and 4.8b, the temperature is shown to have a greater impact on the

individual reactions than the variation in pressure; for example, see reactions $H + O_2 \rightleftharpoons O + OH$ and $CH_3 + HO_2 \rightleftharpoons CH_3O + OH$. In general, it is shown that regardless of the reaction model used, the reactions involving small radicals, *e.g.*, H, O, OH, $HO_2$, and $CH_3$, dominate the ignition regime.

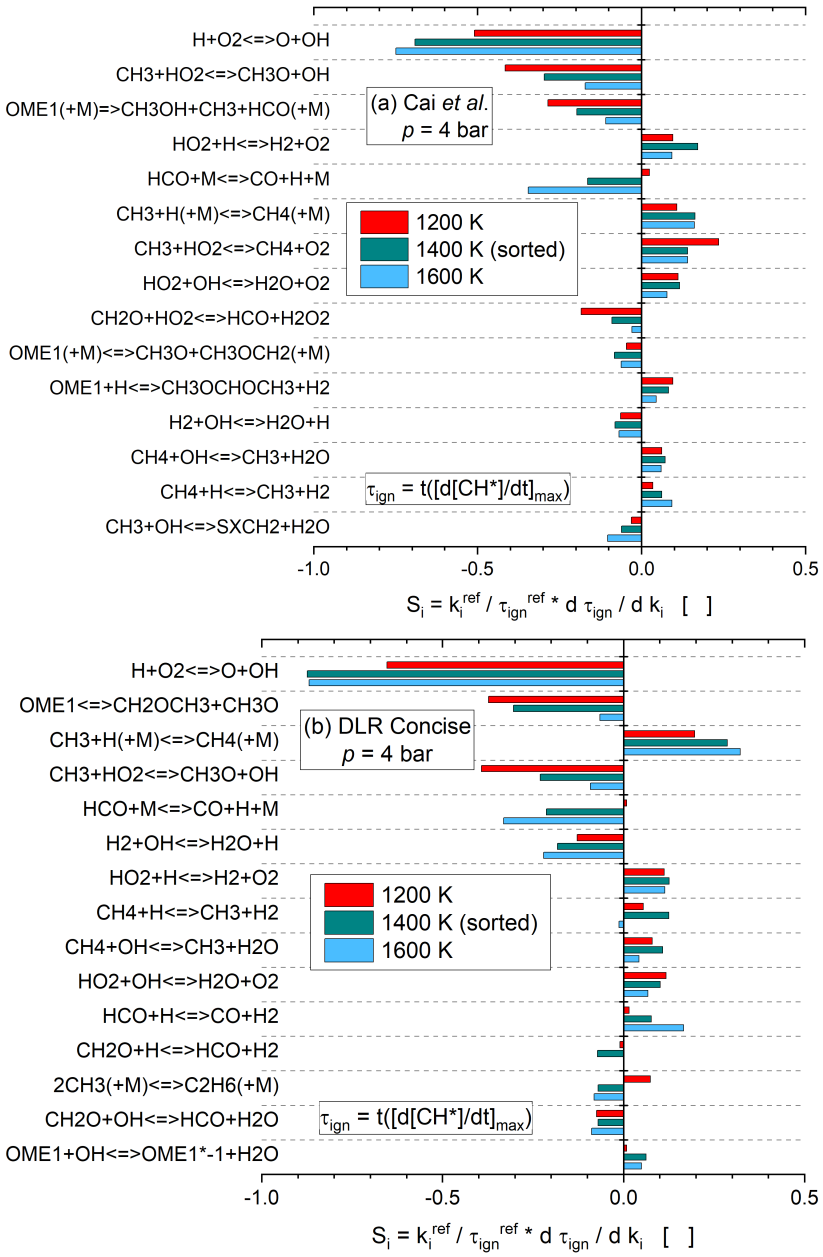


**Figure 4.8:** $OME_1$ / synthetic air (20% $O_2$ + 80% $N_2$): IDT sensitivity coefficients for three different temperatures at $\varphi = 1.0$, $p = 4$ bar, and dilution = 1:5 in $N_2$ at 4 bar. Models used: (a) Cai *et al.* [7] and (b) DLR-Concise [1].

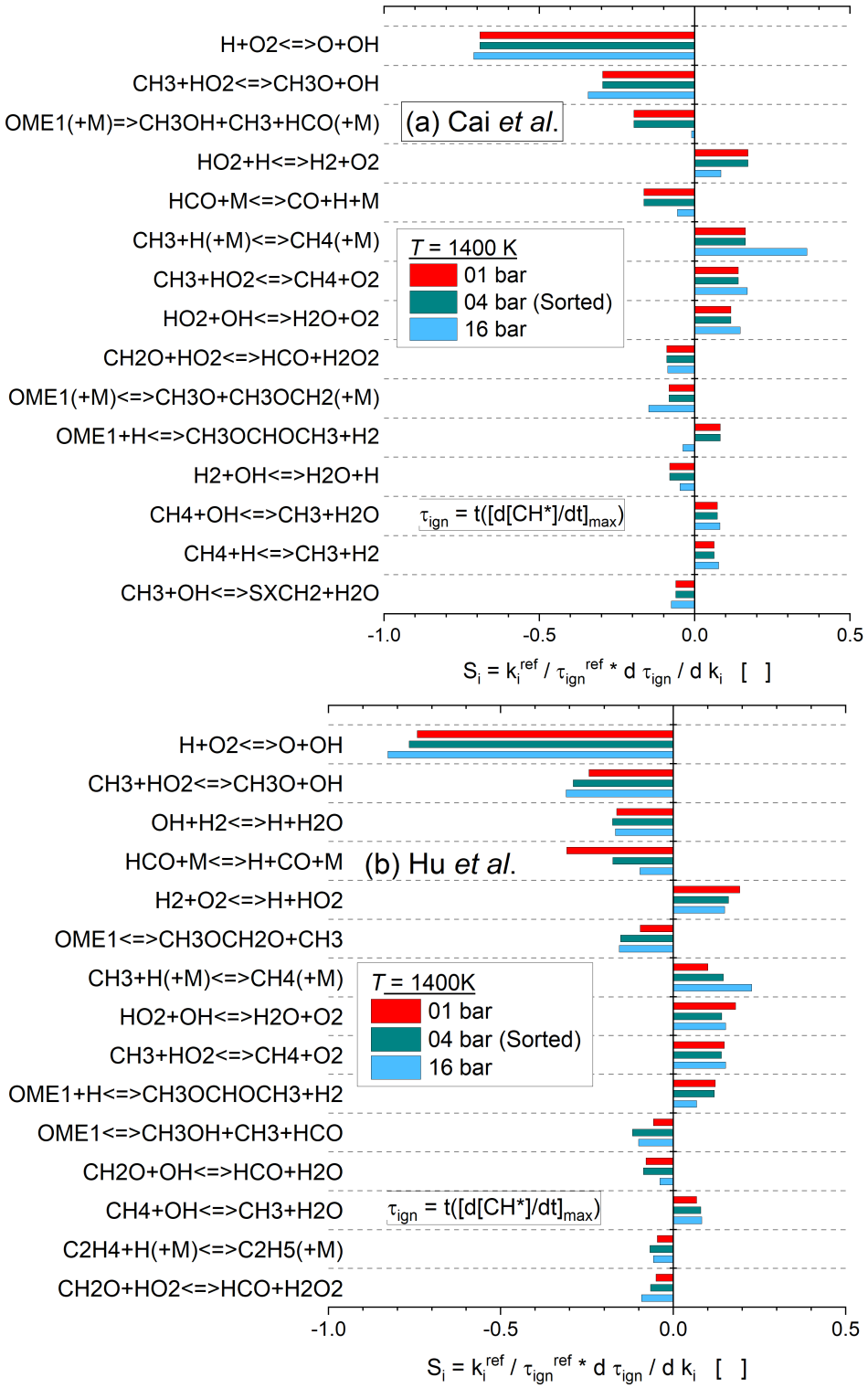


**Figure 4.9:** $OME_1$ / synthetic air (20% $O_2$ + 80% $N_2$): IDT sensitivity coefficients for three different pressures at $\varphi = 1.0$, $T$ / K = 1400 K, and dilution = 1:5 in $N_2$. Models used: (a) Cai *et al.* [7] and (b) Hu *et al.*[65].

#### 4.2.2.4 Reaction pathway analysis – $OME_1$

To get further insight into the decomposition pathways of $OME_1$, a reaction pathway analysis was performed for the Cai *et al.* [7] model using the software package Chemical Workbench [139]. The model is selected because it gives the best temperature and pressure dependencies of the measured ignition delay time data. Figure 4.10 represents the reaction pathway diagram at 20% fuel decomposition (stoichiometric $OME_1$ / synthetic air mixture diluted 1:5 with $N_2$) at $p = 16$ bar and for two temperatures (1200 K – blue and 1400 K – red). In Fig. 4.10, "+M" denotes a third body molecule and "+R" denotes the type of the H-atom abstracting radicals (H, $CH_3$, O, OH, and $HO_2$, etc).

The results show that the major $OME_1$ decomposition channels are the H-abstraction channels from the central and primary carbon atom leading to the formation of $CH_3OCHOCH_3$ and $CH_3OCH_2OCH_2$ which respectively account for 36% and 37% of $OME_1$. The radical $CH_3OCHOCH_3$ decomposes further into methyl formate ($CH_3OCHO$) and methyl radicals, while $CH_3OCH_2OCH_2$ decomposes further through the elimination of formaldehyde to yield methoxy methyl radicals, $CH_3OCH_2$. $OME_1$ is also decomposing via elimination of formaldehyde to yield dimethyl ether ($CH_3OCH_3$). Through H abstraction, dimethyl ether decomposes first into $CH_3OCH_2$ which subsequently decomposes to form methyl ($CH_3$) and formaldehyde ($CH_2O$) radicals. In addition, $OME_1$ is also reacting via the cleavage of the C-O bond forming methoxy methyl ($CH_3OCH_2$) and methoxy ($CH_3O$) radicals accounting for 4% of $OME_1$ at 1400 K. About 6% of $OME_1$ at 1400 K decomposes via the C-O bond breaking into $CH_3OCH_2O$ and $CH_3$, followed by subsequent dehydrogenation of $CH_3OCH_2O$ to yield methyl formate. In addition, about 5% (at 1400 K) of $OME_1$ decomposes via the reaction $CH_3OCHOCH_3 \rightleftharpoons CH_3OH + HCO + CH_3$ . This reaction, despite accounting for only 5% of $OME_1$, is shown by sensitivity analysis to be dominant reaction with respect to ignition delay time, see Figs. 4.9(a) and 4.9. The reason for this is that subsequent reactions involving $CH_3OH$, HCO, and $CH_3$ lead to further branching and thus more free radicals. Regarding the influence of temperature on reaction channels for $OME_1$, it is seen that an increase in temperature from 1200 K to 1400 K, increases the importance of all the pyrolysis reactions and decreases the importance of H-abstraction reactions, as expected.

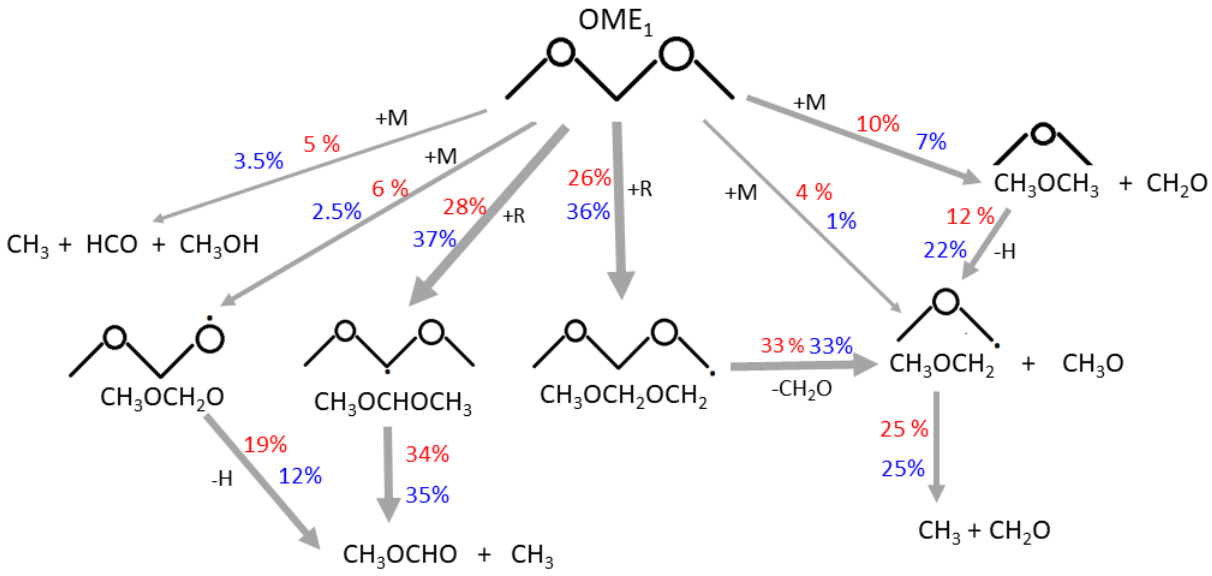


**Figure 4.10:** Reaction pathway diagram during $OME_1$ / synthetic air mixture at $\varphi = 1.0$, $p = 16$ bar, dilution = 1:5 in $N_2$, and 20% fuel consumption for temperatures of $T = 1200$ K (blue) and $T = 1500$ K (red) using the model of Cai *et al.* [7].

### 4.2.3 Laminar burning velocities - $OME_1$

One goal within the present work is to allow a profound estimation of the performance of chemical reaction models toward a detailed understanding of the fundamental combustion properties of the envisaged fuels which is essential for their safe and efficient utilization, neat or in blends. Thus, by broadening the data sets, the predictability of DLR-Concise [1] and Cai *et al.* [7] models is further tested against laminar burning velocities (LBV) of $OME_1$ obtained at an initial temperature of 473, pressures of $p$ / bar = 1, 3, and 6 bar, and for equivalence ratios ($\varphi$) ranging from 0.6-1.8 [2, 4].
The results of the measured LBVs and laminar flame speeds predicted using the DLR-Concise [1] and the Cai *et al.* model [7] are presented in Fig. 4.11. Maximum values of 103.1 cm/s at 1 bar, 80.3 cm/s at 3 bar, and 64.8 cm/s at 6 bar are observed at a $\varphi$-value of 1.2 at each pressure. When compared to the measured data, the DLR-Concise model (solid curves) underpredicts the peak LBV by up to 5% at 1 bar. However, it overpredicts all measured values for $\varphi \leq 1.0$ with up to 25% at $\varphi \leq 0.8$ for 1 bar and underpredicts measured data for $1.0 \leq \varphi \leq 1.8$ (fuel-rich) with up to 30% at $\varphi = 1.8$ for 1 bar. When using the Cai *et al.* model [7] (dashed curves), the maximum of flame speed is shifted to 1.1 by $\Delta\varphi = -0.1$. Also, Cai *et al.* model underpredicts measured values under stoichiometric and fuel-rich conditions by up to 20%, while overestimating them under fuel-lean conditions by about 25% at $\varphi \leq 0.8$. At the fuel-rich regime, the deviation between measured and calculated values is larger for the Cai *et al.* model compared to the DLR-Concise model. By

considering fuel / air mixtures at $\varphi = 1.2$, the measured and calculated data with both models confirm that, with increasing pressure, the differences between the absolute values for the flame speeds are reduced. At higher $\varphi$-values, the models underpredict the measured values, by up to 20 cm/s. Larger deviations between measurements and predictions at $\varphi > 1.1$ are attributed to the mechanism itself and the difficult flame stabilization process at higher fuel-air ratios. A considerable deviation observed between measured LBVs and calculated LFS values using both models is attributed to the fact that the current OMEs models have been based on limited validation data, particularly for laminar burning velocities. For instance, the model of Cai *et al.* [7] was validated against ignition delay time data only, see chapter 2. This fact is considered an argument for the enlargement of the experimental database by including laminar burning velocities when discussing the performance of chemical reaction models.

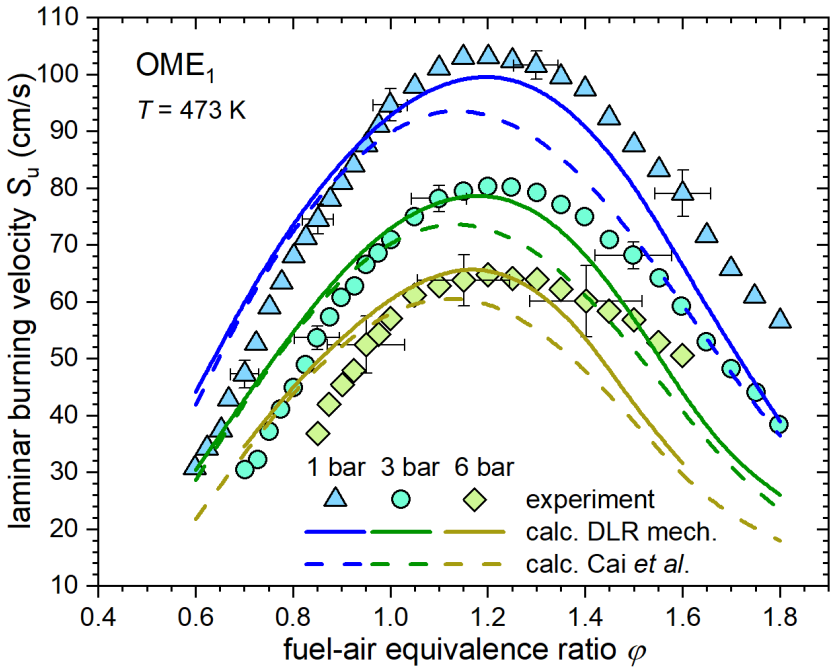


**Figure 4.11:** $OME_1$ / air mixture: Measured laminar burning velocities (symbols) and calculated laminar flame speeds (curves), $T = 473$ K, $p$ / bar = 1 (triangles), 3 (circles), and 6 (diamond). Models used: DLR-Concise (solid curves) [1] and Cai *et al.* (dashed curves) [7].

### 4.2.4 Oxymethylene ether 2 and 4 ($OME_2$ and $OME_4$)

#### 4.2.4.1 Ignition delay times – Experimental data

Ignition delay times ($\tau_{ign}$) of stoichiometric mixtures of $OME_2$ / synthetic air and $OME_4$ / synthetic air have been experimentally determined for similar conditions used for DME ($OME_0$) and $OME_1$; *i.e.*, at a dilution level of 1:5 with nitrogen and initial pressures of 1, 4, and 16 bar. These data are plotted against the inverse temperature in Fig. 4.12(a) for $OME_2$ and Fig. 4.12(b) for $OME_4$. The measurements were taken at $T$ = 850-1700 K for $OME_2$ and $T$ = 850-2000 K for $OME_4$. In the high-temperature regime, the IDT data are indicating an Arrhenius behavior for temperatures up to about 1100 K (quasi-linear trend). Below 1100 K, ignition delay times are not showing a linear dependency from temperature any longer, with the deviation resulting in some shorter ignition delay times, particularly for elevated pressures of 4 and 16 bar; again, mainly due to post-shock pressure increase. Therefore, the experimental data including the experimentally derived pressure profiles for $OME_2$ and $OME_4$, respectively are available in Appendix G and H.

The results obtained for $OME_2$ and $OME_4$ revealed a pre-ignition phenomenon at temperatures lower than about 1100 K for elevated pressures, at 4 and 16 bar. This is illustrated by an earlier increase in $CH^*$ and $OH^*$ emissions before the main ignition: Figure 4.13 shows representative emission and pressure signals from a single experiment ($OME_4$ / synthetic air mixture) at initial pressures of 15 bar and temperature of 900 K, clearly exhibiting the pre-ignition phenomena. The pre-ignition behavior (first peak on blue and magenta curves), imposes a strong effect of (pre-ignition) heat release on the reactive pressure profile (black curve). Note that the gradual increase in pressure behind the reflected shock wave that ends at around 4000 $\mu$s (see black curve) is caused by viscous gas dynamics (see solid red curve), not by pre-ignition: The second pressure increase (solid black curve), starting at around 4000 $\mu$s, is attributed to the combined effect of gas dynamics and heat release. Nevertheless, pressure relaxation towards the "open end", *i.e.*, the contact surface, is limiting the pressure increase as long as the heat release rate is comparable to the pressure relaxation, and the blast wave has not been established yet. To be able to account only for pressure increases due to viscous gas dynamics when calculating ignition delay times, normalized non-reactive pressure profiles (red curve) obtained from a non-ignitable and therefore, a non-reactive mixture of 20% synthetic air + 80% $N_2$ with an almost similar acoustic impedance to the combustible mixtures are applied when deriving the pressure profiles, as described in section 3.9.4.

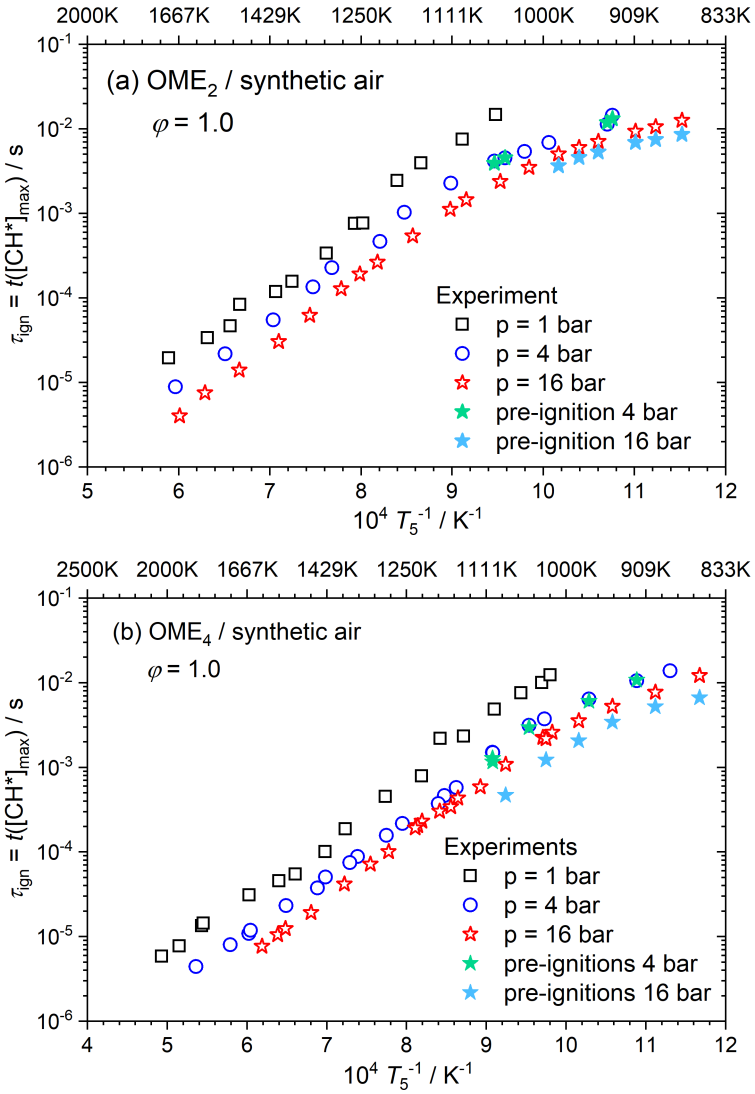


**Figure 4.12:** Measured ignition delay times of (a) $OME_2$ / synthetic air and (b) $OME_4$ / synthetic air mixtures for $\varphi = 1.0$, $p$ / bar = 1, 4, and 16; dilution = 1:5 in $N_2$.

The $CH^*$ (axial and radial) and $OH^*$ (radial) emission signals demonstrate a two-step ignition process, with the pre-ignition occurring at around 5200 $\mu$s and the primary ignition at about 7700 $\mu$s. The pre-ignition peak is very distinguishable from the radial (side-on) pressure trace than from the end wall signal. The reason for this is that the detector in the axial (head-on) position monitors a wide volume and produces an integrated signal of light arriving from all locations in the tube since it is directly looking into the tube and thus, monitors a wider volume. On the other hand, the side wall emission is highly resolved due to the 1 mm slit in front of the detector and thus only monitors a slice of the gas directly behind the reflected shock wave. For this reason, pre-ignition peaks were defined as those derived from the radial location of the emission. Nevertheless, the location of pre-ignition peaks from radial and axial directions coincide. For $OH^*$ and $CH^*$ signals, the times

for the pre-ignition peak and main ignition coincide, as expected. In Fig. 4.12, a comparison of pre-ignition data (full green stars – 4 bar and full cyan stars – 16 bar) and main ignition data (blue circles – 4 bar and red stars – 16 bar) is also given; for $OME_2$, see Fig. 4.12(a) and for $OME_4$, see Fig. 4.12(b). The results obtained show that at 4 bar, pre-ignition peaks are very close to main ignition peaks, but not at 16 bar.

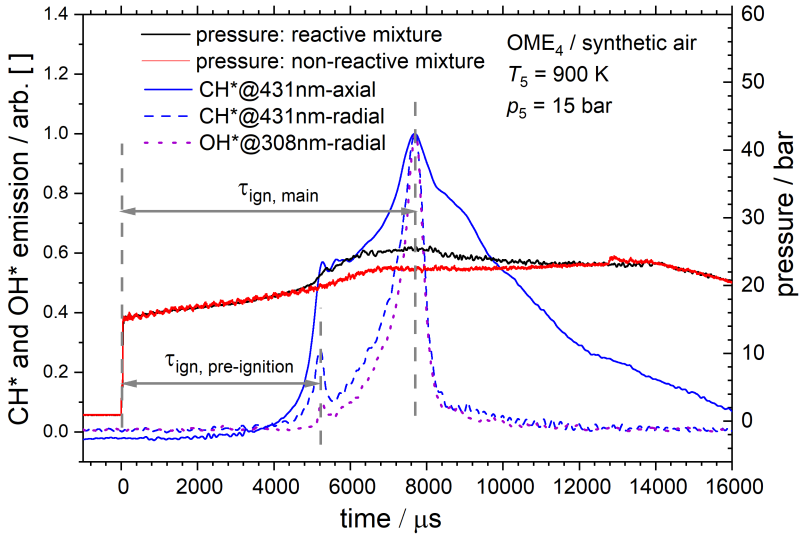


**Figure 4.13:** Pressure and emission signals of a stoichiometric $OME_4$ / synthetic air mixture diluted 1:5 with $N_2$ at initial $T(t = 0) = 900$ K and $p(t = 0) = 15$ bar. The pressure signal of a non-reactive mixture (red – curve) is also shown.

#### 4.2.4.2 Ignition delay times – Results by model predictions

The comparison of the measured (symbols) and predicted (curves) ignition delay times using DLR-Concise [1], Cai *et al.* [7], and Niu *et al.* [8] models are presented in Fig. 4.14 for $OME_2$ and in Fig. 4.15 for $OME_4$. The predictions by the three models match satisfactorily the measured data for the main ignition of $OME_2$ and $OME_4$. All the models reproduce the non-linear dependency of ignition delay time data becoming shorter with decreasing temperature, as discussed earlier for DME and $OME_1$. Note that to address appropriately the effect of pre-ignition heat release on the perturbation of the pressure profile (see Fig. 4.13), the numerical calculations need to be and are performed with the normalized profile $p(t) / p(t = 0)$ derived from pressure profiles of non-reactive mixtures, as explained before, to account for pressure increases due to viscous gas dynamics resulting from exploiting the tailoring approach.

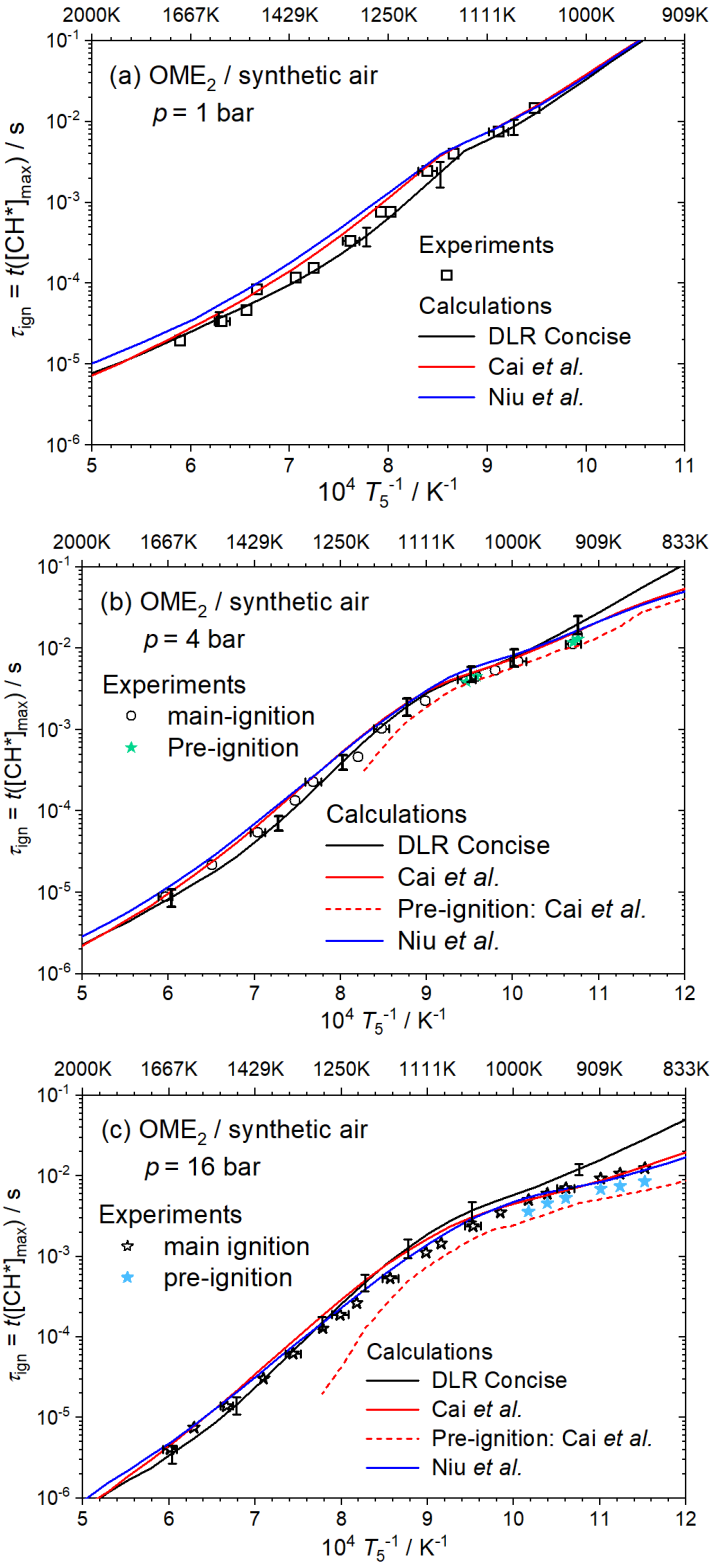


**Figure 4.14:** $OME_2$ / synthetic air (20% $O_2$ + 80% $N_2$): Comparison of measured (symbols) and predictions (curves) for $\varphi = 1.0$, $p$ / bar = 1 (squares), 4 (circles), and 1 (stars), and dilution = 1:5 in $N_2$. Models used: (a) DLR-Concise (solid black curve) [1], (b) Cai *et al.* (solid red curve) [7], and (c) Niu *et al.* (solid blue curve) [8].

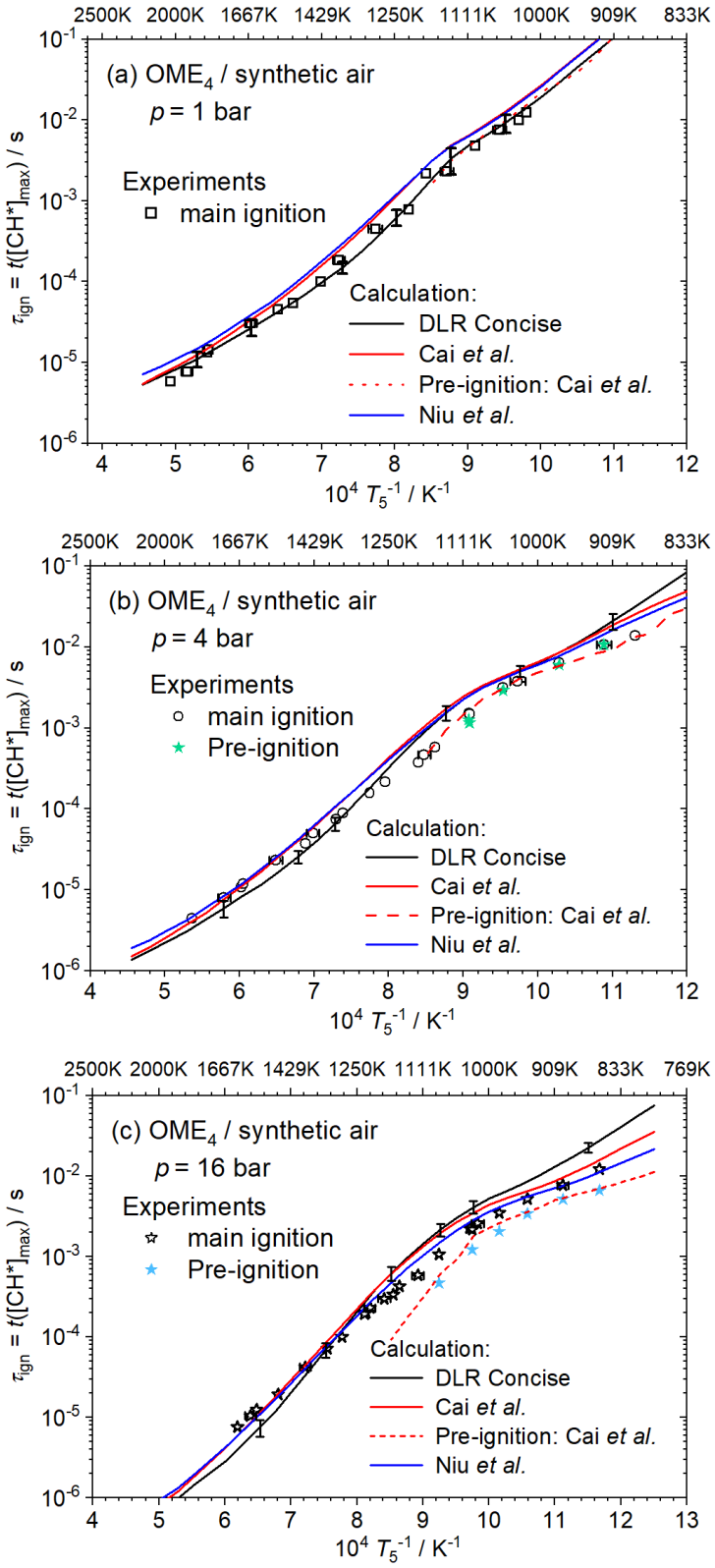


**Figure 4.15:** $OME_4$ / synthetic air (20% $O_2$ + 80% $N_2$): Comparison of measured data (symbols) and predictions (curves) for $\varphi = 1.0$, $p$ / bar = 1 (squares), 4 (circles), and 16 (stars), and dilution = 1:5 in $N_2$. Models used: (a) DLR-Concise (solid black curve) [1], (b) Cai *et al.* (solid red curve) [7], and (c) Niu *et al.* (solid blue curve) [8].

The model of Cai *et al.* [7] reproduces the pre-ignition behavior of $OME_2$ and $OME_4$ observed in the experiments, see the red-dashed curve in Figs. 4.14 and 4.15. As the Niu *et al.* model [8] is a reduced model based on the Cai *et al.* model, the predictions by the two models are quite close for all the conditions considered. Furthermore, the pre-ignition behavior is also reproduced by the model of Niu *et al.* [8]. The DLR-Concisemodel [1], on the other hand, best reproduces the temperature dependency of the measured data at 1 bar for both fuels. At elevated pressures of 4 and 16 bar, the DLR-Concise model overpredicts the measured data for all temperatures lower than 1400 K, *e.g.*, by about 2 ms at 1000 K. Furthermore, the DLR-Concise model does not reproduce the measured pre-ignition behavior.

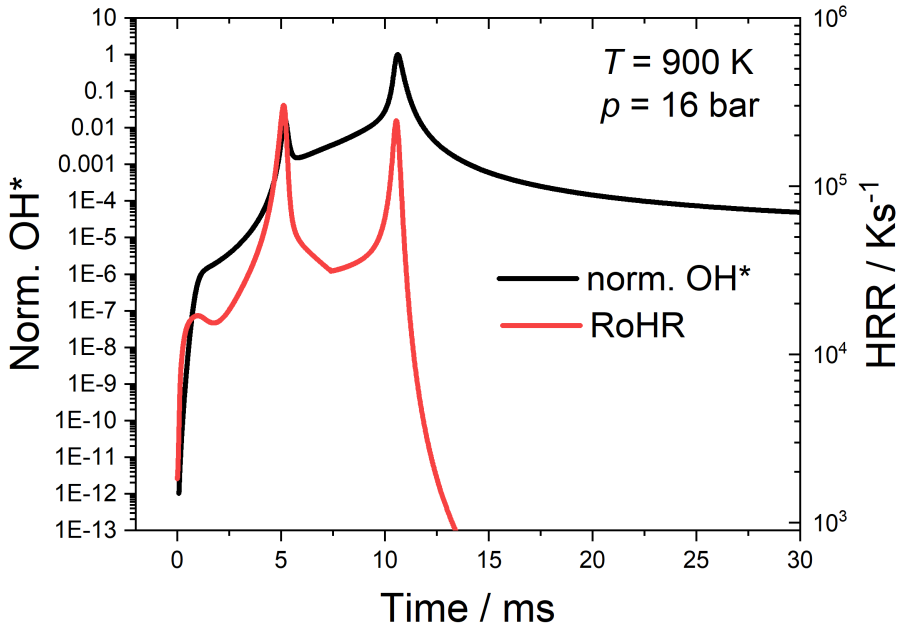


**Figure 4.16:** Normalized $CH^*$ mole fraction profile and rate of heat release (HRR) during ignition of $OME_4$ / synthetic air at $\varphi = 1.0$, $p$ / bar = 16, and $T = 900$ K, and dilution = 1:5 in $N_2$ using Cai *et al.* [7] reaction model.

Figure 4.16 shows the $OH^*$ emission profile (solid black curve) and the rate of heat release (HRR – solid red curve) versus time obtained during computation of a specific and representative $OME_4$ / synthetic air mixture ($\varphi = 1.0$, dilution level of 1:5 with $N_2$) at an initial temperature of 900 K and pressure of 16 bar based on the Cai *et al.* model [7] and applying the specific pressure profile. From the $OH^*$ profile, the pre-ignition peak is observed at about 5.2 ms and the main ignition peak at 10.6 ms. The heat release profile shows a three-stage heat release process. The first-stage heat release (at 1 ms) is the smallest compared to the second and third stages, respectively, at 5.2 and

10.6 ms. The second and third stages of heat-release coincide, respectively, with the pre-ignition and main ignition peaks, as seen from the $OH^*$ profile. In Fig. 4.16 there is no distortion on the reactive pressure profile or the $OH^*$ emissions profile before pre-ignition. This implies that the first-stage heat release seen in 4.16 at about 1 ms is not resolved in the measurements at our experimental conditions.

Pre-ignition in engines takes place when the fuel-air mixture combination ignites abruptly and unpredictably, or before the spark plug fires [140]. Pre-ignition leads to formation of knocks, *i.e.*, unwanted high-pressures that are harmful to the engine's structural integrity. In addition, it lowers the efficiency of the engine. Thus, it is important to understand the conditions of ($T$ and $p$) that promote ignition, and fuels and fuel / oxidizer compositions that are prone to ignition. In addition, being able to predict pre-ignition behavior using detailed chemical kinetic models is important. Regarding pre-ignition of OMEs at other conditions, Butin *et al.* [141] reported on the three-stage heat release during auto-ignition of $OME_1$ / oxidizer mixtures. They investigated numerically auto-ignition of $OME_1$ / air mixtures in a constant volume adiabatic reactor over a wide range of conditions, including temperatures rangining from 900 to 1400 K, pressures ranging from 10 to 40 bar, and equivalence ratios ranging from 0.1 to 2.0. They observed three stage-heat release behavior within low-to-intermediate initial temperatures ranging between 600 and 900 K at equivalence ratios below 0.5. Pre-ignition behavior has also been observed during auto-ignition of other fuels in the shock tube, *i.e.* ethanol and methanol [140, 142, 143]. For example, Figueroa-Labastida *et al.* [140] measured IDTs of ethanol / air mixtures at fuel-air ratios $\varphi$ of 0.5 and 1.0, $p$ / bar = 2 and 4. They observed pre-ignition events in mixtures containing higher ethanol concentrations, particularly at lower temperatures.

#### 4.2.4.3 Ignition delay times – Sensitivity analysis

To examine further the pre-ignition phenomenon and thus, also to determine the reactions that are dominant during pre-ignition and main ignition, sensitivity analysis was carried out using the model of Cai *et al.* [7] for $OME_4$ / synthetic air ($\varphi$ = 1.0, dilution of 1:5 with $N_2$) for an initial temperature of $T$ = 900 K and an initial pressure of $p$ = 16 bar. The results obtained are shown in Fig. 4.17 for (a) pre-ignition (@5.2 ms) and (b) for main ignition (@10.6 ms) showing all the reactions with a sensitivity greater than 5%. In the pre-ignition regime, the chain branching reaction $H_2O_2\,(+M) \rightleftharpoons 2OH\,(+M)$ is the most important reaction promoting ignition. Ignition of $OME_4$ is further promoted by H-abstraction reactions from the fuel molecule via $HO_2$ leading to the formation of $H_2O_2$, *i.e.*, $OME_4 + HO_2 \rightleftharpoons OME4RX5 + H_2O_2$,

$OME_4 + HO_2 \rightleftharpoons OME4RX3 + H_2O_2$, and $OME_4 + HO_2 \rightleftharpoons OME4RX1 + H_2O_2$. OME4RX1, OME4RX3, and OME4RX5 represent primary fuel radicals with the radical site located at the first, the second, and the third carbon atom, respectively. Ignition is further promoted by fuel-specific reactions: $OME_4 + OH \rightleftharpoons OME4RX1 + H_2O$ and $OME_4 + CH_3O_2 \rightleftharpoons OME4RX1 + CH_3O_2H$. The main inhibiting reaction is the reaction $2HO_2 \rightleftharpoons H_2O_2 + O_2$. In general, in the pre-ignition regime, reactions involving $H_2O_2$ and $HO_2$ are dominating. In addition, it is also shown in Fig. 4.17 that several reactions associated with low-temperature chemistry are promoting $OME_4$ ignition, *e.g.*, $OME4RX5 + O_2 \rightleftharpoons OME4ROOX5$, $CH_3OCH_2 + O_2 \rightleftharpoons CH_3OCH_2O_2$, and $CH_3O_2 + CH_2O \rightleftharpoons CH_3O + OH + HCO$.

In the main ignition regime, (see Fig. 4.17 b), the most promoting reaction is the chain branching reaction $H + O_2 \rightleftharpoons O + OH$. The most inhibiting reaction, on the other hand, is the reaction $H+O_2(+M) \rightleftharpoons HO_2(+M)$ which consumes H radicals producing the less active $HO_2$ radical. Ignition of $OME_4$ is further promoted by the fuel-specific reaction $OME_4 + OH \rightleftharpoons OME4RX1 + H_2O$ and the CO oxidation reaction $CO + O + M \rightleftharpoons CO_2(A) + M$. In general, in the main ignition regime, the identified sensitive reaction pattern is typical for this type of ignition: The system is sensitive to reactions with small radicals involved with the reactions being a part of the base chemistry ($C_0$ - $C_2$ sub-model); for example, reactions involving H, O, OH, $CH_3$, $HO_2$, and $CH_2O$.

#### 4.2.4.4 Radical profiles analysis – $OME_4$

In the pre-ignition regime, it was shown from the results of the sensitivity analysis that the $H_2O_2$ system plays a major role, and reactions involving low-temperature chemistry are also promoting the pre-ignition. To further understand the pre-ignition behavior, first the mole fraction profiles of OH∗ during ignition of $OME_4$ / synthetic air diluted 1:5 with nitrogen at $\varphi = 1.0$, $T(t = 0) = 900$ K, and $p(t = 0) = 16$ bar are considered. The analysis is carried out with the model of Cai *et al.* [7] for three different cases: with the full mechanism as presented in Table 3.2 (case 1), with the full mechanism minus the low-temperature chemistry of DME, $OME_1$, $OME_2$, $OME_3$, and $OME_4$ (case 2), and with full mechanism minus $H_2O_2$ producing reactions (case 3). In case 2, the low-temperature chemistry, *i.e.*, reactions involving peroxy radicals, hydroperoxyl, and ketohydroperoxy species for all OMEs and DME ($OME_0$) were deactivated. The results are presented in Fig. 4.18 showing that the pre-ignition behavior is not observed in the absence of low-temperature chemistry; see full red curve. This is an indication that the pre-ignition behavior is a consequence of the low-temperature chemistry. For case 3, the major $H_2O_2$-producing reactions as determined through rate of production analysis (see Fig. 4.19) are blocked. It is observed that under this condition

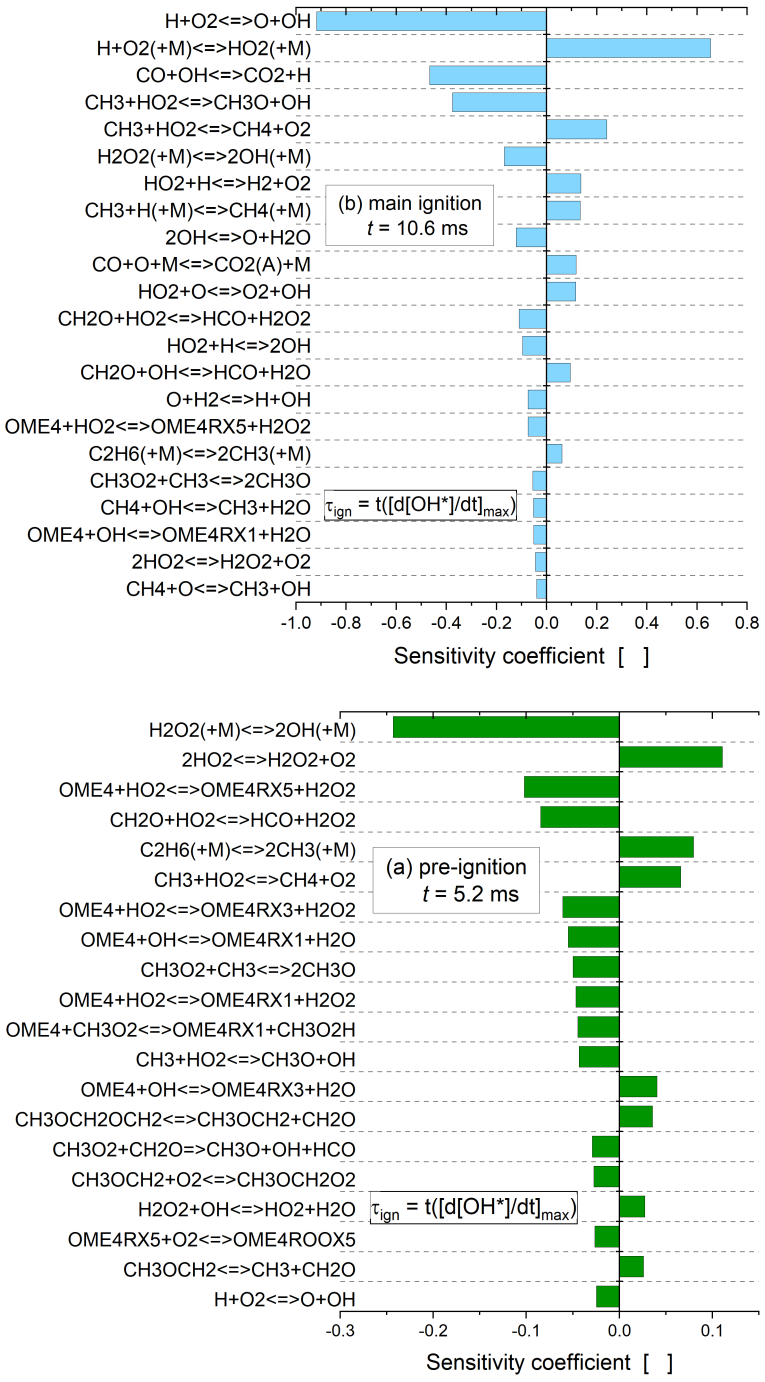


**Figure 4.17:** $OME_4$ / synthetic air (20% $O_2$ + 80% $N_2$): IDT sensitivity coefficients at, $\varphi = 1.0$, initial temperature $T(\mathrm{t} = 0) = 900\,\mathrm{K}$, initial pressure $p(t = 0) = 16\,\mathrm{bar}$, and dilution = 1:5 in $N_2$ for (a) pre-ignition (green) and (b) main ignition (cyan) using the Cai *et al.* model [7]

.

the pre-ignition peak (Fig. 4.18-full blue curve) and the first stage heat release (dotted blue curve, first peak) are subdued considerably; also, the location of the peaks of the maximum of the OH∗ concentration and the rate of heat release (HRR) is shifted to much longer reaction times thus implying a much-reduced reactivity. These findings show that the $H_2O_2$ system plays an important

role in the pre-ignition regime. Through the chain branching reaction $H_2O_2$ (+M) $\rightleftharpoons$ 2OH (+M), identified as the most important reaction according to the results of sensitivity analysis in the pre-ignition regime (see Fig. 4.17), $H_2O_2$ acts as the source of OH radicals that go on reacting with other intermediate species thus releasing heat and, finally, accelerating the whole fuel oxidation system. In Fig. 4.20, an analysis of the mole fraction profile of major species and

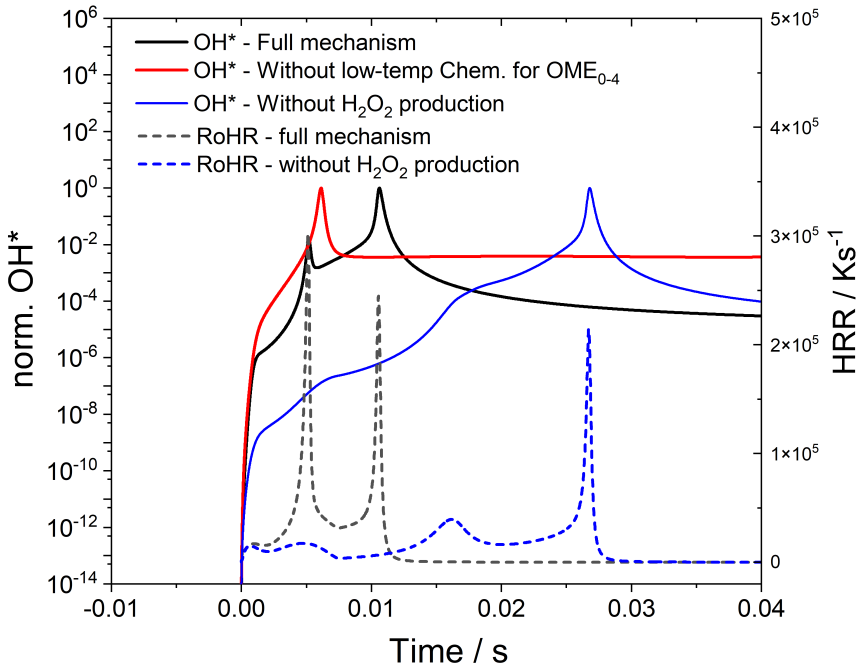


**Figure 4.18:** OH* mole fraction profile and rate of heat release (HRR) during ignition of $OME_4$ / synthetic air mixture diluted 1:5 with $N_2$ at $\varphi = 1.0$, $T(t = 0) = 900$ K, $p(t = 0) = 16$ bar, and dilution = 1:5 in $N_2$ using the model of Cai *et al.* [7].

the temperature profile during ignition of $OME_4$ / synthetic air ($\varphi = 1.0$ and diluted 1:5 with $N_2$) at $T(t = 0) = 900$ K and $p(t = 0) = 16$ bar is presented. The temperature profile shows a two-step ignition process as envisaged (see Fig. 4.18). It is seen that the fuel ($OME_4$) is consumed entirely within the pre-ignition period. High concentrations of formaldehyde and hydrogen peroxide are observed in the pre-ignition regime. In addition, the decomposition of $OME_4$ and the subsequent oxidation of fuel fragments generate CO radicals. Their concentration increases sharply in the pre-ignition regime (first stage heat release) and reaches a maximum of about 0.0056 seconds at the end of the pre-ignition period. From here, the concentration of CO radicals decreases slowly as the temperature continues to rise indicating a slow oxidation process. Rapid oxidation of CO takes place through the reaction CO + OH $\rightleftharpoons$ $CO_2$ + H. The conclusion is that the second stage of the heat release is strongly connected to the oxidation of CO radicals as expected.

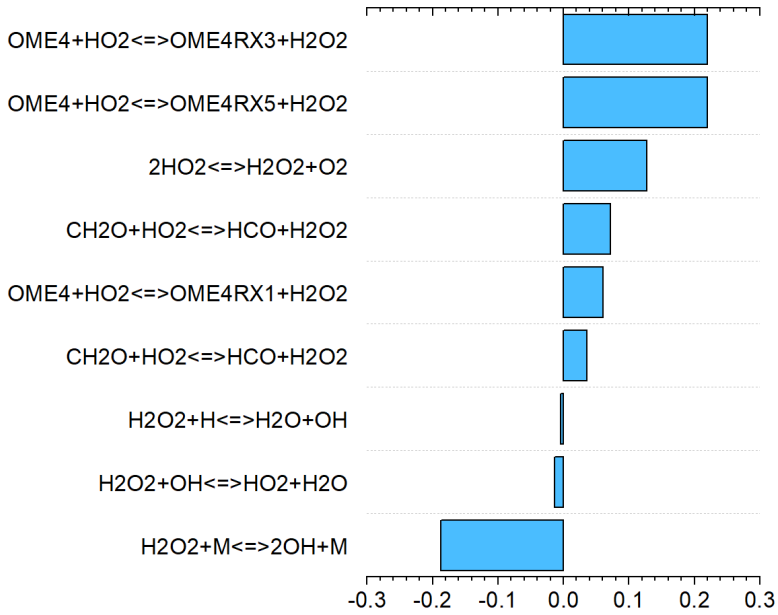


**Figure 4.19:** Normalized rate of production (ROP) of $H_2O_2$ during ignition of $OME_4$ / synthetic air at $\varphi = 1.0$, $T(t = 0) = 900\,\mathrm{K}$, $p(t = 0) = 16$ bar, and dilution = 1:5 with $N_2$. Calculated at 20% fuel consumption using the Cai *et al.* model [7].

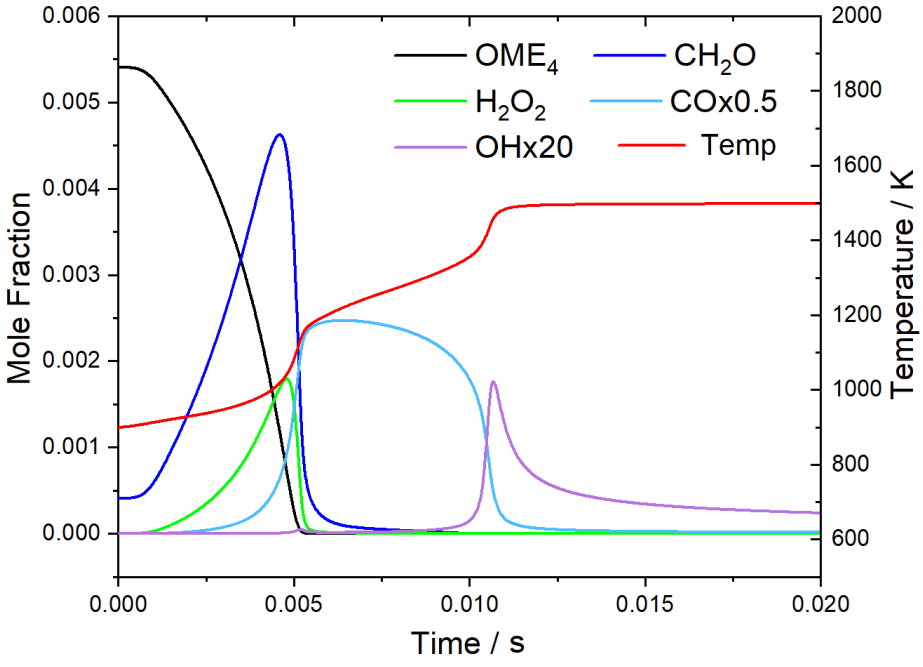


**Figure 4.20:** Temperature profile and mole fraction profiles of $OME_4$, $H_2O_2$, OH, $CH_2O$, and CO during ignition of $OME_4$ / synthetic air at $\varphi = 1.0$, $T(t = 0) = 900\,\mathrm{K}$, $p(t = 0) = 16$ bar, and dilution = 1:5 with $N_2$ using the Cai *et al.* reaction model [7].

#### 4.2.4.5 Reaction pathway analysis – $OME_4$

To examine the important fuel degradation pathways and key species during the auto-ignition of $OME_2$ and $OME_4$, a reaction pathway analysis is performed at $p(t = 0) = 16$ bar and for temperatures of 900 K and 1500 K representing the low- and high-temperature regions achieved in the measurements. Since the OMEs have a similar molecular structure differing only in the chain length *i.e.*, by the number of -$OCH_2$- groups, their reaction pathways are believed to be similar. Thus, here, the reaction pathway analysis is demonstrated only for a stoichiometric mixture of $OME_4$ / synthetic air at a dilution level of 1:5 using Cai's model [7] (at 900 K and 1500 K) and the high-temperature DLR-Concise model [1] at 1200 K and 1500 K. The DLR-Concise model is only considered in the high-temperature regime, *i.e.*, at 1200 K and 1500 K because it lacks low-temperature chemistry. The plots constructed using the Chemical Workbench software package [139] are presented in Fig. 4.21 for the model of Cai *et al.* [7] and in Fig. 4.22 for the DLR-Concise model [1], respectively. In Figs. 4.21 and 4.22, the '+M' denotes the third body molecule and '+R' denotes the type of the H-atom abstracting radicals such as $HO_2$, OH, $CH_3$, H, $CH_3O$, $CH_3O_2$, and OH.

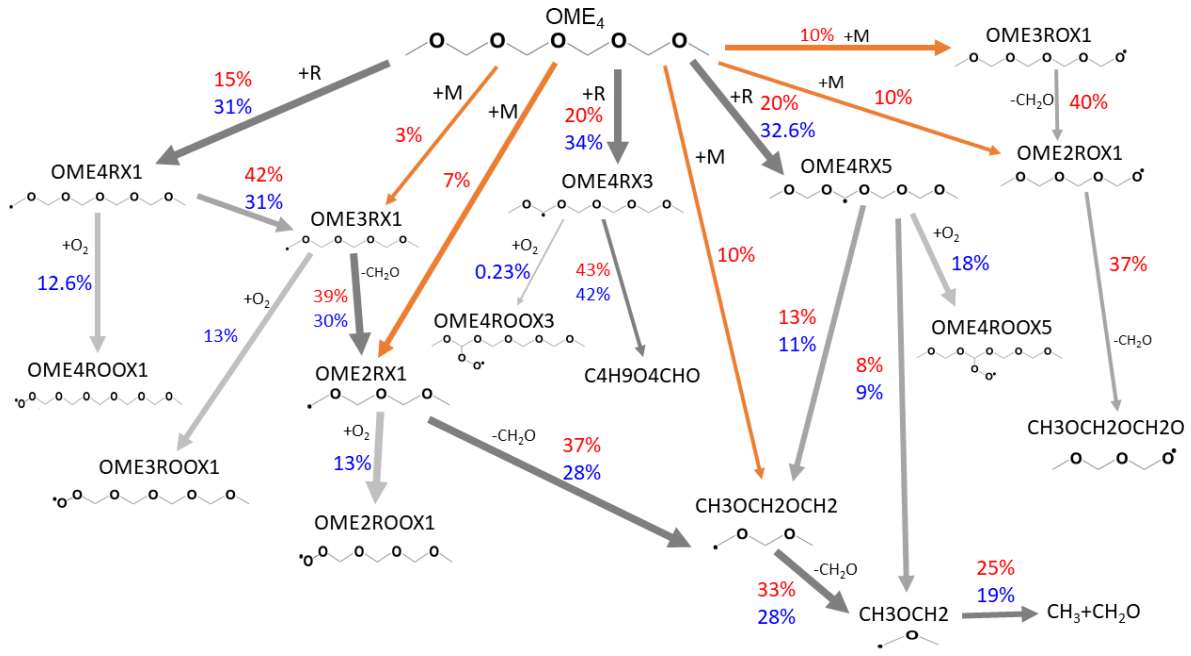


**Figure 4.21:** Reaction pathway analysis during ignition of an $OME_4$ / synthetic air mixture at $\varphi = 1.0$, $p = 16$ bar, dilution = 1:5 with $N_2$, and 20% fuel-consumption for temperature of $T = 900$ K (blue) and $T = 1500$ K (red). Cai *et al.* model was used [7]. Orange arrows – decomposition pathways (exclusively) at high-temperature.

In Figure 4.21, it is shown that unimolecular fuel decomposition and H-atom abstraction pathways

are the main decomposition pathways for $OME_4$ at high temperatures (1500 K – see orange arrows), while at low temperatures (900 K – see grey arrows), the degradation of the fuel is exclusively occurring by H-atom abstraction reactions. The H-abstraction reactions from the first, second, and third carbon atoms, respectively lead to the formation of the primary fuel radicals OME4RX1, OME4RX3, and OME4RX5. At 1500 K, these alkyl radicals formed to break down into smaller secondary fuel radicals by breaking off the C-O bonds, for example, OME4RX1 breakdown into OME3RX1 and OME4RX5 breakdown into $CH_3OCH_2OCH_2$ and $CH_3OCH_2$ radicals. At 900 K, the primary fuel radicals (OME4RX1, OME4RX3, and OME4RX5) in addition to decomposing into a smaller alkyl radical through the scission of the C-O bond, also undergo the addition of oxygen to form alkyl peroxy radicals, *i.e.*, OME4ROOX1 for OME4RX1. The degradation of the alkyl radicals continues in a similar way leading to the formation of even smaller alkyl radicals and alkyl peroxy radicals. Though not shown, alkyl peroxy radicals are followed by isomerization reactions, followed by a second addition of oxygen in a similar fashion to regular alkanes; see Fig. 3.8.

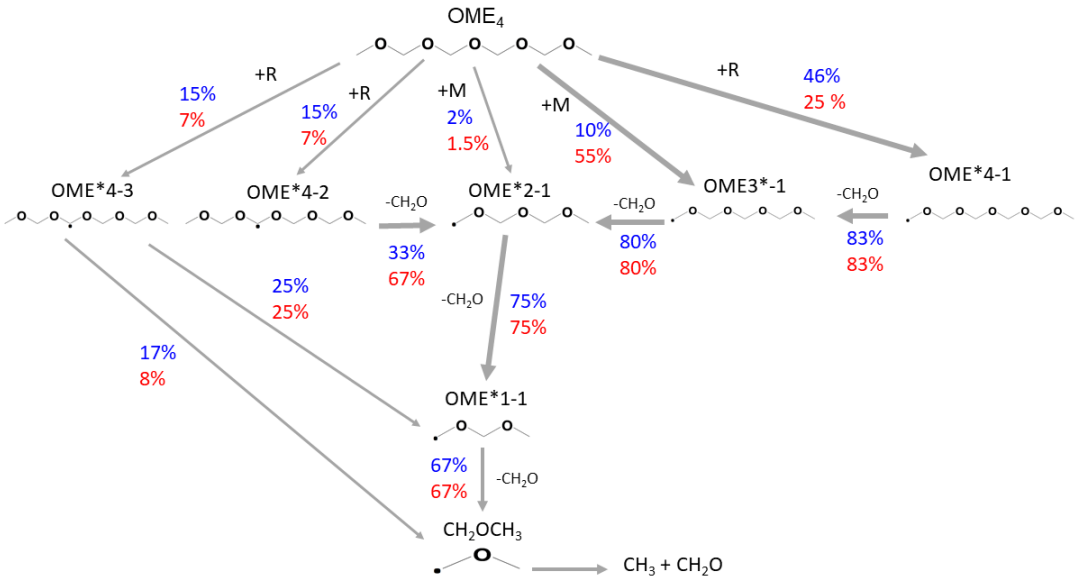


**Figure 4.22:** Reaction pathway analysis during auto-ignition of an $OME_4$ / synthetic air mixture at $\varphi = 1.0$, $p = 16$ bar, dilution = 1:5 with $N_2$, and 20% fuel-consumption for, $T = 1200$ K (blue) and $T = 1500$ K (red). DLR-Concise model was used [1].

When focusing on the high-temperature degradation pathways for $OME_4$, major similarities are observed between the results obtained using the Cai *et al.* model and the (high-temperature) DLR-Concise model; see Figs. 4.21 and 4.22. According to both models, the degradation of the primary fuel radicals proceeds to the $CH_3OCH_2OCH_2$ (OME*1-1) radical. This radical undergoes a C–C cleavage yielding $CH_2OCH_3$ radicals which further break down into $CH_2$ radicals and $CH_2O$.

In general, and regardless of the specific reaction model used, it is observed that $CH_2O$ is an important intermediate species during the oxidation of $OME_4$ and thus, also during the oxidation of all OMEs. This is confirmed by the results of sensitivity analyses; see Fig. 4.17 which showed that reactions involving $CH_2O$ are amongst the most sensitive reactions.

### 4.2.5 Comparison of ignition delay times (IDTs) and laminar burning velocities (LBVs) of $OME_1$, $OME_2$, $OME_4$, and DME

#### 4.2.5.1 Comparison of IDTs of $OME_1$, $OME_2$, $OME_4$, and DME

The ignition delay times of DME, $OME_1$, $OME_2$, and $OME_4$ determined in this work are presented in Fig. 4.23 as a function of temperature for the three pressure regimes: (a) – 1 bar, (b) – 4 bar, and (c) – 16 bar; thus, the effect of chain length on ignition delay times might be clear. Dimethyl ether ($CH_3OCH_3$) considered to represent $OME_0$ is the starting point. It is shown that the IDTs are longest for DME (blue symbols) and the shortest for $OME_4$ (cyan symbols), especially for temperatures lower than 1500 K at 1 and 4 bar, and within the entire temperature range for 16 bar. From this finding it is concluded that, in general, the reactivity of OMEs increases with an increase in chain length, as is also true for most hydrocarbon fuels. The IDTs of $OME_2$ (green symbols) are close to those of $OME_4$, particularly at elevated pressures of 4 and 16 bar. This finding indicates that for OMEs, the increase in reactivity in OMEs is less pronounced with increasing chain length. The dependence of IDTs on the temperature between these specific fuels is well observed in the transition regime between 1500 and 1000 K. Furthermore, this trend is by their respective cetane numbers, which increase from 29 for $OME_1$ to 63 for $OME_2$, and 76 for $OME_4$. In the high-temperature regime, for temperatures above 1500 K, the ignition delay times of these fuels appear to converge to a similar value. This is because the ignition is largely controlled by the rate of fuel pyrolysis and H-abstract reactions; thus, the dependence of reactivity on chain length is weak in the high-temperature region. For the same reason, the ignition delay times of hydrocarbons, *i.e.*, alkanes, alkenes, and various distillate fuel mixtures including gasoline, diesel, and jet fuels converge in the high-temperature regime [82, 144, 145].

#### 4.2.5.2 Comparison of laminar flame speeds of $OME_1$, $OME_2$, and $OME_4$

Figure 4.24 presents a comparison between the measured laminar burning velocities (LBVs) of mixtures of $OME_1$ / air (blue symbols), $OME_2$ / air (red symbols), and $OME_4$ / air (green symbols) at 473 K (preheat temperature) and pressures of 1 (triangles), 3 (circles), and 6 (diamond) bar, with fuel-air ratios ranging from about 0.6 up to about 2.0 [2, 3, 6]. At each pressure, the maximum laminar burning velocities for all fuels are located at a $\varphi$ value of 1.2. Note that a similar value of 1.2 was reported by Eckart *et al.* [69, 146] for $OME_1$ and $OME_2$. Because of its high reactivity, $OME_4$ has the highest measured LBV values at all pressures and over the entire equivalence ratio range.

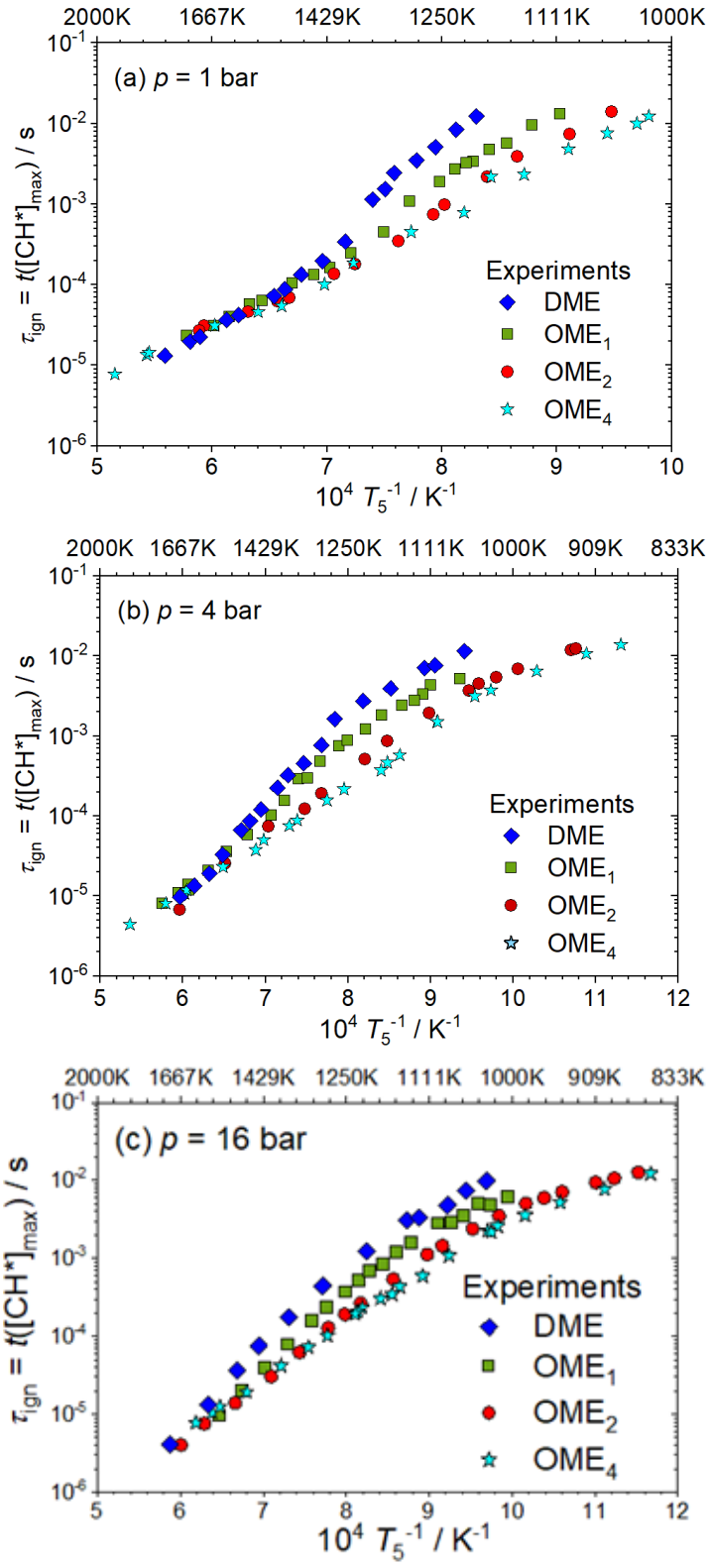


**Figure 4.23:** Comparison of measured ignition delay time data of DME / synthetic air (blue diamonds), $OME_1$ / synthetic air (green squares), $OME_2$ / synthetic air (red circles), and $OME_4$ / synthetic air (cyan stars) at $\varphi = 1.0$, dilution = 1:5 in $N_2$ at initial pressures of (a) 1 bar, (b) 4 bar, and (c) 16 bar.

Concerning the influence of chain length, it is demonstrated that LBVs increase as chain length increases; for example, the peak value of LBV for $OME_1$, $OME_2$, and $OME_4$ at 1 bar are 103 cm/s, 105 cm/s, and 108 cm/s, respectively. Interestingly, it is seen that the LBVs of $OME_2$ are converging to those of $OME_4$ for $\varphi \leq 1.0$ and those of $OME_1$ for $\varphi \geq 1.25$, at all pressures. The closeness of the measured results for $OME_2$ and $OME_4$ for $\varphi \leq 1.0$ is consistent with the behavior seen for IDTs at temperatures below 1450 K. The results also reveal that the overall characteristic of LBVs decreases as pressure increases. The LBVs of $OME_1$ decrease from 103 cm/s at 1 bar to 80.4 cm/s at 3 bar and 64.8 cm/s at 6 bar.

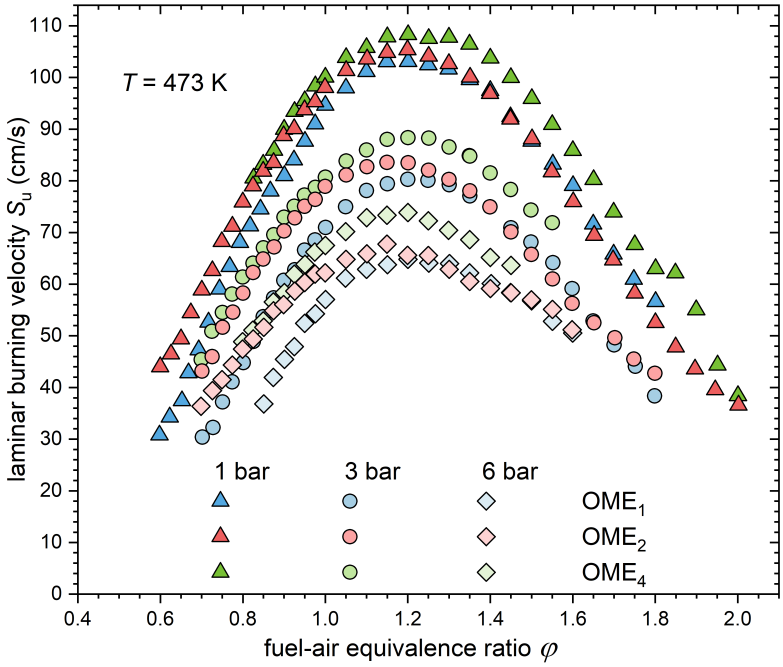


**Figure 4.24:** Comparison measured laminar burning velocities [2, 3, 6] of (a) $OME_1$ / air (blue), (b) $OME_2$ / air (red), and (c) $OME_4$ / air (green) at $T$ = 473 K and for $p$ / bar = 1 (triangles), 3 (circles), and 6 (diamonds).

Figure 4.25 compares the measured laminar burning velocities and the calculated laminar flame speeds of (a) $OME_2$ and (b) $OME_4$, at pressures of 1 (triangles), 3 (circles), and 6 (diamond) bar. Again, the models of DLR-Concise and Cai *et al.* [7] were used for the calculations. The DLR-Concise model matches the position of the peak LBVs of $OME_2$ and $OME_4$ at a $\varphi$-value of 1.2. The predictions with the Cai *et al.* model [7], on the other hand, predict a shift in the position of the maximum laminar burning velocity to the less fuel-rich regime, in detail to a $\varphi$-value of 1.1 for the two fuels. With only a marginal overprediction of LBVs on the fuel-lean side of about 2 cm/s, the DLR-Concise model [1] matches correctly the measured data for $OME_2$. On the other hand, the model of Cai *et al.* [7] matches the measured LBVs of $OME_2$ on the fuel-lean side as well as up to a $\varphi$-value of 1.3 at 6 bar.

The large deviation at $\varphi \geq 1.35$ for 6 bar is attributed to both flame stabilization difficulties and the accuracies of mass flow controllers; see also discussion in [6, 121]. At 1 and 3 bar, calculations made with the model of Cai *et al.* [7] coincide with the measured data only for the fuel-lean mixtures. The experimental data are underpredicted for $\varphi \geq 0.9$ by up to 10%, with an increasing divergence toward fuel-rich conditions.

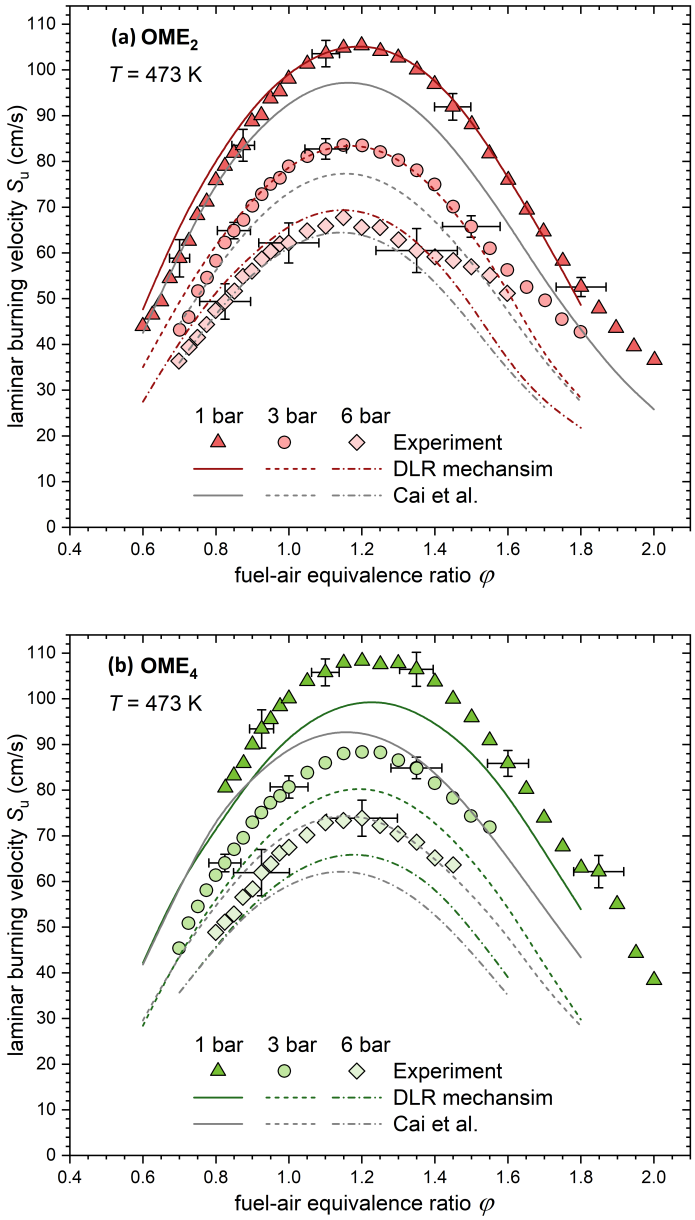


**Figure 4.25:** A comparison of measured (symbols) and calculated (curves) flame speeds of (a) $OME_2$ / air (red) and (b) $OME_4$ / air (green), at $T = 473$ K and $p$ / bar = 1 (triangles), 3 (circles), and 6 (diamonds). Models used: DLR-Concise [1] and Cai *et al.* [7].

For $OME_4$, both models –the DLR-Concise [1] and the Cai *et al.* [7] – underpredict the measured values over the whole regime. Higher deviations of about 20% at $\varphi = 1.4$ observed for Cai *et al.* [7]. In addition, considerable disparities between the two models at fuel-rich conditions are seen. In the fuel-lean region at $\varphi \leq 0.8$, the deviation observed is within the experimental uncertainties. A substantial deviation was observed between measured LBVs and calculated LFS values using both models is attributed to the fact that the current OMEs models have been based on limited validation, particularly regarding LBVs data, especially for $OME_4$; see Table 2.3. Also, note that the model of Cai *et al.* [7] has been tuned for IDTs.

### 4.2.6 Trimethyl orthoformate (*iso*-$OME_2$)

#### 4.2.6.1 Ignition delay times – Experimental results

Ignition delay time data have been measured for stoichiometric ($\varphi = 1.0$) mixtures of TMOF / synthetic air at a dilution level of 1:5 with $N_2$, and pressures of 1, 4, and 16 bar. The results are presented in Fig. 4.26. The measurements were extended up to about 11 ms (see the dashed black line) in the intermediate to high-temperature regime, between about 830 and 2000 K. The measured data exhibit a linear relationship with temperature up to about 1100 K (3 ms), thus following an Arrhenius behavior. At temperatures below 1100 K (around 3 ms), the IDTs deviate slightly from this linear behavior, becoming shorter due to post-shock pressure increase. The experimental pressure profile $p(t) = p(t = 0)$ must and is used to account for this tendency in modelling as explained before. The experimental data for *iso*-$OME_2$ including the experimentally derived profiles are provided in Appendix I.

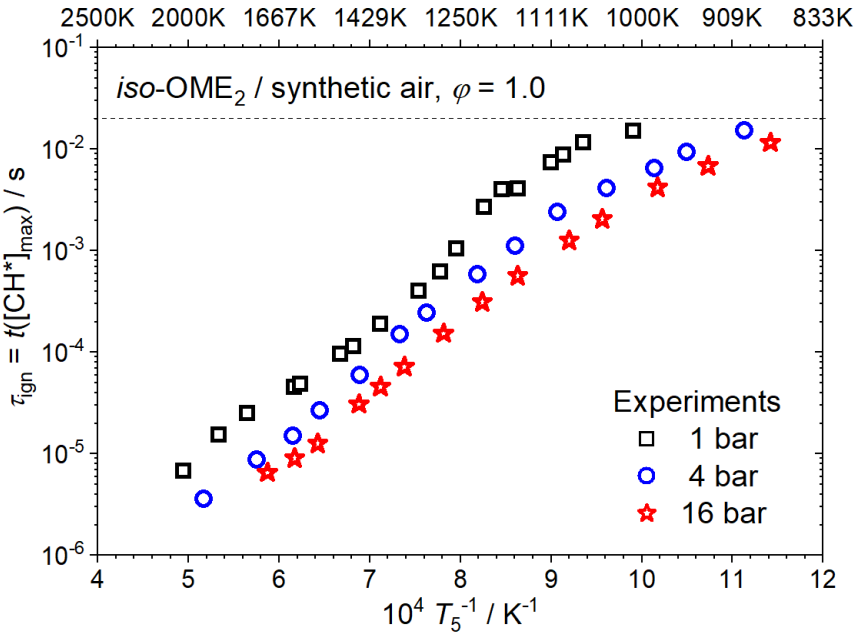


**Figure 4.26:** *Iso*-$OME_2$ / synthetic air (20% $O_2$ + 80% $N_2$): Measured ignition delay time data for $\varphi = 1.0$, $p$ / bar = 1 (black squares), 4 (blue circles), and 16 (red stars); dilution = 1:5 in $N_2$.

*Iso*-$OME_2$ and $OME_2$ are isomers and both have the potential to reduce the formation of soot particles due to their high oxygen content. Therefore, the experimentally determined *iso*-$OME_2$ ignition delay time data are compared to those of its linear isomer, $OME_2$, measured under identical conditions. The objective is to analyze if an effect of the structural differences on IDTs exists, and if so to which extent. In Fig. 4.27, a comparison is given of the measured IDT data for mixtures of *iso*-$OME_2$ / synthetic air (green symbols) and $OME_2$ / synthetic air (red symbols) at $p = 1$ bar

(squares) and 16 bar (stars). Very small deviations are observed between *iso*-$OME_2$ and $OME_2$ data. The conclusion is that the IDTs of these two fuels are similar for the conditions considered, within the experimental uncertainty on the measured ignition delay times.

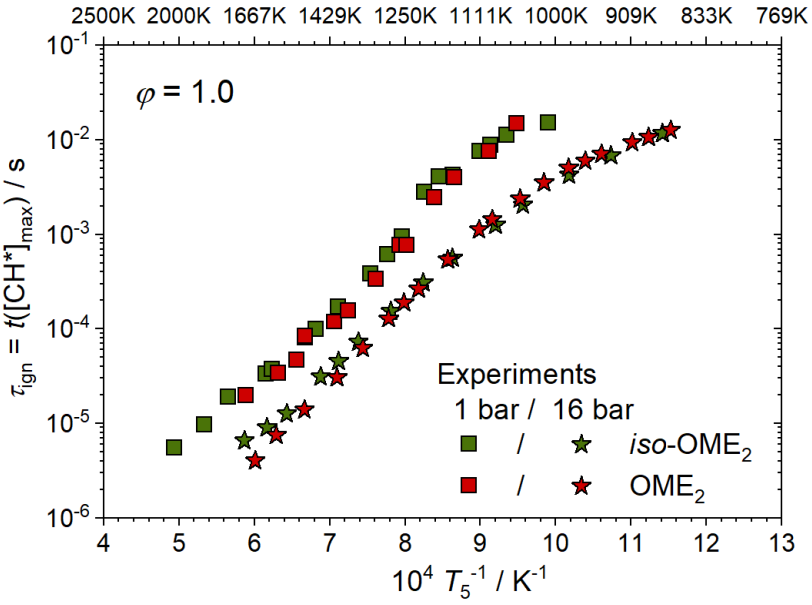


**Figure 4.27:** Comparison of measured IDTs of *iso*-$OME_2$ / synthetic air (green symbols) and $OME_2$ / synthetic air (red symbols) at $\varphi$ = 1.0, $p$ / bar = 1 (squares) and 16 (triangles), and dilution = 1:5 with $N_2$.

#### 4.2.6.2 Ignition delay times – Results by model predictions

Figure 4.28 shows the comparison between the measured and calculated IDT data for stoichiometric *iso*-$OME_2$ / synthetic air mixtures. The calculations were carried out with the DLR-Concise model [1]. For temperatures ranging from about 1250 to 2000 K, the closeness of the predicted and the experimental data is obvious. Below 1250 K, the model predictions are not reflecting the experimentally observed temperature dependencies of the IDT data, particularly for 4 and 16 bar. The model overpredicts the observed data for all temperatures less than 1100 K at 16 bar, *e.g.*, by 50% at 1000 K. In addition, the model underpredicts the measured data for all temperatures less than 1300 K at 1 bar, with a maximum deviation of about 60% observed at about 1200 K. This deviance is a result of the model's insufficient validation. The oxidation chemistry of *iso*-$OME_2$ is in the starting phase; thus, its chemistry in the in DLR-Concise model [1] is based on limited experiments and reaction kinetic rate data. This study provides useful data for model validation and future improvement of reaction models for *iso*-$OME_2$.

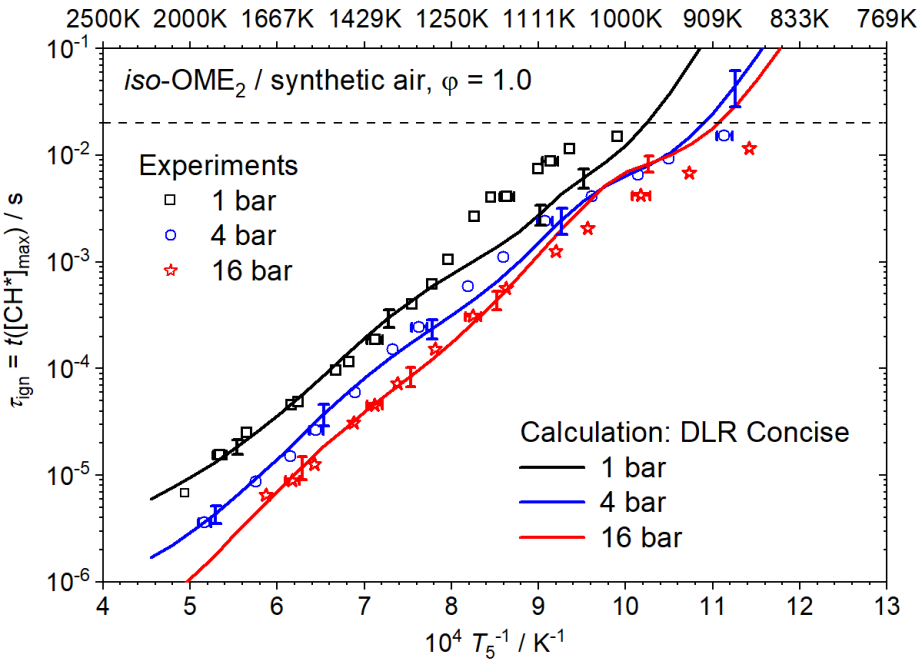


**Figure 4.28:** *Iso*-$OME_2$ / synthetic air (20% $O_2$ + 80% $N_2$): Comparison of measured data (symbols) and predicted (curve) for $\varphi = 1.0$, $p$ / bar = 1 (squares), 4 (circles), and 16 (stars), and dilution = 1:5 in $N_2$. The DLR-Concise model was used [1].

#### 4.2.6.3 Ignition delay times – Sensitivity analysis

To examine further whether the auto-ignition of *iso*-$OME_2$ at high-temperatures where a good match between measured and predicted data, sensitivity analysis calculations were carried out. The results obtained for the stoichiometric ($\varphi = 1.0$) *iso*-$OME_2$ / synthetic air mixture, again at a dilution level of 1:5 with $N_2$, for $T = 1300\,K$, and for pressures of 1 bar (red), 4 bar (blue), and bar 16 (green) are displayed in Fig. 4.29 showing the 15 most sensitive reactions. The results indicate that, like for most hydrocarbon fuels, *iso*-$OME_2$ ignition is extremely sensitive to the chain branching reaction $H + O_2 \rightleftharpoons O + OH$, with the highest negative sensitivity. Ignition of *iso*-$OME_2$ is also promoted by branching reactions: $CH_3 + HO_2 \rightleftharpoons CH_3O + OH$, $HCO + M \rightleftharpoons CO + H + M$, and $H_2 + OH \rightleftharpoons H_2O + H$. Furthermore, *iso*-$OME_2$ ($HC(OCH_3)_3$) ignition is sensitive to reactions involving methyl formate ($OCHOCH_3$), *i.e.*, $OCHOCH_3 + H \rightleftharpoons OCHOCH_2 + H_2$ and $OCHOCH_3 + H \rightleftharpoons OCOCH_3 + H_2$ with negative sensitivity coefficient (promoting) and $OCHOCH_3 + OH \rightleftharpoons OCHOCH_2 + H_2O$ with a positive one (inhibiting). Ignition of *iso*-$OME_2$ is mostly inhibited by $CH_3 + H\,(+M) \rightleftharpoons CH_4\,(+M)$ which leads to the formation of stable species. According to the DLR-Concise model, *iso*-$OME_2$ almost exclusively decomposes – at the experimental conditions selected – by the breaking of the C-O bond via the reaction *iso*-$OME_2 \rightleftharpoons O^*CH(OCH_3)_2 + CH_3$. The primary fuel radical, *i.e.*, $O^*CH(OCH_3)_2$, breaks

down through $\beta$-scission forming methyl formate ($OCHOCH_3$) and methoxy ($CH_3O$) radicals through $O^*CH(OCH_3)_2 \rightleftharpoons OCHOCH_3 + CH_3O$. Thus, methyl formate ($OCHOCH_3$) is an important intermediate providing the build-up of reactive radicals. Like most OMEs, the fuel molecule *iso*-$OME_2$ is consumed within the early stages of combustion. For OMEs, on the other hand, formaldehyde ($CH_2O$) and $HO_2$ are the most important oxygenated species, see sections 4.2.4.4 and 4.2.4.5.

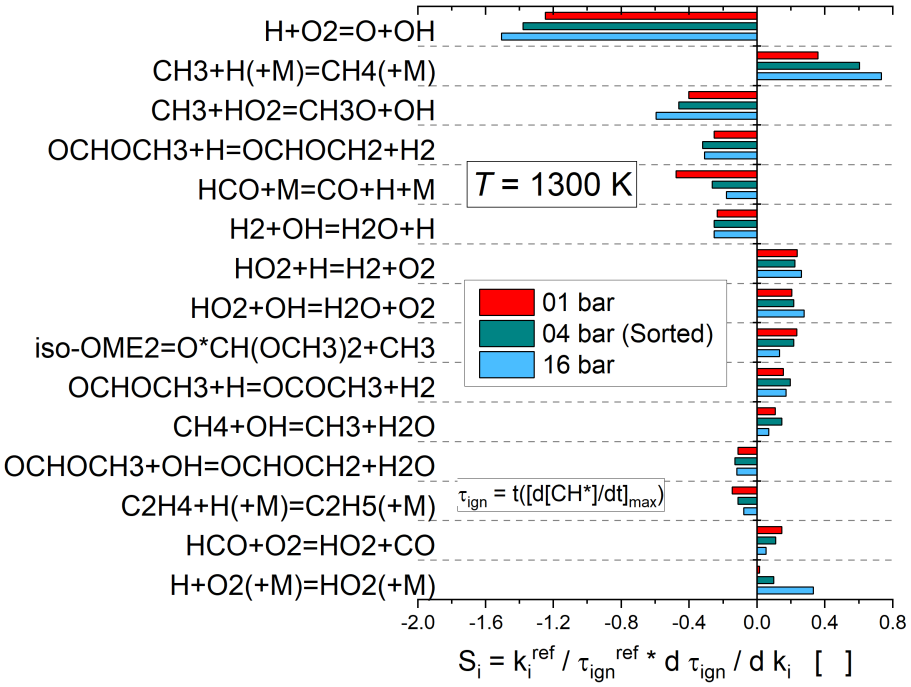


**Figure 4.29:** *Iso*-$OME_2$ / synthetic air (20% $O_2$ + 80% $N_2$): IDT sensitivity coefficients for $p$ / bar = 1 (red bar), 4 (green bar), and 16 (blue bar) at $T$ / K = 1300 K, $\varphi$ = 1.0, and dilution = 1:5 with $N_2$. The DLR-Concise model was used [1].

When applying the DLR-Concise model in the high-temperature regime, it is observed that *iso*-$OME_2$ mainly decomposes via the channel *iso*-$OME_2 \rightleftharpoons O^*CH(OCH_3)_2 + CH_3$ which accounts for over 90% of *iso*-$OME_2$. The decomposition of *iso*-$OME_2$ via the scission of the weak C-O bond at the central carbon atom, through *iso*-$OME_2 \rightleftharpoons OME^*1\text{-}2 + CH_3O$, accounts for 3% of the total *iso*-$OME_2$ depletion. Methyl ($CH_3$) radicals as formed *e.g.*, from the decomposition of methoxy radicals, collide with other radicals such as OH and $CH_3O$, respectively, forming $CH_3OH$ and $CH_3OCH_3$. In addition, the recombination of $CH_3$ produces $C_2H_6$ radicals and subsequently other hydrocarbon species, for example, $C_2H_4$, $C_2H_5$, and $C_3H_6$. For these reasons, ignition of *iso*-$OME_2$ is shown to be sensitive to a reaction involving ethene, too: $C_2H_4 + H\,(+M) \rightleftharpoons C_2H_5\,(+M)$. The results here are consistent with the findings of Gaiser *et al.* [74], which showed higher mole fractions of hydrocarbons ($C_2H_4$, $C_2H_6$,

and $C_2H_6$) and of the oxygenated species acetaldehyde ($CH_3CHO$) and methyl formate ($OCHOCH_3$) for *iso*-$OME_2$ than for $OME_2$ during their oxidation at $\varphi = 0.8$ and 1.2, and at atmospheric pressure in a flow reactor.

#### 4.2.6.4 Laminar burning velocities - *iso*-$OME_2$

To get further insight into the oxidation network of *iso*-$OME_2$, the results of the measured laminar burning velocities (LBV) [5] as well as of the calculated laminar flame speeds (LFS) of *iso*-$OME_2$ - air mixtures are presented. The results obtained at a preheat temperature of 473 K, pressures of 1 (triangles), 3 (circles), and 6 (diamonds) bar, and for fuel-air ratios in the range between about 0.6-1.8 are presented in Fig. 4.30. The peak values of LBVs are recorded at $\varphi = 1.1$ for all pressures examined. Peak values of 100 cm/s were obtained at 1 bar (triangles), 78.4 cm/s at 3 bar, (circles) and 65.6 cm/s at 6 bar (diamonds). The results of calculations using the DLR-Concise model [1] show that the peak laminar flame speeds (LFSs) are located at about the $\varphi = 1.10$-1.15 for all the pressures studied. The results also show that the model overpredicts the measured values over nearly the entire $\varphi$-values covered and at all pressures studied, with maximum overprediction of up to 30% at $\varphi > 1.2$ at 1 bar. However, at high pressures and large fuel-air ratios ($\varphi > 1.50$), the model underpredicts the experimental data; one reason might be the larger uncertainties in the measurements at these specific conditions resulting from difficulties in flame stabilization resulting in varying cone angles [5]. The error analysis revealed that pressure and fuel-air ratio have the greatest effect on the measurement uncertainty: At 1 bar, uncertainties of around ±2 cm/s are observed on average, corresponding to a relative error of ±2-4%. The uncertainties at high pressures range from ±3% to ±10%, with up to ±15% for fuel-rich mixtures ($\varphi > 1.4$).

The measured (symbols) laminar burning velocities data [5] and the calculated (curves) laminar flame speed data for *iso*-$OME_2$ (full, symbols) and $OME_2$ (open symbols) acquired under identical conditions are compared in Fig. 4.31. The predicted data for $OME_2$ (grey curves) are in very good agreement with the experimental data. Both the experiments and the calculations show that the peak LBV-value for $OME_2$ is at $\varphi = 1.2$.

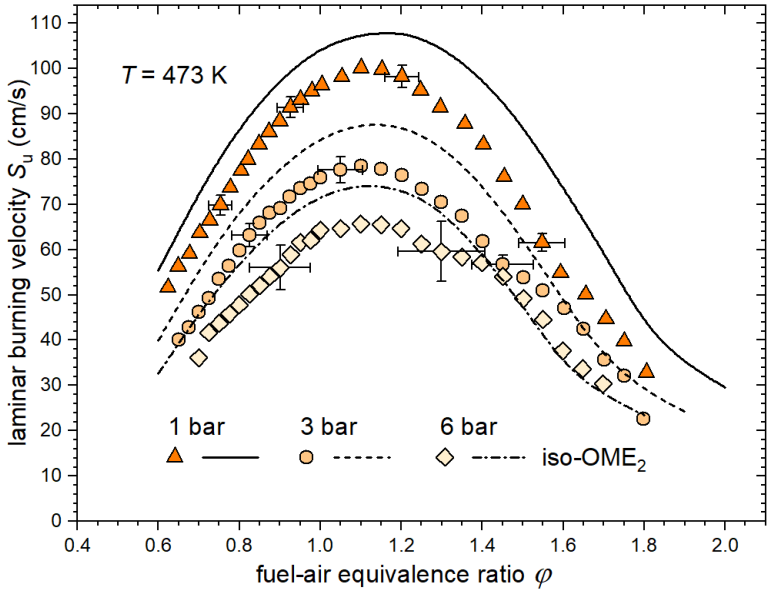


**Figure 4.30:** *Iso*-$OME_2$ / air mixture: Measured laminar burning velocities (symbols) and calculated laminar flame speeds (curves), $T = 473$ K, $p$ / bar = 1 (triangles), 3 (circles), and 6 (diamonds). DLR-Concise model was used [1].

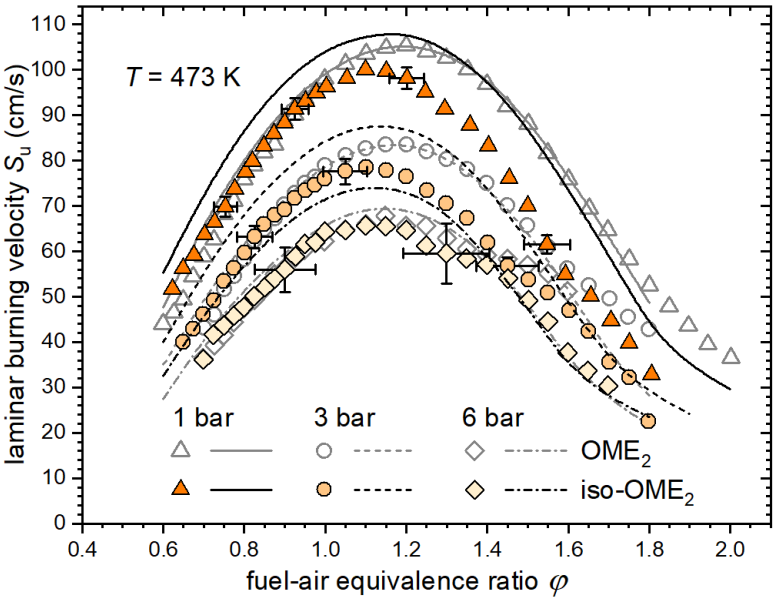


**Figure 4.31:** Comparison of measured laminar burning velocities (symbols) and laminar flame speeds (curves) of *iso*-$OME_2$ / air mixtures (closed symbols) and $OME_2$ / air mixtures (open symbols). The DLR-Concise model was used [1].

The experimental findings demonstrate that the LBVs of the two fuels are equal for stoichiometric and fuel-lean mixtures ($\varphi \leq 1.0$). This is identical to the trend reported for the ignition delay times of these two fuels. On the other hand, for fuel-rich ($\varphi > 1.0$) mixtures, the LBVs of $OME_2$ are much

larger, by up to 20 cm/s at $\varphi > 1.50$ and 1 bar. The results obtained here, particularly for $\varphi > 1.0$ are confirming that branching lowers the laminar burning velocities of oxygenated fuels which is also classical for hydrocarbon fuels [147, 148]. Furthermore, the trend observed for laminar burning velocities of $OME_2$ and *iso*-$OME_2$ at $\varphi > 1.0$ is similar to the trend seen for laminar burning velocities of *iso*-butanol and *n*-butanol [5, 90, 149]. Although there are no C-C bonds neither in $OME_2$ nor in *iso*-$OME_2$, $OME_2$ shows the higher LBV as it is also the case for *n*-butanol compared to *iso*-butanol. Thus, the influence of a branched structure in fuel components to the laminar burning velocities seen for pure hydrocarbons is also similar to oxygenated fuels.

## 4.3 Blends of OMEs with the gasoline surrogate, the primary reference fuel 90

In this sub-section, the experimental and modeling efforts on ignition delay times of the specific gasoline surrogate called primary reference fuel 90 (PRF90) consisting of 90% *iso*-octane and 10% *n*-heptane as well as of three blends with three specific oxygenated fuels will be presented and discussed. As explained in Section 2.6, the primary reference fuel 90 (PRF90) was chosen to represent the gasoline surrogate in this work since it has been demonstrated to reflect target gasoline's ignition tendencies and heat release. In detail, blends (by liq. vol.) of (i) 70% $OME_1$ + 30% PRF90 / synthetic air, (ii) 70% $OME_2$ + 30% PRF90 / synthetic air, and of (iii) 70% *iso*-$OME_2$ + 30% PRF90 / synthetic air were all investigated at similar conditions under a wide range of conditions: fuel-air ratio $\varphi$ = 1.0, dilution level of 1:5 with $N_2$, $T$ = 900 − 2000 K, and initial pressures of 1, 4, and 16 bar.

### 4.3.1 The primary reference fuel 90 (PRF90)

#### 4.3.1.1 Ignition delay times – Measured and predicted

In this work, PRF90 (90% *iso*-octane (*i*-$C_8H_{18}$) and 10% *n*-heptane (*n*-$C_7H_{16}$), by liquid volume) was used to represent the gasoline surrogate. The IDTs of PRF90 were measured to provide the baseline for the comparisons with the results obtained for the blends of the three selected OMEs with PRF90; see Table 3.8. The results obtained for PRF90 / synthetic air diluted 1:5 with nitrogen at $\varphi$ = 1.0, pressures of 1 (black squares), 4 (blue circles), and 16 (red stars) bar are presented in Fig. 4.32 together with the model predictions. The measured data exhibit a linear relationship with temperature up to about 1 ms thus following an Arrhenius behavior. After 1 ms, the IDTs deviate from this linear behavior, particularly for elevated pressures of 4 and 16 bar; they are becoming shorter mainly due to larger reactivity induced by the post-shock compression effect as discussed earlier in section 3.9.4. The measured data sets are provided in Appendix J.

The predictions were carried using three reaction models: again, (i) the DLR-Concise model [1] and two models from Lawrence Livermore as published by (ii) Mehl *et al.* [134] and Cheng *et al.* [79]; for more details, see section 3.11.2. The DLR-Concise model (full curves) best matches the temperature and pressure dependency of the experimentally determined values of the ignition delay times, for most of the conditions covered. Mehl's model (dashed curves) overpredicts the measured ignition delay times at 16 bar for temperatures less than 1400 K, with a maximum overprediction of 5% at around 1250 K. The Cheng *et al.* model [79] (dotted curves), on the other hand, overpredicts the measured data at temperatures greater than 1450 K for 1 and 4 bar, with a maximum overprediction

of 6% at 2000 K for 1 bar. To obtain a more comprehensive understanding on oxidatiion of PRF90, the results obtained for sensitivity calculations of PRF90 / synthetic air mixtures have been discussed alongside those of 70% $OME_1$ + 30% PRF90 / synthetic air in section 4.3.2.3. The data obtained for IDTs of PRF90 / synthetic air mixtures diluted with nitrogen in this work are not comparable to published data of Ngugi *et al.* [4] and Richter *et al.* [90] for IDTs of PRF90 / synthetic air mixtures diluted in argon, due to the choice of diluent.

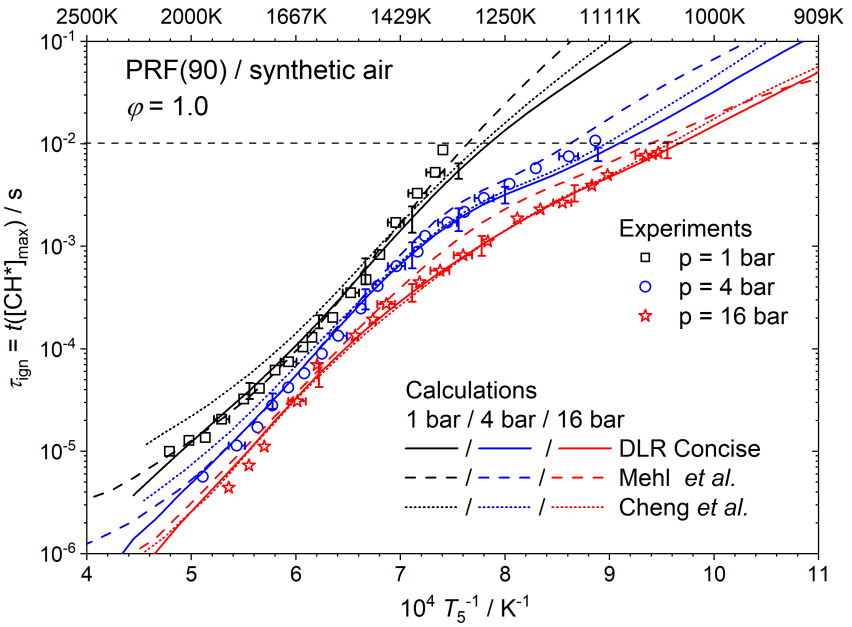


**Figure 4.32:** PRF90 / synthetic air: Comparison of measured data (symbols) and predictions (curves) for $\varphi = 1.0$, $p$ / bar = 1 (squares, black curves), 4 (circles, blue curves), and 16 (stars, red curves); dilution = 1:5 in $N_2$. Models used: (a) DLR-Concise [1] (b) Mehl *et al.* [134], and (c) Cheng *et al.* [79].

### 4.3.1.2 Laminar burning velocities - Measured and predicted

Laminar burning velocities of PRF90 / air mixture were recently measured in our group as a function of equivalence ratio [4, 90]. To enlarge the experimental database when checking the performance of the reaction models used focusing on fundamental combustion properties (ignition delay time as a measure for knocking behavior and laminar burning velocity as a measure for heat release), these data will also be discussed within the frame of this work.

The measured values (symbols) as well as the calculated (curves) are presented in Fig. 4.33, for pressures of 1, 3, and 6 bar and a preheat temperature of $T$ = 473 K. The error bars represent the maximum uncertainties observed during the measurements [4, 90]. The peak values are identified at $\varphi = 1.1$. The calculations were carried out using the DLR-Concise model and Mehl *et al.*'s model

[134]. Calculations employing the mechanism proposed by Cheng *et al.* [79] were not viable due to its inherent stiffness. The calculations using Mehl *et al.* [134] model produce a virtually accurate prediction of the experimental results up to $\varphi \leq 1.5$ at $p = 1$ bar. At higher pressures, the mechanism matches the experimental data up to $\varphi \leq 1.3$ (at 3 bar) and up to $\varphi \leq 1.0$ (at 6 bar), respectively. The obtained LBV data for $\varphi \leq 1.0$ are predicted almost perfectly using the DLR-Concise model [1], within the experimental uncertainty. At higher $\varphi$-values ($\varphi \geq 1.0$), both models underpredict the experimental results for all pressures, to some extent within the uncertainty range, but not for higher pressures and very high $\varphi$-values. However, these larger discrepancies, regardless of the type of fuel, might be ascribed not just to the combustion of a specific fuel as described by the specific reaction model but also to the difficulties in the stabilization of the flames at very fuel-rich mixtures and high pressures; see discussion in section 4.2.6.4.

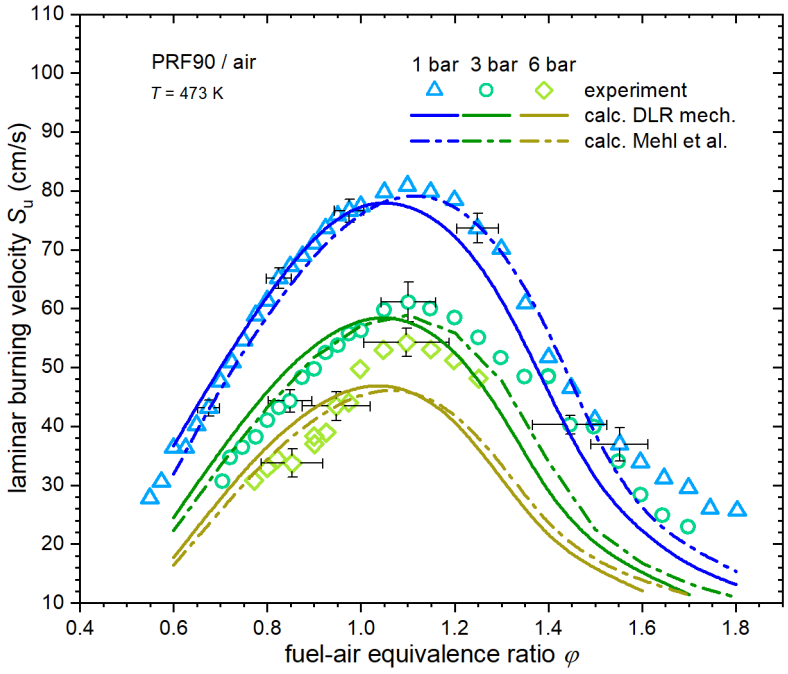


**Figure 4.33:** PRF90 / air mixtures: Measured laminar burning velocities (symbols) and calculated laminar flame speeds (curves), $T = 473$ K, $p$ / bar = 1 (triangles), 3 (circles), and 6 (diamonds). Models used: DLR-Concise – full curves [1] and Mehl *et al.* – dash-dotted curves [134].

.

### 4.3.2 $OME_1$ blended with gasoline surrogate (primary reference fuel 90)

As said earlier, detailed knowledge of fundamental combustion properties – in particular, auto ignition and flame speed – is a prerequisite to enable a reliable and safe operation when using these advanced oxygenated fuels in spark-ignition engines. Therefore, measurements of the ignition delay times of blends of these new fuel molecules in a relevant gasoline surrogate were also done within this work, for similar conditions to allow a meaningful comparison between the data of all the fuels studied.

The objective of this work also was to test the DLR-Concise model's ability to predict the targeted data for the blended fuels, including data of the laminar flame speed. Therefore, the blending ratio must be appropriately selected so that studying the blend would give a clear "kinetic response", *i.e.*, a significant difference with respect to measured ignition delay time data, outside its uncertainty limit. For low blending ratios, say 30% $OME_1$ fraction, the difference in the values of the predicted data and the experimental data might be too small, also when interpreted within the experimental error margin. As a result, a mixture with a high share of the specific fuel – here, 70% $OME_1$ – was selected for measuring the ignition delay times of the blend with the gasoline surrogate, the primary reference fuel 90. Thus, a clear kinetic study necessary for testing a detailed kinetic mechanism will be realized.

#### 4.3.2.1 Ignition delay time – Measured and predicted

Ignition delay times of a blend of 70% $OME_1$ + 30% PRF90 by liquid volume in synthetic air were obtained for $\varphi = 1.0$, a dilution ratio of 1:5 in $N_2$, and at initial pressures of 1, 4, and 16 bar, and in the temperature range between 900 and 2000 K. The measured data (symbols) as determined from the peak emission of excited CH* radicals measured at a wavelength ($\lambda$) of 431 nm, together with the results of calculations (curves) using the DLR-Concise model [1], are shown in Fig. 4.34. The DLR-Concise model [1], in general, matches the temperature and pressure dependency of the blended fuel for all pressures and within the whole temperature range covered. The measured data sets are provided in Appendix K.

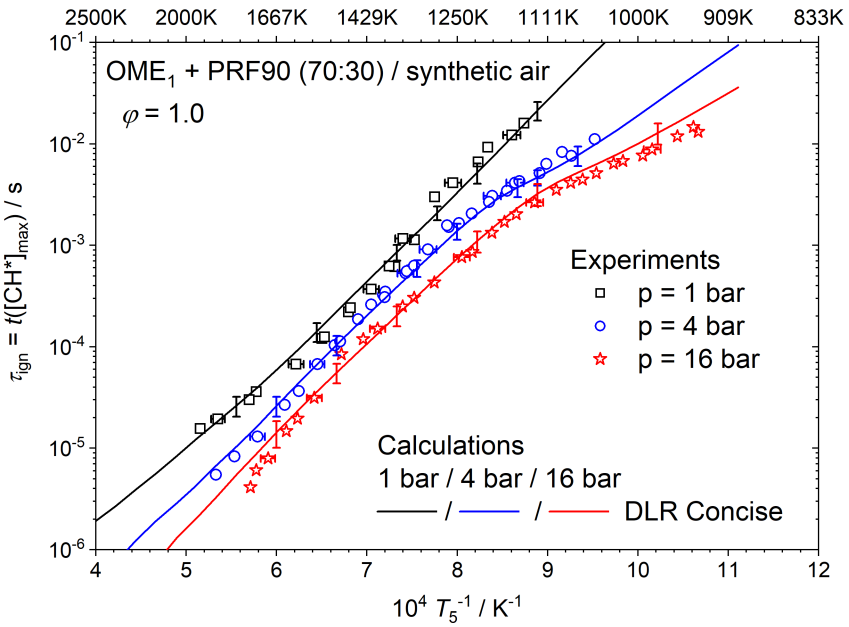


**Figure 4.34:** 70% $OME_1$ + 30% PRF90 / synthetic air mixture: Comparison of measured data (symbols) and predictions (curves) for $\varphi = 1.0$, $p$ / bar = 1 (squares, black curves), 4 (circles, blue curves), and 16 (stars, red curves), and dilution = 1:5 in $N_2$. DLR-Concise model was used [1].

#### 4.3.2.2 Interpreting the effects of $OME_1$ addition to PRF90

To analyze the impact of adding 70% $OME_1$ (by liq. volume) to PRF90 on the IDTs, the results obtained for this blend are compared to those for the neat fuels, $OME_1$ (see Section 4.2.2) and PRF90 (see Section 4.3.1), obtained at similar conditions. Also, a detailed reaction model for a blend should be able to predict the target property, *e.g.*, IDTs for both the blend and the neat fuels the blend is consisting of. Therefore, all experimental data (blend and the individual fuels) are compared to calculations based on the DLR-Concise model [1]. The results of the measurements (symbols) and computations (curves) obtained are shown in Fig. 4.35 for pressures of 1 (a), 4 (b), and 16 (c) bar, respectively. The results demonstrate that adding $OME_1$ accelerates the ignition of PRF90 over the whole temperature regime. In Fig. 4.35, the x-direction error bars represent the uncertainty in temperature due to the error in the incident shock velocity, while the y-direction error bars on the calculated data represent the response of the DLR-Concise model [1] to the error in temperature, as discussed in Section 3.10.2. Considering the uncertainty limits, it is seen that predictions using the DLR-Concise model [1] match the measured data for the blend and the individual fuel components satisfactorily for most of the conditions.

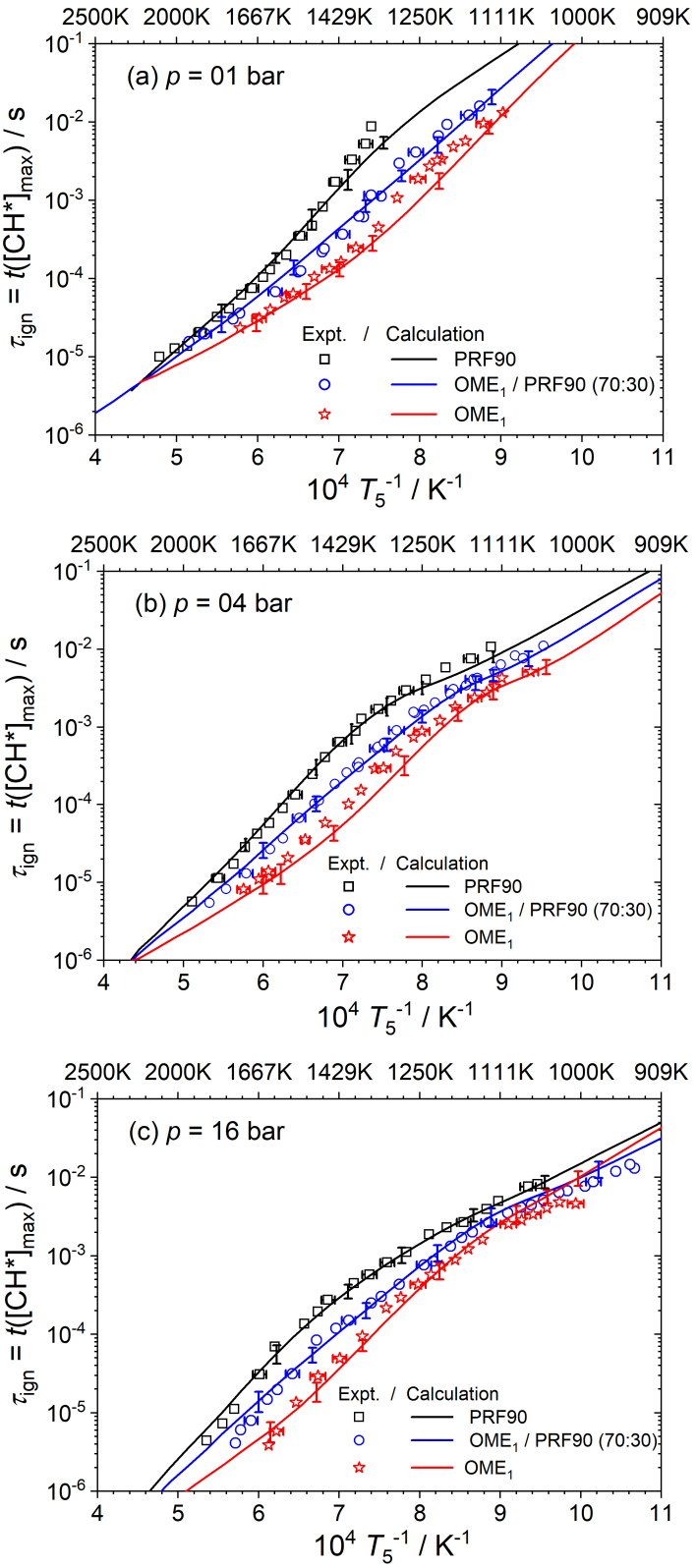


**Figure 4.35:** Comparison of measured data (symbols) and predicted (curves) IDTs of $OME_1$ / synthetic air (stars, red curves), PRF90 / synthetic air (circles, blue curves), and 70% $OME_1$ + 30% PRF90 / synthetic air (squares, black curves) mixtures at $\varphi = 1.0$, dilution = 1:5 in $N_2$, and for $p$ / bar = 1 (a), 4 (b), and 16 (c). The DLR-Concise model was used [1].

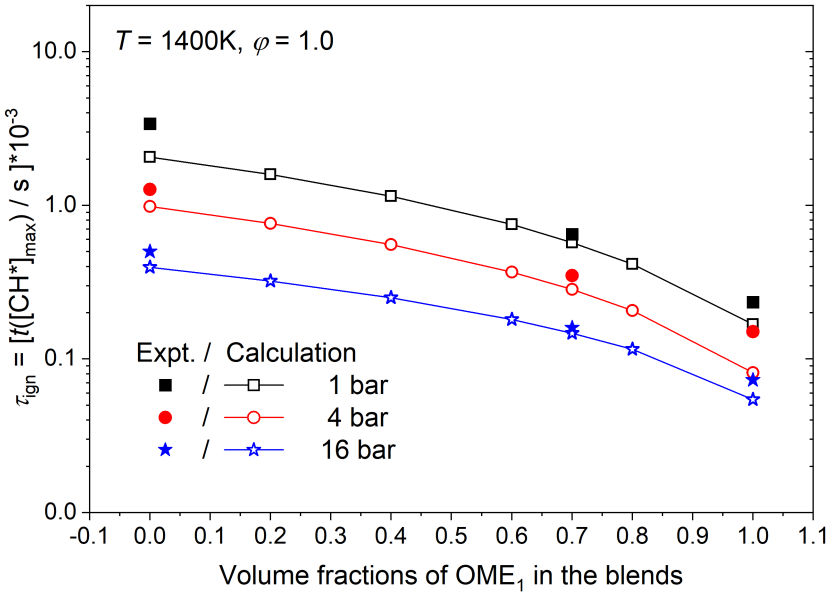


**Figure 4.36:** Ignition delay times (Measured: closed symbols; calculated: open symbols) vs. versus addition fractions (in liq. vol.) of $OME_1$ in the blend at $T$ = 1400 K, $\varphi$ = 1.0, and pressures of 1 (black symbols), 4 (red symbols), and 16 (blue symbols). Closed symbols represent the experimental data points. The DLR-Concise model was used [1].

Figure 4.36 depicts the effect of increasing the $OME_1$ addition fraction on the ignition delay times of the mixture at 1400 K for 1, 4, and 16 bar. The experimental data points (closed symbols) are provided for 0%, 70%, and 100% $OME_1$ fraction (in liq. vol.) in the blend. The open symbols data points presented in Fig. 4.36 – indicating the addition fraction from 0 to 100% with a 20% step width – were computed using the DLR-Concise model [1]. Figure 4.36 shows that at all pressures, increasing the volume percent of $OME_1$ reduces the blend's ignition delay times, for instance, by roughly 70% for a 70% $OME_1$ fraction (in liq. vol.) in the blend. This suggests that $OME_1$ promotes PRF90 ignition. Additionally, independent of pressure, the trends shown in the measured and computed data show that increasing the volume percent of $OME_1$ in the blend decreases ignition delay times in a weakly non-linear fashion. It is observed that the promoting effect on the IDTs of the blend is weak for $OME_1$ addition fractions of up to 50%. The IDTs reduction is stronger for blends with over 50% $OME_1$ blending fractions.

#### 4.3.2.3 Ignition delay times - Sensitivity analysis

Sensitivity calculations of the ignition delay times for mixtures of fuel / synthetic air, with fuel = $OME_1$, PRF90, and $OME_1$ / PRF90 (70:30), were calculated using the DLR-Concise model [1] at $\varphi$ = 1.0, a dilution of 1:5 with $N_2$, and a temperature of 1200 K for pressures of 1, 4, and 16 bar. The sensitivity coefficient is as defined in Section 3.6. Again, the peak of $CH^*$ emission was chosen

as an indicator of ignition.

The results, sorted according to the most sensitive reactions identified for the 4 bar measurements, are shown in Fig. 4.37 depicting the 12 most significant reactions. As is true for practically all hydrocarbon systems, the chain branching reaction $H+O_2 \rightleftharpoons O + OH$ is the most sensitive for all of three combustible mixtures. Further chain propagation reactions enhance $OME_1$ ignition: $CH_3+HO_2 \rightleftharpoons CH_3O+OH$ and $H_2 + OH \rightleftharpoons H_2O + H$. Furthermore, it is demonstrated that reactions involving formaldehyde $CH_2O$, an important intermediate in the oxidation of oxymethylene ethers, enhance the ignition via the reactions: $CH_2O + HO_2 \rightleftharpoons HCO + H_2O_2$ and $CH_2O + O \rightleftharpoons HCO + H_2O$, due to the quick decay of HCO leading to H radicals. The fuel-specific reaction $OME_1 \rightleftharpoons CH_2OCH_3 + CH_3O$ also promotes $OME_1$ ignition. The successive $\beta$-decomposition of the $CH_2OCH_3$ radical yields $CH_3$ radicals and $CH_2O$. On the other hand, methoxy $CH_3O$ radicals promote the building up of the radical pool and hence, accelerate ignition, for example, through $CH_3O + H \rightleftharpoons CH_3 + OH$, $CH_3O + O_2 \rightleftharpoons CH_2O + HO_2$, and $CH_3O + O \rightleftharpoons CH_2O + OH$. The reactions $CH_3 + H(+M) \rightleftharpoons CH_4 (+M)$ and $HO_2 + OH \rightleftharpoons H_2O + O_2$ are the major inhibitors of $OME_1$ ignition, with transforming two radicals into stable molecules.

Ignition of PRF90 is enhanced in addition to the chain branching reaction $H + O_2 \rightleftharpoons O + OH$ by the chain propagation reaction $CH_3 + HO_2 \rightleftharpoons CH_3O + OH$, which has the second highest sensitivity, and reactions involving $C_2$-$C_3$ hydrocarbons, such as $C_2H_4$, $C_2H_3$, $C_3H_5$, and $C_3H_6$. PRF90 ignition is mostly hindered by $HCO + M \rightleftharpoons CO + H + M$ and $C_3H_5 + H (+M) \rightleftharpoons C_3H_6 (+M)$ reactions.

For the $OME_1$ / PRF90 blend – in addition to the chain branching reaction $H + O_2 \rightleftharpoons O + OH$ – ignition is promoted by the chain propagating reaction $CH_3 + HO_2 \rightleftharpoons CH_3O + OH$ as well as by the fuel-specific reaction $OME_1 \rightleftharpoons CH_2OCH_3 + CH_3O$ which leads to chain branching by generating $CH_2OCH_3$ and $CH_3O$ radicals. This reaction accelerates the ignition process by producing $CH_2OCH_3$ and $CH_3O$ radicals, which are the major initial source of radicals as explained for $OME_1$. Moreover, ignition of $OME_1$ / PRF90 is favored by reactions of $C_2H_4$ and $C_2H_3$, respectively with $O_2$ and OH radicals.

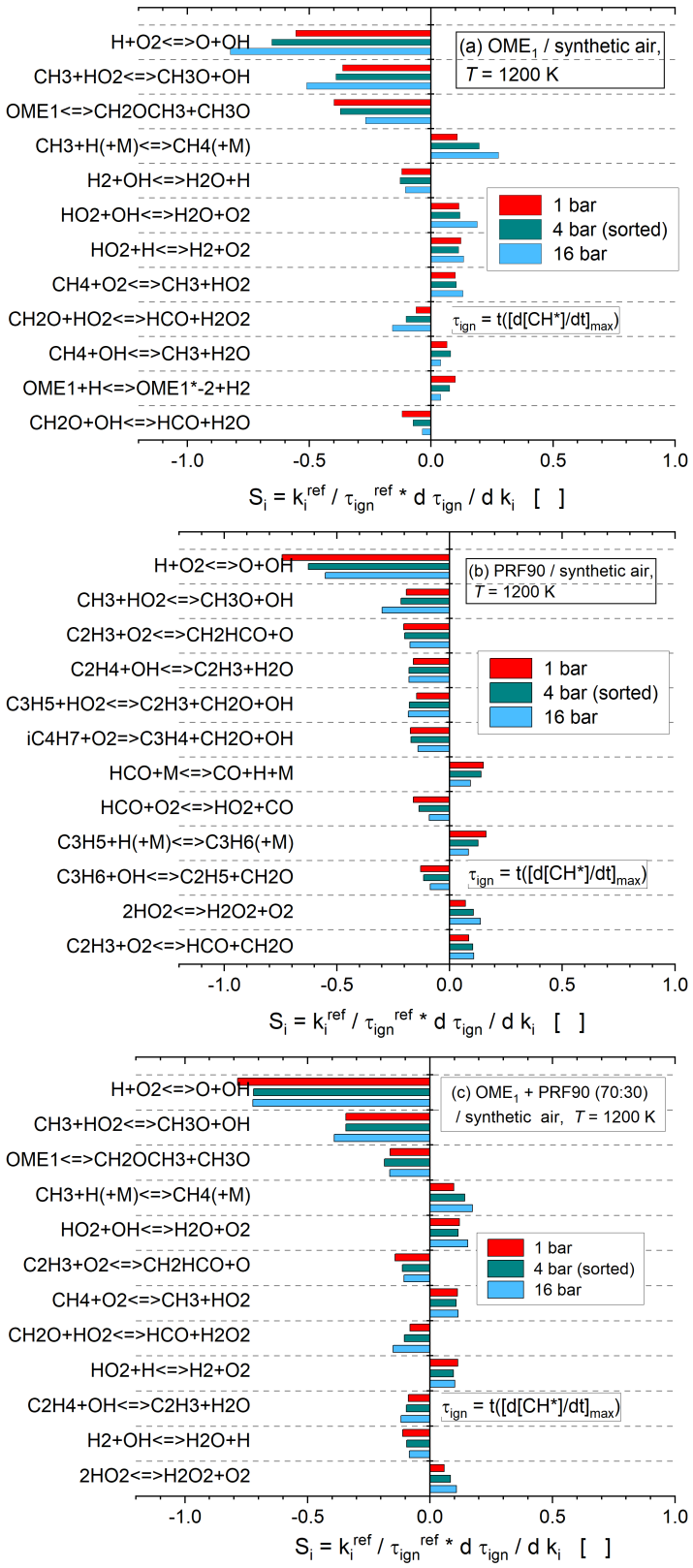


**Figure 4.37:** IDT sensitivity coefficients for (a) $OME_1$ / synthetic air, (b) PRF90 / synthetic air, and (c) $OME_1$ + PRF90 (70:30) / synthetic air at $\varphi = 1.0$, $p$ / bar = 1 (red), 3 (green), and 6 (cyan) at $T = 1200$ K, and dilution = 1:5 with $N_2$. The DLR-Concise reaction model used [1].

#### 4.3.2.4 Rate of production analysis

According to the sensitivity analysis results, the relative contribution of the chain propagation reaction $CH_3 + HO_2 \rightleftharpoons CH_3O + OH$ is increasing with the addition of $OME_1$. This reaction elevates the system's reactivity by providing more reactive OH radicals as well as H radicals formed by the decomposition of the less reactive methoxy ($CH_3O$) radicals. For this reason, a rate of production analysis for $CH_2O$ and $HO_2$ radicals is done to assess the influence of $OME_1$ addition on the relevance of this reaction. The findings shown in Fig. 4.38 reveal that the $CH_2O$ radical is mostly produced by processes involving $CH_3O$, $CH_2OCH_3$, and $OME_1$*1 (the primary fuel radical - $CH_3OCH_2OCH_2$ (COCOC*)) radicals produced in the breakdown of the fuel. Furthermore, it is demonstrated that $CH_2O$ is mostly consumed by H-abstraction reactions that produce HCO radicals, which is the primary source of $HO_2$ radicals. As a result, the concentrations of $CH_2O$, HCO, and $HO_2$ are proportional to the quantity of $OME_1$ fraction in the blend. Because of the high concentration of $HO_2$ radicals, the oxidation of $CH_3$ radicals is preferable via the reaction $CH_3 + HO_2 \rightleftharpoons CH_3O + OH$ and not via other competing reactions with O and $O_2$ involved. Consequently, as seen in Fig. 4.37, the relative relevance of this response is growing with increasing $OME_1$ blending.

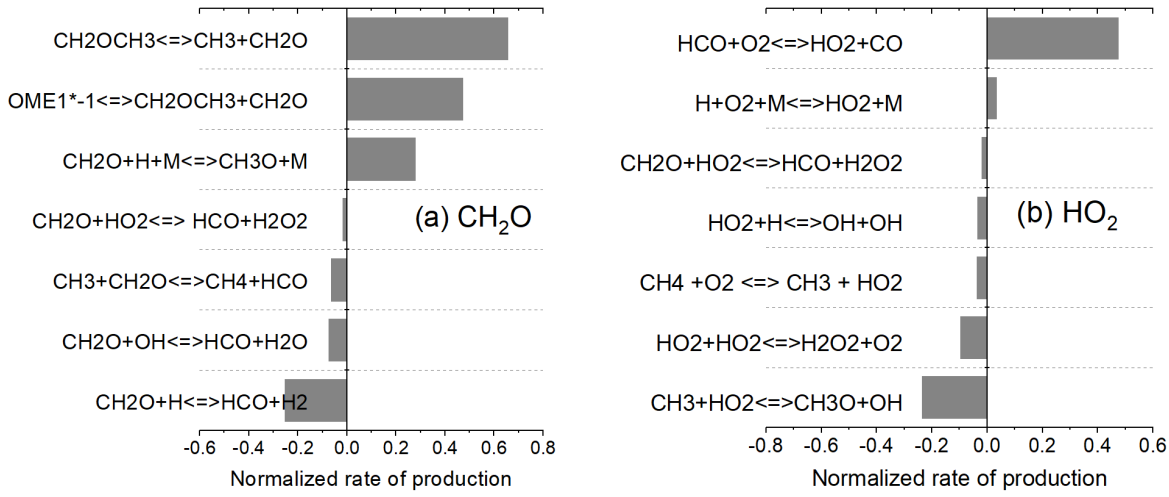


**Figure 4.38:** Rate of production (ROP) analysis of $CH_2O$ (a) and $HO_2$ (b) radicals during the ignition of $OME_1$ / synthetic air mixture at $\varphi = 1.0$, $T = 1200$ K, $p = 4$ bar, and dilution = 1:5 with $N_2$ calculated at 20% fuel consumption. The DLR-Concise model was used [1]. $OME_1$*-1 represents the primary fuel radical $CH_3OCH_2OCH_2$ (COCOC*)

.

#### 4.3.2.5 Radical profiles analysis

The results of the sensitivity analysis discussed indicate that reactions involving small radicals such as O, OH, H, $HO_2$, and $CH_3$ play a huge role in the ignition process. To evaluate further the influence of $OME_1$ blending to gasoline surrogate (PRF90) on ignition delay times as predicted by the DLR-Concise model [1], the evolution of these radicals is analyzed during ignition $OME_1$, $OME_1$ / PRF90 (70:30), and PRF90 – all mixed with synthetic air and diluted 1:5 with $N_2$, and $\varphi = 1.0$. Additionally, HCO and $CH_2O$ are considered because they are crucial intermediary species observed in the ignition process of OMEs, as illustrated above by the sensitivity analysis results. The results achieved for an equivalence ratio $\varphi = 1.0$, a pressure of 16 bar, at a temperature of 1300 K and a dilution of 1:5 in $N_2$ are given in Fig. 4.39. It is shown that the peak concentrations of O, OH, and H radicals increase dramatically at roughly 0.2, 0.4, and 0.9 ms for $OME_1$, $OME_1$ / PRF90, and PRF90, respectively, indicating the commencement of ignition. However, the concentrations of $CH_2O$, $CH_3$, $HO_2$, and HCO fall dramatically within this phase; thus, showing that they are crucial species for the radical pool's build-up during the pre-ignition period. The inclusion of $OME_1$ raises the peak concentration of all radicals. As the concentration of these radicals grows, so does the system's reactivity; hence, ignition delay times decrease.

#### 4.3.2.6 Laminar burning velocities - Measured and predicted

The results of the measured laminar burning velocities of $OME_1$, PRF90, and 30% $OME_1$ + 70% PRF90, each in a mixture with air at an initial temperature of 473 K, as a function of equivalence ratio, are presented in Fig. 4.40a for pressures of 1 (triangles), 3 (circles), and 6 (diamonds) bar. Again, these experiments were recently done within our group; see ref. [4]. The error bars given are quite high at high pressures and very high fuel-air ratios, as discussed in [4], too. The peak value of LBVs of $OME_1$, PRF90, and 30% $OME_1$ + 70% PRF90 are observed at the equivalence ratios of $\varphi = 1.2$, 1.1, and 1.1, respectively. It is seen that the LBVs of $OME_1$ are higher than those of the blend and PRF90 for all pressures, particularly for equivalence ratios larger than $\varphi = 0.9$. In general, the decomposition and oxidation of saturated hydrocarbons reveal a lower reactivity than $OME_n$ explaining the lower values of the LBVs obtained for PRF90. Regarding the effects of blending, the experimental data suggest that adding 30% $OME_1$ to PRF90 results in higher LBVs, notably for $\varphi \leq 1.0$ by approximately 10% at 1 and 3 bar and 20% at 6 bar – compared to those of the neat PRF90. At $\varphi \geq 1.1$, the blend's LBVs are almost identical to those of the gasoline surrogate (PRF90), at all the pressures.

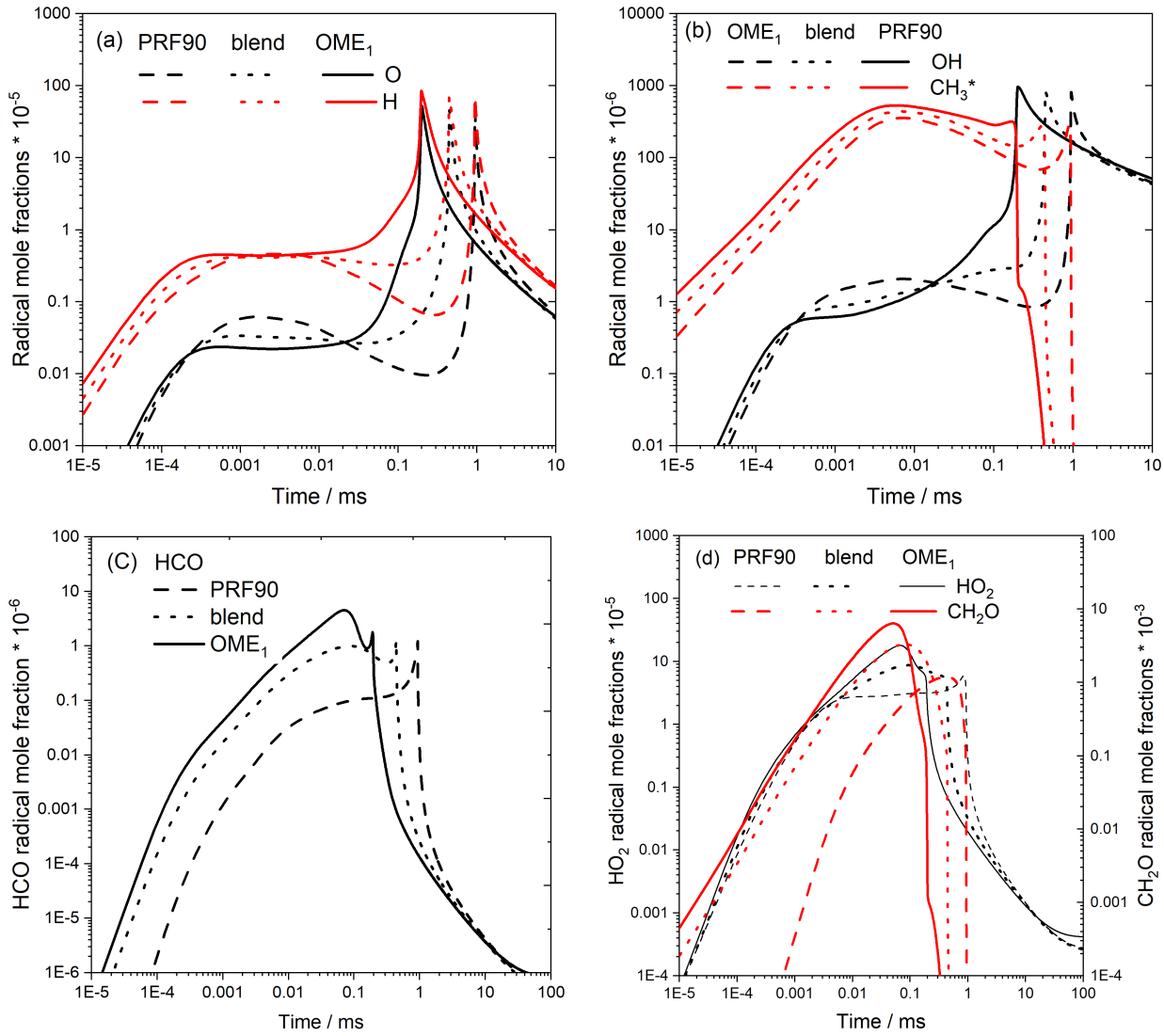


**Figure 4.39:** Mole fractions profiles of O, H (a); OH, $CH_3$ (b); HCO (c), and $HO_2$, $CH_2O$ (d) for three mixtures: $OME_1$ (full curve), $OME_1$ / PRF90 (70:30) blend (dotted curve), and PRF90 (dashed curve); for $\varphi = 1.0$, $T = 1300$ K, $p = 16$ bar, and dilution = 1:5 with $N_2$. The DLR-Concise model was used [1].

In Fig. 4.40, the measured and predicted data for $OME_1$(b), 30% $OME_1$ + 70% PRF90 (c), and PRF90 (d) are compared. Calculations were performed using the DLR-Concise model [1] for all the fuels. Additionally, the models of Cai *et al.*[7] and Mehl *et al.* [134] have been applied respectively to $OME_1$ and PRF90, as discussed respectively in sections 4.2.3 and 4.3.1.2. The results presented in Fig. 4.40c show that the DLR-Concise model [1] predicts better the measured laminar burning velocities for the blend compared to the ones for pure $OME_1$ (see Fig. 4.40b) or PRF90 (see Fig. 4.40d). As presented in Fig. 4.40c, the DLR-Concise model [1] matches the experimental data for the blend up to $\varphi \leq 1.4$ at 1 and 3 bar, and up to $\varphi \leq 1.2$ at 6 bar, within experimental uncertainty. At very fuel-rich mixtures, the DLR-Concise model [1] underpredicts the experimental data, particularly

at elevated (3 and 6 bar), for example, by up to 30% at $\varphi$ = ~ 1.4 at 6 bar. Independent of the fuel, larger deviations observed in the fuel-rich regime may be attributed not only to the mechanisms but also to the difficult flame stabilization of fuel-rich mixtures, see discussion in section 4.2.6.4.

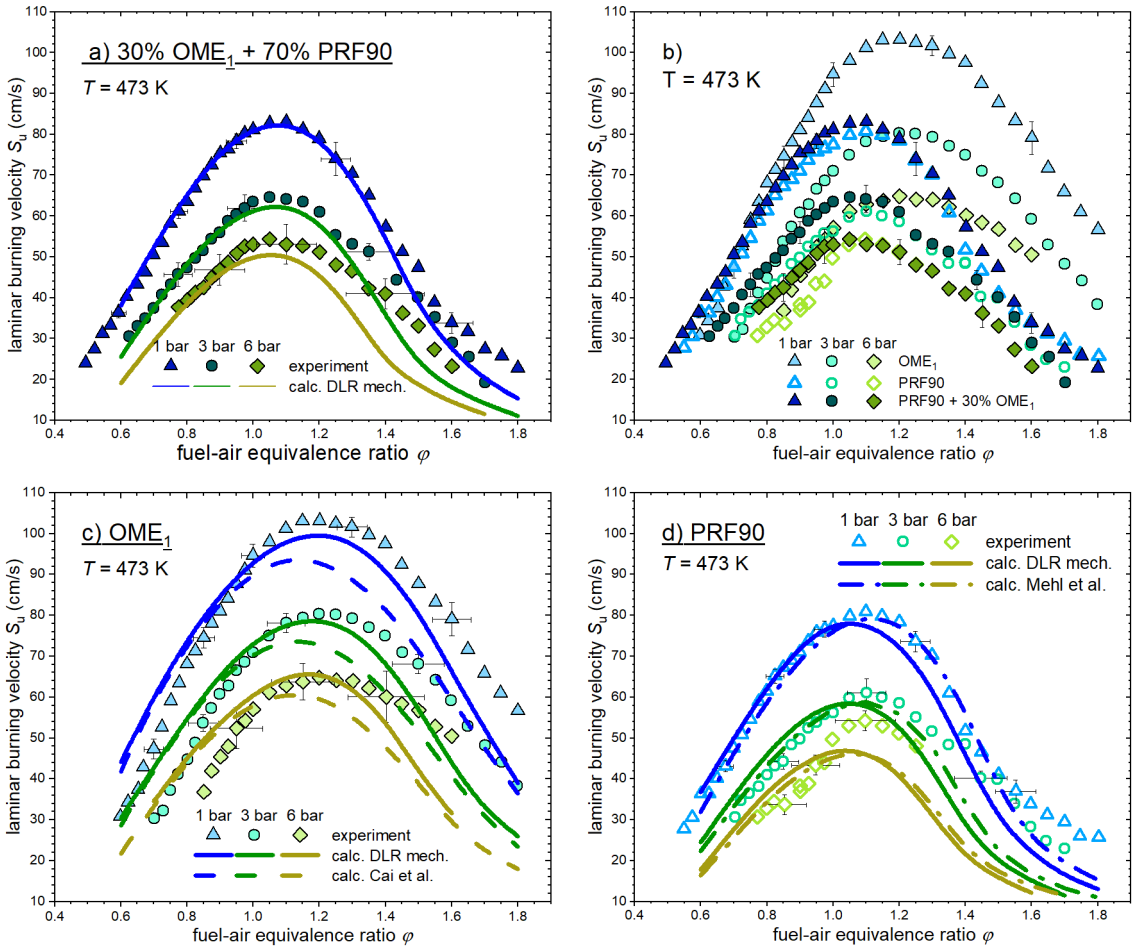


**Figure 4.40:** Results of the measured laminar burning velocities at $T$ = 473 K of PRF90 / air, neat $OME_1$ / air, and 30%$OME_1$ + 70% PRF90 / air: (a) Comparison between the experimental data and the calculated laminar flame speeds for 1 bar (b), 3 bar (c), and 6 bar (d). Models used: Cai *et al.*[7] for $OME_1$, Mehl *et al.* [134] for PRF90, and DLR-Concise model [1] for $OME_1$, PRF90, and $OME_1$ / PRF90 blend.

### 4.3.3 $OME_2$ and *iso*-$OME_2$ blended with gasoline surrogate (PRF90)

#### 4.3.3.1 Ignition delay times - Experiment and modeling

The results of measured (symbols) and calculated (curves) ignition delay times of the two stoichiometric mixtures of 70% $OME_2$ + 30% PRF90 / synthetic air and 70% *iso*-$OME_2$ + 30% PRF90 / synthetic air, respectively – both blends diluted 1:5 with nitrogen for a pressure of 4 bar and temperature range between 900 and 2000 K – are presented in Fig. 4.41 and 4.42, respectively. The calculations were carried out using the DLR-Concise model [1]. Again, they have been compared to those of the neat fuels obtained under comparable conditions as discussed above for $OME_1$ / PRF90 blends.

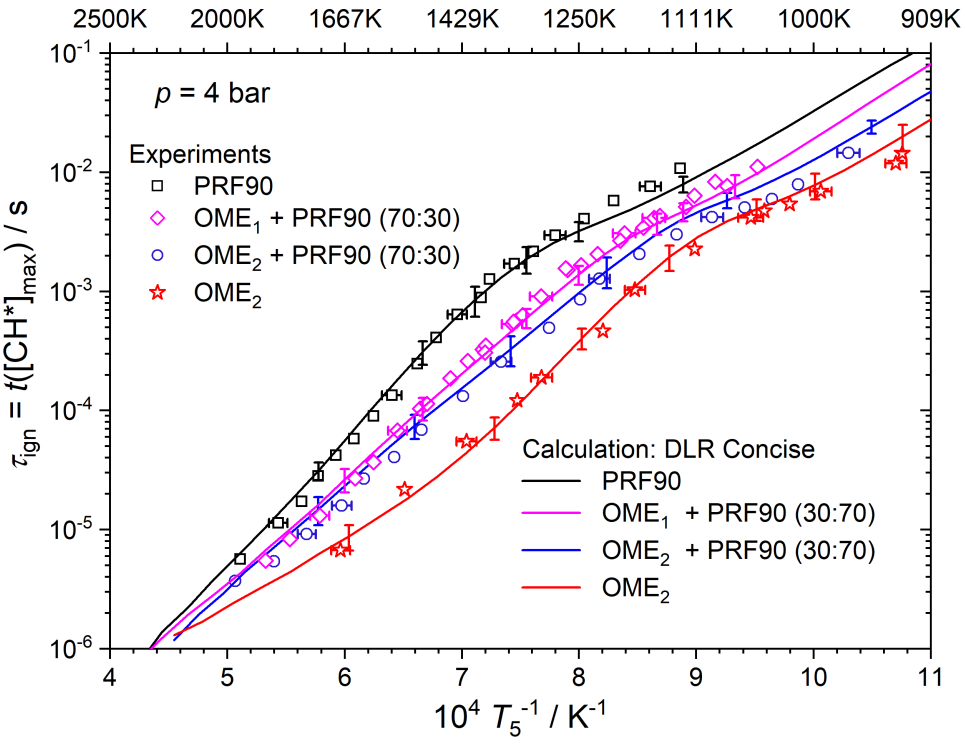


**Figure 4.41:** Comparison of measured (symbols) and predicted (curves) ignition delay times of mixtures of fuel / synthetic air with fuel = PRF90 (squares, black curve), $OME_2$ (stars, red curve), 70%$OME_2$ + 30% PRF90 (circles, blue curve), and 70% $OME_1$ + 30% PRF90 (diamonds, magenta curve) – all diluted 1:5 with $N_2$ at $\varphi$ = 1.0, initial pressure of 4 bar. The DLR-Concise model was used [1].

The results demonstrate that the addition of $OME_2$ as well as of *iso*-$OME_2$ results in shorter IDTs over the entire temperature regime. Fig. 4.41 shows the results obtained for $OME_1$ blending (magenta diamonds) at comparable conditions are also shown. Above 1450 K, the IDTs of $OME_2$ / PRF90 and $OME_1$ / PRF90 blends are essentially identical. Below 1400 K, it has been demonstrated that the

$OME_2$ / PRF90 blend is more reactive; and consequently, has a greater promoting impact on PRF90. For example, at 1250 K, the measured ignition delay times of blended fuels are shorter by 60% for $OME_1$ / PRF90 (cyan circles) and 80% for $OME_2$ / PRF90 (blue circles) compared to measured data for PRF90 (black squares).

In Fig. 4.42, the measured data for $OME_2$ / PRF90 (full-blue circles) at comparable conditions are also shown. In the entire temperature regime, the ignition delay times of $OME_2$ / PRF90 and iso-$OME_2$ / PRF90 are similar, and thus have similar promoting effects on PRF90. Similarly, the measured ignition delay times of neat $OME_2$ and *iso*-$OME_2$ are similar in the entire temperature regime for 1, 4, and 16 bar; for more details, see section 4.2.6. The comparison of measured and predicted data in Figs. 4.41 and 4.42 demonstrates that, within experimental uncertainty, predictions using the in-house DLR-Concise model [1] are close to the measured data for both the neat fuels and the blended fuel within the experimental uncertainty.

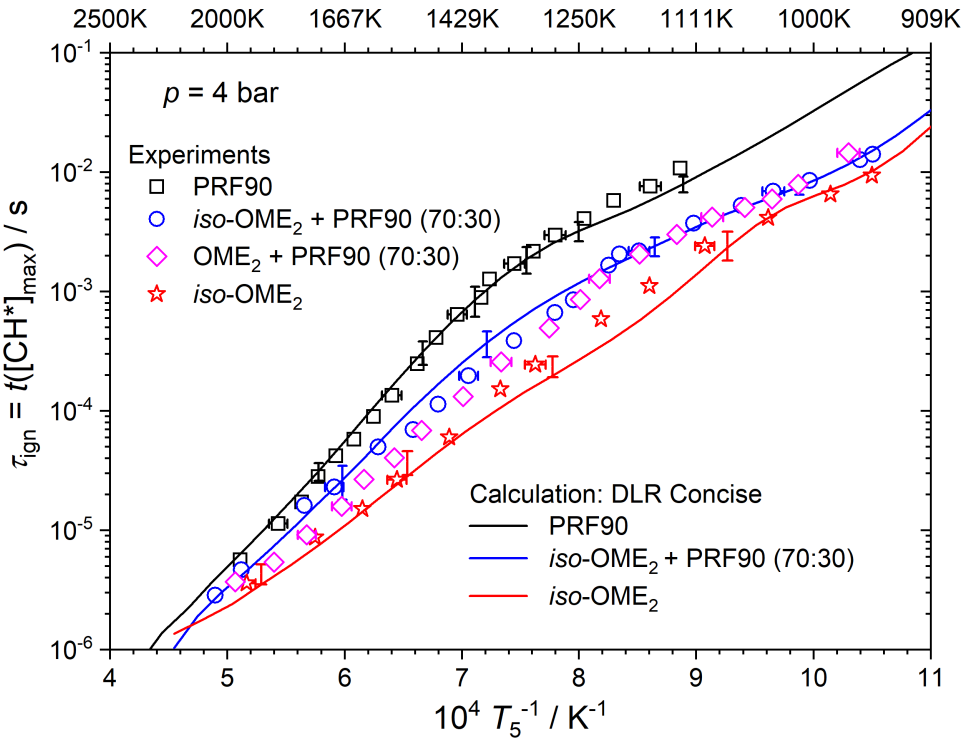


**Figure 4.42:** Comparison of measured (symbols) and predicted (curves) ignition delay times of mixtures of fuel / synthetic air with fuel = PRF90 (squares, black curve), *iso*-$OME_2$ (stars, red curve), 70% *iso*-$OME_2$ + 30% PRF90 (circles, blue curve), and 70% $OME_2$ + 30% PRF90 (diamonds) – all diluted 1:5 with $N_2$ at $\varphi$ = 1.0, initial pressure of 4 bar. The DLR-Concise model was used [1].

The results obtained here for $OME_1$ / PRF90 and $OME_2$ / PRF90 (Fig. 4.41) as well as for

iso-$OME_2$ / PRF90 (Fig. 4.42) – including also the measured and predicted ignition delay time data for the relevant neat fuels as discussed in section 4.2 – reveal that, within experimental uncertainties, the DLR-Concise model performs best for PRF90 and least for the neat fuels $OME_1$, $OME_2$, and TMOF. It is interesting to note that this attribute is also evident in the data obtained for laminar burning velocities of neat $OME_1$ (Fig. 4.11), PRF90 (Fig. 4.33), and $OME_1$ / PRF90 (Fig. 4.40) as reported in [2–5]. One reason is the fact that the chemical kinetic sub-models of *iso*-octane and *n*-heptane, as well as the $C_0$-$C_2$-chemistry, are well-studied and validated within the model. On the other hand, the chemistry of OMEs is still in its early stages, and the reaction models available have been developed based on limited experimental data both in the type of validation-target and range of parameters.

# 5 Summary and outlook

The current study was conducted to create a larger database of ignition delay times (IDTs) of oxymethylene ethers (OMEs) since these oxygenated molecules are sustainable fuels and attractive alternative fuels due to their ability to suppress the formation of soot particles. Shock tube experiments were conducted to determine the IDTs of stoichiometric mixtures of DME ($OME_0$) / synthetic air, $OME_1$ / synthetic air, $OME_2$ / synthetic air, and $OME_4$ / synthetic air mixtures – all at pressures of 1, 4, and 16 bar, dilution level of 1:5 with nitrogen, and in the temperature range $T$ = 800-2000 K. The measured IDT data are compared to the results of calculations using the in-house DLR-Concise model [1] and other public domain models. Furthermore, the ignition delay times data obtained in this work are supplemented with corresponding results for measured laminar burning velocities (LBVs) [2–6] determined at initial temperatures of $T$ = 473 K, pressures of 1, 3, and 6 bar, and $\varphi$-values ranging from 0.6 to 1.8, thereby expanding the experimental database for testing the reaction models' predictions.

To understand the effect of an increase in (-$CH_2O$-) units on the reactivity of oxymethylene ethers, the data for IDTs and LBVs of DME ($OME_0$), $OME_1$, $OME_2$, and $OME_4$ obtained at similar conditions have been compared. The measured IDT data are longest for DME and shortest for $OME_4$. Thus, the reactivity of OMEs increases with an increase in chain length. This finding is consistent with the measured LBVs which are highest for $OME_4$ and lowest for $OME_1$. The peak values of LBVs of $OME_1$, $OME_2$ and $OME_4$, regardless of pressure, were observed at a $\varphi$–value of 1.2. The measured data for IDTs of $OME_2$ are close to those of $OME_4$, particularly at elevated pressures of 4 and 16 bar, indicating that for OMEs, the increase in reactivity is weakening as the chain length increases. Similarly, the measured LBVs of $OME_2$ and $OME_4$ are close for $\varphi \leq 1.0$. Interestingly, at all pressures, the measured LBVs of $OME_2$ converge to those of $OME_4$ for $\varphi \leq 1.0$ and those of $OME_1$ for $\varphi \geq 1.25$. The measured IDT data obtained for $OME_2$ / synthetic air and $OME_4$ / synthetic air mixtures showed that $OME_2$ and $OME_4$ exhibit pre-ignition phenomenon at temperatures lower than 1100 K at 4 and 16 bar. This was demonstrated by an increase in OH* and CH* before the main-ignition.

Ignition delay times of *iso*-$OME_2$ / synthetic air mixtures were also measured since this molecule is a viable sustainable owing to similarities to $OME_2$. The comparison of the measured IDTs of *iso*-$OME_2$ and $OME_2$ obtained at similar conditions showed that the two fuels have similar IDTs within the experimental uncertainity at all the conditions considered. Laminar burning velocities of *iso*-$OME_2$ were obtained at an initial temperature of 473 K, pressures of 1, 3, and 6 bar, and for fuel-air ratios in the range between 0.6 and 1.8 [3]. For all pressures, the peak LBVs were

observed at $\varphi = 1.1$. The laminar burning velocities of *iso*-$OME_2$ and $OME_2$ obtained under similar conditions were compared, with the results showing that the LBVs of the two fuels are fairly equal for stoichiometric and fuel-lean mixtures ($\varphi \leq 1.0$), as seen for IDTs. On the other hand, for fuel-rich ($\varphi > 1.0$) mixtures, LBVs of $OME_2$ are higher than those of *iso*-$OME_2$. The results obtained here, particularly for $\varphi > 1.0$, confirm that branching reduces reactivity as is true for conventional hydrocarbon fuels.

In addition, since OMEs are discussed as suitable alternatives and blending compounds for fossil-based fuels, the effect of the addition of $OME_1$, $OME_2$, and *iso*-$OME_2$ to a gasoline surrogate, the primary reference fuel 90 (PRF90: 90% *iso*-octane + 10% *n*-heptane by liquid vol.) on IDTs was investigated. In detail, ignition delay times at $\varphi = 1.0$, dilution level of 1:5 with $N_2$ were determined for blends (by liq. vol.) of 70% $OME_1$ + 30% PRF90 / synthetic air at 1, 4, and 16 bar, 70% $OME_2$ + 30% PRF90 / synthetic air at 4 bar, and 70% *iso*-$OME_2$ + 30% PRF90 / synthetic air at 4 bar. IDTs of PRF90 / synthetic air mixture were also determined at similar conditions to give the baseline for comparison. The data sets obtained for the blended fuels have been compared to those of the pure OMEs ($OME_1$, $OME_2$, and *iso*-$OME_2$) and PRF90 at similar conditions. The IDTs for the blended fuels were shorter than those of PRF90 and longer than those of the pure fuels, thus indicating that the addition of OMEs increases PRF90's reactivity. This is consistent to the results of the LBVs that were higher for the $OME_1$ / PRF90 blend compared to those of PRF90 [4].

To interpret the experimental findings and to discuss the performance of detailed chemical kinetic models, the measured IDT data have been compared to the results of calculations using the DLR-Concise model [1] and other public domain models taken from the literature. For DME ($OME_0$) / synthetic air, the Polimi v1412 [133] reaction model best reproduces the temperature and pressure dependencies for the mid- to high-temperature domain between 1000 and 1700 K. Predictions using the DLR-Concise [1], Cai *et al.* [7], and Aramco v3.0 [132] models, on the other hand, overpredict the measured data above 1400 K for 4 and 16 bar. For $OME_1$ / synthetic air mixture, the measured data is matched by DLR-Concise [1], Cai *et al.* [7], and Hu *et al.* [65] models. For $OME_2$ / synthetic air and $OME_4$ / synthetic air mixtures, the DLR-Concise [1], Cai *et al.* [7], and Niu *et al.* [8] models matched the measured data for the main-ignition of the two fuels for all the conditions considered. Further, the models of Cai *et al* [7]. and Niu *et al* [8]. reproduced the pre-ignition behavior as observed in the measurements and acceptably matched the measured pre-ignition times. The pre-ignition phenomenon was kinetically characterized using the model of Cai *et al.* [7] with the results showing that the pre-ignition feature is a consequence of the low-temperature chemistry. The results of the kinetic analysis also showed that the decomposition of $OME_2$ and $OME_4$ yields high concentrations of formaldehyde ($CH_2O$) and hydrogen peroxide

($H_2O_2$), which then subsequently break down into OH* radicals. The reactions of OH radicals with other intermediates, *e.g.*, with $CH_2O$, produce high concentrations of CO, hence the pre-ignition heat release. The heat release at the main ignition regime is mainly due to the oxidation of CO to $CO_2$. For *iso*-$OME_2$, calculations with the DLR-Concise model [1] matched the measured data for temperatures above 1250 K. Below 1250 K, the model deviates from the measured data with a maximum deviation of about 70% at 1200 K and 900 K, respectively at 1 and 16 bar. This deviation is attributed to insufficient validation of the DLR-Concise model [1] for the *iso*-$OME_2$ chemistry. *Iso*-$OME_2$ oxidation chemistry is still in its early stages, and the DLR-Concise Model [1] chemistry is based on limited experiments and reaction kinetic rate data.

The results of LBVs of $OME_1$ / air [2], $OME_2$ / air [3], and $OME_4$ / air [6] mixtures obtained at pressures of 1, 3, and 6 bars and in the $\varphi$-range between 0.6 and 1.8 have compared to the results of calculations using different reaction models. For $OME_1$, the DLR-Concise model [1] is closest to the measured data at 1 bar. For all the pressures., both the DLR-Concise [1] and the Cai *et al.* [7] models underpredict the measured values for $\varphi$-values ranging from 1.0-1.8, and overpredict the measured values at $\varphi \leq 1.0$. In the fuel-rich domain ($1.0 \leq \varphi \leq 1.8$), the deviation is higher for the Cai *et al.* [7] model. For $OME_2$, the DLR-Concise model matches measured LBVs with a slight overprediction on the fuel lean-side. On the other hand, the model of Cai *et al.* [7] matches the measured data only for fuel-lean mixtures. For $OME_4$, the calculations with both the DLR-Concise model [1] and the Cai *et al.* [7] model underpredict the measured values in the entire $\varphi$-regime, with large differences in the fuel-rich regime. The results obtained for LBVs of *iso*-$OME_2$ are compared to calculations using the DLR-Concise model [1]. The results obtained show that the DLR-Concise model [1] overpredicts the measured values for nearly the entire $\varphi$-values covered and for all pressures. The large discrepancy between measured and calculated laminar flame speed values using all models is attributed to insufficient validation, notably regarding LBVs data. Also, the model of Cai *et al.* [7] has been tuned for IDTs.

The measured data for IDTs of fuel blends ($OME_1$ / PRF90, $OME_2$ / PRF90, and *iso*-$OME_2$ / PRF90) have been compared to calculations using the DLR-Concise model [1]. The results show that the DLR-Concise model [1] satisfactorily matches the measured data for IDTs of the fuel blends within experimental uncertainity despite the model having been validated separately with respect to PRFs and OMEs. The model also matches the LBVs of $OME_1$ / PRF90 blend, $OME_1$, and PRF90. The results of sensitivity and radical mole fraction analyses using the DLR-Concise model [1] showed that the addition of $OME_1$ and thus OMEs to PRF90 increases reactivity of the system by promoting the build-up of radicals early during the oxidation process.

In conclusion, the current study has generated a large experimental data sets of IDTs and LBVs

for oxymethylene ethers (DME ($OME_0$), $OME_1$, $OME_2$, and $OME_4$) for testing reaction models with the goal of providing validation data as well as highlighting possible areas for improvement. The measured data have been compared with predictions made with the DLR-Concise model [1] and other public domain models taken from the literature. Satisfactorily good agreement is seen between measured and calculated ignition delay times using all the models. While for laminar burning velocities, major discrepancies are observed between the measured and calculated data for most of the fuels and conditions investigated. Further enhancement, including low-temperature chemistry extension and validation also at technologically relevant conditions (of high pressures), is an ongoing subject for the DLR-Concise model [1]. To enhance the development of accurate chemical-kinetic models for OMEs, the validation targets, *e.g.*, species profiles and IDTs measurement should be extended to cover more conditions. Further work on direct measurement of reaction rates (kinetic rate data) is warranted for enhancement of the models as this has not been explored.

This study also provided a large number of experimental data sets for IDTs of blends of $OME_1$, $OME_2$, and *iso*-$OME_2$ with a gasoline surrogate (PRF90), as well as for the laminar burning velocities of a blend of PRF90 with $OME_1$; this large data base serves for testing and further optimizing chemical-kinetic reaction models, such as the DLR-Concise model [1]. The results obtained showed that OMEs are reactive and thus greatly contribute to the production of radicals and intermediates earlier in the oxidation process. Thus, when OMEs are blended with surrogate mixtures of gasoline and diesel, cross interactions between the radical pools of the different fuels in the blend are expected, especially at low temperatures where residence periods are greater. Most reaction models for blended fuels, including the DLR-Concise model [1], are validated independently with respect to the individual fuels, and therefore, it becomes a challenge to study cross-reaction chemistries using these models. As a result, more research on the measurement of species profiles for blends of OMEs with gasoline and diesel surrogate mixtures is warranted, *e.g.*, in shock tubes during pyrolysis and oxidation conditions, to provide more specific validation targets for further improvement and optimization of kinetic models for the blends.

# Bibliography


[1] T. Kathrotia, P. Oßwald, C. Naumann, S. Richter, and M. Köhler, “Combustion kinetics of alternative jet fuels, part-II: Reaction model for fuel surrogate,'' *Fuel*, vol. 302, no. 15, p. 120736, 2021.

[2] J. M. Ngugi, S. Richter, M. Braun-Unkhoff, C. Naumann, and U. Riedel, “An investigation of fundamental combustion properties of the oxygenated fuels DME and $OME_1$,'' 2020. Presented at the *Proc. ASME Turbo. Expo.*, GT2020-14702, London, Virtual.

[3] J. M. Ngugi, S. Richter, M. Braun-Unkhoff, C. Naumann, M. Köhler, and U. Riedel, “A study on fundamental combustion properties of oxymethylene ether-2,'' *J. Eng. Gas Turb. Power*, vol. 144, no. 1, 2022.

[4] J. M. Ngũgĩ, S. Richter, M. Braun-Unkhoff, C. Naumann, and U. Riedel, “A study on fundamental combustion properties of oxymethylene ether-1, the primary reference fuel 90, and their blend: Experiments and modelling,'' *Combust. Flame*, vol. 243, p. 111996, 2022.

[5] J. M. Ngũgĩ, S. Richter, M. Braun-Unkhoff, C. Naumann, and U. Riedel, “A study on fundamental combustion properties of trimethyl orthoformate: Experiments and modelling,'' 2022. Presented at the *Proc. ASME Turbo. Expo.*, GT2022-83029, Rotterdam, Netherlands.

[6] S. Richter, T. Kathrotia, M. Braun-Unkhoff, C. Naumann, and M. Köhler, “Influence of oxymethylene ethers ($OME_n$) in mixtures with a diesel surrogate,'' *Energies*, vol. 14, no. 23, p. 7848, 2021.

[7] L. Cai, S. Jacobs, R. Langer, F. vom Lehn, K. A. Heufer, and H. Pitsch, “Auto-ignition of oxymethylene ethers ($OME_n$, n=2–4) as promising synthetic e-fuels from renewable electricity: shock tube experiments and automatic mechanism generation,'' *Fuel*, vol. 264, p. 116711, 2020.

[8] B. Niu, M. Jia, Y. Chang, H. Duan, X. Dong, and P. Wang, “Construction of reduced oxidation mechanisms of polyoxymethylene dimethyl ethers ($pode_{1–6}$) with consistent structure using decoupling methodology and reaction rate rule,'' *Combust. Flame*, vol. 232, p. 111534, 2021.

[9] U.S. Energy Information Administration, “Short-term energy outlook,'' 2022. `https://www.eia.gov/outlooks/steo/pdf/steofull.pdf`, Accessed: 24.08.2022.

[10] U.S. Energy Information Administration, “International energy outlook 2021 (IEO2021),'' 2021. `https://www.eia.gov/outlooks/ieo/pdf/IEO2021ReleasePresentation.pdf`, Accessed: 24.08.2022.

[11] D. Welsby, J. Price, S. Pye, and P. Ekins, “Unextractable fossil fuels in a 1.5°c world,'' *Nature*, vol. 597, no. 7875, pp. 230–234, 2021.

[12] D. Kodjak, “Policies to reduce fuel consumption, air pollution, and carbon emissions from vehicles in G20 nations,'' 2015. https://theicct.org/sites/default/files/publications/ICCTG20-briefing-paperJun2015updated.pdf, Accessed: 24.08.2022.

[13] The International Council on Clean Transportation (ICCT), “Comments and technical recommendations on future euro 7/VII emission standards),'' 2022. https://theicct.org/sites/default/files/eu-commission-euro-7-and-VI-may2021.pdf, Accessed: 24.08.2022.

[14] International Energy Agency (IEA), “Global energy review 2021,'' 2022. https://www.iea.org/reports/global-energy-review-2021/CO$2$-emissions, Accessed: 24.08.2022.

[15] United Nations Framework Convention on Climate Change, (UNFCCC), “Report of the conference of the parties on its twenty-first session, held in paris from 30 november to 13 december 2015,'' 2015. https://www.un.org/en/development/desa/population/migration/generalassembly/docs/globalcompact/FCCCCP201510Add.1.pdf, Accessed: 24.08.2022.

[16] European Commission, “Stepping up europe's 2030 climate ambition: Investing in a climate-neutral future for the benefit of our people,'' 2020. https://eur-lex.europa.eu/resource.html?uri=cellar:749e04bb-f8c5-11ea-991b-01aa75ed71a1.0001.02/DOC1&format=PDF, Accessed: 24.08.2022.

[17] P. Plötz, J. Wachsmuth, T. Gnann, F. Neuner, D. Speth, and S. Link, “Net-zero-carbon transport in europe until 2050 - targets, technologies and policies for a long-term eu strategy,'' 2021. https://www.isi.fraunhofer.de/content/dam/isi/dokumente/cce/2021/EUTransportpolicybrieflong.pdf, Karlsruhe: Fraunhofer Institute for Systems and Innovation Research ISI, Accessed: 24.08.2022.

[18] T. Haasz, J. J. Vilchez, R. Kunze, P. Deane, D. Fraboulet, U. Fahl, and E. Mulholland, “Perspectives on decarbonizing the transport sector in the EU-28,'' *Energy Strategy Rev.*, vol. 20, pp. 124–132, 2018.

[19] G. Emberger, “Low carbon transport strategy in europe: A critical review,'' *Int. J. Sustain. Transp.*, vol. 11, no. 1, pp. 31–35, 2017.

[20] J. Zawieska and J. Pieriegud, “Smart city as a tool for sustainable mobility and transport decarbonisation,'' *Transp. Policy*, vol. 63, pp. 39–50, 2018.

[21] S. Deutz, D. Bongartz, B. Heuser, A. Kätelhön, L. S. Langenhorst, A. Omari, M. Walters, J. Klankermayer, W. Leitner, and A. Mitsos, “Cleaner production of cleaner fuels: wind-to-wheel–environmental assessment of $CO_2$-based oxymethylene ether as a drop-in fuel,'' *Energy Environ. Sci.*, vol. 11, no. 2, pp. 331–343, 2018.

[22] S. E. Iannuzzi, C. Barro, K. Boulouchos, and J. Burger, “Combustion behavior and soot formation / oxidation of oxygenated fuels in a cylindrical constant volume chamber,'' *Fuel*, vol. 167, pp. 49–59, 2016.

[23] L. Cai, F. vom Lehn, and H. Pitsch, “Higher alcohol and ether biofuels for compression-ignition engine application: a review with emphasis on combustion kinetics,'' *Energy Fuels*, vol. 35, no. 3, pp. 1890–1917, 2021.

[24] A. Garcia, J. Monsalve-Serrano, D. Villalta, and M. Guzman-Mendoza, “Methanol and $OME_x$ as fuel candidates to fulfill the potential EURO VII emissions regulation under dual-mode dual-fuel combustion,'' *Fuel*, vol. 287, p. 119548, 2021.

[25] H. Liu, Z. Wang, Y. Li, Y. Zheng, T. He, and J. Wang, “Recent progress in the application in compression ignition engines and the synthesis technologies of polyoxymethylene dimethyl ethers,'' *Appl. energy*, vol. 233, pp. 599–611, 2019.

[26] A. Omari, B. Heuser, S. Pischinger, and C. Rüdinger, “Potential of long-chain oxymethylene ether and oxymethylene ether-diesel blends for ultra-low emission engines,'' *Appl. energy*, vol. 239, pp. 1242–1249, 2019.

[27] C. Arcoumanis, C. Bae, R. Crookes, and E. Kinoshita, “The potential of di-methyl ether (DME) as an alternative fuel for compression-ignition engines: A review.,'' *Fuel*, vol. 87, no. 7, pp. 1014–1030, 2008.

[28] L. Pellegrini, M. Marchionna, R. Patrini, C. Beatrice, N. Del Giacomo, and C. Guido, “Combustion behaviour and emission performance of neat and blended polyoxymethylene dimethyl ethers in a light-duty diesel engine..''

[29] F. Ferraro, C. Russo, R. Schmitz, C. Hasse, and M. Sirignano, “Experimental and numerical study on the effect of oxymethylene ether-3 ($OME_3$) on soot particle formation,'' *Fuel*, vol. 286, p. 119353, 2021.

[30] Y. R. Tan, M. Salamanca, L. Pascazio, J. Akroyd, and M. Kraft, “The effect of poly (oxymethylene) dimethyl ethers ($PODE_3$) on soot formation in ethylene / $PODE_3$ laminar coflow diffusion flames,'' *Fuel*, vol. 283, p. 118769, 2021.

[31] T. He, Z. Wang, X. You, H. Liu, Y. Wang, X. Li, and X. He, “A chemical kinetic mechanism for the low-and intermediate-temperature combustion of polyoxymethylene dimethyl ether-3 ($PODE_3$),'' *Fuel*, vol. 212, pp. 223–235, 2018.

[32] J. Liu, P. Sun, H. Huang, J. Meng, and X. Yao, “Experimental investigation on performance, combustion and emission characteristics of a common-rail diesel engine fueled with polyoxymethylene dimethyl ethers-diesel blends,'' *Appl. Energy*, vol. 202, pp. 527–536, 2017.

[33] M. Rumayor, J. Fernández-González, A. Domínguez-Ramos, and A. Irabien, “Deep decarbonization of the cement sector: A prospective environmental assessment of $co_2$ recycling to methanol,'' *ACS Sustain. Chem. Eng.*, vol. 10, no. 1, pp. 267–278, 2021.

[34] J. Schittkowski, H. Ruland, D. Laudenschleger, K. Girod, K. Kähler, S. Kaluza, M. Muhler, and R. Schlögl, “Methanol synthesis from steel mill exhaust gases: Challenges for the industrial Cu / ZnO / $Al_2O_3$ catalyst,'' *Chem. Ing. Tech.*, vol. 90, no. 10, pp. 1419–1429, 2018.

[35] K. P. Shrestha, S. Eckart, S. Drost, C. Fritsche, R. Schießl, L. Seidel, U. Maas, H. Krause, and F. Mauss, “A comprehensive kinetic modeling of oxymethylene ethers ($OME_n$, n=1–3) oxidation - laminar flame speed and ignition delay time measurements,'' *Combust. Flame*, vol. 246, p. 112426, 2022.

[36] C. J. Baranowski, A. M. Bahmanpour, and O. Kröcher, “Catalytic synthesis of polyoxymethylene dimethyl ethers (OME): A review,'' *Appl. Catal. B: Environ.*, vol. 217, pp. 407–420, 2017.

[37] J. Burger, M. Siegert, E. Ströfer, and H. Hasse, “Poly (oxymethylene) dimethyl ethers as components of tailored diesel fuel: Properties, synthesis and purification concepts,'' *Fuel*, vol. 89, no. 11, pp. 3315–3319, 2010.

[38] J. Qi, Y. Hu, J. Niu, W. Ma, S. Jiang, Y. Wang, X. Zhang, and Y. Jiang, “Evaluation of polyoxymethylene dimethyl ethers as a new type of diesel additives,'' *Fuel*, vol. 234, pp. 135–141, 2018.

[39] W. Ying, L. Genbao, Z. Wei, and Z. Longbao, “Study on the application of dme/diesel blends in a diesel engine,'' *Fuel Process. Technol.*, vol. 89, no. 12, pp. 1272–1280, 2008.

[40] A. Nicolle, N. Naser, T. Javed, N. Rankovic, and S. M. Sarathy, “Autoignition characteristics of ethers blended with low cetane distillates,'' *Energy Fuels*, vol. 33, no. 7, pp. 6775–6787, 2019.

[41] G. Kalghatgi, H. Levinsky, and M. Colket, “Future transportation fuels,'' *Prog. Energy Combust. Sci.*, vol. 69, pp. 103–105, 2018.

[42] J. Badra, Y. Viollet, A. Elwardany, H. G. Im, and J. Chang, “Physical and chemical effects of low octane gasoline fuels on compression ignition combustion,'' *Appl. Energy*, vol. 183, pp. 1197–1208, 2016.

[43] M. Schappals, T. Breug-Nissen, K. Langenbach, J. Burger, and H. Hasse, “Solubility of carbon dioxide in poly (oxymethylene) dimethyl ethers,'' *J. Chem. Eng. Data*, vol. 62, no. 11, pp. 4027–4031, 2017.

[44] A. Zhenova, A. Pellis, R. A. Milescu, C. R. McElroy, R. J. White, and J. H. Clark, “Solvent applications of short-chain oxymethylene dimethyl ether oligomers,'' *ACS Sustain. Chem. Eng.*, vol. 7, no. 17, pp. 14834–14840, 2019.

[45] K. Wakai, T. Yoshizaki, K. Nishida, H. Hiroyasu, and Y. Kawaguchi, “Numerical and experimental analyses of the injection characteristics of dimethyl ether with a DI diesel injection system,'' tech. rep., SAE Tech. Pap., 1999.

[46] K. F. Hansen, L. Nielsen, J. B. Hansen, S.-E. Mikkelsen, H. Landälv, T. Ristola, and K. Vielwerth, "Demonstration of a dme (dimethyl ether) fuelled city bus," tech. rep., SAE Tech. Pap., 2000.

[47] Y. Zhao, Y. Wang, D. Li, X. Lei, and S. Liu, "Combustion and emission characteristics of a dme (dimethyl ether)-diesel dual fuel premixed charge compression ignition engine with exhaust gas recirculation," *Energy*, vol. 72, pp. 608–617, 2014.

[48] E. E. Dames, A. S. Rosen, B. W. Weber, C. W. Gao, C.-J. Sung, and W. H. Green, "A detailed combined experimental and theoretical study on dimethyl ether / propane blended oxidation," *Combust. Flame*, vol. 168, pp. 310–330, 2016.

[49] L. Zander, J. Vinkeloe, and N. Djordjevic, "Ignition delay and chemical–kinetic modelling of undiluted mixtures in a high-pressure shock tube: Nonideal effects and comparative uncertainty analysis," *Int. J. Chem. Kinet*, vol. 53, no. 5, pp. 611–637, 2021.

[50] Z. Huang, Y. Ren, D. Jiang, L. Liu, K. Zeng, B. Liu, and X. Wang, "Combustion and emission characteristics of a compression ignition engine fuelled with diesel–dimethoxy methane blends," *Energy Convers. Manag.*, vol. 47, no. 11-12, pp. 1402–1415, 2006.

[51] Y. Ren, Z. Huang, H. Miao, Y. Di, D. Jiang, K. Zeng, B. Liu, and X. Wang, "Combustion and emissions of a di diesel engine fuelled with diesel-oxygenate blends," *Fuel*, vol. 87, no. 12, pp. 2691–2697, 2008.

[52] A. Omari, B. Heuser, and S. Pischinger, "Potential of oxymethylenether-diesel blends for ultra-low emission engines," *Fuel*, vol. 209, pp. 232–237, 2017.

[53] R. Zhu, X. Wang, H. Miao, X. Yang, and Z. Huang, "Effect of dimethoxy-methane and exhaust gas recirculation on combustion and emission characteristics of a direct injection diesel engine," *Fuel*, vol. 90, no. 5, pp. 1731–1737, 2011.

[54] P. Dworschak, V. Berger, M. Härtl, and G. Wachtmeister, "Neat oxymethylene ethers: Combustion performance and emissions of $OME_2$, $OME_3$, $OME_4$ and $OME_5$ in a single-cylinder diesel engine," tech. rep., SAE Tech. Pap., 2020.

[55] Y. Zhao, C. Geng, X. Li, P. Cheng, T. Niu, *et al.*, "Experimental study on the effects of blending $PODE_n$ on performance, combustion and emission characteristics of heavy-duty diesel engines meeting china VI emission standard," *Sci. Rep.*, vol. 11, no. 1, pp. 1–11, 2021.

[56] K. P. Shrestha, S. Eckart, A. M. Elbaz, B. R. Giri, C. Fritsche, L. Seidel, W. L. Roberts, H. Krause, and F. Mauss, "A comprehensive kinetic model for dimethyl ether and dimethoxymethane oxidation and $no_x$ interaction utilizing experimental laminar flame speed measurements at elevated pressure and temperature," *Combust. Flame*, vol. 218, pp. 57–74, 2020.

[57] F. R. Gillespie, *An experimental and modelling study of the combustion of oxygenated hydrocarbons.* Doctoral dissertation, National University of Ireland–Galway, 2014.

[58] U. Pfahl, K. Fieweger, and G. Adomeit, “Self-ignition of diesel-relevant hydrocarbon-air mixtures under engine conditions,'' in *Proc. Combust. Symp.*, vol. 26, pp. 781–789, 1996.

[59] P. Dagaut, C. Daly, J. M. Simmie, and M. Cathonnet, “The oxidation and ignition of dimethylether from low to high temperature (500–1600 k): Experiments and kinetic modelling,'' in *Int. Symp. Combust.*, vol. 27, pp. 361–369, 1998.

[60] G. Mittal, M. Chaos, C.-J. Sung, and F. L. Dryer, “Dimethyl ether auto-ignition in a rapid compression machine: Experiments and chemical kinetic modelling,'' *Fuel Proc. Technol.*, vol. 89, no. 12, pp. 1244–1254, 2008.

[61] R. Cook, D. Davidson, and R. Hanson, “Shock tube measurements of ignition delay times and oh time-histories in dimethyl ether oxidation,'' *Proc. Combust. Inst.*, vol. 32, no. 1, pp. 189–196, 2009.

[62] Z. Li, W. Wang, Z. Huang, and M. A. Oehlschlaeger, “Dimethyl ether autoignition at engine-relevant conditions,'' *Energy Fuels*, vol. 27, no. 5, pp. 2811–2817, 2013.

[63] L. Pan, E. Hu, Z. Tian, F. Yang, and Z. Huang, “Experimental and kinetic study on ignition delay times of dimethyl ether at high temperatures,'' *Energy Fuels*, vol. 29, no. 5, pp. 3495–3506, 2015.

[64] C. Zhang, P. Li, Y. Li, J. He, and X. Li, “Shock-tube study of dimethoxymethane ignition at high temperatures,'' *Energy Fuels*, vol. 28, no. 7, pp. 4603–4610, 2014.

[65] E. Hu, Z. Gao, Y. Liu, G. Yin, and Z. Huang, “Experimental and modelling study on ignition delay times of dimethoxy methane / *n*-heptane blends,'' *Fuel*, vol. 189, pp. 350–357, 2017.

[66] S. Jacobs, M. Döntgen, A. B. Alquaity, W. A. Kopp, L. C. Kröger, U. Burke, H. Pitsch, K. Leonhard, H. J. Curran, and K. A. Heufer, “Detailed kinetic modelling of dimethoxymethane. part ii: Experimental and theoretical study of the kinetics and reaction mechanism,'' *Combust. Flame*, vol. 205, pp. 522–533, 2019.

[67] S. Drost, R. Schießl, M. Werler, J. Sommerer, and U. Maas, “Ignition delay times of polyoxymethylene dimethyl ether fuels ($OME_2$ and $OME_3$) and air: Measurements in a rapid compression machine,'' *Fuel*, vol. 258, p. 116070, 2019.

[68] W. Sun, G. Wang, S. Li, R. Zhang, B. Yang, J. Yang, Y. Li, C. K. Westbrook, and C. K. Law, “Speciation and the laminar burning velocities of poly (oxymethylene) dimethyl ether-3 (POMDME-3) flames: An experimental and modelling study,'' *Proc. Combust. Inst.*, vol. 36, no. 1, pp. 1269–1278, 2017.

[69] S. Eckart, L. Cai, C. Fritsche, F. vom Lehn, H. Pitsch, and H. Krause, “Laminar burning velocities, co, and $no_x$ emissions of premixed poly(oxymethylene) dimethyl ether flames,'' *Fuel*, vol. 293, p. 120321, 2021.

[70] L. Yeh, D. Rickeard, J. Duff, J. Bateman, R. Schlosberg, and R. Caers, “Oxygenates: An evaluation of their effects on diesel emissions,'' *SAE trans.*, pp. 1482–1498, 2001.

[71] J. Platz, J. Sehested, O. Nielsen, and T. Wallington, “Atmospheric chemistry of trimethoxymethane,$(CH_3O)_3CH$; laboratory studies,'' *J. Phys. Chem. A*, vol. 103, no. 15, pp. 2632–2640, 1999.

[72] D. G. Potter, S. Wiseman, M. A. Blitz, and P. W. Seakins, “Laser photolysis kinetic study of oh radical reactions with methyl tert-butyl ether and trimethyl orthoformate under conditions relevant to low temperature combustion: Measurements of rate coefficients and oh recycling,'' *J. Phys. Chem. A*, vol. 122, no. 50, pp. 9701–9711, 2018.

[73] B. Du and W. Zhang, “Theoretical study of the reaction mechanism and kinetics of the OH + trimethyl orthoformate ($(CH_3O)_3CH + O_2$) reaction,'' *Comput. Theor. Chem.*, vol. 1159, pp. 38–45, 2019.

[74] N. Gaiser, T. Bierkandt, J. Zinsmeister, P. Hemberger, S. Shaqiri, T. Kasper, M. Köhler, and M. Aigner, “Disentangling of linear and branched ethers: Flow reactor study of $OME_2$ and trimethoxy methane using molecular beam mass spectrometry and synchrotron photoionization,'' 2021. Presented at the *$10^{th}$ Proc.European Combust. Meeting.*, April 14 - 15, pp. 120-125, virtual.

[75] M. Döntgen and K. A. Heufer, “Shock tube study and chemical kinetic modelling of trimethoxymethane combustion,'' 2021. Presented at the *$10^{th}$ Proc. European Combust. Meeting.*, April 14-15, virtual.

[76] M. Döntgen, M. E. Fuller, S. Peukert, D. Nativel, C. Schulz, K. A. Heufer, and C. F. Goldsmith, “Shock tube study of the pyrolysis kinetics of di-and trimethoxy methane,'' *Combustion and Flame*, vol. 242, p. 112186, 2022.

[77] W. J. Pitz and C. J. Mueller, “Recent progress in the development of diesel surrogate fuels,'' *Prog. Energy Combust. Sci.*, vol. 37, no. 3, pp. 330–350, 2011.

[78] L. Cancino, A. da Silva Jr, A. De Toni, M. Fikri, A. Oliveira, C. Schulz, and H. Curran, “A six-compound, high performance gasoline surrogate for internal combustion engines: Experimental and numerical study of autoignition using high-pressure shock tubes,'' *Fuel*, vol. 261, p. 116439, 2020.

[79] S. Cheng, C. Saggese, D. Kang, S. S. Goldsborough, S. W. Wagnon, G. Kukkadapu, K. Zhang, M. Mehl, and W. J. Pitz, “Autoignition and preliminary heat release of gasoline surrogates and their blends with ethanol at engine-relevant conditions: Experiments and comprehensive kinetic modelling,'' *Combust. Flame*, vol. 228, pp. 57–77, 2021.

[80] D. Kang, A. Fridlyand, S. S. Goldsborough, S. W. Wagnon, M. Mehl, W. J. Pitz, and M. J. McNenly, “Auto-ignition study of face gasoline and its surrogates at advanced ic engine conditions,'' *Proc. Combust. Inst .*, vol. 37, no. 4, pp. 4699–4707, 2019.

[81] C. Pera and V. Knop, “Methodology to define gasoline surrogates dedicated to auto-ignition in engines,'' *Fuel*, vol. 96, pp. 59–69, 2012.

[82] S. M. Sarathy, A. Farooq, and G. T. Kalghatgi, “Recent progress in gasoline surrogate fuels,'' *Prog. Energy Combust. Sci.*, vol. 65, pp. 67–108, 2018.

[83] Y. Ra and R. D. Reitz, “A reduced chemical kinetic model for ic engine combustion simulations with primary reference fuels,'' *Combust. Flame*, vol. 155, no. 4, pp. 713–738, 2008.

[84] H. Selim, S. Y. Mohamed, N. Hansen, and S. M. Sarathy, “Premixed flame chemistry of a gasoline primary reference fuel surrogate,'' *Combust. Flame*, vol. 179, pp. 300–311, 2017.

[85] J. C. Andrae, “Development of a detailed kinetic model for gasoline surrogate fuels,'' *Fuel*, vol. 87, no. 10-11, pp. 2013–2022, 2008.

[86] J. C. Andrae, P. Björnbom, R. Cracknell, and G. Kalghatgi, “Auto-ignition of toluene reference fuels at high pressures modeled with detailed chemical kinetics,'' *Combust. Flame*, vol. 149, no. 1-2, pp. 2–24, 2007.

[87] K. Fieweger, R. Blumenthal, and G. Adomeit, “Self-ignition of si engine model fuels: a shock tube investigation at high pressure,'' *Combust. Flame*, vol. 109, no. 4, pp. 599–619, 1997.

[88] S. M. Sarathy, G. Kukkadapu, M. Mehl, W. Wang, T. Javed, S. Park, M. A. Oehlschlaeger, A. Farooq, W. J. Pitz, and C.-J. Sung, “Ignition of alkane-rich face gasoline fuels and their surrogate mixtures,'' *Proc. Combust. Inst.*, vol. 35, no. 1, pp. 249–257, 2015.

[89] M. AlAbbad, T. Javed, F. Khaled, J. Badra, and A. Farooq, “Ignition delay time measurements of primary reference fuel blends,'' *Combust. Flame*, vol. 178, pp. 205–216, 2017.

[90] S. Richter, M. Braun-Unkhoff, J. Herzler, T. Methling, C. Naumann, and U. Riedel, “An investigation of combustion properties of a gasoline primary reference fuel surrogate blended with butanol,'' 2019.

[91] J. Van Lipzig, E. Nilsson, L. De Goey, and A. Konnov, “Laminar burning velocities of *n*-heptane, *iso*-octane, ethanol and their binary and tertiary mixtures,'' *Fuel*, vol. 90, no. 8, pp. 2773–2781, 2011.

[92] O. Mannaa, M. S. Mansour, W. L. Roberts, and S. H. Chung, “Laminar burning velocities at elevated pressures for gasoline and gasoline surrogates associated with ron,'' *Combust. Flame*, vol. 162, no. 6, pp. 2311–2321, 2015.

[93] S. Jerzembeck, N. Peters, P. Pepiot-Desjardins, and H. Pitsch, “Laminar burning velocities at high pressure for primary reference fuels and gasoline: Experimental and numerical investigation,'' *Combust. Flame*, vol. 156, no. 2, pp. 292–301, 2009.

[94] Y. Huang, C. Sung, and J. Eng, “Laminar flame speeds of primary reference fuels and reformer gas mixtures,'' *Combust. Flame*, vol. 139, no. 3, pp. 239–251, 2004.

[95] Y.-H. Liao and W. L. Roberts, “Laminar flame speeds of gasoline surrogates measured with the flat flame method,'' *Energy Fuels*, vol. 30, no. 2, pp. 1317–1324, 2016.

[96] D. Bradley, R. Hicks, M. Lawes, C. Sheppard, and R. Woolley, “The measurement of laminar burning velocities and markstein numbers for *iso*-octane–air and *iso*-octane–*n*-heptane–air mixtures at elevated temperatures and pressures in an explosion bomb,'' *Combust. Flame*, vol. 115, no. 1-2, pp. 126–144, 1998.

[97] M. Fikri, Y. Sakai, J. Herzler, and C. Schulz, “Experimental and numerical study of the ignition delay times of primary reference fuels containing diethyl ether,'' in *26$^{th}$ International Colloquium on the Dynamics of Explosions and Reactive Systems (ICDERS)*, 2017. Presented at the *26$^{th}$ International Colloquium on the Dynamics of Explosions and Reactive Systems (ICDERS).*, AIAA 2006-8109, Boston, USA.

[98] Z. Gao, E. Hu, Z. Xu, G. Yin, and Z. Huang, “Low to intermediate temperature oxidation studies of dimethoxymethane/*n*-heptane blends in a jet-stirred reactor,'' *Combust. Flame*, vol. 207, pp. 20–35, 2019.

[99] D. Goeb, M. Davidovic, L. Cai, P. Pancharia, M. Bode, S. Jacobs, J. Beeckmann, W. Willems, K. A. Heufer, and H. Pitsch, “Oxymethylene ether–*n*-dodecane blend spray combustion: Experimental study and large-eddy simulations,'' *Proc. Combust. Inst.*, vol. 38, no. 2, pp. 3417–3425, 2021.

[100] S. Ren, Z. Wang, B. Li, H. Liu, and J. Wang, “Development of a reduced polyoxymethylene dimethyl ethers (pode$_n$) mechanism for engine applications,'' *Fuel*, vol. 238, pp. 208–224, 2019.

[101] Q. Lin, K. L. Tay, D. Zhou, and W. Yang, “Development of a compact and robust polyoxymethylene dimethyl ether 3 reaction mechanism for internal combustion engines,'' *Energy Convers. Manag.*, vol. 185, pp. 35–43, 2019.

[102] J. Warnatz, U. Maas, and R. W. Dibble, *Combustion*, vol. 2. Springer, 2$^{nd}$ ed., 2006.

[103] X. Fang, X. Huang, W. Chen, X. Qiao, and D. Ju, “Development of a skeletal surrogate mechanism for emulating combustion characteristics of diesel from direct coal liquefaction,'' *Combust. Flame*, vol. 218, pp. 84–97, 2020.

[104] T. Kathrotia, U. Riedel, A. Seipel, K. Moshammer, and A. Brockhinke, “Experimental and numerical study of chemiluminescent species in low-pressure flames,'' *Appl. Phy. B*, vol. 107, no. 3, pp. 571–584, 2012.

[105] T. Turányi and A. S. Tomlin, *Reaction kinetics basics*, pp. 5–37. Springer, 2014.

[106] C. Conroy, *A High-pressure shock Tube and rapid compression machine study of n-butylcyclohexane and its mixtures with n-heptane.* Doctoral dissertation, NUI Galway, 2013.

[107] K. Yasunaga and R. S. Tranter, *Speciation in shock tubes*, pp. 143–161. Springer, 2013.

[108] I. Stotz, G. Lamanna, B. Weigand, and J. Steelant, "A double-diaphragm shock tube for hydrocarbon disintegration studies," in *14th AIAA / AHI Space Planes and Hypersonic Systems and Technologies Conference*, p. 8109, 2006.

[109] J. R. Barker, "Chapter 7 - monte carlo stochastic simulation of the master equation for unimolecular reaction systems," in *Unimolecular Kinetics*, vol. 43 of *Comprehensive Chemical Kinetics*, pp. 409–463, Elsevier, 2019.

[110] Design, Reaction, "Ansys chemkin theory manual," 2007. `https://personal.ems.psu.edu/radovic/ChemKinTheoryPaSR.pdf`, Accessed: 31.03.2022.

[111] A. Amadio, *Driver-gas tailoring For test-time extension using unconventional driver mixtures*. Masters thesis, University of Central Florida, 2006.

[112] H. Palmer and B. E. Knox, "Contact surface tailoring in a chemical shock tube," *J. Am. Rocket Soc.*, vol. 31, no. 6, pp. 826–828, 1961.

[113] O. Trass and D. Mackay, "Contact surface tailoring in a chemical shock tube," *AIAA Journal*, vol. 1, no. 9, pp. 2161–2163, 1963.

[114] Z. Hong, D. F. Davidson, and R. K. Hanson, "Contact surface tailoring condition for shock tubes with different driver and driven section diameters," *Shock Waves*, vol. 19, no. 4, pp. 331–336, 2009.

[115] H. Polachek and R. J. Seeger, "On shock-wave phenomena; refraction of shock waves at a gaseous interface," *Phys. Rev.*, vol. 84, no. 5, p. 922, 1951.

[116] T. A. Brabbs and F. E. Belles, *Contact-surface tailoring in real shock tubes*. National Aeronautics and Space Administration (NASA), USA, 1965.

[117] N. Reddy, "An analytical method for real gas tailoring in a shock tube," *AIAA Journal*, vol. 9, no. 12, pp. 2458–2460, 1971.

[118] A. R. Amadio, M. W. Crofton, and E. L. Petersen, "Test-time extension behind reflected shock waves using $CO_2$–He and $C_3H_8$–he driver mixtures," *Shock Waves*, vol. 16, no. 2, pp. 157–165, 2006.

[119] R. Djuric, *Messung der Zündverzugszeit unterstöchiometrischer Gemische aus Ethan und Ethen mit Distickstoffmonoxid für die Charakterisierung grundlegender Verbrennungseigenschaften*. Masters thesis, Institut für Verbrennung der Luft- und Raumfahrt, Uni Stuttgart, 2018.

[120] C. Naumann, C. Janzer, and U. Riedel, "Ethane / nitrous oxide mixtures as a green propellant to substitute hydrazine: validation of reaction mechanism," 2019. Presented at the *9th European Combust. Meeting.*, Paper ECM2019S5AII21, Lisbon, Portugal.

[121] S. Richter, *Charakterisierung grundlegender Verbrennungseigenschaften von alternativen Treibstoffen und Treibstoffkomponenten.* Doctoral dissertation, Technische Universität Bergakademie Freiberg, 2019.

[122] S. Richter, T. Kathrotia, C. Naumann, T. Kick, N. Slavinskaya, M. Braun-Unkhoff, and U. Riedel, "Experimental and modelling study of farnesane," *Fuel*, vol. 215, pp. 22–29, 2018.

[123] D. F. Schuler, *Validierung von Reaktionsmechanismen für biogene Kraftstoffkomponenten.* Doctoral dissertation, University of Stuttgart, 2016.

[124] E. L. Petersen, "Interpreting endwall and sidewall measurements in shock-tube ignition studies," *Combust. Sci. Technol.*, vol. 181, no. 9, pp. 1123–1144, 2009.

[125] E. L. Petersen, *A shock tube and diagnostics for chemistry measurements at elevated pressures with application to methane ignition.* Doctoral dissertation, Stanford University (USA), 1999.

[126] Z. Hong, G. A. Pang, S. S. Vasu, D. F. Davidson, and R. K. Hanson, "The use of driver inserts to reduce non-ideal pressure variations behind reflected shock waves," *Shock Waves*, vol. 19, no. 2, pp. 113–123, 2009.

[127] R. K. Hanson, G. A. Pang, S. Chakraborty, W. Ren, S. Wang, and D. F. Davidson, "Constrained reaction volume approach for studying chemical kinetics behind reflected shock waves," *Combust. Flame*, vol. 160, no. 9, pp. 1550–1558, 2013.

[128] E. L. Petersen, M. J. Rickard, M. W. Crofton, E. D. Abbey, M. J. Traum, and D. M. Kalitan, "A facility for gas-and condensed-phase measurements behind shock waves," *Meas. Sci. Technol.*, vol. 16, no. 9, p. 1716, 2005.

[129] H. J. Curran, P. Gaffuri, W. J. Pitz, and C. K. Westbrook, "A comprehensive modelling study of *n*-heptane oxidation," *Combust. Flame*, vol. 114, no. 1-2, pp. 149–177, 1998.

[130] H. J. Curran, P. Gaffuri, W. J. Pitz, and C. K. Westbrook, "A comprehensive modelling study of *iso*-octane oxidation," *Combust. Flame*, vol. 129, no. 3, pp. 253–280, 2002.

[131] S. M. Sarathy, C. K. Westbrook, M. Mehl, W. J. Pitz, C. Togbe, P. Dagaut, H. Wang, M. A. Oehlschlaeger, U. Niemann, and K. Seshadri, "Comprehensive chemical kinetic modelling of the oxidation of 2-methylalkanes from $C_7$ to $C_{20}$," *Combust. Flame*, vol. 158, no. 12, pp. 2338–2357, 2011.

[132] C.-W. Zhou, Y. Li, U. Burke, C. Banyon, K. P. Somers, S. Ding, S. Khan, J. W. Hargis, T. Sikes, and O. Mathieu, "An experimental and chemical kinetic modelling study of 1, 3-butadiene combustion: Ignition delay time and laminar flame speed measurements," *Combust. Flame*, vol. 197, pp. 423–438, 2018.

[133] The Creck Modelling group, "Kinetic mechanisms," 2021. `http://creckmodeling.chem.polimi.it/menu-kinetics/menu-kinetics-detailed-mechanisms`, Accessed: 07.06.2022.

[134] M. Mehl, W. J. Pitz, C. K. Westbrook, and H. J. Curran, "Kinetic modelling of gasoline surrogate components and mixtures under engine conditions," *Proc. Comb. Inst.*, vol. 33, no. 1, pp. 193–200, 2011.

[135] G. Blanquart, P. Pepiot-Desjardins, and H. Pitsch, "Chemical mechanism for high temperature combustion of engine relevant fuels with emphasis on soot precursors," *Combust. Flame*, vol. 156, no. 3, pp. 588–607, 2009.

[136] H. J. Curran, E. M. Fisher, P.-A. Glaude, N. M. Marinov, W. Pitz, C. Westbrook, D. Layton, P. F. Flynn, R. P. Durrett, and A. Zur Loye, "Detailed chemical kinetic modelling of diesel combustion with oxygenated fuels," *SAE Trans.*, pp. 514–521, 2001.

[137] K. P. Somers, J. M. Simmie, F. Gillespie, C. Conroy, G. Black, W. K. Metcalfe, F. Battin-Leclerc, P. Dirrenberger, O. Herbinet, and P.-A. Glaude, "A comprehensive experimental and detailed chemical kinetic modelling study of 2, 5-dimethylfuran pyrolysis and oxidation," *Combust. Flame*, vol. 160, no. 11, pp. 2291–2318, 2013.

[138] A. E. Lutz, R. J. Kee, and J. A. Miller, "Senkin: A FORTRAN program for predicting homogeneous gas phase chemical kinetics with sensitivity analysis," report, Sandia National Labs., Livermore, CA (USA), 1988.

[139] Kintech Laboratory, "Chemical Workbench," 2022. `https://www.kintechlab.com/products/chemical-workbench/`, Accessed: 07.06.2022.

[140] M. Figueroa-Labastida, J. Badra, A. M. Elbaz, and A. Farooq, "Shock tube studies of ethanol preignition," *Combust. Flame*, vol. 198, pp. 176–185, 2018.

[141] D. Buntin and L. Tartakovsky, "Heat release peculiarities of polyoxymethylene dimethyl ether 1 – part I: Effect of initial thermochemical conditions," *Fuel*, vol. 321, p. 124007, 2022.

[142] D. Nativel, P. Niegemann, J. Herzler, M. Fikri, and C. Schulz, "Ethanol ignition in a high-pressure shock tube: Ignition delay time and high-repetition-rate imaging measurements," *Proc. Combust. Inst.*, vol. 38, no. 1, pp. 901–909, 2021.

[143] M. Figueroa-Labastida, M. B. Luong, J. Badra, H. G. Im, and A. Farooq, "Experimental and computational studies of methanol and ethanol preignition behind reflected shock waves," *Combust. Flame*, vol. 234, p. 111621, 2021.

[144] D. F. Davidson, Y. Zhu, J. Shao, and R. Hanson, "Ignition delay time correlations for distillate fuels," *Fuel*, vol. 187, pp. 26–32, 2017.

[145] Y. Muharam, *Detailed kinetic modelling of the oxidation and Combustion of large hydrocarbons using an uutomatic generation of mechanisms.* Doctoral dissertation, University of Heidelberg, 2005.

[146] S. Eckart, C. Fritsche, C. Krasselt, and H. Krause, "Determining the laminar burning velocity of nitrogen diluted dimethoxymethane ($OME_1$) using the heat-flux burner method: Numerical and experimental investigations," *Int. J. Energy Res.*, vol. 45, no. 2, pp. 2824–2836, 2020.

[147] T. Kathrotia, S. Richter, C. Naumann, N. Slavinskaya, T. Methling, M. Braun-Unkhoff, and U. Riedel, “Reaction model development for synthetic jet fuels: Surrogate fuels as a flexible tool to predict their performance," in *Pro. ASME Turbo Expo., GT2018-76997*, 2018.

[148] J. T. Farrell, R. Johnston, and I. Androulakis, “Molecular structure effects on laminar burning velocities at elevated temperature and pressure," *SAE Trans.*, vol. 113, no. 3, pp. 1404–1425, 2004.

[149] T. Methling, S. Richter, T. Kathrotia, M. Braun-Unkhoff, C. Naumann, and U. Riedel, “An investigation of combustion properties of butanol and its potential for power generation," *J. Eng. Gas Turbines Power*, vol. 140, no. 9, 2018.

[150] H.-H. Carstensen and A. M. Dean, *The kinetics of pressure-dependent reactions*, vol. 42, pp. 101–184. Elsevier, 2007.

[151] J. Troe, “Theory of thermal unimolecular reactions in the fall-off range. i. strong collision rate constants," *Ber. Bunsenges. Phys. Chem.*, vol. 87, no. 2, pp. 161–169, 1983.

[152] E. Goos and A. Burcat, “Overview of thermochemistry and its application to reaction kinetics," *John Wiley & Sons*, pp. 3–32, 2011.

[153] A. Burcat and B. Ruscic, “Third millenium ideal gas and condensed phase thermochemical database for combustion (with update from active thermochemical tables)," report, Argonne National Lab.(ANL), Argonne, IL (United States), 2005.

[154] C. Jiping, H. Yuzhong, W. Su, W. Jing, and F. Bingcheng, “Temperature measurement of reflected shock wave by using chemical indicator," *Acta Mech. Sinica*, vol. 16, no. 1, pp. 63–69, 2000.

[155] D. Zheng, D. He, Q.-D. Wang, Y. Ding, and Z. Peng, “Simultaneous measurements of temperature, CO, and $CO_2$ time-history in reacting *n*-heptane / $O_2$ / argon mixtures blended with diethyl ether behind reflected shock waves," *Combust. Flame*, vol. 241, p. 112057, 2022.

[156] M. A. Oehlschlaeger, D. F. Davidson, and J. B. Jeffries, “Temperature measurement using ultraviolet laser absorption of carbon dioxide behind shock waves," *Appl. optics*, vol. 44, no. 31, pp. 6599–6605, 2005.

# A Publications and conferences

## A.1 Journal publications

1. J. M. Ngũgĩ,, S. Richter, M. Braun-Unkhoff, C. Naumann, M. Köhler, and U. Riedel, "A study on fundamental combustion properties of oxymethylene Ether-2," *J. Eng. Gas Turbines Power*, vol. 144, no. 1, p. 011014, 2022.

2. J. M. Ngũgĩ, S. Richter, M. Braun-Unkhoff, C. Naumann, and U. Riedel, "A study on fundamental combustion properties of oxymethylene ether-1, the primary reference fuel 90, and their blend: Experiments and modelling," *Combust. Flame*, vol. 243, p. 111996, 2022.

3. J. M. Ngũgĩ, S. Richter, M. Braun-Unkhoff, C. Naumann, and U. Riedel, "A study on fundamental combustion properties of trimethyl orthoformate: Experiments and modelling," *J. Eng. Gas Turbines Power*, vol. 145, no. 2, p. 021011, 2023.

## A.2 Conference presentations

1. J. M. Ngũgĩ, S. Richter, M. Braun-Unkhoff, C. Naumann, and U. Riedel, "An Investigation of Fundamental Combustion Properties of the Oxygenated Fuels DME and $OME_1$," *Proc. ASME Turbo Expo 2020.*, GT2020-14702, London, Virtual, 2020.

2. J. M. Ngũgĩ, S. Richter, M. Braun-Unkhoff, C. Naumann, M. Köhler, and U. Riedel, "A Study on Fundamental Combustion Properties of Oxymethylene Ether-2," *Proc. ASME Turbo. Expo.*, GT2021-60078, Virtual, 2021.

3. J. M. Ngũgĩ, S. Richter, M. Braun-Unkhoff, C. Naumann, and U. Riedel, "A study on fundamental combustion properties of trimethyl orthoformate: Experiments and modelling," *Proc. ASME Turbo Expo.*, GT2022-83029, Rotterdam, Netherlands, 2022.

# B Fundamentals of chemical kinetics

## B.1 Introduction

This work focuses on ignition delay times and laminar burning velocities of various $OME_n$ and on blends of selected $OME_n$ with a gasoline surrogate; see Table 3.1. Ignition delay times and laminar burning velocities are important fundamental combustion properties that serve to describe the combustion process of the fuel. In combustion experiments, the knowledge of kinetic kinetics is important in the interpretation of fundamental kinetics experiments, *e.g.*, on how different experimental conditions of temperature, pressure, fuel-air equivalence ratio, and grade of dilution can influence the speed of chemical processes. In addition, detailed chemical kinetic models are a prerequisite, among others, in CFD modeling focusing on optimization and ultimately in the development of more advanced, safe, and combustion devices, and in helping to understand complex phenomena in combustion devices. This section introduces the fundamentals of gas-phase chemical kinetics.

## B.2 Stoichiometry and reaction rate

In combustion, the equation of an elementary reaction r in a reaction mechanism can be represented by [102, 105]:

$$\sum_{s=1}^{S} {v_{rs}}^{(e)} A_s \xrightarrow{k_r} \sum_{s=1}^{S} {v_{rs}}^{(p)} A_s, \tag{B.1}$$

where $A_s$ represents species $s$, ${v_{rs}}^{(e)}$ and ${v_{rs}}^{(p)}$ are respectively the stoichiometric coefficients of species $A_s$ in the educts (reactants) and products, $k_r$ is the rate coefficient of the of the elementary reaction, and $S$ represents the total number of species. According to the rule of mass action, the rate of the elementary reaction is expressed as:

$$r_i = k_r \prod_{s=1}^{S} {C_s}^{{v_{rs}}^{e}}, \tag{B.2}$$

where, $r_i$ is the is the rate of the elementary reaction and $C_s$ is the molar concentration of species $s$. The overall production rate ($\dot{w}$) of $i^{th}$ species in an elementary reaction $r$ is given by:

$$\left(\frac{\partial c_i}{\partial t}\right)_{chem,r} = k_r \left({v_{ri}}^{(e)} - {v_{ri}}^{(p)}\right) \prod_{s=1}^{S} {c_s}^{{v_{rs}}^{(e)}}. \tag{B.3}$$

The generalized expression for a reaction mechanism composed of S species taking part in R reactions is given by

$$\sum_{s=1}^{S} {v_{rs}}^{(e)} A_s \xrightarrow{k_r} \sum_{s=1}^{S} {v_{rs}}^{(p)} A_s, \quad \text{with} \quad r = 1, ..., R. \tag{B.4}$$

The rate of formation of species $s$ is formulated as follows by summation over the rate equations of all the elementary reactions:

$$\dot{w} = \left(\frac{\partial c_i}{\partial t}\right)_{chem} = \sum_{r=1}^{R} k_r \left({v_{ri}}^{(p)} - {v_{ri}}^{(e)}\right) \prod_{s=1}^{S} {c_s}^{{v_{rs}}^{(e)}} \quad \text{with} \quad i = 1, \ldots, S. \tag{B.5}$$

## B.3 Temperature dependence of reaction rates

The rate coefficient of the elementary step $r$ depend strongly in a nonlinear way on temperature [92]. This dependence is expressed by Arrhenius law as:

$$K_r = AT^n \exp\left(\frac{-E_a}{RT}\right) \tag{B.6}$$

where, $A$ is the pre-exponential factor, $-E_a$ is the activation energy, $R$ is the gas constant, $T$ is the temperature, and $b$ is the temperature exponent. The parameters $A$, $n$ and $-E_a$ are specified in the reaction mechanism for all the elementary reaction steps.

## B.4 Pressure dependence of reaction rate expressions

The rate coefficients of radical-radical recombination reactions, isomerization reactions, and dissociation reactions are pressure-dependent. According to Lindemann model, a pressure dependent reaction, *e.g.*, reaction (B.7) occurs in two-steps [102, 150]. In the first step, the activated species $A^*$ is produced in an excitation process through collision with a third body molecule M; see reaction (B.8). In the second step, the activated species $A^*$ can either deactivate through reaction (B.9) by collision with a third body molecule or decompose into products through reaction (B.10).

$$A \xrightarrow{k_{uni}} \text{Products (P)} \tag{B.7}$$

$$A + \text{M} \xrightarrow{k_a} A^* + \text{M} \tag{B.8}$$

$$A^* + \text{M} \xrightarrow{k_{-a}} A + \text{M} \tag{B.9}$$

$$A^* \xrightarrow{k_u} \text{Products (P)} \tag{B.10}$$

The rate expressions for this case are given by:

$$\frac{dP}{dt} = K_u[A^*], \quad \text{and} \tag{B.11}$$

$$\frac{d[A^*]}{dt} = K_a[A][\mathrm{M}] - K_{-a}[A^*][\mathrm{M}] - K_u[A^*] \tag{B.12}$$

By considering the steady-state assumption, *i.e.*, $\frac{d[A^*]}{dt} = 0$, the concentration of the activated species $[A^*]$ and the formation of the product (P) are given by:

$$[A^*] = \frac{K_u A[\mathrm{M}]}{K_a \mathrm{M} + K_u} \tag{B.13}$$

$$\frac{d\mathrm{P}}{dt} = K_u[A^*] = \frac{K_u K_a A[\mathrm{M}]}{K_a \mathrm{M} + K_u} = K_{uni}[A] \tag{B.14}$$

From Eqn. (B.14), $K_{uni}$ can be expressed as follows:

$$K_{uni} = \frac{K_u K_a[\mathrm{M}]}{K_a M + K_u} \tag{B.15}$$

At low pressures, the concentration of M is very small, such that [M]→0 and at high-pressures the concentration of M is large, *i.e.* $[M]\rightarrow\infty$. The rate coefficients for these cases are:

$$[\mathrm{M}]\rightarrow 0, \qquad K_{uni} = K_0 = K_a[\mathrm{M}] \tag{B.16}$$

$$[\mathrm{M}]\rightarrow \infty, \qquad K_{uni} = K_\infty = \frac{K_u K_a}{K_{-a}} \tag{B.17}$$

where, $K_0$ and $K_\infty$ are the rate coefficients at low-pressure and high-pressures respectively. In the low-pressure regime, the rate-coefficient is proportional to the concentration [M], and thus giving a linear dependence between $K_{uni}$ and pressure. However, the linear dependence ceases at a certain pressure and falls-off to the high-pressure limit. In the high-pressure regime, the rate coefficient is independent of pressure. The transition region corresponding to intermediate pressure regime where $K_0$ departs from the linear relationship and 'falls-off" to $K_\infty$ is called the fall-off region. Figure B.1 shows an example of typical fall-off curves obtained for $C_2H_6 \longrightarrow 2CH_3$ (+M). It is shown that the fall-off curves are strongly dependent on temperatures. Thus, the rate coefficients of unimolecular reactions show different temperature dependencies at different values of pressures. The F-center approach is commonly used in treatment of pressure dependent reactions.

The unimolecular rate coefficient at any pressure is expressed in terms of reduced pressure ($p_r$) as,

$$K = K_\infty \left( \frac{P_r}{1 + P_r} \right) F \tag{B.18}$$

where, $F$ is the broadening factor. The reduced pressure ($p_r$) is given by:

$$P_r = \frac{K_0[\mathrm{M}]}{K_\infty} = 0. \tag{B.19}$$

When calculating the effective concentrations [M] of the third body, the collision efficiencies $m_{y,i}$

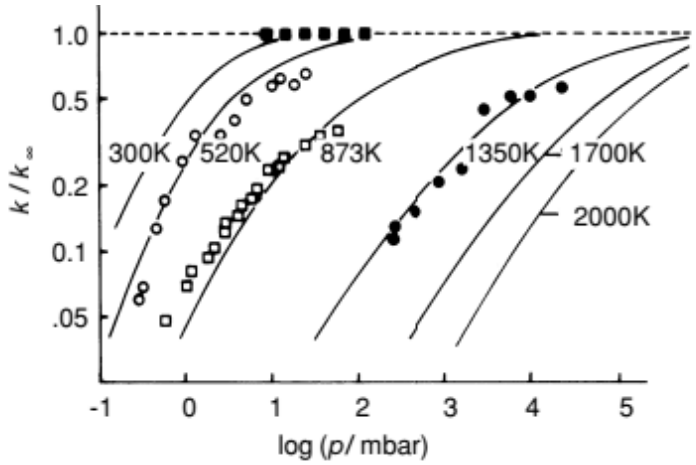


**Figure B.1:** Fall-off curves for the unimolecular decomposition $C_2H_6 \longrightarrow 2CH_3$ ($+M$). Adopted from Warnatz *et al.* [102]

are taken into consideration as follows:

$$[\mathrm{M}] = \sum_i m_{y,i}[Yi] \tag{B.20}$$

Nitrogen is the most commonly used bath gas and it is assumed to have a collision efficiency of unity. Other collisions partners are compared against it because it is the most commonly used bath gas in experiments [105]. In Eqn. (B.18), the simplest approach also known as Lindemann assumes a value of unity for parameter $F$. In practice, this approach does not adequately describe the pressure dependence in the fall-off region, and hence, the $F$-center approach as suggested by Troe [151] is commonly used to compute the value of $F$, see Eqns. (B.21) and (B.22).

$$F_{cent} = a.exp\left(\frac{T}{T^*}\right) + exp\left(\frac{T}{T^{**}}\right) + (1 - a).exp\left(\frac{T}{T^{***}}\right) \tag{B.21}$$

This equation is used to calculate the value of $F$ via:

$$logF = logF_{cent}\left[1 + \left(\frac{logp_r + c}{n - d.(logp_r + c)}\right)\right]^{-1} \tag{B.22}$$

with, $c = -0.4 - 0.67logF_{cent}$, $n = 0.75 - 1.27logF_{cent}$, $d = 0.14$, and $p_r = \frac{K_0[\mathrm{M}]}{K_\infty}$ The parameters $a$, $T^{***}$, $T^*$ and in Eqn. (B.21) are provided as input or are defined in the reaction mechanism.

## B.5 Thermodynamic properties

The rate constant of the reverse reaction $k_{r,i}$ for the reaction step $i$ is related to the forward rate constant $k_{f,i}$ through the equilibrium constant $k_{c,i}$ as follows:

$$k_{r,i} = \frac{k_{f,i}}{k_{c,i}} \tag{B.23}$$

The equilibrium composition of the mixture in concentration units (mol / sec) is calculated from standard thermodynamic state-properties of the mixture as follows:

$$k_{c,i} = k_{p,i}\left(\frac{P_o}{RT}\right)^{v_{i,j}^{p} - v_{i,j}^{(}e} \tag{B.24}$$

where, $k_{p,i}$ is given by:

$$k_{p,i} = exp\left(\frac{{G_r}^o}{RT}\right) = \left(\frac{\Delta {s_i}^o}{R} - \frac{\Delta {H_i}^o}{RT}\right) \tag{B.25}$$

In Eqn. (B.25), $\Delta {G_r}^o$ is the standard molar Gibbs free energy of a reaction. $\Delta {H_i}^o$ is the molar standard enthalpy of a reaction and $\Delta {s_i}^o$ is the molar standard entropy of a reaction. $\Delta {H_i}^o$ and $\Delta {s_i}^o$ are defined as follows:

$$\Delta {H_i}^o(T) = \sum_j ({v_{i,j}}^p - {v_{i,j}}^e){H_i}^o(T), and \tag{B.26}$$

$$\Delta {S}_i{}^o(T) = \sum_j (v_{i,j}^p - v_{i,j}^e){s_i}^o(T). \tag{B.27}$$

The standard state molar enthalpy (${H_i}^o$) and entropy (${s_i}^o$) are expressed as follows:

$$H_i^o(T) = H_{i,298\ K}^o + \int_{298\ K}^{T} C_{p,i}^o\, dt \tag{B.28}$$

$$s_i^o(T) = s_{i,298\ K}^o + \int_{298\ K}^{T} s_{p,i}^o\, dt \tag{B.29}$$

The parameters $H^o_{i,298\ K}$ and $s^o_{i,298\ K}$ are the standard heat of formation at 298 K and standard state entropy at 298 K. The standard state $c^o_{p,i}$, $H^o_{i,298\ K}$ and $s^o_{i,298\ K}$ are required to compute reverse rate constants through equilibrium constants and other thermodynamic properties *i.e.*, $c^o_{v,i}$, $G^o_i$, and $\gamma = c_p/c_v$. The thermodynamic properties of many species are tabulated in thermodynamic data bases as functions of temperatures, for example by Goos and Burcat [152] and Burcat and Ruscic [153]. The thermodynamic data is provided in form of polynomial fits of the following form:

$$\frac{C^o_{p,i}}{R} = a_1 + a_2T + a_3T^2 + a_4T^3 + a_5T^4, \tag{B.30}$$

$$\frac{H^o_i}{RT} = a_1 + \frac{a_2T}{2} + \frac{a_3T^2}{3} + \frac{a_4T^3}{4} + \frac{a_5T^4}{5} + \frac{a_6}{T}, \tag{B.31}$$

$$\frac{S^o_i}{R} = a_1 lnT + a_2T + \frac{a_3T^2}{2} + \frac{a_4T^3}{3} + \frac{a_5T^4}{4} + a_7. \tag{B.32}$$

For each species, 14 coefficients ($a_1 - a_{14}$) are specified in the input file containing thermodynamic data. The first seven coefficients ($a_1 - a_7$) as shown in Eqns. (B.30)–(B.32) are used for calculating thermodynamics functions in the high-temperature range, typically between 1000-5000 K and the last seven coefficients ($a_8 - a_{14}$) are used in the low-temperature regime, typically between 300-1000 K. The common temperature connecting the two regimes is arbitrarily set at 1000 K.

# C CH* and OH* chemiluminescence reactions from Kathrotia *et al.* [104]

| Reactions | A [cm, mol, s] | n [-] | E [cal·mol$^{-1}$] |
|---|---|---|---|
| H + O + M ⇌ OH* + M | 1.50E+13 | 0.00 | 5975.14 |
| CH + O2 ⇌ OH* + CO | 1.80E+11 | 0.00 | 0.00 |
| OH* ⇌ OH | 1.45E+06 | 0.00 | 0.00 |
| OH* + O2 ⇌ OH + O2 | 2.10E+12 | 0.50 | -482.79 |
| OH* + H2O ⇌ OH + H2O | 5.93E+12 | 0.50 | -862.81 |
| OH* + H2 ⇌ OH + H2 | 2.95E+12 | 0.50 | -444.55 |
| OH* + CO2 ⇌ OH + CO2 | 2.76E+12 | 0.50 | -970.36 |
| OH* + CO ⇌ OH + CO | 3.23E+12 | 0.50 | -788.72 |
| OH* + CH4⇌ OH + CH4 | 3.36E+12 | 0.50 | -635.76 |
| OH* + OH ⇌OH + OH | 6.01E+12 | 0.50 | -762.43 |
| OH* + H ⇌OH + H | 1.31E+13 | 0.50 | -167.30 |
| OH* + Ar ⇌ OH + Ar | 1.69E+12 | 0.00 | 4139.58 |
| OH* + M ⇌ OH + M | 2.53E+12 | 0.00 | 4139.58 |
| C2H + O2 ⇌ CH* + CO2 | 3.20E+11 | 0.00 | 1601.34 |
| C2H + O ⇌ CH* + CO | 2.50E+12 | 0.00 | 0.00 |
| C2 + OH ⇌ CH* + CO | 1.11E+13 | 0.00 | 0.00 |
| C + H + M ⇌ CH* + M | 3.63E+13 | 0.00 | 0.00 |
| CH* ⇌ CH | 1.86E+06 | 0.00 | 0.00 |
| CH* + O2 ⇌ CH + O2 | 2.48E+06 | 2.10 | -1720.84 |
| CH* + CO2 ⇌ CH + CO2 | 2.40E-01 | 4.30 | -1696.94 |
| CH* + CO ⇌ CH + CO | 2.44E+12 | 0.50 | 0.00 |
| CH* + CH4 ⇌ CH + CH4 | 1.73E+13 | 0.00 | 167.30 |
| CH* + H2O ⇌ CH + H2O | 5.30E+13 | 0.00 | 0.00 |
| CH* + H ⇌ CH + H | 2.01E+14 | 0.00 | 1362.33 |
| CH* + OH ⇌ CH + OH | 7.13E+13 | 0.00 | 1362.33 |
| CH* + H2 ⇌ CH + H2 | 1.47E+14 | 0.50 | 1362.33 |
| CH* + Ar ⇌ CH + Ar | 3.13E+11 | 0.00 | 0.00 |
| CH* + M ⇌ CH + M | 4.69E+11 | 0.00 | 0.00 |
| O2/0.0/ OH/0.0/ H2/0.0/ AR/0.0/ H/0.0/ H2O/0.0/ CO/0.0/ CO2/0.0/ CH4/0.0/ | | | |

# D Shock tube relations

## D.1 Determination of the conditions behind the reflected shock wave

The observable parameters in shock tube ignition delay time measurements are shock wave arrival times at the test section and pressure signals. Because the processes involved are so fast and do not coincide with the response time of thermocouples, direct determination of temperature behind the reflected shock wave via thermocouples is difficult. Conventionally, gas dynamics relationships are used to deduce the conditions behind the reflected shock wave with the incident shock velocity and initial test gas composition as input parameters. Even though, the temperature behind the reflected shock waves has been determined using chemical thermometers and laser absorption spectroscopic techniques, and the results are comparable to those obtained using the generally used gas dynamic approach [154–156].
When applying the gas dynamics method, the following assumptions and simplifications for the ideal behavior of the shock tube are made [111, 123]:

- The shock front is homogeneous, planar, one-dimensional and propagates through the tube at constant velocity. Mixing and spatial gradients are neglected;
- The gas in the tube is assumed to be a perfect gas with a constant specific heat;
- The chemical composition of the driver and driven gases are not changing (non-reacting flow);
- No mass diffusion across the contact surface, *i.e.*, the driver and the driven gases do not mix at the contact surface;
- The diaphragm opens instantaneously and completely and that the incident shock wave attains the full strength within a short time period;
- The flow processes in the shock tube are assumed to be adiabatic;
- No reflected waves from the expansion fan overtake the contact surface;
- Interactions of the shock wave with the shock tube wall can also be neglected, since the diameter of the shock tube over the boundary layer thickness is sufficiently large.

- Test times behind shock waves are typically about a few hundred microseconds; hence, neglect of these transport processes is of little consequence.

By starting from the shock fixed co-ordinates, *i.e.*, by considering the motion of the gas in relation to the shock front, the conservation equations for mass, momentum and energy, see Eqns. D.1 - D.3 are applied before and behind the reflected shock front (Rankine Hugoniot relations).

- Continuity

$$\rho_1 u_1 = \rho_2 u_2 \tag{D.1}$$

- Momentum

$$p_1 u_1 + \rho_1 {u_1}^2 = p_2 u_2 + \rho_2 {u_2}^2 \tag{D.2}$$

- Energy

$$h_1 + \frac{1}{2}{u_1}^2 = h_2 + \frac{1}{2}{u_2}^2 \tag{D.3}$$

In Eqns. D.1 - D.3, $\rho$ is the density, $u$ is the velocity, $p$ is the pressure and $h$ is the enthalpy. The conditions immediately behind the reflected shock wave (test region), *i.e.*, $p_5 = p(t = 0)$ and $T_5 = T(t = 0)$ are then obtained only as a function of the Mach number $\mathrm{M}_1$ of the incident shock wave, see Eqns. D.4 - D.5. Details on their derivations have been detailed in various literature sources; for example, by [111].

$$\frac{p_5}{p_1} = \left[\frac{2\gamma_1 {\mathrm{M}_1}^2 - (\gamma_1 - 1)}{\gamma_1 + 1}\right] \cdot \left[\frac{(3\gamma_1 - 1){\mathrm{M}_1}^2 - 2(\gamma_1 - 1)}{(\gamma_1 - 1){\mathrm{M}_1}^2 + 2}\right] \tag{D.4}$$

$$\frac{T_5}{T_1} = \frac{[(2\gamma_1 - 1){\mathrm{M}_1}^2 + (3 - \gamma_1)] \cdot [(3\gamma_1 - 1){\mathrm{M}_1}^2 - 2(\gamma_1 - 1)]}{(\gamma_1 + 1)^2 {\mathrm{M}_1}^2} \tag{D.5}$$

In Eqns. D.6 - D.9, $\mathrm{M}_1$ is the Mach number of the incident shock wave, $\gamma$ is the ratio of the specific heat capacities, and $p_1$ and $T_1$ are respectively the initial pressure and temperature in the driven section. Mach number $\mathrm{M}_1$ is determined from Eqn. D.6 in which the incident velocity $u_1$ is derived from the experiment and the speed of the sound $c_1$ is determined from Eqn. D.7. Because the test gas (fuel and air mixture) consists of a mixture of N-different gases, the averaged molar weight $\bar{M}$ and the ratio of specific heat capacity $k$ in Eqn. D.7 are weighted based on the molar fraction $x_i$ of the gases in the mixture, see Eqns. D.8 and D.9.

- Mach number, $\mathrm{M}_1$

$$\mathrm{M}_1 = \frac{u_1}{c_1} \tag{D.6}$$

- The speed of the sound, $c_1$

$$c_1 = \sqrt{\frac{KRT_1}{\bar{M}}} \tag{D.7}$$

- Averaged molar mass, $\bar{M}$

$$\bar{M} = \sum_{i=1}^{N} x_i M_i \tag{D.8}$$

- Averaged ratio

$$\bar{\gamma} = \sum_{i=1}^{N} x_i \gamma_i = \sum_{i=1}^{N} x_i \frac{c_{p,i}}{c_{v,i}} \tag{D.9}$$

In Eqn. D.9, the thermodynamics properties, namely the specific heat capacities $c_{p,i}$ and $c_{v,i}$ are required to determine the value of $\gamma$. The specific heat capacity at constant pressure $c_{p,i}$ of each species present in the fuel mixture are determined from the NASA $4^{th}$ order polynomial curve fits as shown in Eqn. D.10 [152].The parameters $a_1$ to $a_5$ for each species are found in the supplied thermodynamic data file. The thermodynamic data file contains the two sets of coefficients for low-temperature and high-temperature regime. The specific heat capacity at constant volume $c_{v,i}$ of each species is determined from the relation $c_{p,i} = c_{v,i} + R$ , where $R$ is the gas constant.

$$\frac{c_{p,i}(T)}{R} = a_1 + a_2 T + a_3 T^2 + a_4 T^3 + a_5 T^4 \tag{D.10}$$

From Eqns. D.8 and D.9 it is implied that the experimental conditions behind the reflected shock wave (test region), namely $p_5$ and $T_5$ are determined from initial operating conditions and the geometry of the shock tube.

# E Dimethyl ether (DME)

## E.1 Measured ignition delay time data for DME

| Expt. No | $T_5$ [K] | $p_5$ [bar] | $\tau_{head-on}$ [$\mu s$] $\gamma$ = 431 nm (CH*) | $\tau_{side-on}$ [$\mu s$] $\gamma$ = 431 nm (CH*) | $\tau_{head-on}$ [$\mu s$] $\gamma$= 308 nm (OH*) | $\tau_{side-on}$ [$\mu s$] $\gamma$ = 308 nm (OH*) |
|---|---|---|---|---|---|---|
| 6216 | 1633 | 0.9 | 43 | 37 | 49 | 38 |
| 6217 | 1721 | 1 | 30 | 21 | 27 | 21 |
| 6218 | 1789 | 1 | 25 | 14 | 19 | 12 |
| 6219 | 1697 | 1 | 36 | 24 | 29 | 24 |
| 6220 | 1529 | 1 | 93 | 74 | 90 | 75 |
| 6221 | 1507 | 1 | 92 | 89 | 109 | 87 |
| 6224 | 1436 | 1 | 217 | 200 | 214 | 194 |
| 6229 | 1397 | 1.1 | 444 | 344 | 351 | 333 |
| 6230 | 1352 | 1 | 769 | 1141 | 733 | 1045 |
| 6234 | 1476 | 1.1 | 143 | 135 | 163 | 129 |
| 6236 | 1205 | 1.1 | 10550 | 12310 | 10397 | 12170 |
| 6238 | 1604 | 1 | 58 | 43 | 55 | 46 |
| 6239 | 1332 | 1.1 | 1619 | 1552 | 936 | 740 |
| 6241 | 1318 | 1.1 | 2080 | 2446 | 1951 | 2489 |
| 6243 | 1231 | 1 | 7557 | 8410 | 7500 | 8076 |
| 6248 | 1286 | 1.1 | 3132 | 3511 | 3107 | 3559 |
| 6250 | 1259 | 1.1 | 4298 | 5137 | 4237 | 5086 |
| 6172 | 1468 | 4.1 | 118 | 86 | 84 | 86 |
| 6173 | 1543 | 4.1 | 33 | 33 | 53 | 35 |
| 6174 | 1676 | 4.1 | 10 | 10 | 11 | 11 |
| 6175 | 1629 | 4.1 | 18 | 13 | 18 | 15 |
| 6177 | 1399 | 4 | 316 | 224 | 342 | 217 |
| 6178 | 1275 | 3.8 | 1340 | 1633 | 1236 | 1510 |
| 6179 | 1340 | 3.9 | 599 | 455 | 448 | 453 |

| | | | | | | |
|---|---|---|---|---|---|---|
| Cont'd | | | | | | |
| 6180 | 1375 | 3.7 | 444 | 323 | 425 | 315 |
| 6181 | 1302 | 3.6 | 880 | 766 | 858 | 754 |
| 6182 | 1120 | 4.1 | 5427 | 7097 | 5444 | 7048 |
| 6183 | 1104 | 4 | 6881 | 7640 | 6843 | 7723 |
| 6184 | 1222 | 4 | 2541 | 2726 | 2245 | 2713 |
| 6185 | 1174 | 4.1 | 3648 | 3916 | 3595 | 4110 |
| 6186 | 1491 | 4 | 62 | 66 | 62 | 66 |
| 6192 | 1063 | 3.8 | 9621 | 11491 | 9599 | 11582 |
| 6193 | 1582 | 4 | 24 | 19 | 32 | 22 |
| 6194 | 1440 | 4.1 | 149 | 120 | 129 | 115 |
| 6196 | 1700 | 16 | 5 | 4 | 5 | 5 |
| 6199 | 1368 | 15.3 | 230 | 176 | 183 | 175 |
| 6200 | 1578 | 14.3 | 15 | 13 | 15 | 14 |
| 6202 | 1439 | 16.5 | 96 | 75 | 91 | 76 |
| 6203 | 1212 | 16.5 | 1307 | 1234 | 1267 | 1247 |
| 6205 | 1296 | 16.2 | 490 | 445 | 488 | 442 |
| 6206 | 1145 | 16.3 | 2527 | 3070 | 2515 | 3103 |
| 6207 | 1496 | 15.8 | 37 | 37 | 52 | 39 |
| 6208 | 1126 | 15.9 | 2930 | 3284 | 2925 | 3404 |
| 6209 | 1084 | 16.2 | 4094 | 4805 | 4090 | 4778 |
| 6211 | 1058 | 16.5 | 5457 | 7400 | 5441 | 7466 |
| 6214 | 1032 | 16.1 | 7833 | 9918 | 7792 | 9860 |
| Combustible mixture in ppm: DME: 13104; $O_2$: 39298; $N_2$: 947598 | | | | | | |

## E.2 Experimental pressure profile for DME at 4 bar

| time [$\mu s$] | $p(t)$ / $p(t = 0)$ | | | | |
|---|---|---|---|---|---|
| 0 | 1 | Cont'd | | Cont'd | |
| 51 | 1 | 1566 | 1.07 | 3081 | 1.26 |
| 101 | 1 | 1616 | 1.07 | 3131 | 1.27 |
| 152 | 1 | 1667 | 1.08 | 3182 | 1.28 |
| 202 | 1 | 1717 | 1.08 | 3232 | 1.29 |
| 253 | 1 | 1768 | 1.09 | 3283 | 1.3 |
| 303 | 1 | 1818 | 1.09 | 3333 | 1.3 |
| 354 | 1 | 1869 | 1.1 | 3384 | 1.31 |
| 404 | 1.01 | 1919 | 1.1 | 3434 | 1.32 |
| 455 | 1.01 | 1970 | 1.11 | 3485 | 1.33 |
| 505 | 1.01 | 2020 | 1.11 | 3535 | 1.34 |
| 556 | 1.01 | 2071 | 1.12 | 3586 | 1.34 |
| 606 | 1.01 | 2121 | 1.13 | 3636 | 1.35 |
| 657 | 1.01 | 2172 | 1.13 | 3687 | 1.36 |
| 707 | 1.02 | 2222 | 1.14 | 3737 | 1.37 |
| 758 | 1.02 | 2273 | 1.15 | 3788 | 1.37 |
| 808 | 1.02 | 2323 | 1.15 | 3838 | 1.38 |
| 859 | 1.02 | 2374 | 1.16 | 3889 | 1.39 |
| 909 | 1.02 | 2424 | 1.17 | 3939 | 1.39 |
| 960 | 1.03 | 2475 | 1.17 | 3990 | 1.4 |
| 1010 | 1.03 | 2525 | 1.18 | 4040 | 1.4 |
| 1061 | 1.03 | 2576 | 1.19 | 4091 | 1.41 |
| 1111 | 1.04 | 2626 | 1.19 | 4141 | 1.41 |
| 1162 | 1.04 | 2677 | 1.2 | 4192 | 1.42 |
| 1212 | 1.04 | 2727 | 1.21 | 4242 | 1.42 |
| 1263 | 1.05 | 2778 | 1.22 | 4293 | 1.42 |
| 1313 | 1.05 | 2828 | 1.22 | 4343 | 1.43 |
| 1364 | 1.05 | 2879 | 1.23 | 4394 | 1.43 |
| 1414 | 1.06 | 2929 | 1.24 | 4444 | 1.43 |
| 1465 | 1.06 | 2980 | 1.25 | 4495 | 1.43 |
| 1515 | 1.07 | 3030 | 1.26 | 1000000 | 1.43 (Extrapolation) |
| Combustible mixture in ppm: DME: 13104; $O_2$: 39298; $N_2$: 947598 | | | | | |

## E.3 Experimental pressure profile for DME at 16 bar

| time [$\mu s$] | $p(t)$ / $p(t = 0)$ | | | | |
|---|---|---|---|---|---|
| 0 | 1 | Cont'd | | Cont'd | |
| 79 | 1 | 2048 | 1.12 | 4018 | 1.3 |
| 158 | 1 | 2127 | 1.13 | 4097 | 1.31 |
| 236 | 1 | 2206 | 1.14 | 4176 | 1.31 |
| 315 | 1 | 2285 | 1.15 | 4255 | 1.31 |
| 394 | 1 | 2364 | 1.16 | 4333 | 1.32 |
| 473 | 1.01 | 2442 | 1.17 | 4412 | 1.32 |
| 552 | 1.01 | 2521 | 1.17 | 4491 | 1.32 |
| 630 | 1.01 | 2600 | 1.18 | 4570 | 1.32 |
| 709 | 1.02 | 2679 | 1.19 | 4648 | 1.32 |
| 788 | 1.02 | 2758 | 1.2 | 4727 | 1.32 |
| 867 | 1.02 | 2836 | 1.21 | 4806 | 1.32 |
| 945 | 1.03 | 2915 | 1.21 | 1000000 | 1.32 (Extrapolation) |
| 1024 | 1.03 | 2994 | 1.22 | | |
| 1103 | 1.04 | 3073 | 1.23 | | |
| 1182 | 1.04 | 3152 | 1.24 | | |
| 1261 | 1.05 | 3230 | 1.25 | | |
| 1339 | 1.06 | 3309 | 1.25 | | |
| 1418 | 1.06 | 3388 | 1.26 | | |
| 1497 | 1.07 | 3467 | 1.27 | | |
| 1576 | 1.08 | 3545 | 1.27 | | |
| 1655 | 1.08 | 3624 | 1.28 | | |
| 1733 | 1.09 | 3703 | 1.28 | | |
| 1812 | 1.1 | 3782 | 1.29 | | |
| 1891 | 1.11 | 3861 | 1.29 | | |
| 1970 | 1.11 | 3939 | 1.3 | | |

Combustible mixture in ppm: DME: 13104; $O_2$: 39298; $N_2$: 947598

# F Oxymethylene ether–1 ($OME_1$)

## F.1 Measured ignition delay time data for $OME_1$

| Expt. No | $T_5$ [K] | $p_5$ [bar] | $\tau_{head-on}$ [$\mu s$] $\gamma$ = 431 nm (CH*) | $\tau_{side-on}$ [$\mu s$] $\gamma$ = 431 nm (CH*) | $\tau_{head-on}$ [$\mu s$] $\gamma$ = 308 nm (OH*) | $\tau_{side-on}$ [$\mu s$] $\gamma$ = 308 nm (OH*) |
|---|---|---|---|---|---|---|
| 6258 | 1625 | 1.1 | 40 | 32 | 44 | 25 |
| 6259 | 1553 | 1 | 64 | 53 | 56 | 52 |
| 6260 | 1662 | 1.1 | 31 | 24 | 26 | 26 |
| 6261 | 1493 | 1 | 104 | 92 | 75 | 90 |
| 6264 | 1452 | 1 | 133 | 121 | 131 | 114 |
| 6266 | 1423 | 1 | 164 | 147 | 162 | 148 |
| 6267 | 1387 | 1 | 250 | 237 | 248 | 230 |
| 6269 | 1335 | 1 | 452 | 588 | 435 | 363 |
| 6270 | 1253 | 0.9 | 1880 | 1850 | 1090 | 1840 |
| 6271 | 1295 | 1 | 1080 | 943 | 650 | 535 |
| 6272 | 1232 | 0.9 | 2710 | 2640 | 1520 | 2420 |
| 6273 | 1208 | 0.9 | 3360 | 3780 | 2450 | 3670 |
| 6274 | 1580 | 1 | 57 | 47 | 44 | 34 |
| 6276 | 1217 | 1 | 3250 | 3640 | 1990 | 3530 |
| 6277 | 1188 | 1.1 | 4790 | 4830 | 3840 | 4730 |
| 6278 | 1138 | 1.1 | 9630 | 10610 | 9060 | 9820 |
| 6279 | 1108 | 1.1 | 13120 | 14760 | 12000 | 14620 |
| 6280 | 1168 | 1.1 | 5710 | 7250 | 4740 | 7130 |
| 6283 | 1569 | 4 | 21 | 19 | 22 | 21 |
| 6284 | 1630 | 4.3 | 12 | 12 | 14 | 13 |
| 6285 | 1631 | 4 | 14 | 13 | 13 | 13 |
| 6287 | 1665 | 3.8 | 11 | 10 | 12 | 12 |
| 6288 | 1720 | 3.9 | 8 | 8 | 8 | 9 |
| 6291 | 1460 | 4.2 | 58 | 56 | 57 | 56 |
| 6292 | 1516 | 4.1 | 35 | 30 | 34 | 32 |
| 6293 | 1400 | 4.2 | 101 | 100 | 100 | 97 |
| 6294 | 1338 | 4.4 | 291 | 222 | 212 | 216 |

| | | | | | | |
|---|---|---|---|---|---|---|
| Cont'd | | | | | | |
| 6295 | 1370 | 4 | 155 | 153 | 153 | 149 |
| 6296 | 1319 | 4 | 299 | 278 | 275 | 271 |
| 6297 | 1256 | 4.2 | 740 | 612 | 627 | 602 |
| 6298 | 1293 | 3.9 | 485 | 401 | 401 | 391 |
| 6299 | 1239 | 4.1 | 879 | 1090 | 853 | 771 |
| 6300 | 1177 | 4.1 | 1800 | 2230 | 1700 | 2300 |
| 6301 | 1101 | 4 | 4280 | 4260 | 3530 | 4180 |
| 6302 | 1205 | 4.2 | 1210 | 1500 | 1180 | 1490 |
| 6303 | 1112 | 4.1 | 3310 | 4280 | 3290 | 4330 |
| 6304 | 1059 | 4.1 | 5120 | 7290 | 5130 | 7110 |
| 6307 | 1144 | 4.3 | 2390 | 3240 | 2360 | 3020 |
| 6345 | 1135 | 4.5 | 2770 | 3340 | 2320 | 3140 |
| 6323 | 1633 | 16.6 | 4 | 2 | 4 | 3 |
| 6324 | 1607 | 16.5 | 6 | 3 | 6 | 4 |
| 6325 | 1428 | 13.9 | 49 | 40 | 45 | 40 |
| 6326 | 1485 | 14.4 | 29 | 20 | 22 | 21 |
| 6327 | 1546 | 15.1 | 14 | 10 | 20 | 19 |
| 6329 | 1372 | 15.5 | 94 | 80 | 107 | 80 |
| 6330 | 1288 | 16.1 | 293 | 239 | 292 | 237 |
| 6331 | 1253 | 15.5 | 432 | 380 | 428 | 378 |
| 6332 | 1228 | 15.8 | 574 | 526 | 564 | 524 |
| 6333 | 1208 | 16.5 | 738 | 694 | 727 | 693 |
| 6334 | 1163 | 15.6 | 1230 | 1210 | 1210 | 1210 |
| 6335 | 1139 | 16 | 1600 | 1600 | 1590 | 1610 |
| 6336 | 1319 | 15.6 | 218 | 161 | 210 | 156 |
| 6337 | 1099 | 15.9 | 2540 | 2900 | 2540 | 2900 |
| 6338 | 1079 | 16.3 | 2850 | 2980 | 2850 | 2980 |
| 6339 | 1063 | 16.1 | 3390 | 3530 | 3390 | 3510 |
| 6340 | 1044 | 16.3 | 4060 | 5130 | 4060 | 5470 |
| 6343 | 1006 | 16.3 | 4660 | 6310 | 7140 | 9530 |
| 6344 | 1185 | 16.1 | 889 | 846 | 881 | 818 |
| Combustible mixture in ppm: DME: 13104; $O_2$: 39298; $N_2$: 947598 | | | | | | |

## F.2 Experimental pressure profile for $OME_1$ at 4 bar

| time [$\mu$s] | $p(t)$ / $p(t = 0)$ | | | | |
|---|---|---|---|---|---|
| 0 | 1 | Cont'd | | Cont'd | |
| 67 | 1 | 1600 | 1.09 | 3438 | 1.36 |
| 135 | 1 | 1618 | 1.09 | 3506 | 1.37 |
| 200 | 1 | 1685 | 1.09 | 3573 | 1.38 |
| 202 | 1 | 1753 | 1.1 | 3640 | 1.39 |
| 270 | 1.01 | 1800 | 1.11 | 3708 | 1.39 |
| 337 | 1.01 | 1820 | 1.11 | 3775 | 1.4 |
| 400 | 1.01 | 1888 | 1.12 | 3843 | 1.41 |
| 404 | 1.01 | 1955 | 1.12 | 3910 | 1.41 |
| 472 | 1.02 | 2000 | 1.13 | 3978 | 1.42 |
| 539 | 1.02 | 2022 | 1.13 | 4045 | 1.42 |
| 600 | 1.02 | 2090 | 1.14 | 4112 | 1.43 |
| 607 | 1.02 | 2157 | 1.15 | 4180 | 1.43 |
| 674 | 1.03 | 2225 | 1.16 | 4247 | 1.43 |
| 742 | 1.03 | 2292 | 1.17 | 4315 | 1.43 |
| 800 | 1.03 | 2360 | 1.18 | 1000000 | 1.43 (Extrapolation) |
| 809 | 1.03 | 2427 | 1.19 | | |
| 876 | 1.04 | 2494 | 1.2 | | |
| 944 | 1.04 | 2562 | 1.21 | | |
| 1000 | 1.04 | 2629 | 1.22 | | |
| 1011 | 1.04 | 2697 | 1.23 | | |
| 1079 | 1.05 | 2764 | 1.24 | | |
| 1146 | 1.05 | 2831 | 1.26 | | |
| 1200 | 1.06 | 2899 | 1.27 | | |
| 1213 | 1.06 | 2966 | 1.28 | | |
| 1281 | 1.06 | 3034 | 1.29 | | |
| 1348 | 1.07 | 3101 | 1.3 | | |
| 1400 | 1.07 | 3169 | 1.31 | | |
| 1416 | 1.07 | 3236 | 1.33 | | |
| 1483 | 1.08 | 3303 | 1.34 | | |
| 1551 | 1.08 | 3371 | 1.35 | | |
| Combustible mixture in ppm: $OME_1$: 9490; $O_2$: 38277; $N_2$: 952233 | | | | | |

## F.3 Experimental pressure profile for $OME_1$ at 16 bar

| time [$\mu s$] | $p(t)$ / $p(t = 0)$ | | | | |
|---|---|---|---|---|---|
| 0 | 1 | Cont'd | | Cont'd | |
| 67 | 1 | 1416 | 1.07 | 3034 | 1.19 |
| 135 | 1 | 1483 | 1.07 | 3101 | 1.19 |
| 200 | 1.01 | 1551 | 1.08 | 3169 | 1.2 |
| 202 | 1.01 | 1600 | 1.08 | 3236 | 1.21 |
| 270 | 1.01 | 1618 | 1.08 | 3303 | 1.21 |
| 337 | 1.01 | 1685 | 1.08 | 3371 | 1.22 |
| 400 | 1.02 | 1753 | 1.09 | 3438 | 1.22 |
| 404 | 1.02 | 1800 | 1.09 | 3506 | 1.22 |
| 472 | 1.02 | 1820 | 1.09 | 3573 | 1.23 |
| 539 | 1.03 | 1888 | 1.1 | 3640 | 1.23 |
| 600 | 1.03 | 1955 | 1.1 | 3708 | 1.24 |
| 607 | 1.03 | 2000 | 1.1 | 3775 | 1.24 |
| 674 | 1.04 | 2022 | 1.11 | 3843 | 1.24 |
| 742 | 1.04 | 2090 | 1.11 | 3910 | 1.24 |
| 800 | 1.04 | 2157 | 1.12 | 3978 | 1.25 |
| 809 | 1.04 | 2225 | 1.12 | 4045 | 1.25 |
| 876 | 1.05 | 2292 | 1.13 | 4112 | 1.25 |
| 944 | 1.05 | 2360 | 1.13 | 4180 | 1.25 |
| 1000 | 1.05 | 2427 | 1.14 | 4247 | 1.25 |
| 1011 | 1.05 | 2494 | 1.14 | 4315 | 1.25 |
| 1079 | 1.06 | 2562 | 1.15 | 1000000 | 1.25 (Extrapolation) |
| 1146 | 1.06 | 2629 | 1.16 | | |
| 1200 | 1.06 | 2697 | 1.16 | | |
| 1213 | 1.06 | 2764 | 1.17 | | |
| 1281 | 1.06 | 2831 | 1.17 | | |
| 1348 | 1.07 | 2899 | 1.18 | | |
| 1400 | 1.07 | 2966 | 1.18 | | |
| Combustible mixture in ppm: $OME_1$: 9490; $O_2$: 38277; $N_2$: 952233 | | | | | |

# G Oxymethylene ether–2 ($OME_2$)

## G.1 Measured ignition delay time data for $OME_2$

| Expt. No | $T_5$ [K] | $p_5$ [bar] | $\tau_{head-on}$ [$\mu s$] $\gamma$ = 431 nm (CH*) | $\tau_{side-on}$ [$\mu s$] $\gamma$ = 431 nm (CH*) | $\tau_{head-on}$ [$\mu s$] $\gamma$ = 308 nm (OH*) |
|---|---|---|---|---|---|
| 6663 | 1686 | 0.9 | 31 | | 8 |
| 6664 | 1697 | 1.1 | 27 | 19 | 9 |
| 6665 | 1499 | 0.9 | 68 | 83 | 64 |
| 6666 | 1583 | 1.1 | 46 | 34 | 36 |
| 6667 | 1523 | 1.1 | 62 | 46 | 46 |
| 6668 | 1415 | 1.1 | 135 | 118 | 113 |
| 6669 | 1380 | 1.1 | 179 | 156 | 154 |
| 6672 | 1191 | 0.8 | 2180 | 2440 | 2310 |
| 6673 | 1312 | 1.1 | 350 | 335 | 300 |
| 6674 | 1261 | 1.1 | 740 | 756 | 531 |
| 6678 | 1247 | 1.1 | 984 | 765 | 590 |
| 6679 | 1097 | 1 | 7420 | 7530 | 7590 |
| 6680 | 1055 | 1 | 13970 | 14700 | 13320 |
| 6681 | 1155 | 1.1 | 3860 | 3950 | 3760 |
| 6646 | 1676 | 4.2 | 7 | 9 | 7 |
| 6647 | 1536 | 4.4 | 25 | 22 | 19 |
| 6648 | 1421 | 4.2 | 74 | 55 | 53 |
| 6649 | 1302 | 4.1 | 189 | 227 | 179 |
| 6650 | 1219 | 4.3 | 507 | 464 | 451 |
| 6651 | 1180 | 4.2 | 869 | 1030 | 744 |
| 6652 | 1113 | 4.3 | 1940 | 2270 | 2260 |

| | | | | | |
|---|---|---|---|---|---|
| Cont'd | | | | | |
| 6653 | 1056 | 4.1 | 3660 | 4160 | 4100 |
| 6654 | 994 | 4.1 | 6810 | 6900 | 6640 |
| 6655 | 934 | 4 | 11850 | 11250 | 11340 |
| 6656 | 930 | 4.3 | 12230 | 14380 | 13070 |
| 6685 | 1338 | 4.3 | 121 | 135 | 113 |
| 6688 | 1044 | 4.3 | 4510 | 4520 | 4520 |
| 6689 | 1021 | 4 | 5390 | 5390 | 5390 |
| 6615 | 1664 | 15 | 5 | 4 | 5 |
| 6623 | 1285 | 15.1 | 159 | 128 | 126 |
| 6625 | 1500 | 15.4 | 20 | 14 | 14 |
| 6626 | 1409 | 15.4 | 50 | 30 | 29 |
| 6627 | 1252 | 15.3 | 221 | 190 | 186 |
| 6628 | 1223 | 16.1 | 297 | 264 | 261 |
| 6629 | 1167 | 15.3 | 580 | 537 | 535 |
| 6630 | 1113 | 15.1 | 1190 | 1110 | 1110 |
| 6631 | 1092 | 15.5 | 1510 | 1440 | 1440 |
| 6632 | 1016 | 14.4 | 3600 | 3500 | 3500 |
| 6633 | 983 | 14.7 | 5090 | 5030 | 5040 |
| 6634 | 962 | 14.6 | 6050 | 5980 | 5980 |
| 6635 | 943 | 15 | 7150 | 7030 | 7060 |
| 6636 | 908 | 14.4 | 9340 | 9340 | 9320 |
| 6638 | 868 | 14.3 | 12550 | 12590 | 12660 |
| 6639 | 1049 | 15 | 2430 | 2380 | 2380 |
| 6642 | 1344 | 15.4 | 90 | 62 | 62 |
| 6643 | 1590 | 13.2 | 10 | 8 | 7 |
| Combustible mixture in ppm: $OME_2$: 7428; $OME_1$: 274; $CH_3OH$: 133; $O_2$: 38493: $N_2$: 953672 | | | | | |

## G.2 Experimental pressure profile for $OME_2$ at 1 bar

| time [$\mu$s] | $p(t)$ / $p(t = 0)$ | | | | |
|---|---|---|---|---|---|
| 0 | 1 | Cont'd | | Cont'd | |
| 76 | 1 | 1681 | 1 | 3820 | 1.03 |
| 153 | 1 | 1757 | 1 | 3897 | 1.04 |
| 200 | 1 | 1800 | 1 | 3973 | 1.05 |
| 229 | 1 | 1910 | 1 | 4049 | 1.06 |
| 306 | 1 | 1987 | 1 | 4126 | 1.07 |
| 382 | 1 | 2000 | 1 | 4202 | 1.08 |
| 400 | 1 | 2063 | 1 | 4279 | 1.09 |
| 458 | 1 | 2139 | 1 | 4355 | 1.1 |
| 535 | 1 | 2216 | 1 | 4431 | 1.11 |
| 600 | 1 | 2292 | 1 | 4508 | 1.12 |
| 611 | 1 | 2369 | 1 | 4584 | 1.13 |
| 688 | 1 | 2445 | 1 | 4661 | 1.14 |
| 764 | 1 | 2521 | 1 | 4737 | 1.15 |
| 800 | 1 | 2598 | 1 | 4813 | 1.15 |
| 840 | 1 | 2674 | 1 | 4890 | 1.16 |
| 917 | 1 | 2751 | 1 | 4966 | 1.17 |
| 993 | 1 | 2827 | 1 | 5043 | 1.18 |
| 1000 | 1 | 2903 | 1 | 5119 | 1.183 |
| 1070 | 1 | 2980 | 1 | 5196 | 1.189 |
| 1146 | 1 | 3056 | 1 | 5272 | 1.193 |
| 1200 | 1 | 3133 | 1 | 5348 | 1.196 |
| 1222 | 1 | 3209 | 1 | 5425 | 1.199 |
| 1299 | 1 | 3285 | 1 | 5501 | 1.201 |
| 1375 | 1 | 3362 | 1 | 5578 | 1.202 |
| 1400 | 1 | 3438 | 1.01 | 5654 | 1.202 |
| 1452 | 1 | 3515 | 1.01 | 1000000 | 1.202 (Extrapolation) |
| 1528 | 1 | 3591 | 1.02 | | |
| 1600 | 1 | 3667 | 1.02 | | |
| 1604 | 1 | 3744 | 1.03 | | |

Combustible mixture in ppm: $OME_2$: 7428; $OME_1$: 274; $CH_3OH$: 133;

$O_2$: 38493: $N_2$: 953672

## G.3 Experimental pressure profile for $OME_2$ at 4 bar

| time [$\mu s$] | $p(t)$ / $p(t = 0)$ | | | | |
|---|---|---|---|---|---|
| 0 | 1 | Cont'd | | Cont'd | |
| 108 | 1 | 1942 | 1.08 | 5070 | 1.31 |
| 200 | 1 | 2000 | 1.08 | 5178 | 1.32 |
| 216 | 1 | 2049 | 1.09 | 5285 | 1.34 |
| 324 | 1.01 | 2589 | 1.11 | 5393 | 1.35 |
| 400 | 1.01 | 2697 | 1.12 | 5501 | 1.36 |
| 431 | 1.01 | 2804 | 1.12 | 5609 | 1.38 |
| 539 | 1.02 | 2912 | 1.13 | 6148 | 1.44 |
| 600 | 1.02 | 3020 | 1.14 | 6256 | 1.45 |
| 647 | 1.02 | 3128 | 1.14 | 6364 | 1.46 |
| 755 | 1.03 | 3236 | 1.15 | 6472 | 1.47 |
| 800 | 1.03 | 3344 | 1.16 | 6580 | 1.48 |
| 863 | 1.03 | 3452 | 1.16 | 6688 | 1.49 |
| 971 | 1.04 | 3560 | 1.17 | 6796 | 1.5 |
| 1000 | 1.04 | 3667 | 1.18 | 6903 | 1.5 |
| 1079 | 1.04 | 3775 | 1.19 | 7011 | 1.51 |
| 1187 | 1.05 | 3883 | 1.2 | 7119 | 1.51 |
| 1200 | 1.05 | 3991 | 1.2 | 7227 | 1.51 |
| 1294 | 1.05 | 4099 | 1.21 | 7335 | 1.51 |
| 1400 | 1.06 | 4207 | 1.22 | 1000000 | 1.51 (Extrapolation) |
| 1402 | 1.06 | 4315 | 1.23 | | |
| 1510 | 1.06 | 4422 | 1.24 | | |
| 1600 | 1.07 | 4530 | 1.25 | | |
| 1618 | 1.07 | 4638 | 1.26 | | |
| 1726 | 1.07 | 4746 | 1.27 | | |
| 1800 | 1.07 | 4854 | 1.29 | | |
| 1834 | 1.08 | 4962 | 1.3 | | |

Combustible mixture in ppm: $OME_2$: 7428; $OME_1$: 274; $CH_3OH$: 133;

$O_2$: 38493: $N_2$: 953672

## G.4 Experimental pressure profile for $OME_2$ at 16 bar

| time [µs] | $p(t)$ / $p(t = 0)$ | | | | |
|---|---|---|---|---|---|
| 0 | 1 | Cont'd | | Cont'd | |
| 94 | 1 | 1800 | 1.08 | 5097 | 1.26 |
| 189 | 1 | 1888 | 1.08 | 5191 | 1.26 |
| 200 | 1 | 2737 | 1.11 | 5285 | 1.27 |
| 283 | 1.01 | 2831 | 1.12 | 5380 | 1.28 |
| 378 | 1.01 | 2926 | 1.12 | 6324 | 1.38 |
| 400 | 1.01 | 3020 | 1.13 | 6418 | 1.39 |
| 472 | 1.02 | 3115 | 1.13 | 6512 | 1.4 |
| 566 | 1.02 | 3209 | 1.14 | 6607 | 1.41 |
| 600 | 1.02 | 3303 | 1.14 | 6701 | 1.42 |
| 661 | 1.03 | 3398 | 1.15 | 6796 | 1.43 |
| 755 | 1.03 | 3492 | 1.15 | 6890 | 1.44 |
| 800 | 1.03 | 3587 | 1.16 | 6984 | 1.45 |
| 849 | 1.04 | 3681 | 1.16 | 7079 | 1.45 |
| 944 | 1.04 | 3775 | 1.17 | 7173 | 1.46 |
| 1000 | 1.04 | 3870 | 1.17 | 7267 | 1.46 |
| 1038 | 1.05 | 3964 | 1.18 | 7362 | 1.46 |
| 1133 | 1.05 | 4058 | 1.19 | 1000000 | 1.46 (Extrapolation) |
| 1200 | 1.05 | 4153 | 1.19 | | |
| 1227 | 1.05 | 4247 | 1.2 | | |
| 1321 | 1.06 | 4342 | 1.2 | | |
| 1400 | 1.06 | 4436 | 1.21 | | |
| 1416 | 1.06 | 4530 | 1.21 | | |
| 1510 | 1.07 | 4625 | 1.22 | | |
| 1600 | 1.07 | 4719 | 1.23 | | |
| 1604 | 1.07 | 4813 | 1.23 | | |
| 1699 | 1.07 | 4908 | 1.24 | | |
| 1793 | 1.08 | 5002 | 1.25 | | |

Combustible mixture in ppm: $OME_2$: 7428; $OME_1$: 274; $CH_3OH$: 133;

$O_2$: 38493: $N_2$: 953672

# H Oxymethylene ether–4 ($OME_4$)

## H.1 Measured ignition delay time data for $OME_4$

| Expt. No | $T_5$ [K] | $p_5$ [bar] | $\tau_{head-on}$ [$\mu s$] $\gamma$ = 431 nm (CH*) | $\tau_{side-on}$ [$\mu s$] $\gamma$ = 431 nm (CH*) | $\tau_{head-on}$ [$\mu s$] $\gamma$ = 308 nm (OH*) |
|---|---|---|---|---|---|
| 6842 | 1841 | 1.1 | 13 | 11 | 11 |
| 6843 | 1659 | 1.1 | 31 | 20 | 22 |
| 6847 | 1562 | 1.1 | 45 | 32 | 36 |
| 6848 | 1514 | 1.2 | 54 | 43 | 42 |
| 6849 | 1432 | 1.1 | 100 | 84 | 84 |
| 6850 | 1293 | 1.1 | 452 | 345 | 290 |
| 6851 | 1221 | 1.1 | 786 | 667 | 596 |
| 6852 | 1147 | 1.1 | 2330 | 2410 | 2320 |
| 6853 | 1098 | 1.1 | 4820 | 4660 | 4630 |
| 6865 | 1031 | 1.1 | 9990 | 10040 | 9920 |
| 6867 | 1020 | 1.1 | 12290 | 12010 | 11990 |
| 6887 | 1187 | 1.1 | 2180 | 1410 | 1360 |
| 6888 | 1059 | 1.1 | 7570 | 7190 | 6910 |
| 6889 | 1834 | 1 | 14 | 12 | 12 |
| 6900 | 1940 | 0.9 | 8 | 6 | |
| 6901 | 2027 | 1 | 6 | | |
| 6818 | 1660 | 4 | 12 | 11 | 11 |
| 6819 | 1541 | 4 | 24 | 23 | 20 |
| 6820 | 1453 | 4.1 | 44 | 37 | 35 |
| 6821 | 1354 | 4.2 | 99 | 88 | 80 |
| 6822 | 1257 | 3.9 | 237 | 216 | 201 |
| 6828 | 1179 | 4 | 484 | 462 | 435 |
| 6829 | 1102 | 4.1 | 1390 | 1510 | 1530 |
| 6836 | 1028 | 4.2 | 3700 | 3730 | 3690 |
| 6838 | 972 | 4.2 | 6340 | 6390 | 6430 |
| 6841 | 918 | 4.1 | 12110 | 10560 | 10630 |
| 6845 | 885 | 4.2 | 14490 | 13740 | 13700 |

| | | | | | |
|---|---|---|---|---|---|
| Cont'd | | | | | |
| 6856 | 1101 | 4.5 | 1640 | 1490 | 1470 |
| 6857 | 1049 | 4.1 | 3120 | 3130 | 2940 |
| 6860 | 1159 | 4.2 | 682 | 574 | 560 |
| 6861 | 1190 | 3.8 | 475 | 372 | 356 |
| 6879 | 1291 | 3.8 | 191 | 157 | 145 |
| 6880 | 1432 | 4 | 52 | 50 | 44 |
| 6881 | 1372 | 4 | 84 | 75 | 68 |
| 6882 | 1654 | 3.9 | 15 | 12 | 13 |
| 6884 | 1866 | 4.4 | 9 | 4 | 6 |
| 6885 | 1727 | 3.8 | 11 | 8 | 8 |
| 6823 | 1566 | 14.1 | 8 | 10 | 8 |
| 6825 | 1543 | 16.2 | 8 | 12 | 8 |
| 6826 | 1385 | 14.4 | 32 | 42 | 32 |
| 6827 | 1470 | 16.5 | 15 | 19 | 15 |
| 6830 | 1220 | 13.7 | 162 | 230 | 160 |
| 6831 | 1325 | 16.3 | 47 | 71 | 47 |
| 6832 | 1157 | 15.2 | 347 | 430 | 347 |
| 6833 | 1082 | 15.4 | 973 | 1070 | 973 |
| 6834 | 1017 | 15 | 2430 | 2580 | 2430 |
| 6837 | 984 | 15.1 | 3640 | 3520 | 3530 |
| 6839 | 945 | 15.2 | 5320 | 5220 | 5230 |
| 6844 | 899 | 14.6 | 7680 | 7660 | 7680 |
| 6854 | 1228 | 15 | 143 | 203 | 141 |
| 6858 | 1233 | 15 | 133 | 192 | 132 |
| 6859 | 1188 | 13.2 | 225 | 302 | 225 |
| 6862 | 1169 | 13.4 | 309 | 341 | 309 |
| 6863 | 1286 | 16.5 | 72 | 100 | 70 |
| 6873 | 857 | 14.7 | 12050 | 12120 | 12120 |
| 6874 | 1030 | 14.8 | 2080 | 2250 | 2090 |
| 6875 | 1120 | 14.2 | 676 | 587 | 587 |
| 6876 | 1616 | 15.7 | 7 | 8 | 7 |
| 6878 | 1026 | 14.3 | 2110 | 2160 | 2110 |
| Combustible mixture in ppm: $OME_4$: 7428; $OME_3$: 75; $OME_1$: 44; $CH_2O$: 406; $O_2$: 38898; $N_2$: 955130 | | | | | |

## H.2 Experimental pressure profile for $OME_4$ at 1 bar

| time [$\mu$s] | $p(t)$ / $p(t = 0)$ | | | | |
|---|---|---|---|---|---|
| 0 | 1 | Cont'd | | Cont'd | |
| 76 | 1 | 1681 | 1 | 3744 | 1.03 |
| 153 | 1 | 1757 | 1 | 3820 | 1.03 |
| 200 | 1 | 1800 | 1 | 3897 | 1.04 |
| 229 | 1 | 1834 | 1 | 3973 | 1.05 |
| 306 | 1 | 1910 | 1 | 4049 | 1.06 |
| 382 | 1 | 1987 | 1 | 4126 | 1.07 |
| 400 | 1 | 2000 | 1 | 4202 | 1.08 |
| 458 | 1 | 2063 | 1 | 4279 | 1.09 |
| 535 | 1 | 2139 | 1 | 4355 | 1.1 |
| 600 | 1 | 2216 | 1 | 4431 | 1.11 |
| 611 | 1 | 2292 | 1 | 4508 | 1.12 |
| 688 | 1 | 2369 | 1 | 4584 | 1.13 |
| 764 | 1 | 2445 | 1 | 4661 | 1.14 |
| 800 | 1 | 2521 | 1 | 4737 | 1.15 |
| 840 | 1 | 2598 | 1 | 4890 | 1.16 |
| 917 | 1 | 2674 | 1 | 4966 | 1.17 |
| 993 | 1 | 2751 | 1 | 5043 | 1.18 |
| 1000 | 1 | 2827 | 1 | 5119 | 1.18 |
| 1070 | 1 | 2903 | 1 | 5196 | 1.19 |
| 1146 | 1 | 2980 | 1 | 5272 | 1.19 |
| 1200 | 1 | 3056 | 1 | 5348 | 1.2 |
| 1222 | 1 | 3133 | 1 | 5425 | 1.2 |
| 1299 | 1 | 3209 | 1 | 5501 | 1.2 |
| 1375 | 1 | 3285 | 1 | 5578 | 1.2 |
| 1400 | 1 | 3362 | 1 | 5654 | 1.2 |
| 1452 | 1 | 3438 | 1.01 | 1000000 | 1.202427 (Extrapolation) |
| 1528 | 1 | 3515 | 1.01 | | |
| 1600 | 1 | 3591 | 1.02 | | |
| 1604 | 1 | 3667 | 1.02 | | |

Combustible mixture in ppm: $OME_4$: 7428; $OME_3$: 75; $OME_1$: 44; $CH_2O$: 406; $O_2$: 38898; $N_2$: 955130

## H.3 Experimental pressure profile for $OME_4$ at 4 bar

| time [$\mu$s] | $p(t)$ / $p(t = 0)$ | | | | |
|---|---|---|---|---|---|
| 0 | 1 | Cont'd | | Cont'd | |
| 79 | 1 | 1652 | 1.09 | 3697 | 1.31 |
| 157 | 1 | 1730 | 1.09 | 3775 | 1.32 |
| 200 | 1 | 1800 | 1.1 | 3854 | 1.33 |
| 236 | 1.01 | 1809 | 1.1 | 3933 | 1.34 |
| 315 | 1.01 | 1888 | 1.1 | 4011 | 1.35 |
| 393 | 1.01 | 1966 | 1.11 | 4090 | 1.36 |
| 400 | 1.01 | 2000 | 1.11 | 4169 | 1.37 |
| 472 | 1.02 | 2045 | 1.12 | 4247 | 1.38 |
| 551 | 1.02 | 2124 | 1.12 | 4326 | 1.39 |
| 600 | 1.03 | 2202 | 1.13 | 4404 | 1.4 |
| 629 | 1.03 | 2281 | 1.14 | 4483 | 1.41 |
| 708 | 1.03 | 2360 | 1.14 | 4562 | 1.42 |
| 787 | 1.04 | 2438 | 1.15 | 4640 | 1.42 |
| 800 | 1.04 | 2517 | 1.16 | 4719 | 1.43 |
| 865 | 1.04 | 2596 | 1.17 | 4798 | 1.43 |
| 944 | 1.05 | 2674 | 1.18 | 4876 | 1.44 |
| 1000 | 1.05 | 2753 | 1.19 | 4955 | 1.44 |
| 1022 | 1.05 | 2831 | 1.19 | 5034 | 1.45 |
| 1101 | 1.06 | 2910 | 1.2 | 5112 | 1.45 |
| 1180 | 1.06 | 2989 | 1.21 | 5191 | 1.45 |
| 1200 | 1.06 | 3067 | 1.22 | 5270 | 1.45 |
| 1258 | 1.07 | 3146 | 1.23 | 5348 | 1.45 |
| 1337 | 1.07 | 3225 | 1.25 | 5427 | 1.45 |
| 1400 | 1.07 | 3303 | 1.26 | 1000000 | 1.45 (Extrapolation) |
| 1416 | 1.07 | 3382 | 1.27 | | |
| 1494 | 1.08 | 3461 | 1.28 | | |
| 1573 | 1.08 | 3539 | 1.29 | | |
| 1600 | 1.09 | 3618 | 1.3 | | |
| Combustible mixture in ppm: $OME_4$: 7428; $OME_3$: 75; $OME_1$: 44; $CH_2O$: 406; $O_2$: 38898; $N_2$: 955130 | | | | | |

## H.4 Experimental pressure profile for $OME_4$ at 16 bar

| time [$\mu$s] | $p(t)$ / $p(t = 0)$ | | | | |
|---|---|---|---|---|---|
| 0 | 1 | Cont'd | | Cont'd | |
| 110 | 1 | 2092 | 1.11 | 5175 | 1.34 |
| 200 | 1 | 2202 | 1.12 | 5285 | 1.35 |
| 220 | 1.01 | 2312 | 1.12 | 5396 | 1.36 |
| 330 | 1.01 | 2422 | 1.13 | 5506 | 1.37 |
| 400 | 1.02 | 2533 | 1.13 | 5616 | 1.37 |
| 440 | 1.02 | 2643 | 1.14 | 5726 | 1.38 |
| 551 | 1.02 | 2753 | 1.15 | 5836 | 1.39 |
| 600 | 1.03 | 2863 | 1.15 | 5946 | 1.4 |
| 661 | 1.03 | 2973 | 1.16 | 6056 | 1.41 |
| 771 | 1.04 | 3083 | 1.17 | 6166 | 1.41 |
| 800 | 1.04 | 3193 | 1.17 | 6276 | 1.42 |
| 881 | 1.05 | 3303 | 1.18 | 6387 | 1.43 |
| 991 | 1.06 | 3413 | 1.19 | 6497 | 1.43 |
| 1000 | 1.06 | 3524 | 1.2 | 6607 | 1.44 |
| 1101 | 1.06 | 3634 | 1.2 | 6717 | 1.44 |
| 1200 | 1.07 | 3744 | 1.21 | 6827 | 1.44 |
| 1211 | 1.07 | 3854 | 1.22 | 6937 | 1.45 |
| 1321 | 1.08 | 3964 | 1.23 | 7047 | 1.45 |
| 1400 | 1.08 | 4074 | 1.24 | 7157 | 1.45 |
| 1431 | 1.08 | 4184 | 1.25 | 7267 | 1.45 |
| 1542 | 1.09 | 4294 | 1.26 | 7378 | 1.45 |
| 1600 | 1.09 | 4404 | 1.27 | 1000000 | 1.45 (Extrapolation) |
| 1652 | 1.09 | 4515 | 1.28 | | |
| 1762 | 1.1 | 4625 | 1.29 | | |
| 1800 | 1.1 | 4735 | 1.3 | | |
| 1872 | 1.1 | 4845 | 1.31 | | |
| 1982 | 1.11 | 4955 | 1.32 | | |
| 2000 | 1.11 | 5065 | 1.33 | | |
| Combustible mixture in ppm: $OME_4$: 7428; $OME_3$: 75; $OME_1$: 44; $CH_2O$: 406; $O_2$: 38898; $N_2$: 955130 | | | | | |

# I Trimethyl orthoformate (*iso*-$OME_2$)

## I.1 Measured ignition delay time data for *iso*-$OME_2$

| Expt. No | $T_5$ [K] | $p_5$ [bar] | $\tau_{head-on}$ [$\mu s$] $\gamma$ = 431 nm (CH*) | $\tau_{side-on}$ [$\mu s$] $\gamma$ = 431 nm (CH*) | $\tau_{head-on}$ [$\mu s$] $\gamma$ = 308 nm (OH*) |
|---|---|---|---|---|---|
| 6731 | 1769 | 1 | 25 | 19 | 18 |
| 6735 | 1623 | 1 | 46 | 33 | 36 |
| 6735 | 1604 | 1.1 | 49 | 37 | 38 |
| 6736 | 1499 | 1.1 | 96 | 80 | 79 |
| 6737 | 1467 | 1.1 | 115 | 99 | 98 |
| 6738 | 1405 | 1.1 | 189 | 170 | 168 |
| 6739 | 1326 | 1.1 | 400 | 379 | 379 |
| 6740 | 1256 | 1 | 1050 | 932 | 921 |
| 6742 | 1211 | 1.1 | 2690 | 2760 | 2630 |
| 6743 | 1158 | 1 | 4120 | 4210 | 4190 |
| 6744 | 1111 | 1 | 7420 | 7470 | 7450 |
| 6745 | 1010 | 0.9 | 15030 | 14940 | 14920 |
| 6746 | 1095 | 1 | 8780 | 8720 | 8740 |
| 6747 | 1069 | 1 | 11580 | 11190 | 11130 |
| 6748 | 1183 | 1.1 | 4010 | 4060 | 3780 |
| 6749 | 1286 | 1.1 | 622 | 613 | 596 |
| 6750 | 1874 | 1 | 15 | 10 | 13 |
| 6751 | 2024 | 1 | 7 | 5 | 5 |
| 6700 | 1739 | 4 | 10 | 9 | 10 |
| 6701 | 1626 | 3.9 | 19 | 15 | 17 |
| 6702 | 1551 | 4.1 | 32 | 27 | 28 |

| | | | | | |
|---|---|---|---|---|---|
| Cont'd | | | | | |
| 6703 | 1451 | 4.3 | 70 | 60 | 62 |
| 6704 | 1365 | 4 | 166 | 151 | 151 |
| 6705 | 1311 | 4.1 | 265 | 245 | 242 |
| 6706 | 1221 | 4.1 | 623 | 587 | 574 |
| 6707 | 1162 | 4.1 | 1180 | 1110 | 1090 |
| 6708 | 1102 | 4 | 2130 | 2400 | 2390 |
| 6709 | 1040 | 4 | 3770 | 4140 | 4130 |
| 6710 | 986 | 3.9 | 6450 | 6510 | 6450 |
| 6711 | 952 | 4 | 8640 | 9330 | 9400 |
| 6712 | 898 | 3.9 | 15380 | 15300 | 15360 |
| 6752 | 1936 | 4 | 4 | 4 | 7 |
| 6716 | 1620 | 15.4 | 11 | 9 | 10 |
| 6717 | 1556 | 15.9 | 15 | 13 | 13 |
| 6718 | 1454 | 15.4 | 35 | 31 | 33 |
| 6719 | 1405 | 15.5 | 51 | 46 | 47 |
| 6720 | 1355 | 16 | 77 | 72 | 72 |
| 6721 | 1280 | 15.7 | 178 | 154 | 153 |
| 6722 | 1213 | 15.5 | 337 | 310 | 306 |
| 6723 | 1159 | 15 | 601 | 564 | 556 |
| 6724 | 1087 | 15.6 | 1330 | 1250 | 1250 |
| 6725 | 1045 | 16 | 2110 | 2050 | 2050 |
| 6726 | 983 | 15.4 | 4290 | 4200 | 4200 |
| 6727 | 932 | 15.3 | 6900 | 6830 | 6860 |
| 6728 | 876 | 14.7 | 11690 | 11600 | 11600 |
| 6729 | 842 | 15 | 16200 | 16250 | 16370 |
| 6730 | 1703 | 15.5 | 5 | 7 | 7 |

Combustible mixture in ppm: *iso*-$OME_2$: 6210; $CH_3OCHO$: 1031; $CH_3OH$: 564; $O_2$: 38424; $N_2$: 953772

## I.2 Experimental pressure profile for *iso*-$OME_2$ at 1 bar

| time [$\mu$s] | $p(t)$ / $p(t = 0)$ | | | | |
|---|---|---|---|---|---|
| 0 | 1.00 | Cont'd | | Cont'd | |
| 76 | 1.00 | 1681 | 1.00 | 3744 | 1.03 |
| 153 | 1.00 | 1757 | 1.00 | 3820 | 1.03 |
| 200 | 1.00 | 1800 | 1.00 | 3897 | 1.04 |
| 229 | 1.00 | 1834 | 1.00 | 3973 | 1.05 |
| 306 | 1.00 | 1910 | 1.00 | 4049 | 1.06 |
| 382 | 1.00 | 1987 | 1.00 | 4126 | 1.07 |
| 400 | 1.00 | 2000 | 1.00 | 4202 | 1.08 |
| 458 | 1.00 | 2063 | 1.00 | 4279 | 1.09 |
| 535 | 1.00 | 2139 | 1.00 | 4355 | 1.10 |
| 600 | 1.00 | 2216 | 1.00 | 4431 | 1.11 |
| 611 | 1.00 | 2292 | 1.00 | 4508 | 1.12 |
| 688 | 1.00 | 2369 | 1.00 | 4584 | 1.13 |
| 764 | 1.00 | 2445 | 1.00 | 4661 | 1.14 |
| 800 | 1.00 | 2521 | 1.00 | 4737 | 1.15 |
| 840 | 1.00 | 2598 | 1.00 | 4813 | 1.15 |
| 917 | 1.00 | 2674 | 1.00 | 4890 | 1.16 |
| 993 | 1.00 | 2751 | 1.00 | 4966 | 1.17 |
| 1000 | 1.00 | 2827 | 1.00 | 5043 | 1.18 |
| 1070 | 1.00 | 2903 | 1.00 | 5119 | 1.18 |
| 1146 | 1.00 | 2980 | 1.00 | 5196 | 1.19 |
| 1200 | 1.00 | 3056 | 1.00 | 5272 | 1.19 |
| 1222 | 1.00 | 3133 | 1.00 | 5348 | 1.20 |
| 1299 | 1.00 | 3209 | 1.00 | 5425 | 1.20 |
| 1375 | 1.00 | 3285 | 1.00 | 5501 | 1.20 |
| 1400 | 1.00 | 3362 | 1.00 | 5578 | 1.20 |
| 1452 | 1.00 | 3438 | 1.01 | 5654 | 1.20 |
| 1528 | 1.00 | 3515 | 1.01 | 1000000 | 1.20 (Extrapolation) |
| 1600 | 1.00 | 3591 | 1.02 | | |
| Combustible mixture in ppm: *iso*-$OME_2$: 6210; $CH_3OCHO$: 1031; $CH_3OH$: 564; $O_2$: 38424; $N_2$: 953772 | | | | | |

## I.3 Experimental pressure profile for *iso*-$OME_2$ at 4 bar

| time [$\mu$s] | $p(t)$ / $p(t = 0)$ | | | | |
|---|---|---|---|---|---|
| 0 | 1.00 | Cont'd | | Cont'd | |
| 101 | 1.00 | 2022 | 1.09 | 4955 | 1.33 |
| 200 | 1.00 | 2124 | 1.09 | 5056 | 1.34 |
| 202 | 1.00 | 2225 | 1.10 | 5157 | 1.35 |
| 303 | 1.00 | 2326 | 1.10 | 5258 | 1.36 |
| 400 | 1.01 | 2427 | 1.11 | 5360 | 1.37 |
| 404 | 1.01 | 2528 | 1.11 | 5461 | 1.39 |
| 506 | 1.01 | 2629 | 1.12 | 5562 | 1.40 |
| 600 | 1.01 | 2730 | 1.13 | 5663 | 1.41 |
| 607 | 1.01 | 2831 | 1.13 | 5764 | 1.42 |
| 708 | 1.02 | 2933 | 1.14 | 5865 | 1.43 |
| 800 | 1.02 | 3034 | 1.14 | 5966 | 1.44 |
| 809 | 1.02 | 3135 | 1.15 | 6067 | 1.45 |
| 910 | 1.02 | 3236 | 1.16 | 6169 | 1.46 |
| 1000 | 1.03 | 3337 | 1.17 | 6270 | 1.47 |
| 1011 | 1.03 | 3438 | 1.17 | 6371 | 1.48 |
| 1112 | 1.04 | 3539 | 1.18 | 6472 | 1.48 |
| 1200 | 1.04 | 3640 | 1.19 | 6573 | 1.49 |
| 1213 | 1.04 | 3742 | 1.20 | 6674 | 1.50 |
| 1315 | 1.05 | 3843 | 1.21 | 6775 | 1.50 |
| 1400 | 1.05 | 3944 | 1.22 | 6876 | 1.50 |
| 1416 | 1.05 | 4045 | 1.23 | 6978 | 1.51 |
| 1517 | 1.06 | 4146 | 1.24 | 7079 | 1.51 |
| 1600 | 1.06 | 4247 | 1.25 | 7180 | 1.51 |
| 1618 | 1.06 | 4348 | 1.26 | 7281 | 1.52 |
| 1719 | 1.07 | 4449 | 1.27 | 7382 | 1.52 |
| 1800 | 1.07 | 4551 | 1.28 | 7483 | 1.52 |
| 1820 | 1.07 | 4652 | 1.29 | 7584 | 1.52 |
| 1921 | 1.08 | 4753 | 1.30 | 7685 | 1.52 |
| 2000 | 1.08 | 4854 | 1.31 | 1000000 | 1.52 (Extrapolation) |

Combustible mixture in ppm: *iso*-$OME_2$: 6210; $CH_3OCHO$: 1031; $CH_3OH$: 564; $O_2$: 38424; $N_2$: 953772

## I.4 Experimental pressure profile for *iso*-$OME_2$ at 16 bar

| time [$\mu$s] | $p(t)$ / $p(t = 0)$ | | | | |
|---|---|---|---|---|---|
| 0 | 1.00 | Cont'd | | Cont'd | |
| 94 | 1.00 | 2000 | 1.09 | 4813 | 1.25 |
| 189 | 1.00 | 2076 | 1.09 | 4908 | 1.26 |
| 200 | 1.00 | 2171 | 1.10 | 5002 | 1.27 |
| 283 | 1.01 | 2265 | 1.10 | 5097 | 1.28 |
| 378 | 1.01 | 2360 | 1.10 | 5191 | 1.29 |
| 400 | 1.01 | 2454 | 1.11 | 5285 | 1.29 |
| 472 | 1.02 | 2548 | 1.11 | 5380 | 1.30 |
| 566 | 1.02 | 2643 | 1.12 | 5474 | 1.31 |
| 600 | 1.02 | 2737 | 1.12 | 5569 | 1.32 |
| 661 | 1.03 | 2831 | 1.13 | 5663 | 1.33 |
| 755 | 1.03 | 2926 | 1.13 | 5757 | 1.34 |
| 800 | 1.04 | 3020 | 1.14 | 5852 | 1.35 |
| 849 | 1.04 | 3115 | 1.14 | 5946 | 1.36 |
| 944 | 1.04 | 3209 | 1.15 | 6040 | 1.37 |
| 1000 | 1.05 | 3303 | 1.15 | 6135 | 1.38 |
| 1038 | 1.05 | 3398 | 1.16 | 6229 | 1.39 |
| 1133 | 1.05 | 3492 | 1.16 | 6324 | 1.40 |
| 1200 | 1.06 | 3587 | 1.17 | 6418 | 1.41 |
| 1227 | 1.06 | 3681 | 1.17 | 6512 | 1.42 |
| 1321 | 1.06 | 3775 | 1.18 | 6607 | 1.42 |
| 1400 | 1.07 | 3870 | 1.19 | 6701 | 1.43 |
| 1416 | 1.07 | 3964 | 1.19 | 6796 | 1.44 |
| 1510 | 1.07 | 4058 | 1.20 | 6890 | 1.45 |
| 1600 | 1.07 | 4153 | 1.21 | 6984 | 1.45 |
| 1604 | 1.07 | 4247 | 1.21 | 7079 | 1.45 |
| 1699 | 1.08 | 4342 | 1.22 | 7173 | 1.46 |
| 1793 | 1.08 | 4436 | 1.23 | 7267 | 1.46 |
| 1800 | 1.08 | 4530 | 1.23 | 7362 | 1.46 |
| 1888 | 1.08 | 4625 | 1.24 | 1000000 | 1.46 (Extrapolation)) |
| 1982 | 1.09 | 4719 | 1.25 | | |

Combustible mixture in ppm: *iso*-$OME_2$: 6210; $CH_3OCHO$: 1031; $CH_3OH$: 564; $O_2$: 38424; $N_2$: 953772

# J Gasoline surrogate (PRF90)

## J.1 Measured ignition delay time data for PRF90

| Expt. No | $T_5$ [K] | $p_5$ [bar] | $\tau_{\text{head-on}}$ [$\mu s$] $\gamma$ = 431 nm (CH*) | $\tau_{\text{side-on}}$ [$\mu s$] $\gamma$ = 431 nm (CH*) | $\tau_{\text{head-on}}$ [$\mu s$] $\gamma$ = 308 nm (OH*) |
|---|---|---|---|---|---|
| 6443 | 1948 | 1 | 14 | 15 | 14 |
| 6445 | 2009 | 1.1 | 13 | 13 | 14 |
| 6446 | 1890 | 1 | 20 | 17 | 18 |
| 6447 | 1818 | 1 | 32 | 24 | 29 |
| 6448 | 1769 | 1.1 | 41 | 33 | 35 |
| 6450 | 1499 | 0.9 | 474 | 544 | 550 |
| 6452 | 1686 | 1.1 | 75 | 60 | 62 |
| 6453 | 1625 | 1.1 | 130 | 114 | 116 |
| 6454 | 1574 | 1.1 | 202 | 181 | 187 |
| 6458 | 1438 | 1 | 1720 | 2270 | 1740 |
| 6462 | 1396 | 1 | 3290 | 3540 | 3320 |
| 6463 | 1350 | 1.1 | 8740 | 9000 | 9370 |
| 6464 | 1364 | 1 | 5270 | 6460 | 6490 |
| 6466 | 1532 | 1 | 352 | 352 | 351 |
| 6471 | 2087 | 1.1 | 10 | 9 | 10 |
| 6472 | 1724 | 1.1 | 62 | 46 | 43 |
| 6488 | 1648 | 1.1 | 104 | 82 | 84 |
| 6489 | 1470 | 1 | 830 | 1120 | 1120 |
| 6371 | 1205 | 4 | 5770 | 6420 | 6320 |
| 6373 | 1162 | 4.3 | 7570 | 8470 | 8570 |
| 6375 | 1314 | 3.8 | 2160 | 2580 | 2610 |
| 6376 | 1562 | 3.9 | 134 | 135 | 131 |
| 6377 | 1282 | 3.8 | 2960 | 3420 | 3320 |
| 6381 | 1600 | 3.9 | 90 | 71 | 72 |
| 6382 | 1687 | 3.8 | 42 | 31 | 33 |
| 6384 | 1840 | 4.1 | 11 | 7 | 9 |
| 6385 | 1957 | 3.6 | 6 | 3 | 6 |

| | | | | | |
|---|---|---|---|---|---|
| Cont'd | | | | | |
| 6390 | 1510 | 4.2 | 247 | 234 | 232 |
| 6391 | 1437 | 4.1 | 641 | 716 | 701 |
| 6392 | 1382 | 4.1 | 1270 | 1500 | 1490 |
| 6395 | 1475 | 3.8 | 409 | 425 | 418 |
| 6397 | 1645 | 3.9 | 58 | 46 | 44 |
| 6399 | 1342 | 4.2 | 1700 | 2150 | 2140 |
| 6400 | 1396 | 4.2 | 889 | 1260 | 1280 |
| 6401 | 1732 | 4 | 28 | 18 | 21 |
| 6403 | 1775 | 4 | 17 | 10 | 13 |
| 6405 | 1243 | 4 | 4060 | 4470 | 4300 |
| 6475 | 1128 | 4.1 | 10760 | 11350 | 11530 |
| 6409 | 1867 | 15.1 | 4 | 4 | 4 |
| 6415 | 1801 | 16.5 | 7 | 7 | 4 |
| 6418 | 1664 | 14.6 | 31 | 24 | 25 |
| 6420 | 1693 | 15.6 | | 17 | 18 |
| 6421 | 1755 | 16.1 | 11 | 11 | 8 |
| 6423 | 1485 | 15.5 | 193 | 166 | 166 |
| 6424 | 1523 | 15.9 | 135 | 107 | 108 |
| 6417 | 1612 | 14 | 70 | 44 | 45 |
| 6427 | 1232 | 14.7 | 1880 | 1730 | 1730 |
| 6428 | 1316 | 16.3 | 818 | 799 | 792 |
| 6429 | 1355 | 16.4 | 579 | 557 | 552 |
| 6430 | 1392 | 15.4 | 447 | 425 | 420 |
| 6432 | 1276 | 16.4 | 1110 | 1090 | 1090 |
| 6434 | 1200 | 15.2 | 2300 | 2170 | 2160 |
| 6436 | 1170 | 16.2 | 2670 | 2630 | 2630 |
| 6442 | 1057 | 16.1 | 8170 | 7580 | 7640 |
| 6479 | 1132 | 16 | 3920 | 3700 | 3690 |
| 6482 | 1114 | 16.3 | 4980 | 4680 | 4670 |
| 6486 | 1457 | 16.4 | 274 | 252 | 249 |

Combustible mixture in ppm: $i C_8H_{18}$: 2872; $n C_7H_{16}$: 319;
$O_2$: 39308; $N_2$: 957901

## J.2 Experimental pressure profile for PRF90 at 4 bar

| time [$\mu$s] | $p(t)/p(t\ =\ 0)$ | | | | |
|---|---|---|---|---|---|
| 0 | 1.00 | Cont'd | | Cont'd | |
| 48 | 1.00 | 1503 | 1.06 | 2958 | 1.22 |
| 97 | 1.00 | 1552 | 1.06 | 3006 | 1.22 |
| 145 | 1.00 | 1600 | 1.07 | 3055 | 1.23 |
| 194 | 1.00 | 1648 | 1.07 | 3103 | 1.24 |
| 242 | 1.00 | 1697 | 1.07 | 3152 | 1.24 |
| 291 | 1.00 | 1745 | 1.08 | 3200 | 1.25 |
| 339 | 1.00 | 1794 | 1.08 | 3248 | 1.26 |
| 388 | 1.01 | 1842 | 1.09 | 3297 | 1.26 |
| 436 | 1.01 | 1891 | 1.09 | 3345 | 1.27 |
| 485 | 1.01 | 1939 | 1.10 | 3394 | 1.28 |
| 533 | 1.01 | 1988 | 1.10 | 3442 | 1.28 |
| 582 | 1.01 | 2036 | 1.11 | 3491 | 1.29 |
| 630 | 1.01 | 2085 | 1.11 | 3539 | 1.29 |
| 679 | 1.01 | 2133 | 1.12 | 3588 | 1.30 |
| 727 | 1.02 | 2182 | 1.12 | 3636 | 1.30 |
| 776 | 1.02 | 2230 | 1.13 | 3685 | 1.31 |
| 824 | 1.02 | 2279 | 1.13 | 3733 | 1.31 |
| 873 | 1.02 | 2327 | 1.14 | 3782 | 1.32 |
| 921 | 1.02 | 2376 | 1.14 | 3830 | 1.32 |
| 970 | 1.03 | 2424 | 1.15 | 3879 | 1.33 |
| 1018 | 1.03 | 2473 | 1.15 | 3927 | 1.33 |
| 1067 | 1.03 | 2521 | 1.16 | 3976 | 1.33 |
| 1115 | 1.03 | 2570 | 1.17 | 4024 | 1.33 |
| 1164 | 1.04 | 2618 | 1.17 | 4073 | 1.34 |
| 1212 | 1.04 | 2667 | 1.18 | 4121 | 1.34 |
| 1261 | 1.04 | 2715 | 1.19 | 4170 | 1.34 |
| 1309 | 1.05 | 2764 | 1.19 | 1000000 | 1.34 (Extrapolation) |
| 1358 | 1.05 | 2812 | 1.20 | | |
| 1406 | 1.05 | 2861 | 1.20 | | |
| 1455 | 1.06 | 2909 | 1.21 | | |
| Combustible mixture in ppm: $i C_8H_{18}$: 2872; $n C_7H_{16}$: 319; $O_2$: 39308; $N_2$: 957901 | | | | | |

## J.3 Experimental pressure profile for PRF90 at 16 bar

| time [$\mu$s] | $p(t)$ / $p(t = 0)$ | | | | |
|---|---|---|---|---|---|
| 0 | 1.00 | Cont'd | | Cont'd | |
| 51 | 1.00 | 1667 | 1.08 | 3283 | 1.19 |
| 101 | 1.00 | 1717 | 1.08 | 3333 | 1.19 |
| 152 | 1.00 | 1768 | 1.08 | 3384 | 1.19 |
| 202 | 1.00 | 1818 | 1.09 | 3434 | 1.20 |
| 253 | 1.00 | 1869 | 1.09 | 3485 | 1.20 |
| 303 | 1.00 | 1919 | 1.09 | 3535 | 1.20 |
| 354 | 1.01 | 1970 | 1.10 | 3586 | 1.21 |
| 404 | 1.01 | 2020 | 1.10 | 3636 | 1.21 |
| 455 | 1.01 | 2071 | 1.10 | 3687 | 1.21 |
| 505 | 1.01 | 2121 | 1.11 | 3737 | 1.22 |
| 556 | 1.01 | 2172 | 1.11 | 3788 | 1.22 |
| 606 | 1.02 | 2222 | 1.11 | 3838 | 1.22 |
| 657 | 1.02 | 2273 | 1.12 | 3889 | 1.23 |
| 707 | 1.02 | 2323 | 1.12 | 3939 | 1.23 |
| 758 | 1.02 | 2374 | 1.12 | 3990 | 1.23 |
| 808 | 1.03 | 2424 | 1.13 | 4040 | 1.24 |
| 859 | 1.03 | 2475 | 1.13 | 4091 | 1.24 |
| 909 | 1.03 | 2525 | 1.13 | 4141 | 1.24 |
| 960 | 1.04 | 2576 | 1.14 | 4192 | 1.25 |
| 1010 | 1.04 | 2626 | 1.14 | 4242 | 1.25 |
| 1061 | 1.04 | 2677 | 1.14 | 4293 | 1.25 |
| 1111 | 1.04 | 2727 | 1.15 | 4343 | 1.25 |
| 1162 | 1.05 | 2778 | 1.15 | 4394 | 1.25 |
| 1212 | 1.05 | 2828 | 1.15 | 4444 | 1.26 |
| 1263 | 1.05 | 2879 | 1.16 | 4495 | 1.26 |
| 1313 | 1.06 | 2929 | 1.16 | 4545 | 1.26 |
| 1364 | 1.06 | 2980 | 1.16 | 4596 | 1.26 |
| 1414 | 1.06 | 3030 | 1.17 | 4646 | 1.26 |
| 1465 | 1.07 | 3081 | 1.17 | 4697 | 1.26 |
| 1515 | 1.07 | 3131 | 1.17 | 1000000 | 1.26 (Extrapolation) |
| 1566 | 1.07 | 3182 | 1.18 | | |
| 1616 | 1.08 | 3232 | 1.18 | | |
| Combustible mixture in ppm: $i$C$_8$H$_{18}$: 2872; $n$C$_7$H$_{16}$: 319; O$_2$: 39308; N$_2$: 957901 | | | | | |

# K $OME_1$ / PRF90 (70:30) blend

## K.1 Measured ignition delay time data for $OME_1$ / PRF90 (70:30)

| Expt. No | $T_5$ [K] | $p_5$ [bar] | $\tau_{head-on}$ [$\mu s$] $\gamma$ = 431 nm (CH*) | $\tau_{side-on}$ [$\mu s$] $\gamma$ = 431 nm (CH*) | $\tau_{head-on}$ [$\mu s$] $\gamma$ = 308 nm (OH*) |
|---|---|---|---|---|---|
| 6578 | 1940 | 0.9 | 16 | 11 | 13 |
| 6579 | 1868 | 0.9 | 19 | 14 | 16 |
| 6580 | 1731 | 1.0 | 36 | 21 | 27 |
| 6581 | 1755 | 0.9 | 30 | 24 | 25 |
| 6582 | 1609 | 1.0 | 68 | 53 | 55 |
| 6583 | 1538 | 1.1 | 120 | 101 | 100 |
| 6584 | 1531 | 1.0 | 125 | 107 | 108 |
| 6585 | 1471 | 1.1 | 220 | 199 | 196 |
| 6586 | 1419 | 1.1 | 371 | 350 | 349 |
| 6587 | 1368 | 1.1 | 617 | 632 | 624 |
| 6588 | 1291 | 1.0 | 3000 | 3210 | 3110 |
| 6589 | 1329 | 1.0 | 1130 | 1900 | 1010 |
| 6590 | 1257 | 1.0 | 4130 | 4850 | 4770 |
| 6591 | 1199 | 1.0 | 9290 | 8730 | 9300 |
| 6592 | 1162 | 1.0 | 12230 | 12350 | 12310 |
| 6594 | 1144 | 1.0 | 15950 | 16350 | 16200 |
| 6595 | 1351 | 1.0 | 1170 | 1240 | 1100 |
| 6597 | 1215 | 1.0 | 6640 | 7370 | 7320 |
| 6599 | 1380 | 1.0 | 626 | 630 | 629 |
| 6600 | 1466 | 1.0 | 242 | 221 | 218 |
| 6495 | 1956 | 4.1 | 5 | 6 | 2 |
| 6496 | 1877 | 4.3 | 8 | 7 | 3 |
| 6497 | 1807 | 4.0 | 13 | 10 | 8 |

| | | | | | |
|---|---|---|---|---|---|
| Cont'd | | | | | |
| 6498 | 1728 | 4.2 | 27 | 21 | 20 |
| 6499 | 1642 | 4.0 | 37 | 31 | 30 |
| 6500 | 1601 | 4.3 | 67 | 57 | 56 |
| 6501 | 1550 | 4.1 | 103 | 91 | 89 |
| 6502 | 1505 | 4.1 | 113 | 99 | 99 |
| 6503 | 1492 | 4.1 | 260 | 239 | 237 |
| 6504 | 1419 | 4.1 | 326 | 303 | 300 |
| 6505 | 1393 | 4.1 | 186 | 167 | 166 |
| 6506 | 1449 | 4.1 | 350 | 316 | 315 |
| 6507 | 1388 | 4.3 | 308 | 287 | 285 |
| 6508 | 1390 | 4.2 | 534 | 514 | 511 |
| 6509 | 1346 | 4.1 | 570 | 535 | 528 |
| 6511 | 1339 | 4.2 | 558 | 525 | 510 |
| 6512 | 1344 | 3.8 | 1510 | 1550 | 1560 |
| 6513 | 1265 | 3.6 | 630 | 611 | 603 |
| 6514 | 1330 | 3.9 | 909 | 824 | 813 |
| 6515 | 1303 | 3.8 | 1570 | 1750 | 1720 |
| 6516 | 1268 | 4.0 | 3440 | 3730 | 3700 |
| 6517 | 1169 | 4.3 | 3070 | 3290 | 3320 |
| 6518 | 1192 | 4.0 | 1660 | 1990 | 1970 |
| 6519 | 1247 | 4.1 | 2050 | 2340 | 2320 |
| 6521 | 1225 | 4.1 | 2670 | 2970 | 2970 |
| 6522 | 1197 | 4.0 | 6330 | 7440 | 7440 |
| 6523 | 1113 | 4.0 | 4140 | 4550 | 4510 |
| 6525 | 1157 | 4.0 | 5140 | 6070 | 6060 |
| 6527 | 1122 | 3.9 | 4270 | 4640 | 4640 |
| 6528 | 1151 | 4.0 | 8330 | 8880 | 8850 |
| 6530 | 1091 | 3.8 | 7640 | 10700 | 10580 |
| 6531 | 1080 | 3.9 | 11100 | 11220 | 11100 |

| | | | | | |
|---|---|---|---|---|---|
| Cont'd | | | | | |
| 6543 | 1489 | 15.9 | 84 | 55 | 54 |
| 6544 | 1405 | 16.1 | 151 | 124 | 123 |
| 6545 | 1558 | 15.6 | 31 | 29 | 28 |
| 6548 | 1352 | 15.8 | 250 | 221 | 218 |
| 6549 | 1329 | 16.3 | 305 | | 276 |
| 6551 | 1242 | 16.1 | 764 | 723 | 714 |
| 6552 | 1173 | 14.6 | 1700 | 1600 | 1590 |
| 6553 | 1156 | 15.0 | 2020 | 1960 | 1950 |
| 6555 | 1129 | 15.4 | 2660 | 2570 | 2560 |
| 6556 | 1099 | 15.4 | 3520 | 3430 | 3430 |
| 6557 | 1080 | 15.3 | 4130 | 4040 | 4040 |
| 6558 | 1065 | 15.9 | 4450 | 4370 | 4370 |
| 6559 | 1193 | 14.9 | 1330 | 1270 | 1260 |
| 6560 | 1224 | 15.0 | 859 | 819 | 811 |
| 6565 | 1604 | 14.9 | 20 | 17 | 17 |
| 6567 | 1637 | 14.5 | 15 | 12 | 12 |
| 6568 | 1017 | 15.2 | 6760 | 6630 | 6630 |
| 6571 | 1437 | 15.4 | 119 | 92 | 92 |
| 6572 | 1291 | 16.0 | 432 | 404 | 403 |
| 6573 | 1028 | 15.1 | 6390 | 6760 | 6170 |
| 6574 | 1048 | 15.3 | 5130 | 5000 | 5000 |
| 6575 | 984 | 15.4 | 8820 | 8750 | 8760 |
| 6576 | 958 | 14.8 | 11880 | 11740 | 11750 |
| 6577 | 942 | 14.7 | 14620 | 14510 | 14550 |

Combustible mixture in ppm: $i C_8H_{18}$: 1612; $n C_7H_{16}$: 179; $OME_1$: 4179; $O_2$: 38489; $N_2$: 955541

## K.2 Experimental pressure profile for $OME_1$ / PRF90 at 1 bar

| time [$\mu$s] | $p(t)$ / $p(t = 0)$ | | | | |
|---|---|---|---|---|---|
| 0 | 1.00 | **Cont'd** | | **Cont'd** | |
| 56 | 1.00 | 1400 | 1.00 | 2753 | 1.02 |
| 112 | 1.00 | 1404 | 1.00 | 2809 | 1.02 |
| 169 | 1.00 | 1461 | 1.00 | 2865 | 1.03 |
| 200 | 1.00 | 1517 | 1.00 | 2921 | 1.04 |
| 225 | 1.00 | 1573 | 1.00 | 2978 | 1.05 |
| 337 | 1.00 | 1600 | 1.00 | 3034 | 1.05 |
| 393 | 1.00 | 1629 | 1.00 | 3090 | 1.06 |
| 400 | 1.00 | 1685 | 1.00 | 3146 | 1.07 |
| 506 | 1.00 | 1742 | 1.00 | 3202 | 1.08 |
| 562 | 1.00 | 1798 | 1.00 | 3258 | 1.09 |
| 600 | 1.00 | 1800 | 1.00 | 3315 | 1.10 |
| 618 | 1.00 | 1854 | 1.00 | 3371 | 1.12 |
| 674 | 1.00 | 1910 | 1.00 | 3427 | 1.13 |
| 730 | 1.00 | 1966 | 1.00 | 3483 | 1.14 |
| 787 | 1.00 | 2000 | 1.00 | 3539 | 1.15 |
| 800 | 1.00 | 2022 | 1.00 | 3596 | 1.16 |
| 843 | 1.00 | 2079 | 1.00 | 3652 | 1.17 |
| 899 | 1.00 | 2135 | 1.00 | 3708 | 1.18 |
| 955 | 1.00 | 2191 | 1.00 | 3764 | 1.18 |
| 1000 | 1.00 | 2247 | 1.00 | 3820 | 1.19 |
| 1011 | 1.00 | 2303 | 1.00 | 3876 | 1.20 |
| 1067 | 1.00 | 2360 | 1.00 | 3933 | 1.20 |
| 1124 | 1.00 | 2416 | 1.00 | 3989 | 1.21 |
| 1180 | 1.00 | 2472 | 1.00 | 4045 | 1.21 |
| 1200 | 1.00 | 2528 | 1.00 | 4101 | 1.21 |
| 1236 | 1.00 | 2584 | 1.01 | 4157 | 1.22 |
| 1292 | 1.00 | 2640 | 1.01 | 4213 | 1.22 |
| 1348 | 1.00 | 2697 | 1.01 | 1000000 | 1.22 (Extrapolation) |

Combustible mixture in ppm: $i C_8H_{18}$: 1612; $n C_7H_{16}$: 179; $OME_1$: 4179; $O_2$: 38489; $N_2$: 955541

## K.3 Experimental pressure profile for $OME_1$ / PRF90 at 4 bar

| time [$\mu$s] | $p(t)$ / $p(t = 0)$ | | | | |
|---|---|---|---|---|---|
| 0 | 1.00 | Cont'd | | Cont'd | |
| 58 | 1.00 | 1461 | 1.06 | 3097 | 1.22 |
| 117 | 1.00 | 1519 | 1.06 | 3155 | 1.23 |
| 175 | 1.00 | 1578 | 1.07 | 3213 | 1.24 |
| 200 | 1.00 | 1600 | 1.07 | 3272 | 1.25 |
| 234 | 1.00 | 1636 | 1.07 | 3330 | 1.25 |
| 292 | 1.01 | 1694 | 1.07 | 3389 | 1.26 |
| 351 | 1.01 | 1753 | 1.08 | 3447 | 1.27 |
| 400 | 1.01 | 1800 | 1.08 | 3506 | 1.28 |
| 409 | 1.01 | 1811 | 1.08 | 3564 | 1.28 |
| 467 | 1.01 | 1870 | 1.08 | 3622 | 1.29 |
| 526 | 1.02 | 1928 | 1.09 | 3681 | 1.30 |
| 584 | 1.02 | 1987 | 1.09 | 3739 | 1.30 |
| 600 | 1.02 | 2000 | 1.09 | 3798 | 1.31 |
| 643 | 1.02 | 2045 | 1.10 | 3856 | 1.32 |
| 701 | 1.03 | 2103 | 1.10 | 3915 | 1.32 |
| 760 | 1.03 | 2162 | 1.11 | 3973 | 1.33 |
| 800 | 1.03 | 2220 | 1.11 | 4031 | 1.34 |
| 818 | 1.03 | 2279 | 1.12 | 4090 | 1.34 |
| 876 | 1.03 | 2337 | 1.13 | 4148 | 1.35 |
| 935 | 1.04 | 2396 | 1.13 | 4207 | 1.35 |
| 993 | 1.04 | 2454 | 1.14 | 4265 | 1.36 |
| 1000 | 1.04 | 2512 | 1.15 | 4324 | 1.36 |
| 1052 | 1.04 | 2571 | 1.15 | 4382 | 1.37 |
| 1110 | 1.04 | 2629 | 1.16 | 4440 | 1.37 |
| 1169 | 1.05 | 2688 | 1.17 | 4499 | 1.37 |
| 1200 | 1.05 | 2746 | 1.18 | 4557 | 1.38 |
| 1227 | 1.05 | 2804 | 1.18 | 4616 | 1.38 |
| 1285 | 1.05 | 2863 | 1.19 | 4674 | 1.38 |
| 1344 | 1.05 | 2921 | 1.20 | 4733 | 1.38 |
| 1400 | 1.06 | 2980 | 1.21 | 1000000 | 1.38 (Extrapolation) |
| 1402 | 1.06 | 3038 | 1.21 | | |
| Combustible mixture in ppm: $i C_8H_{18}$: 1612; $n C_7H_{16}$: 179; $OME_1$: 4179; $O_2$: 38489; $N_2$: 955541 | | | | | |

## K.4 Experimental pressure profile for $OME_1$ / PRF90 at 16 bar

| time [$\mu$s] | $p(t)$ / ($t$ = 0) | | | | |
|---|---|---|---|---|---|
| 0 | 1.00 | Cont'd | | Cont'd | |
| 72 | 1.00 | 1798 | 1.08 | 3955 | 1.23 |
| 144 | 1.00 | 1800 | 1.08 | 4027 | 1.23 |
| 200 | 1.00 | 1870 | 1.08 | 4099 | 1.24 |
| 216 | 1.00 | 1942 | 1.08 | 4171 | 1.25 |
| 288 | 1.01 | 2000 | 1.09 | 4243 | 1.25 |
| 360 | 1.01 | 2013 | 1.09 | 4315 | 1.26 |
| 400 | 1.01 | 2085 | 1.09 | 4387 | 1.27 |
| 431 | 1.02 | 2157 | 1.09 | 4458 | 1.28 |
| 503 | 1.02 | 2229 | 1.10 | 4530 | 1.28 |
| 575 | 1.02 | 2301 | 1.10 | 4602 | 1.29 |
| 600 | 1.02 | 2373 | 1.10 | 4674 | 1.3 |
| 647 | 1.03 | 2445 | 1.11 | 4746 | 1.31 |
| 719 | 1.03 | 2517 | 1.11 | 4818 | 1.32 |
| 791 | 1.04 | 2589 | 1.12 | 4890 | 1.32 |
| 800 | 1.04 | 2661 | 1.12 | 4962 | 1.33 |
| 863 | 1.04 | 2733 | 1.13 | 5034 | 1.34 |
| 935 | 1.04 | 2804 | 1.13 | 5106 | 1.34 |
| 1000 | 1.05 | 2876 | 1.14 | 5178 | 1.35 |
| 1007 | 1.05 | 2948 | 1.14 | 5249 | 1.36 |
| 1079 | 1.05 | 3020 | 1.15 | 5321 | 1.36 |
| 1151 | 1.05 | 3092 | 1.15 | 5393 | 1.37 |
| 1200 | 1.05 | 3164 | 1.16 | 5465 | 1.37 |
| 1222 | 1.06 | 3236 | 1.16 | 5537 | 1.38 |
| 1294 | 1.06 | 3308 | 1.17 | 5609 | 1.38 |
| 1366 | 1.06 | 3380 | 1.18 | 5681 | 1.38 |
| 1400 | 1.06 | 3452 | 1.18 | 5753 | 1.39 |
| 1438 | 1.06 | 3524 | 1.19 | 5825 | 1.39 |
| 1510 | 1.07 | 3596 | 1.19 | 5897 | 1.39 |
| 1582 | 1.07 | 3667 | 1.20 | 5969 | 1.39 |
| 1600 | 1.07 | 3739 | 1.21 | 1000000 | 1.39 (Extrapolation) |
| 1654 | 1.07 | 3811 | 1.21 | | |
| 1726 | 1.07 | 3883 | 1.22 | | |

Combustible mixture in ppm: $i C_8H_{18}$: 1612; $n C_7H_{16}$: 179; $OME_1$: 4179; $O_2$: 38489; $N_2$: 955541

# L $OME_2$ / PRF90 (70:30) blend

## L.1 Measured ignition delay time data for $OME_2$ / PRF90 (70:30)

| Expt. No No | $T_5$ [K] | $p_5$ [bar] | $\tau_{head-on}$ [$\mu s$] $\gamma$ = 431 nm (CH*) | $\tau_{side-on}$ [$\mu s$] $\gamma$ = 431 nm (CH*) | $\tau_{side-on}$ [$\mu s$] $\gamma$ = 308 nm (OH*) |
|---|---|---|---|---|---|
| 6756 | 1761 | 3.9 | 9 | 8 | 9 |
| 6757 | 1974 | 4.0 | 4 | 5 | 6 |
| 6758 | 1622 | 4.1 | 27 | 23 | 25 |
| 6759 | 1502 | 4.1 | 68 | 60 | 63 |
| 6760 | 1363 | 4.0 | 257 | 238 | 237 |
| 6761 | 1291 | 4.2 | 495 | 478 | 469 |
| 6762 | 1223 | 4.0 | 1280 | 1280 | 1280 |
| 6763 | 1132 | 4.0 | 3000 | 3000 | 3010 |
| 6764 | 1062 | 3.9 | 5070 | 5140 | 5060 |
| 6766 | 1036 | 4.0 | 5970 | 6790 | 6710 |
| 6767 | 971 | 3.6 | 14500 | 14970 | 14950 |
| 6768 | 1013 | 3.9 | 7860 | 8670 | 8570 |
| 6769 | 1427 | 4.1 | 132 | 120 | 120 |
| 6770 | 1174 | 4.0 | 2050 | 2210 | 2200 |
| 6772 | 1095 | 3.9 | 4190 | 4260 | 4200 |
| 6773 | 1248 | 4.0 | 858 | 742 | 757 |
| 6774 | 1557 | 4.1 | 40 | 35 | 38 |
| 6775 | 1673 | 3.9 | 16 | 0 | 14 |
| 6776 | 1852 | 3.9 | 5 | 5 | 6 |

Combustible mixture in ppm: $OME_2$: 4029; $OME_1$: 80; $CH_3OH$: 44; $iC_8H_{18}$: 1602; $nC_7H_{16}$: 178; $O_2$: 38774; $N_2$: 955291

## L.2 Experimental pressure profile for $OME_2$ / PRF90 at 4 bar

| time [$\mu$s] | $p(t)$ / $p(t = 0)$ | | | | |
|---|---|---|---|---|---|
| 0 | 1.0 | Cont'd | | Cont'd | |
| 79 | 1.0 | 1800 | 1.09 | 4011 | 1.26 |
| 157 | 1.0 | 1809 | 1.09 | 4090 | 1.27 |
| 200 | 1.0 | 1888 | 1.09 | 4169 | 1.28 |
| 236 | 1.0 | 1966 | 1.09 | 4247 | 1.29 |
| 315 | 1.01 | 2000 | 1.09 | 4326 | 1.30 |
| 393 | 1.01 | 2045 | 1.10 | 4404 | 1.31 |
| 400 | 1.01 | 2124 | 1.10 | 4483 | 1.32 |
| 472 | 1.01 | 2202 | 1.10 | 4562 | 1.33 |
| 551 | 1.02 | 2281 | 1.11 | 4640 | 1.34 |
| 600 | 1.02 | 2360 | 1.11 | 4719 | 1.35 |
| 629 | 1.02 | 2438 | 1.11 | 4798 | 1.36 |
| 708 | 1.02 | 2517 | 1.12 | 4876 | 1.37 |
| 787 | 1.03 | 2596 | 1.12 | 4955 | 1.38 |
| 800 | 1.03 | 2674 | 1.13 | 5034 | 1.39 |
| 865 | 1.03 | 2753 | 1.13 | 5112 | 1.40 |
| 944 | 1.04 | 2831 | 1.14 | 5191 | 1.40 |
| 1000 | 1.04 | 2910 | 1.14 | 5270 | 1.41 |
| 1022 | 1.04 | 2989 | 1.15 | 5348 | 1.42 |
| 1101 | 1.05 | 3067 | 1.16 | 5427 | 1.43 |
| 1180 | 1.05 | 3146 | 1.16 | 5506 | 1.43 |
| 1200 | 1.05 | 3225 | 1.17 | 5584 | 1.44 |
| 1258 | 1.06 | 3303 | 1.18 | 5663 | 1.44 |
| 1337 | 1.06 | 3382 | 1.19 | 5742 | 1.45 |
| 1400 | 1.07 | 3461 | 1.19 | 5820 | 1.45 |
| 1416 | 1.07 | 3539 | 1.20 | 5899 | 1.45 |
| 1494 | 1.07 | 3618 | 1.21 | 5978 | 1.46 |
| 1573 | 1.07 | 3697 | 1.22 | 6056 | 1.46 |
| 1600 | 1.08 | 3775 | 1.23 | 1000000 | 1.46 (Extrapolation) |
| 1652 | 1.08 | 3854 | 1.24 | | |
| 1730 | 1.08 | 3933 | 1.25 | | |

Combustible mixture in ppm: $OME_2$: 4029; $OME_1$: 80; $CH_3OH$: 44; $iC_8H_{18}$: 1602; $nC_7H_{16}$: 178; $O_2$: 38774; $N_2$: 955291

# M *Iso*-$OME_2$ / PRF90 (70:30) blend

## M.1 Measured ignition delay time data for *iso*-$OME_2$ / PRF90 (70:30)

| Expt. No | $T_5$ [K] | $p_5$ [bar] | $\tau_{head-on}$ [$\mu s$] $\gamma$ = 431 nm (CH*) | $\tau_{side-on}$ [$\mu s$] $\gamma$ = 431 nm (CH*) | $\tau_{side-on}$ [$\mu s$] $\gamma$ = 308 nm (OH*) |
|---|---|---|---|---|---|
| 6785 | 2042 | 3.9 | 3 | | 6 |
| 6787 | 1953 | 3.9 | 5 | 6 | 7 |
| 6788 | 1767 | 3.9 | 16 | 9 | 10 |
| 6789 | 1691 | 4.1 | 23 | 13 | 14 |
| 6790 | 1591 | 4.1 | 50 | 32 | 34 |
| 6791 | 1519 | 4.0 | 69 | 62 | 65 |
| 6792 | 1417 | 4.0 | 197 | 179 | 181 |
| 6793 | 1343 | 4.1 | 388 | 365 | 364 |
| 6794 | 1257 | 4.1 | 851 | 835 | 828 |
| 6795 | 1175 | 4.0 | 2180 | 2230 | 2200 |
| 6796 | 1114 | 3.9 | 3720 | 3630 | 3620 |
| 6797 | 1035 | 4.0 | 6910 | 7110 | 7060 |
| 6799 | 1003 | 3.9 | 8490 | 8520 | 8510 |
| 6800 | 962 | 3.8 | 12710 | 12590 | 12500 |
| 6801 | 952 | 3.7 | 14040 | 13980 | 14060 |
| 6802 | 1066 | 3.9 | 5250 | 5130 | 5120 |
| 6803 | 1471 | 4.1 | 113 | 103 | 106 |
| 6804 | 1198 | 3.9 | 2060 | 2000 | 2000 |
| 6805 | 1283 | 3.8 | 666 | 642 | 638 |
| 6806 | 1212 | 4.0 | 1660 | 1670 | 1650 |

Combustible mixture in ppm: *iso*-$OME_2$: 3358; $CH_3OH$: 494; $CH_3OCHO$: 299; *i*$C8H_{18}$: 1601; *n*$C_7H_{16}$: 178; $O_2$: 38799; $N_2$: 955270

## M.2 Experimental pressure profile for *iso*-$OME_2$ / PRF90 4 bar

| time [$\mu$s] | $p(t)$ / $p(t = 0)$ | | | | |
|---|---|---|---|---|---|
| 0 | 1 | Cont'd | | Cont'd | |
| 97 | 1 | 1836 | 1.08 | 4348 | 1.32 |
| 193 | 1 | 1933 | 1.09 | 4445 | 1.33 |
| 200 | 1 | 2000 | 1.09 | 4542 | 1.34 |
| 290 | 1.01 | 2029 | 1.09 | 4638 | 1.35 |
| 387 | 1.01 | 2126 | 1.1 | 4735 | 1.37 |
| 400 | 1.01 | 2222 | 1.11 | 4831 | 1.38 |
| 483 | 1.01 | 2319 | 1.11 | 4928 | 1.39 |
| 580 | 1.02 | 2416 | 1.12 | 5025 | 1.4 |
| 600 | 1.02 | 2512 | 1.12 | 5121 | 1.41 |
| 676 | 1.02 | 2609 | 1.13 | 5218 | 1.42 |
| 773 | 1.03 | 2706 | 1.14 | 5315 | 1.43 |
| 800 | 1.03 | 2802 | 1.14 | 5411 | 1.44 |
| 870 | 1.03 | 2899 | 1.15 | 5508 | 1.44 |
| 966 | 1.04 | 2996 | 1.16 | 5604 | 1.45 |
| 1000 | 1.04 | 3092 | 1.17 | 5701 | 1.46 |
| 1063 | 1.04 | 3189 | 1.18 | 5798 | 1.46 |
| 1160 | 1.05 | 3285 | 1.19 | 5894 | 1.47 |
| 1200 | 1.05 | 3382 | 1.2 | 5991 | 1.47 |
| 1256 | 1.05 | 3479 | 1.21 | 6088 | 1.48 |
| 1353 | 1.06 | 3575 | 1.22 | 6184 | 1.48 |
| 1400 | 1.06 | 3672 | 1.23 | 6281 | 1.48 |
| 1449 | 1.06 | 3769 | 1.24 | 6378 | 1.48 |
| 1546 | 1.07 | 3865 | 1.25 | 6474 | 1.48 |
| 1600 | 1.07 | 3962 | 1.27 | 6571 | 1.48 |
| 1643 | 1.07 | 4058 | 1.28 | 1000000 | 1.48 (Extrapolation)) |
| 1739 | 1.08 | 4155 | 1.29 | | |
| 1800 | 1.08 | 4252 | 1.3 | | |

Combustible mixture in ppm: *iso*-$OME_2$: 3358; $CH_3OH$: 494; $CH_3OCHO$: 299; *i*$C8H_{18}$: 1601; *n*$C_7H_{16}$: 178; $O_2$: 38799; $N_2$: 955270